THÈSE

UNIVERSITE DE PAU ET DES PAYS DE L'ADOUR
ECOLE DOCTORALE DES SCIENCES EXACTES ET DE LEURS APPLICATIONS

Présentée et soutenue le 19 Novembre 2015
par **Atiria FAJARDO RENGIFO**

pour obtenir le grade de docteur
de l'Université de Pau et des Pays de l'Adour
Spécialité : Sciences de la Terre

NEOTECTONIC EVOLUTION OF THE SERRANIA DEL INTERIOR RANGE AND MONAGAS FOLD AND THRUST BELT, EASTERN VENEZUELA: MORPHOTECTONICS, SEISMIC PROFILES ANALYSES AND PALEOMAGNETISM

MEMBRES DU JURY

RAPPORTEURS
- Christian BECK — Professeur émérite / ISTerre, Université de Savoie.
- Juan José VILLALAIN — Professeur / Université de Burgos.

EXAMINATEURS
- Jean Paul CALLOT — Professeur / Université de Pau et des Pays de l'Adour.
- Bernard MONOD — Ingénieur docteur / BRGM.

DIRECTEURS
- Charles AUBOURG — Professeur / Université de Pau et des Pays de l'Adour.
- Bertrand NIVIERE — Maitre de Conférences / Université de Pau et des Pays de l'Adour.

CO-ENCADRANT
- Vincent REGARD — Maitre de Conférences - HDR / Université de Toulouse.

UNIVERSITÉ DE PAU ET DES PAYS DE L'ADOUR

This page is intentionally left in blank

"Cada ser tiene dentro de sí el impulso divino de continuar elevándose hacia escalones superiores. Cada uno con sus propias comprensiones y trabajo a realizar. Al estar preparado para lo siguiente; ese fuego interno los pondrá en la puerta del próximo escalón por alcanzar"

Araceli Egea

This page is intentionally left in blank

To my parents, for giving me
the foundation for living.

This page is intentionally left in blank

ACKNOWLEDGEMENTS

These pages are just a small sample of the true and profound gratitude that I feel in my heart for the people and institutions that I will name here. Their support, help and collaboration made each step of this journey an unforgettable experience.

I want to thank the Fundación Gran Mariscal de Ayacucho (FUNDAYACUCHO) and the French Embassy in Venezuela for awarding me a scholarship during 3 years in France. To PDVSA for giving permission to carry out my studies and to finance the trips to France these last two years.

I want to thank my first advisors, Damien Dhont and Yves Hervouët and my final advisors: Charles Aubourg and Bertrand Nivière. Thanks Charles for taking the direction of this work that was not in your projects, thanks for help me in reorienting the thesis to finally reactivate after nearly a year on standby.

Thanks to the members of the jury, Mrs: Christian BECK, Juan VILLALAÍN, Vincent REGARD, Jean Paul CALLOT and Bernard MONOD for their time and contribution to improve this manuscript.

Very special thanks to my ex-boss, translator and good friend Dr. Frances McCarty for believing in me from the beginning and for insisting to get my permission of job. Thank you for to be always present and for this beautiful friendship that has developed between us.

Thanks to Javier Pérez, exploration manager for allowing me access to the data for my thesis, supporting me with the logistics of the field work and always keeping the door open for me. To Wilfredo Avila, Carlos Márquez and Marta Carrillo, managers at PDVSA-INTEVEP for their unconditional support and understanding during these last 2 years of the thesis. To my co-workers and colleagues: Oswaldo Guzmán, Enrique Toribio, Roberto Wagner, Alejandro González, Brian Vilas and Luis Camposano for the technical discussions that enriched my knowledge and nurtured this work. Also, special thanks to my friend Inti Rodríguez for introducing me to Petrel software and giving me optimism and enthusiasm during this time.

To Lenin Ortega and Professor Redescal Uzcátequi for their valuable intellectual and technical input in the fieldwork during all this time. Thanks guys!!

To the paleomagnetism laboratory staff in Burgos (Spain) and Marseilles (France). Especially, to François Demori and Juan Villalaín for guiding me in the treatment of paleomagnetic samples.

François thanks for the good moments of teamwork and for opening me the doors of your home and family.

To the families who welcomed us during my familiy's stay in France and made us feel at home: Marelis, thanks for encouraging me, for encouraging me in difficult times, thanks to you and your beautiful family. To Jean Xavier Paul and Yves Hervouët for having us from day one within their families, offerings support and showing us the French hospitality.

I would also like to thank to all the laboratory, professors and staff, especially to my PhD and post-PhD friends who are still present: Mohannad, Nesma, Julia, Mathieu, Charlie, Charlotte, Damien, Toqueer, Julian and the youngest, Nemo and Etienne, thanks to all you for the afternoon tea on the terrace and by the funny "soirées".

Finally, I would like to thank my husband Jose Antonio García for being at my side as friend, partner and colleague at the University. To my son Fernando, who unknowingly transported me to a world of smiles and love making me forget the moments of fatigue and difficulty.

Thanks to all those people in France and Venezuela which in one way or another stood by me at this stage of my life.

This page is intentionally left in blank

RÉSUMÉ

La convergence oblique entre les plaques Caraïbes et Amérique du Sud à partir de l'Oligocène a conduit à la formation de la cordillère de la Serranía del Interior (SDI), de son avant pays au sud (bassin de Maturín) et la ceinture plissée de Monagas. D'abord transpressif (direction NW-SE), le déplacement entre les deux plaques devient à compter de ~12 Ma une translation O-E qui s'accommode principalement sur la faille d'El Pilar. Cependant, des indices de compression active ont été identifiés a la terminaison de la faille d'Urica dans la chaine plissée de Monagas. Pour discuter des mécanismes de cette déformation compressive actuelle, nous avons mis en œuvre une interprétation sismique (2D et 3D), une étude géomorphologique et une étude paléomagnétique.

Depuis le front sud de la SDI dans la chaîne plissée de Monagas, l'interprétation sismique et l'analyse géomorphologique se sont concentrées sur les chevauchements de San Félix, Tarragona, Punta de Mata, Jusepín et Amarilis. Deux discordances miocènes (Mid-Miocene Unconformity (MMU) de ~10 Ma et Late Miocene Unconformity (LMU) de ~5,3 Ma) ont été cartographiées sur la sismique. En s'appuyant sur la LMU, il a été calculé à l'aplomb de ces accidents un taux de soulèvement plio-pléistocène de ~0,4 mm/a.

Invisibles sur la sismique, des déformations ont aussi été observées en surface sur ces accidents (des terrasses fluviatiles basculées, plissées et faillées et des anomalies de drainage). Datées par des méthodes cosmonucléides (^{10}Be et ^{26}Al), l'âge des terrasses alluviales déformées sont compris entre ~90 ka sur le chevauchement de Tarragona et ~15 ka dans la zone de Punta de Mata. Un taux minimal de soulèvement pléistocène terminal à l'aplomb des chevauchements a été calculé entre 0,1 et 0,6 mm/a. Cette gamme de vitesse recouvre celle renvoyée par la LMU et montre que la déformation n'a pas varié significativement pendant les derniers 5,3 Ma.

Ces observations montrent que les chevauchements de Tarragona, Pirital El Furrial et d'autres plus jeunes développés dans la formation Carapita restent actifs. Cette déformation superficielle s'estompe rapidement vers l'est près de la ville Maturín. Nous interprétons cette déformation comme liée au jeu récent de la faille d'Urica qui se termine au sud en queue de cheval. La faille d'Urica accommoderait donc une partie du déplacement entre plaques Caraïbe et Amérique du Sud.

Une étude paléomagnétique a été réalisée dans les blocs de Caripe et Bergatín au sein de la SDI où 27 localités ont été échantillonnées dans les sédiments du Crétacé au Paléocène. Une

observation clé de cette étude a été la mise en évidence d'une composante paléomagnétique stable déviée vers le Nord Est avec des polarités normale et inverse. Les analyses statistiques de ces composantes indiquent une acquisition postérieure au plissement de la SDI (< ~12 Ma). La déclinaison moyenne dans les blocs de Caripe et de Bergatín indique une rotation horaire de R=37º±4 º autour d'un axe vertical. Le taux de rotation post-Miocene moyen avoisine ~3.7º/Ma et reste probablement actif. Nous proposons de rattacher cette rotation horaire à un système de failles type "Riedel" (Urica et San Francisco) en relation avec la faille d'El Pilar.

This page is intentionally left in blank

ABSTRACT

In Northeastern Venezuela, the tectonic provinces of the Serranía Del Interior thrust belt (high hills), the Monagas thrust belt (foothills) and the Maturín foreland basin formed as a result of the oblique convergence between the Caribbean and South American plates since the Oligocene. Since ~12 My, the Caribbean plate movement changed from east-southeast transpression to predominately eastward translation. GPS data show that post 12 My wrenching component between the plates is accommodated predominantly by the E-W strike-slip El Pilar Fault. However, evidence of active compression has been identified in the southern limit of the NW-SE dextral Urica Fault, specifically, in the Monagas Fold and Thrust Belt. In order to constrain the neotectonics of this area, this thesis presents a combined approach, which includes geomorphological study, seismic interpretation (2D and 3D) and paleomagnetism.

In the Monagas Fold and Thrust Belt, the geomorphological study and the seismic interpretation were focused on five zones. From the foothills to the deformation front, these zones are: San Felix, Tarragona, Punta de Mata, Jusepín and Amarilis. These areas show surface deformations such as topographic uplifts, tilted terraces, folded terraces, faulted terraces, and drainage anomalies.

The dating of the river terraces through ^{10}Be and ^{26}Al methods indicates that these terraces formed in the Late Pleistocene. The oldest terrace located in the Tarragona zone has a maximum exposure age of ~90 ky and the youngest located in the Punta de Mata zone of ~15 ky. From this dating, a minimum vertical deformation rate between ~0.6-0.1 mm/y was calculated for this area.

Using the seismic interpretation of a 3D block, the surfaces of two unconformities (MMU and LMU) have been mapped. The age obtained for the LMU (~5.3 My), yield a Plio-Pleistocene uplift rate between ~0.3-0.4 mm/y, which is close to the vertical deformation rate calculated from the terraces dated. These similar rates seem to indicate that the deformation rate in the MFTB has not changed significantly for the last 5.3 My.

The deformed surfaces observed in the field and in DEM images coincide vertically with the deep structures interpreted in the seismic lines. I propose that the deformation on the surface is linked to the Tarragona, Pirital, Furrial thrusts and the Amarilis Backthrust activity and to the youngest thrusts developed in the Carapita Formation. However, this surface deformation dies out near the city of Maturín, therefore, the neotectonic deformation is inferred to be caused by local tectonics. I propose that this local compressive deformation could have been generated by

a horsetail termination in the southern limit of the Urica Fault which reactivated the oldest thrusts (Tarragona and Pirital thrusts) and deformed the post-Middle Miocene units until reaching the surface.

In the zones where the El Pilar Fault mainly accommodates the wrenching component, block rotation is likely. For that reason, a paleomagnetic study was conducted in the Caripe and Bergatín blocks of the Serranía Del Interior where 27 sites were sampled in Cretaceous to Paleocene sediments. A key finding was a magnetization component of both normal and reverse polarities with a southwest deviation. Statistics analyses of the components yield a negative bedding-tilt test, indicating that this component was acquired post ~12 My after the folding process in the Serranía del interior. The average declination indicates a clockwise block rotation of R = 37º ± 4º and a post-Middle Miocene rotation rate of ~3.7º/My in both the Caripe and Bergatín blocks. This rotation rate is probably still active. I propose to relate the regional clockwise rotation to the development of a synthetic Riedel shear system formed by the El Pilar Fault (master regional fault) and by the Urica and San Francisco synthetic Riedel shears. At the same time, this system could transfer some material from the Serranía Del Interior towards the Monagas Fold and Thrust Belt through the different thrusts characteristic of this province.

This page is intentionally left in blank

CONTENTS

CHAPTER 1. INTRODUCTION

1.1. Context

Since the Oligocene, the oblique collision between the Caribbean and South American plates formed the Serranía Del Interior (SDI) Mountain Range and the Maturín Foreland Basin. Many authors have developed geological interpretations, structural models, tectono-sedimentary analyses, and stratigraphic modeling from the Cretaceous to Middle Miocene in order to understand the regional tectonic. In addition, many studies are motivated by hydrocarbon exploration within the Maturín Basin, specifically in the Monagas Fold and Thrust Belt (MFTB) (Figure 1.1). In contrast, very few studies have focused on the Neogene geological episode (e.g. Zinck and Urriola, 1970; Singer et al., 1998; Audemard et al., 2002, among others). Active faults and recent deformation have been poorly identified in this area.

In 2004, an unpublished undergraduate study carried out by R. Wagner and supervised by F. Audemard and B. Nivière inspired the main core of this thesis. A report on this study shows the existence of a set of terraces located to the north of the MFTB which suggest recent tectonic activity. However, these terraces were not dated. The active tectonics have been effectively studied by the Fundación Venezolana de Investigaciones Sismológicas (FUNVISIS) through geodesic, seismic data, focal mechanisms (Audemard, 2000; Audemard et al., 2000; 2005) and GPS studies (Jouanne et al., 2011; Reinoza et al., 2015), all data suggest poor evidence of neotectonics within the SDI and MFTB. The published cross-sections within the MFTB carried out by several authors (e.g. Roure et al., 2003; Duerto, 2007; Parra et al., 2011, among others) show the folding of the post-Miocene sequences and unconformities, suggesting a recent deformation younger than 10 My. The motivation of this thesis is to date the deformed surfaces using cosmogenic nuclides (^{10}Be and ^{26}Al method) and in combination with detailed interpretation of 3D seismic to calculate the deformation rate in the area. To understand the origin of the recent deformation, I thought the tectonic system present in SDI accommodated mainly by the major Pilar, Urica and San-Francisco strike-slip faults, is considered to play a role in the active deformation within the MFTB. For this reason, a paleomagnetic study within the SDI was carried out in order to determine the kinematic and quantification of the block rotation in the whole system.

1.2. Location of the Study Area

The study area is located in the Northeastern Venezuelan between 9°30’ N and 10°30’ N latitudes and 62°30 W and 64°30 W longitudes. From north to south, it includes the SDI, the

MFTB and the Maturín foreland basin.

The SDI hinterland range is a thrust belt uplifted from the Oligocene to Middle Miocene period (Duerto, 2007). It is formed by folds with a N60-70E strike direction composed of pre-Cretaceous to Tertiary strata (González de Juana et al., 1980; Vivas and Mactosay, 1995). The San Francisco strike-slip fault divides it into two blocks: Bergatín and Caripe (Salvador and Rosales, 1960). The SDI is limited by the El Pilar right-lateral strike-slip fault to the north, the Urica and Los Bajos right-lateral strike-slip faults to the west and east respectively and by the Pirital Thrust system to the south (Figure 1.1A).

The MFTB is located between the SDI and the deformation front. Here, the thick lithographic section is composed by pre-Cretaceous to Middle Miocene rocks which have been folded and thrusted (Jácome et al., 2003; Parra et al., 2011). The compression in this province is mainly accommodated by the Pirital and El Furrial Thrust systems. The Pirital Thrust contains pre-Cretaceous rocks in a thick section; on the contrary, the Furrial Thrust involves only cretaceous rocks in a thinner section (Roure et al., 2003). The Furrial Thrust is associated with fault-bend fold structures (Marquez et al., 2003). Above, a thin-skinned tectonic wedge is formed by Late Miocene to Pleistocene rocks which have been slightly folded (Figure 1.1B).

1.3.Objectives

The aims of this research are:

- To determine the Neogene kinematics of the Serranía Del Interior using the paleomagnetic method.
- To locate and quantify the active surface deformation in the Monagas Fold and Thrust Belt using geomorphological analysis and dating terraces through ^{10}Be and ^{26}Al dating method.
- To analyze the deep structures (from Cretaceous to Pleistocene units) using 2D and 3D seismic interpretation.
- To establish the relation between the surface deformation and the deep structures of the Monagas Fold and Thrust Belt.
- To propose a Neogene kinematic model in the Serranía Del Interior Range and in the Monagas Fold and Thrust Belt integrating geomorphological, seismic and paleomagnetic data.

.

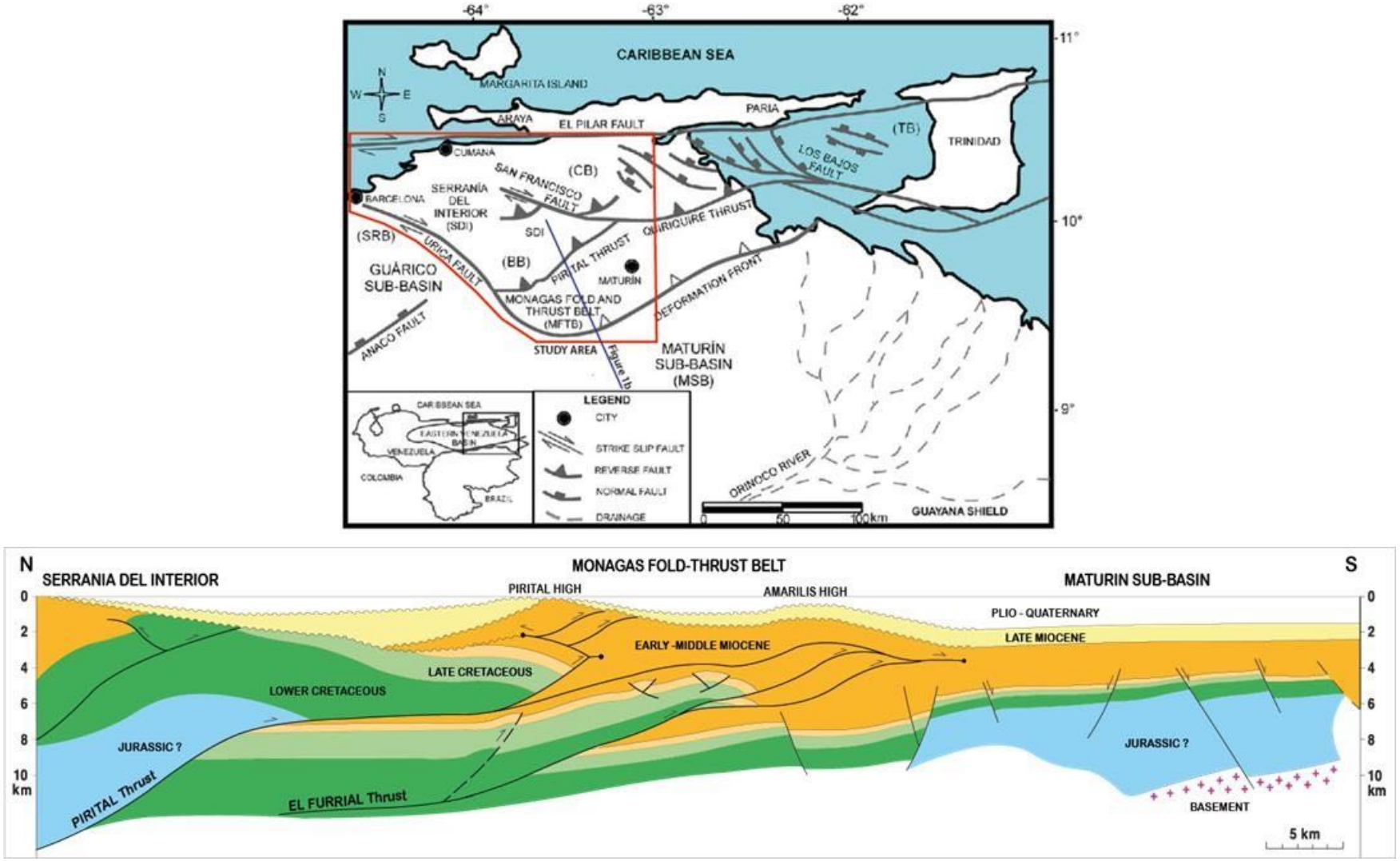

Figure 1.1. Tectonic sketch – map of Eastern Venezuela showing the study area location (top left) (modified from Parra et al., 2011). In depth cross-section showing the general structural configuration of the study area (bottom) (modified from Roure et al., 2003)

1.4. Outline

This thesis begins with a summary of the Caribbean plate geodynamics, tectono-stratigraphy and neotectonics in the Northeastern Venezuelan Basin (CHAPTER 2). The results are shown in three chapters (CHAPTER 3, 4 and 5). Each of these chapters is organized in the same way; explanation of the method, presentation of results and discussion. Geomorphology is present in CHAPTER 3. In the methods section of this chapter, the morphotectonic markers of the quaternary deformation, the ^{10}Be and ^{26}Al dating method and the uplift rates quantification are presented briefly. The results obtained in the Monagas Fold and Thrust Belt will also be presented. These results allow the quantification of vertical deformation rate on the order of ~0.1 – 0.6 mm/y. In CHAPTER 4, the results of 2D and 3D seismic analysis carried out in the Tarragona, San Felix, Punta de Mata, Jusepín and Amarilis zones (Monagas Fold and Thrust Belt) are presented. A vertical uplift rate of ~0.3 mm/y is obtained from this analysis. In 0, the basics of paleomagnetism, followed by a description of the methods used are considered briefly. The paleomagnetic results bring constraints on the rotation rate of the SDI of ~3.7°/My. Finally, in CHAPTER 6, all results are integrated and some conceptual models are proposed to explain the location of active tectonics near the Urica Fault and to explain the origin of clockwise rotation of the SDI.

CHAPTER 2. TECTONIC SETTING OF THE NORTHEASTERN VENEZUELAN BASIN

This chapter presents: 1) A review of the origin, formation and kinematics of the Caribbean Plate and its interaction with North and South American plates; 2) The regional tectonic setting of the Northeastern Venezuelan Basin controlled by the interaction of the Caribbean and South America plates; 3) The description of the different structural provinces present in the area as a result of this interaction; 4) the tectono-stratigraphic evolution of the Maturín Foreland Basin and 5) A description of the neotectonic deformation in the Northeastern Venezuelan Basin.

2.1. Caribbean Plate Kinematics

The tectonics of the Caribbean is mainly determined by the interaction of the Caribbean plate with the South America and Atlantic plates, this being a tectonically complex zone.

Two main models have been proposed to explain the origin and kinematics of the Caribbean plate (Figure 2.1):

1. **The Intra-American Model**. This model suggests the formation of the Caribbean crust to the west from its present position, between the North and South American plates (130 to 80 Ma) (Ball et al., 1969; Aubouin et al., 1982; Sykes et al., 1982; Donnelly, 1985; Frisch et al., 1992; all these in Meschede & Frisch, 1998) (Figure 2.1A)

2. **The Pacific Model.** This model suggests the formation of the Caribbean crust in the Pacific Ocean during the Upper Mesozoic. The crust is then transported eastward to its present position between the two Americas (Ross and Scotese, 1988; Pindell and Barrett, 1990; Stephan et al., 1990, Mann, 1999; Pindell and Kennan 2001; Pindell and Kennan, 2009, among others) (Figure 2.1B).

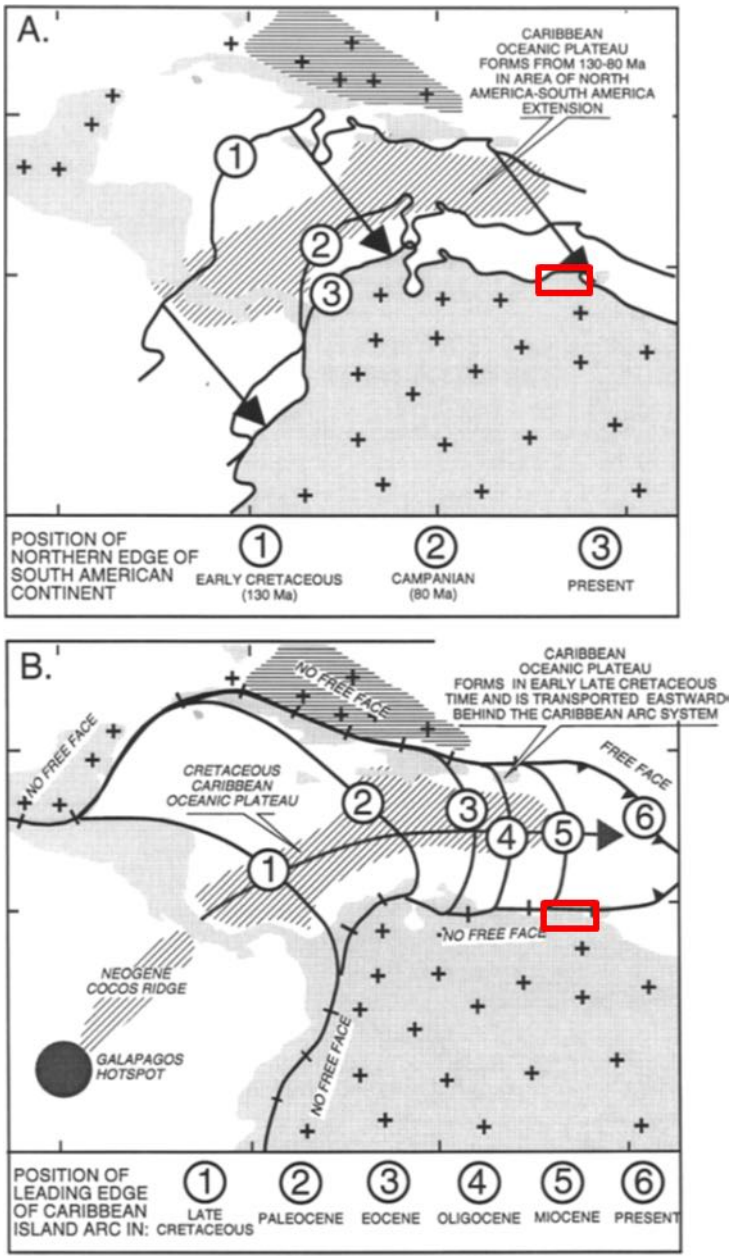

Figure 2.1. Scheme showing the two possible origins for the Caribbean plate. Crosses indicate areas of continental crust. (A) Intra-American model. The numbers give positions of the northern margin of South America according to Pindell and Barrett (1990). (B) The Pacific model. The numbers give positions of the leading edge of the Caribbean arc system and oceanic plateau through time according to Pindell and Barrett (1990). The red square represents the approximate study area location of this thesis (modified from Mann, 1999).

Attention is centered on the Pacific model as it is presently the most accepted. According to this model based on geological and kinematic data, several stages are distinguished during the tectonic evolution of the Caribbean margins:

1. Early to Late Jurassic (190-158 Ma): The rifting stage between continental blocks occurred in this period. Seafloor spreading began in the Central Atlantic and rifting continued through the margins of the Proto-Caribbean and Gulf of Mexico regions (Pindell and

Kennan, 2009). At ~158 Ma to the north, the counterclockwise rotation of the Yucatan block affected the northeast of the Gulf of Mexico. Rifting continued between North America and South America in the Late Jurassic, producing a wide gap presumably occupied by the oceanic crust generated at a Proto-Caribbean spreading ridge (Mann, 1999). The spreading of the Proto-Caribbean Seaway caused the development in Venezuela of several grabens oriented NE-SW, such as: The Espino Graben, The Apure-Mantecal Graben, the Maracaibo Graben and the Andes-Perija Graben (Figure 2.2).

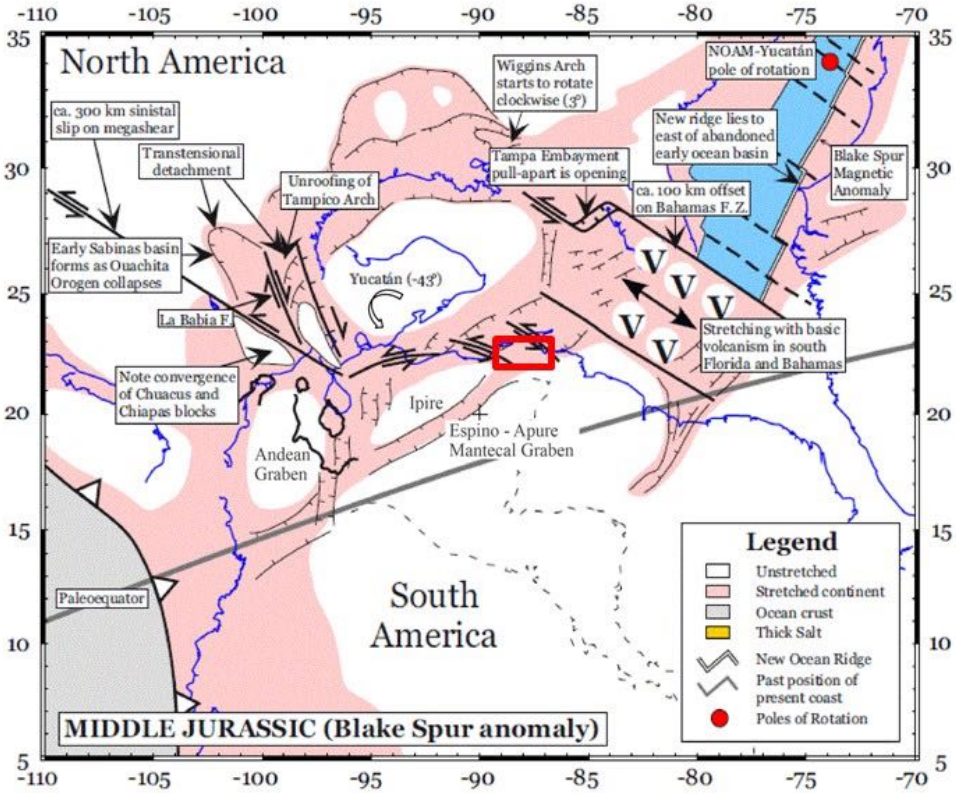

Figure 2.2. Middle Jurassic plate reconstruction. The red square represents the approximate study area location of this thesis (modified from Pindell and Kennan, 2001).

2. Early Cretaceous to Early Aptian (130-120Ma): The Yucatan block rotation ended and is settled at its current position allowing the re-organization of the Proto-Caribbean (Mann, 1999). Rifting ceased but the seafloor spreading continued between the South America and Yucatán blocks in the Early Proto-Caribbean Seaway and in the Colombian Marginal Basin (Pindell and Kennan, 2009) (Figure 2.2). Then a post-rift passive margin developed in the Bahamas, the Gulf of Mexico and the northeastern and northwestern margins of South America (Mann, 1999). At ~120 Ma (Aptian) a change occurred in the direction of movement between the Americas and the Caribbean crust was formed in the Pacific (Pindell et al., 1998; Pindell and Kennan, 2009) (Figure 2.3).

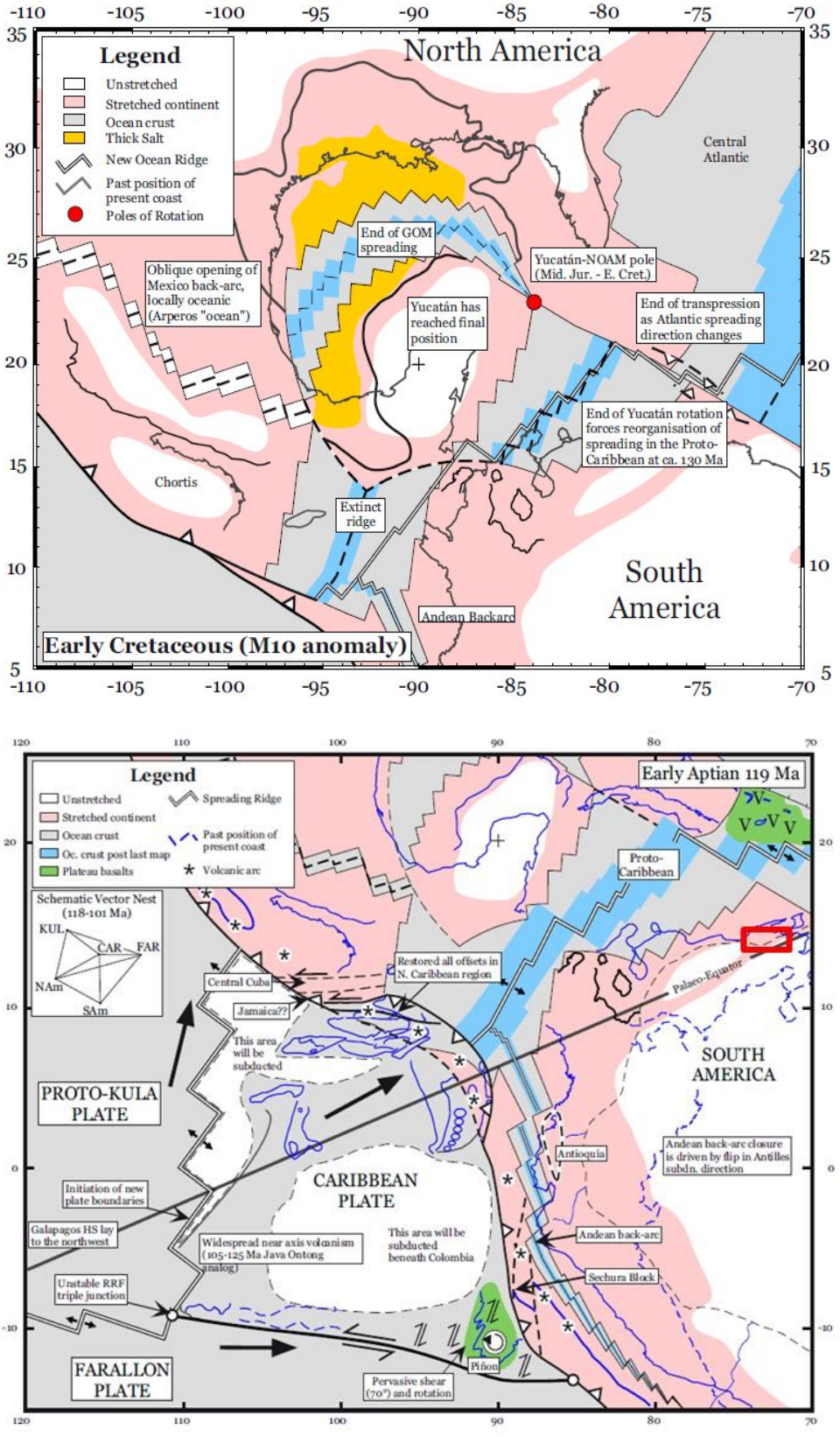

Figure 2.3. Early Cretaceous plate reconstruction (above). Early Aptian plate reconstruction (below). The red square represents the approximate study area location of this thesis (modified from Pindell and Kennan, 2001).

3. Middle Cretaceous to Late Cretaceous (100-84 Ma): Between 90-70 Ma, hotspot volcanism occurred sporadically around the Caribbean (Pindell and Kennan, 2001). The separation between the Americas is rapid, resulting in varying head-on subduction in the northeast Caribbean, while dextral strike-slip dominates over compression in Ecuador and Colombia (Pindell and Kennan, 2001) (Figure 2.4).

   At the Campanian (84 Ma) the South America-Caribbean boundary becomes more compressed due to the start of the Proto-Caribbean seafloor spreading. It ceases dramatically at 71 Ma. The Caribbean plate migrated to the north and reached to the North Andean plate zone (Pindell and Kennan, 2009) (Figure 2.4).

   Most of the convergence between the South America and Caribbean plates can be explained by the beginning of the shortening and closure of the Andean back-arc.

4. Late Paleocene to Middle Eocene (56-46 Ma): By this time (Late Paleocene) The Caribbean plate spread into the Proto-Caribbean seaway and started to migrate northeast (Stephan et al., 1990). At the same time, the Caribbean Arc migrated northeast until its collision with the Bahamas platform and western Venezuela. Toward the southeast Caribbean Plate, the extension initiated creating the Grenada Basin and the opening towards Yucatán to the north (Pindell et al., 2005, 2009). Also at this stage, the subduction of Proto-Caribbean crust beneath the passive margin of northern South America began which produced uplifting in the northern Colombia. Additionally, subduction accommodated the convergence between North and South America (Pindell et al., 1998; Pindell and Kennan, 2001) (Figure 2.5).

During the Early-Middle Eocene in western Venezuela (Maracaibo area), the Lara Nappes was emplaced and a foreland basin was formed (Stephan et al., 1990; Pindell et al., 1998). In addition, the initiation of volcanism in the new Lesser Antilles Arc began, probably as a consequence of the reorganization of the Benioff Zone during the opening of the Grenada Basin (Pindell and Barret, 1990). Another important event was the incorporation into the Caribbean plate of the Nicaragua Rise as the Chortis block as a result of the subduction termination (Figure 2.5).

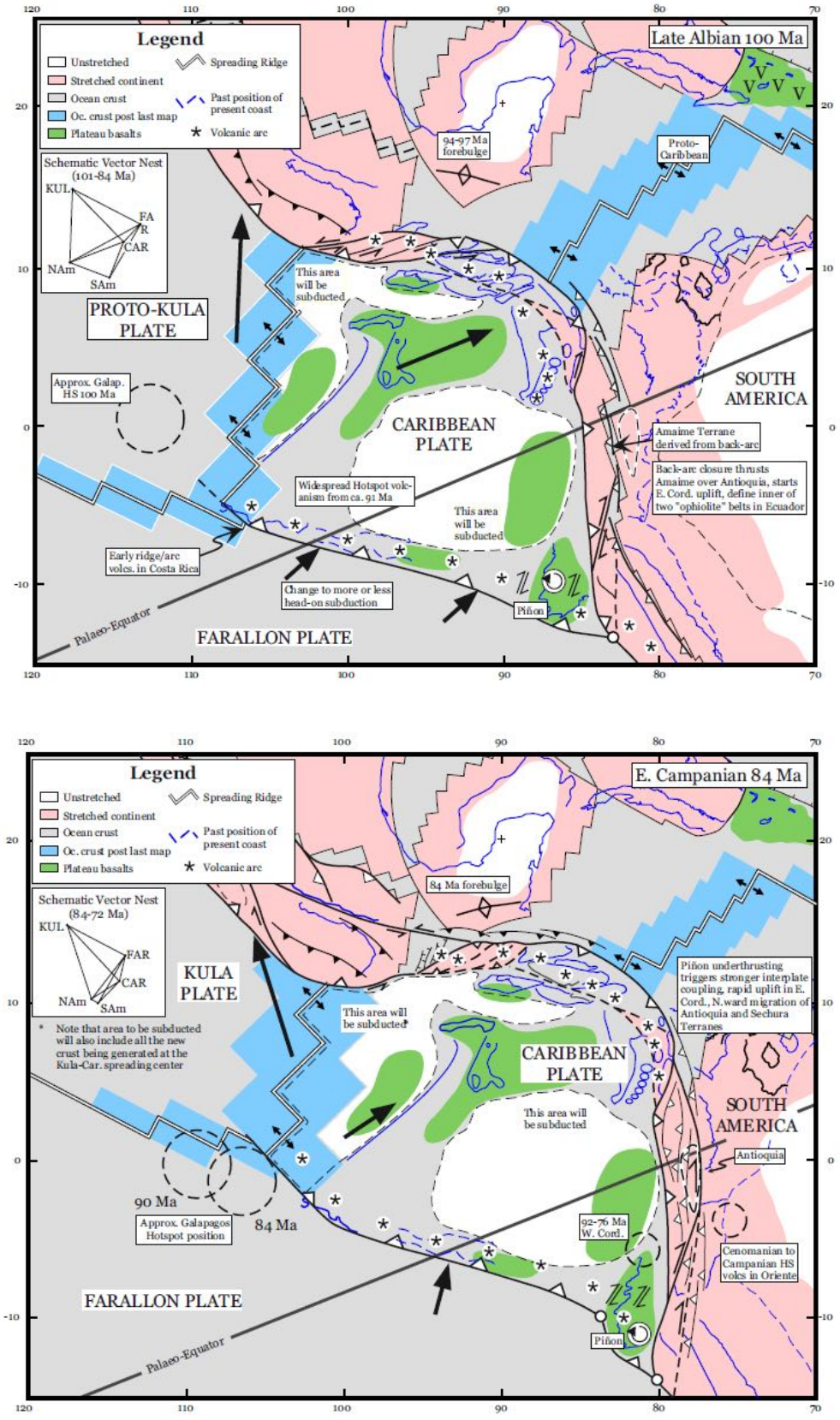

Figure 2.4. Late Albian plate reconstruction (above). Early Campanian plate reconstruction (below). The red square represents the approximate study area location of this thesis (modified from Pindell and Kennan, 2001).

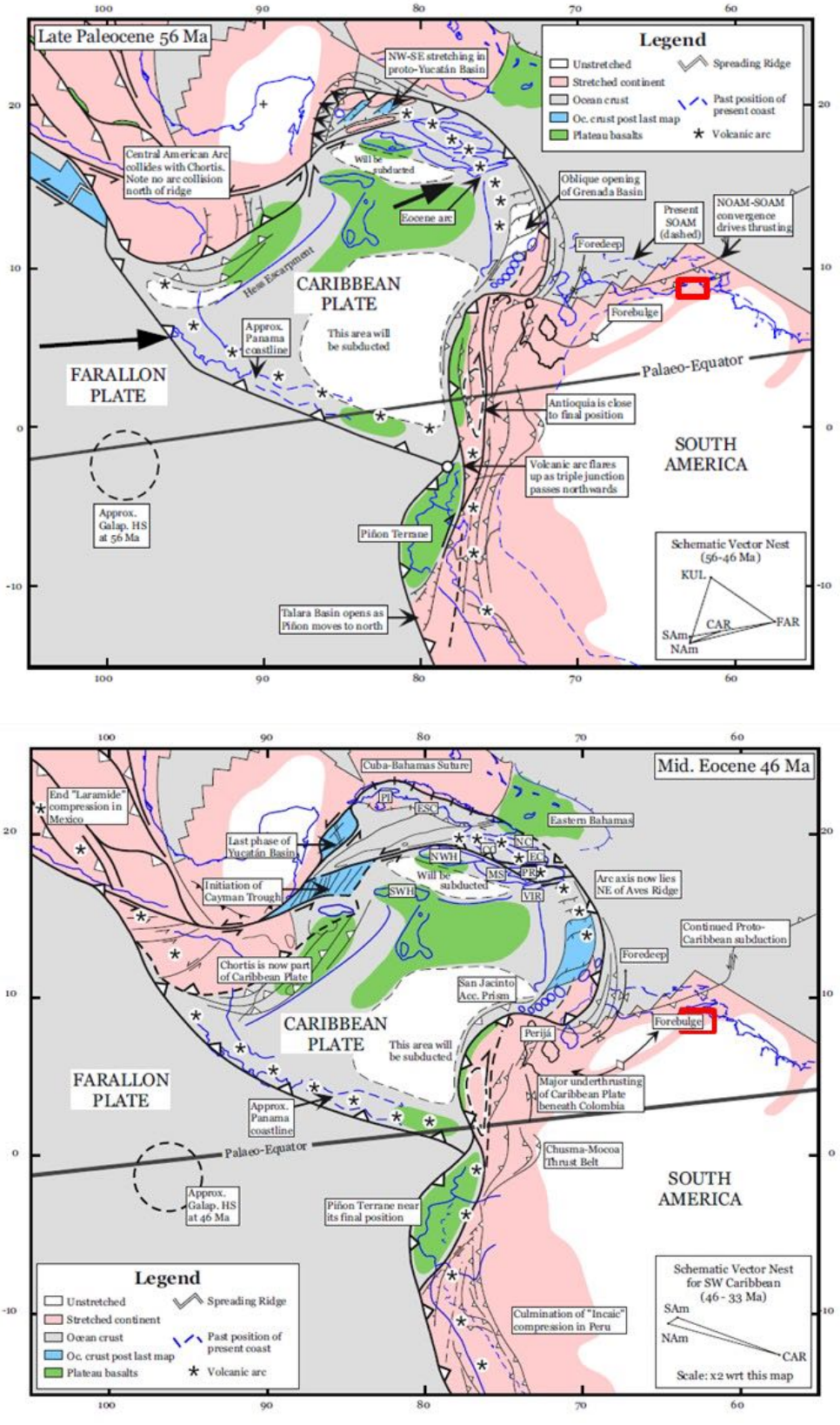

Figure 2.5. Late Paleocene plate reconstruction (above). Middle Eocene plate reconstruction (below). The red square represents the approximate study area location of this thesis (modified from Pindell and Kennan, 2001).

5. Earliest Oligocene to Middle Miocene (33-19 Ma): The movement of the Caribbean plate with respect to the South American plate was directed ENE and the effect of the oblique collision produced overthrusting of Caribbean rocks onto central and eastern Venezuela (Pindell and Kennan 2009).This eastern movement of the Caribbean plate formed strike-slip faults in the north and south of the Caribbean Sea and the foredeep migrated along northern South America. During the Late Eocene, the convergence developed between North and South America is recorded by a regional unconformity present in most of the area (Duerto, 2007) (Figure 2.6).

   In the Middle Miocene (19 Ma) the northern boundary of South America was affected by the migration of the Caribbean plate eastward defined as a diachronous transpressive movement (Pindell and Barret, 1990; Passalacqua et al., 1995; Ave Lallement, 1997; Pindell and Kennan, 1990; Lingrey, 2007) (Figure 2.6).This transpression movement is interpreted as a strain partitioning system, which is accommodated by a northern region of strike-slip deformation and a southern region of fold-thrust belt contraction. This fold-thrust belt system can be seen in the Eastern Venezuela and extends into Trinidad in three fold belt trends: The Serranía del Interior (Hinterland), the Pirital belt and the Furrial Belt (Lingrey, 2007).

6. Late Miocene to Present (10 Ma to present): This stage is called “Neo-Caribbean Phase” by Pindell and Kennan (2009) due to differences between the tectonic developments and structural style pre and post 10 Ma. According to GPS studies (DeMets, 2000; Perez et al., 2001; Weber et al., 2001) the advance of the Caribbean foredeep basin is ~20 mm/y eastward with a change in the azimuth of movement of the Caribbean plate of 85° to 70° with respect to North America (northeast Caribbean Plate) and of about 100° to 85° with respect to South America (southeast Caribbean Plate) (Dolan et al., 1998; DeMets, 2000; Pérez et al., 2001; Weber et al., 2001). This change of the azimuth of movement of the Caribbean plate is possibly the cause of neotectonics in the area (Algar and Pindell 1993; Pindell et al. 1998) (Figure 2.7 and Figure 2.8)

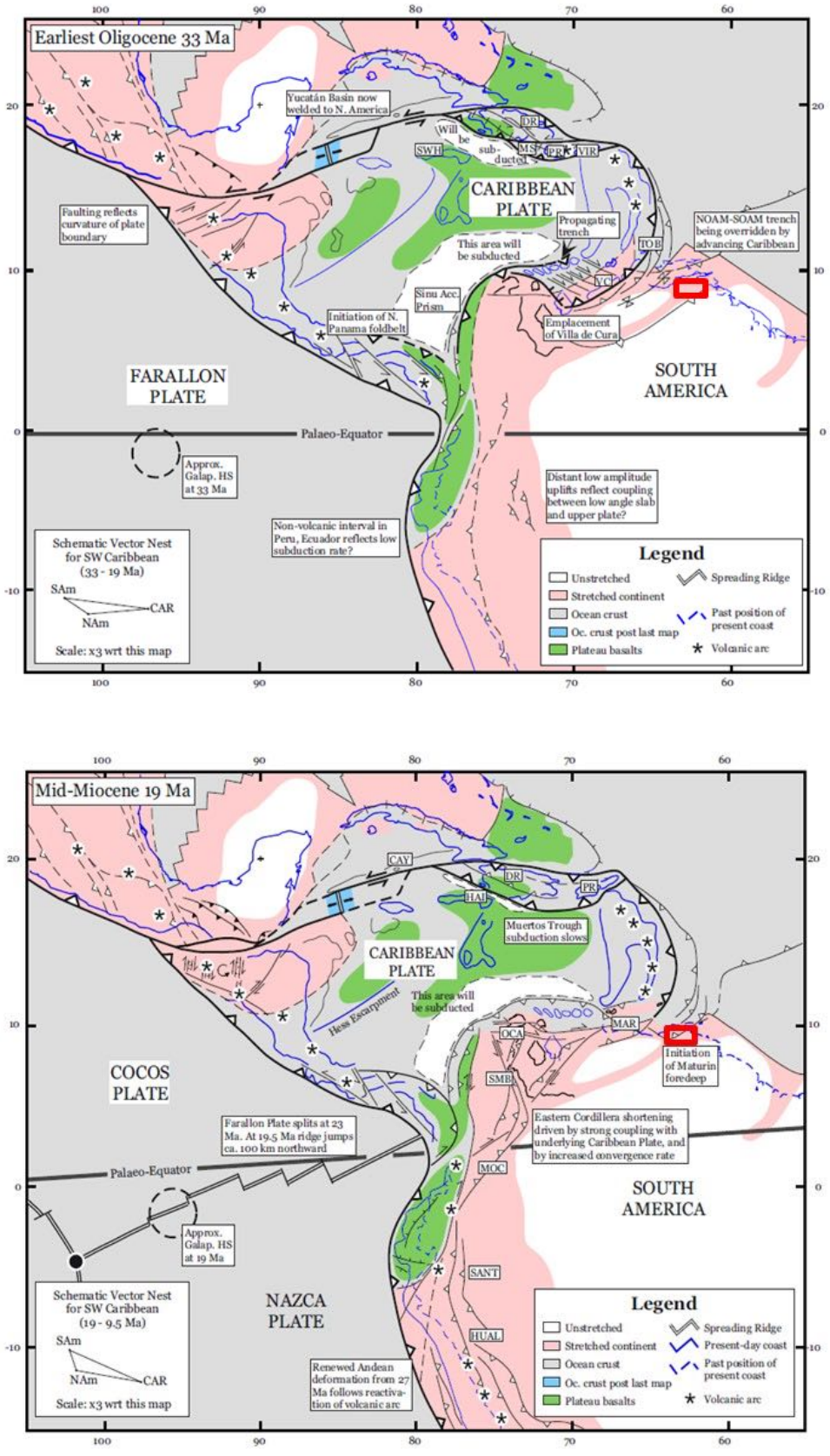

Figure 2.6. Earliest Oligocene plate reconstruction (above). Middle Miocene plate reconstruction (below). The red square represents the approximate study area location of this thesis (modified from Pindell and Kennan, 2001).

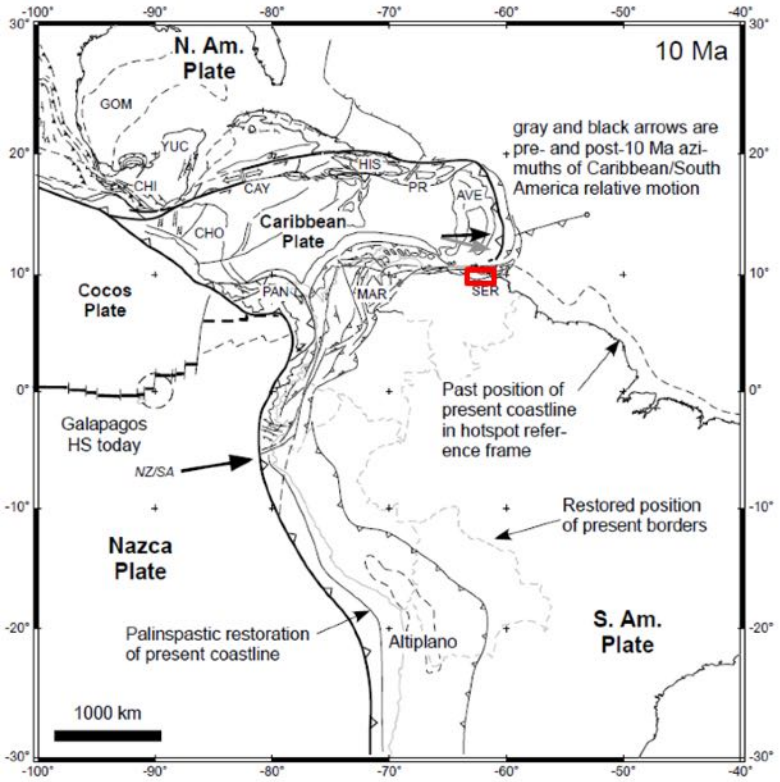

Figure 2.7. Late Miocene plate reconstruction. The red square represents the approximate study area location of this thesis (modified from Pindell and Kennan, 2001).

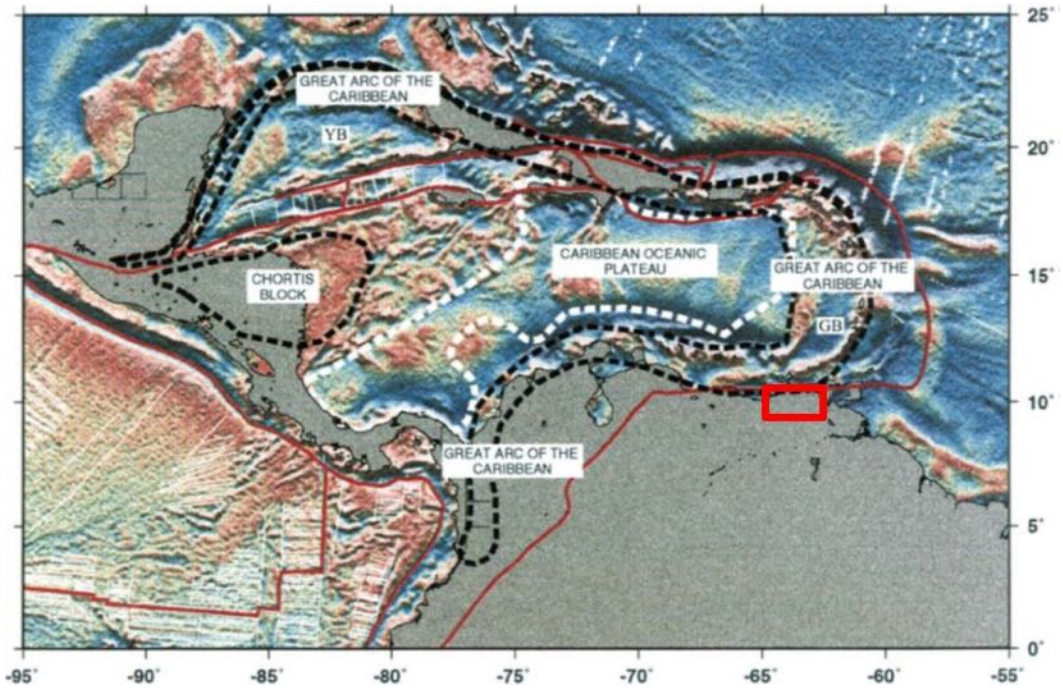

Figure 2.8. Present day tectonic map of the major provinces of the Caribbean. Red lines indicate active plate boundaries and white lines are magnetic anomaly and fracture zone trends from Coffin et al. (1992). Key to abbreviations: YB (Yucatan basin); GB (Grenada basin). Red square represents the approximate study area location of this thesis (modified from Mann, 1999).

The change in the movement in the southeast Caribbean plate caused a change from east-southeast transpression to eastward translation. The strain partitioning continues but the strike-slip component is dominant in the last 10 Ma (Weber et al., 2001; Mann et al., 2001; Lingrey, 2007) (Figure 2.9).

The results of the dominant contraction component prior to 10 Ma can be seen in the development of the linear Morón-Cariaco Basin-El Pilar-Gulf of Paria fault system and the fold–thrust belt of Eastern Venezuela and Trinidad (Pindell and Kennan, 2001). From 10 Ma to the present, the dominant strike-slip component is shown with the alignment of the Orchila Basin–Margarita fault with the Urica Fault (Pindell and Kennan, 2009) and the thick deposits of Upper Miocene and Pliocene sediments in the Gulf of Paria (Figure 2.9). These deposits are thick due to subsidence which suggests that an important right-slip component is accommodated on the right-stepping relay transfer between the El Pilar strike-slip zone in the north and the Warm Springs/Central Range strike-slip zones in the south (Lingrey, 2007).

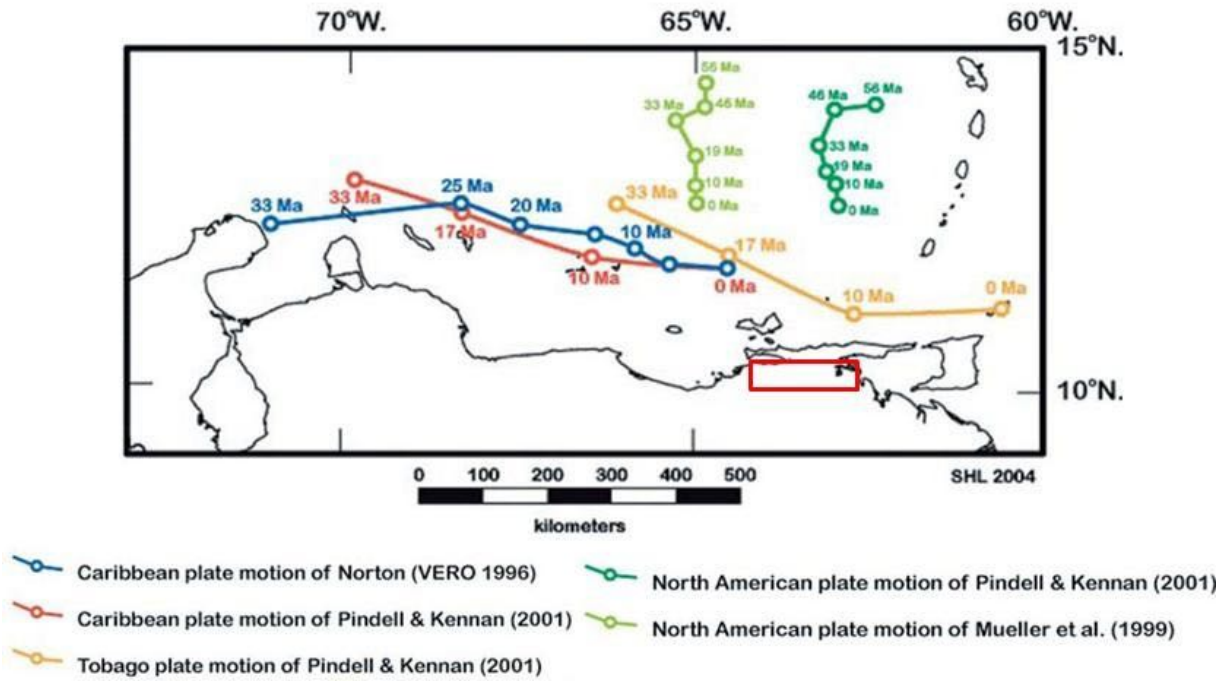

Figure 2.9. Models of Cenozoic plate movements for the Caribbean and North American plates relative to a fixed South American plate. The red square represents the approximate study area location of this thesis (modified from Lingrey, 2007).

More specifically, Escalona and Mann (2011) present a tectonic model of the Eastern Venezuela Basin composed of three-stage kinematics for Caribbean-South America collision based on slab delamination and straining partitioning processes:

First stage: Southeastward of the Caribbean terranes, the collision formed overthrusting onto the passive margin of northern South America. This thrust load produces flexure and extension in the north of the South America Craton, generating foreland basins and SW-NE striking thrust faults. Then, eastward migration of the foreland basins and the fold and thrust belt occur along the tear faults present in the area (Urica, San Francisco and Soldado faults) (Figure 2.10A)

Second stage: The fold-thrust-belt ends and the eastward migration of the tectonic load caused the crust relaxation and rebound in the continental foreland basin. The slab break-off (slab delamination) of South America produced inversion in the rifted basin parallel to the plate margin. Onset of strain partition (Figure 2.10B)

Third stage: The deformation in the foreland basin ceased and the Caribbean Arc is affected by east-west rifting. The straining partitioning is active in the zone developing strike-slip faults due to east-west displacement between the Caribbean and South American plates and back thrusting caused by north-south convergence between the North and South American plates. The Caribbean plate subducted below the Caribbean Arc terranes (Figure 2.10C).

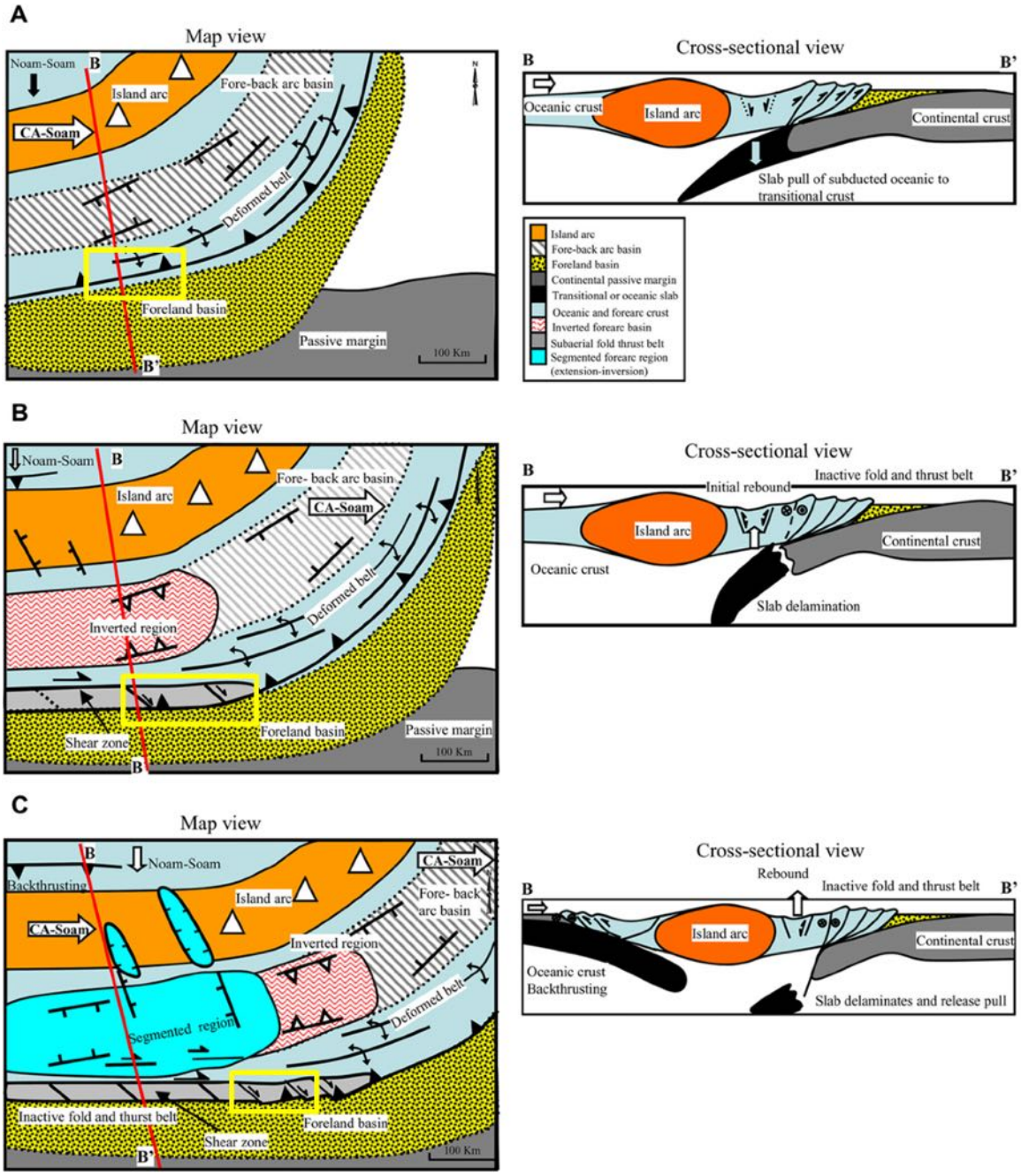

Figure 2.10. Kinematics model for the oblique convergence between the Caribbean and South America margin. A. First stage. B. Second stage. C. Third stage. Yellow square represents the approximate study area location of this thesis (modified from Escalona and Mann, 2011).

2.2. Tectonic Setting of the Northeastern Venezuelan Basin

The Eastern Venezuela Basin is located between the latitudes 8°N and 11°N and the longitudes 61°W and 66°W. Four major geodynamic events contributed to its formation: the Paleozoic orogeny, the Jurassic rifting associated with the break-up of Pangea, the Cretaceous to Paleogene passive-margin and the Neogene active margin produced by the oblique collision between the Caribbean and South American plates (Jácome et al 2003).

The Caribbean and South American plate boundary is defined by the El Pilar strike-slip fault system. South of it, an orogenic wedge develops, from north to south: The Serranía Del Interior (SDI) Hinterland, the Monagas Fold and Thrust Belt (MFTB) and the Maturín Foreland Basin (Roure et al., 2003; Hung, 2005) (Figure 2.11 and Figure 2.12).

The topography of the SDI caused the tectonic loading producing the subsidence that formed the Maturín Foreland Basin to the south. According to Jácome et al. (2003), in addition to the subsidence, there is a contribution of a pulling down of the South American plate caused by continental subduction.

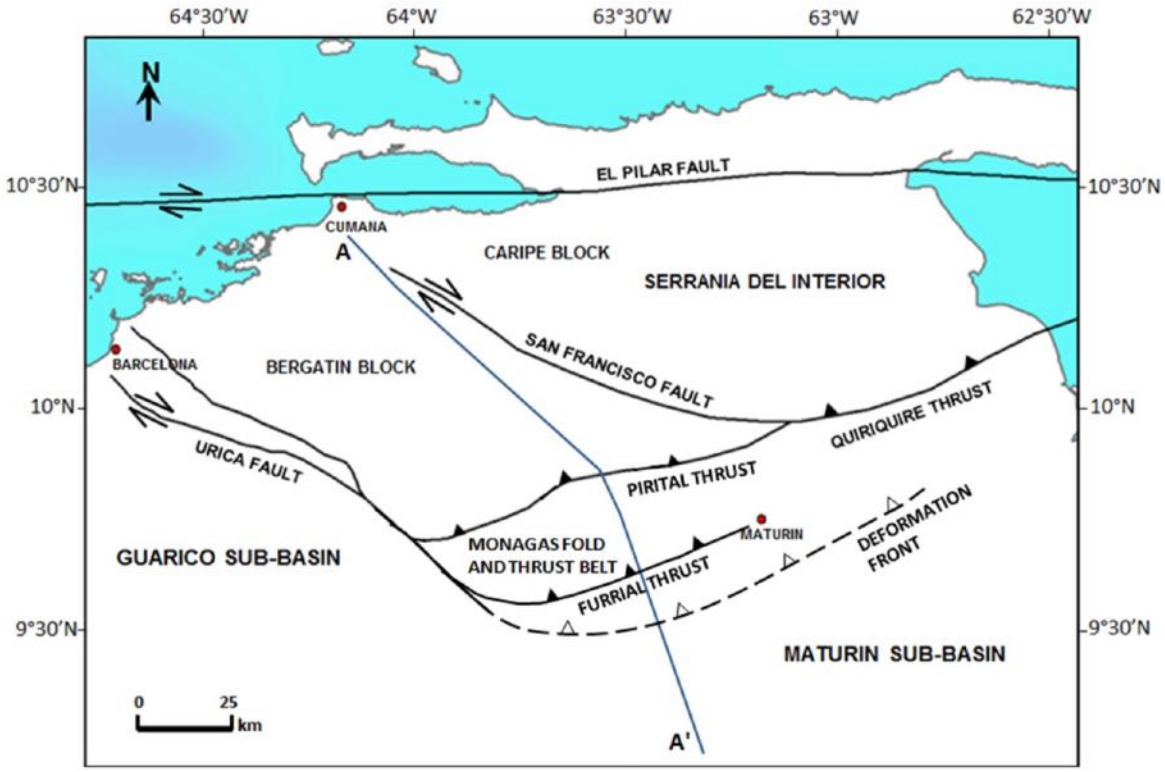

Figure 2.11. Map of Eastern Venezuela showing the main tectonic provinces. Serranía Del Interior Mountain Range, Monagas Fold and Thrust Belt and Maturín Sub-Basin. A-A' locates the structural section (modified from Parra et al., 2011).

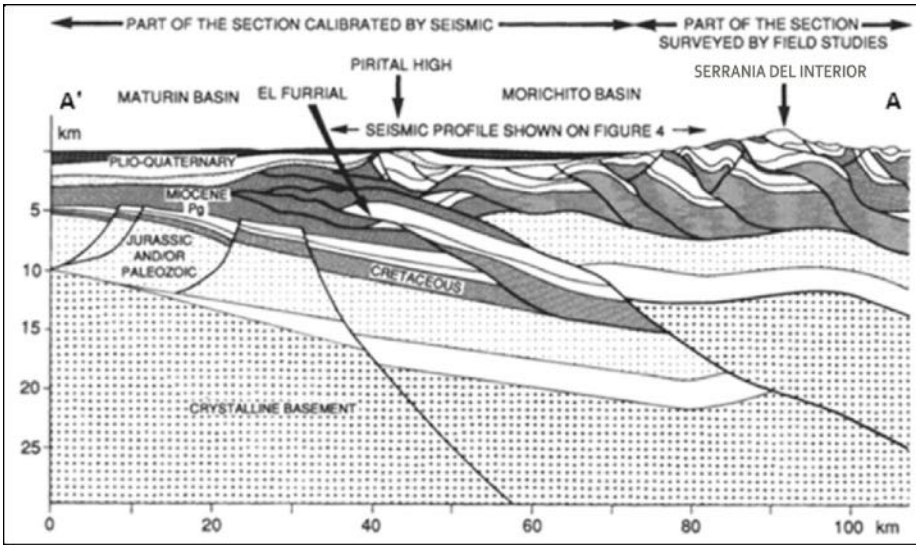

Figure 2.12. Cross section example across the SDI, MFTB and Maturín Basin. The interpretation of the MFTB and Maturín Basin was based on seismic and well data. Interpretation of SDI was based on field data. See location in Figure 2.11 (modified from Passalacqua et al., 1995)

2.2.1. The Serranía Del Interior Mountain Range

The Serranía Del Interior is a fold and thrust belt limited by the Pilar Fault to the north, by the Pirital Thrust system fault to the south and across by the right-lateral Urica and San Francisco faults to the west and east respectively (Figure 2.11). The uplifting of this range occurred from the Middle Eocene to the Miocene period (Locke and Garver, 2005; Sisson et al., 2005). The sedimentary sequence involves the pre-Cretaceous and Tertiary strata deformed by folds which are parallel to the longitudinal axis of the range (González de Juana et. al. 1980; Vivas and Macsotay, 1995). Two main fault systems affect the SDI: the thrust faults parallel to the strike of the range and second set of conjugate synthetic faults striking NW-SE and NE-SW (Vivas and Macsotay, 1995).

The tectonic structures are associated with detachment, reverses and transcurrent faults and are truncated by the NW-SE Urica, San Francisco and Los Bajos right-lateral tear faults (Hung, 2005; Escalona and Mann, 2006). The San Francisco right-lateral fault divides the SDI into two blocks: The Bergatín block to the west and Caripe block to the east (Figure 2.11). The greatest number of formation outcroppings in the eastern basin (from Cretaceous to recent) is observed in the SDI (González de Juana et. al., 1980).

Apatite fission track data show that the shortening in the eastern Serranía Del Interior ceased at ~12 Ma (Locke and Garver, 2005), reflecting the end of collision. After the end of oblique convergence between the Caribbean and South American plates in the Late Miocene, the Caribbean plate acquired its present movement and the plate boundary evolved to the almost

purely strike-slip margin observed today (Pindell et al., 2005; Ysaccis, 1997).

Due to the lack of in depth data in the SDI, the published cross-sections involve a wide range of models, involving total shortening between 16 km and 120 km (Passalacqua et al., 1995; Jácome et al., 2003; Schneider, 2003; Roure et al., 2003, Hung, 2005; Clark et al., 2008). Hung (2005) has proposed six thick-skin and thin-skin tectonic structural models (Figure 2.13). These models emphasize basement-involved, inverted grabens, multiple decollements and duplex structures. There are two kinds of basements: a pre-rift Paleozoic basement and a Precambrian crystalline and metamorphic basement. The models 1 to 3 are thick-skin tectonics, while models 4 to 6 are thin-skin.

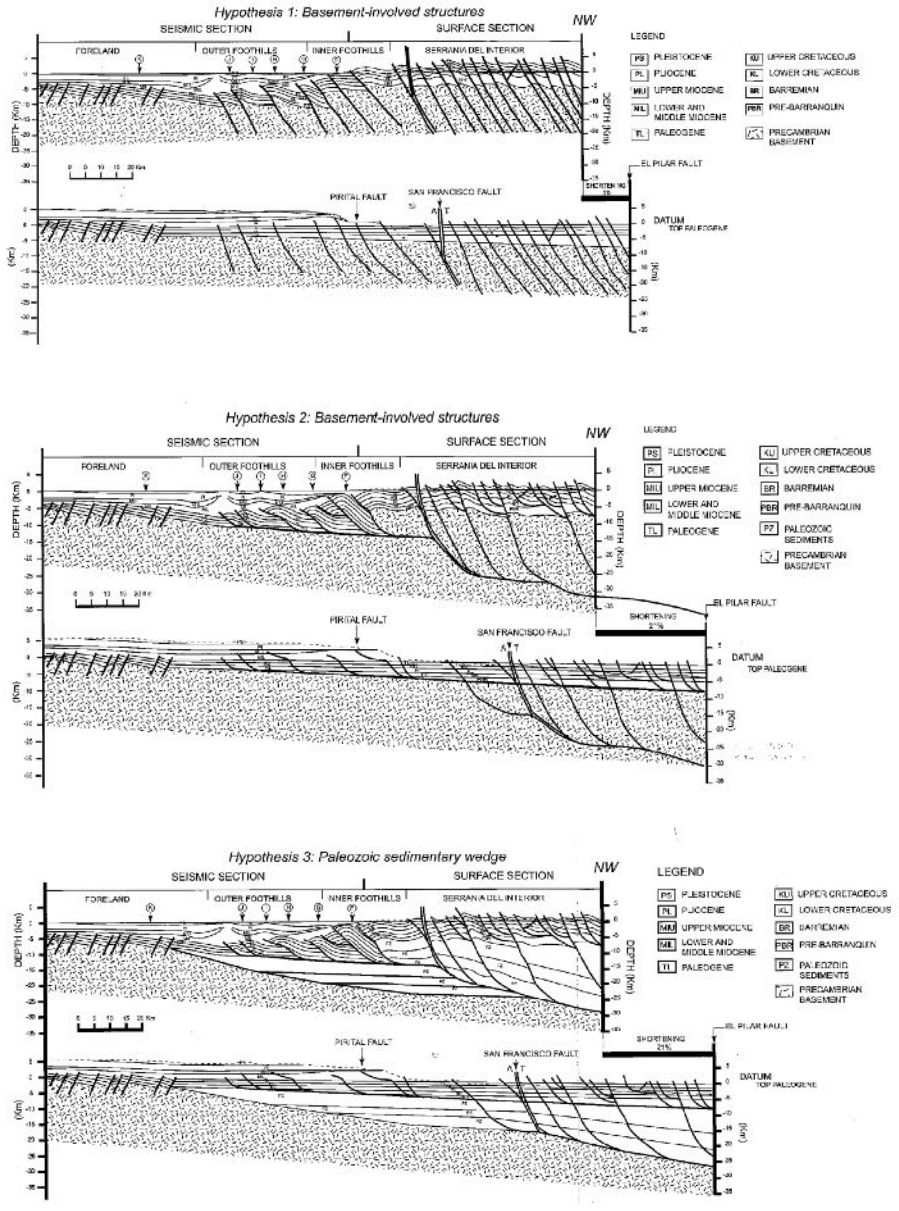

Figure 2.13. Structural models proposed of the Serranía Del Interior (from Hung, 2005).

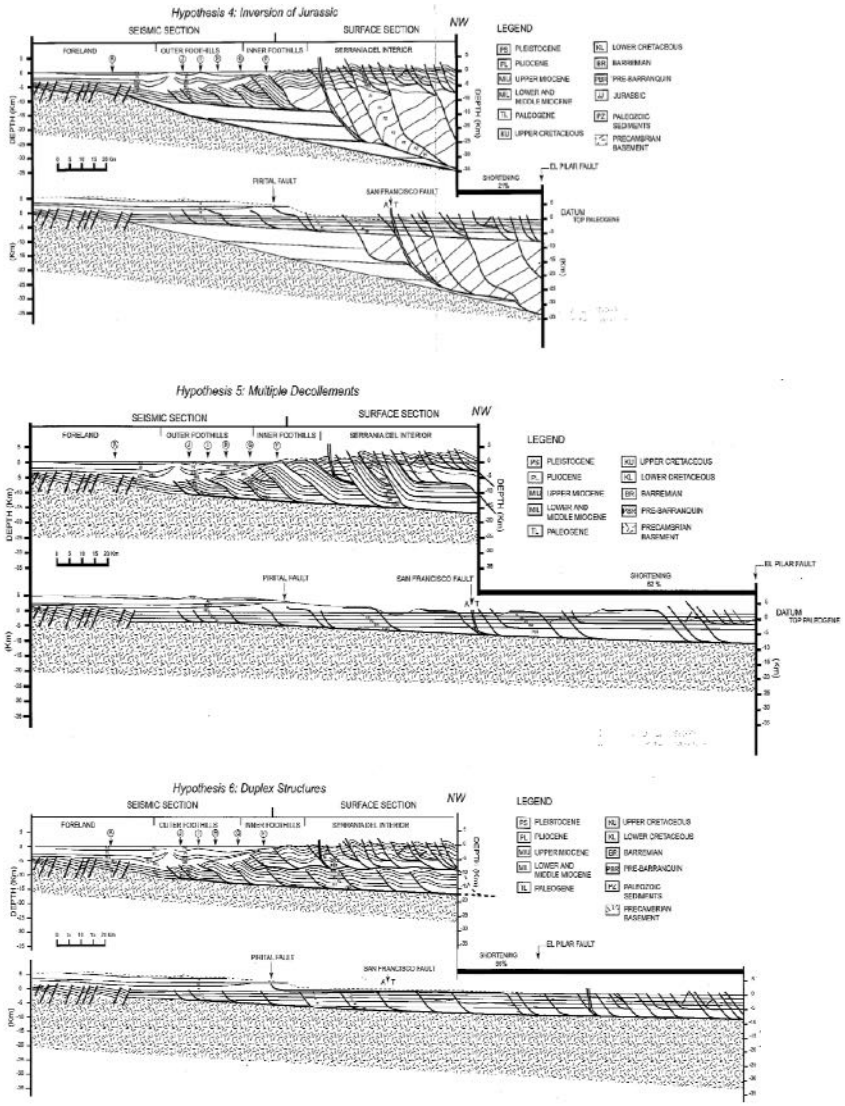

Figure 2.13. (continued)

In order to investigate the structures related to the Caribbean-South American plate boundary, the “Geodinámica Reciente del Límite Norte de la Placa Suramericana” (GEODINOS) Project was created. This project consisted of acquiring wide angle and reflection seismic data along a series of profiles across the plate boundary. The model velocity carried out on a profile at 64° W longitude and with a depth observation of 10 km shows thinning of the passive margin sedimentary rocks below the Serranía del Interior due to pre-Cretaceous basement deformation. This deformation was the result of the pre-Tertiary normal faults reactivation as reverse faults of the Espino Graben during the Miocene transpression that formed the Serranía Del Interior (Liuzzi et al., 2006) (Figure 2.14). This model is consistent with the models 4 (Inversion of Jurassic) proposed by Hung (2005) (Figure 2.13). Also, this model coincides with the one proposed by Rossi (1985) and Chevalier et al., (1995) where the pre-Cretaceous basement is involved in the Serranía Del Interior deformation (Liuzzi et al., 2006). Additionally, the velocity model supports a thin-skin tectonic in the SDI.

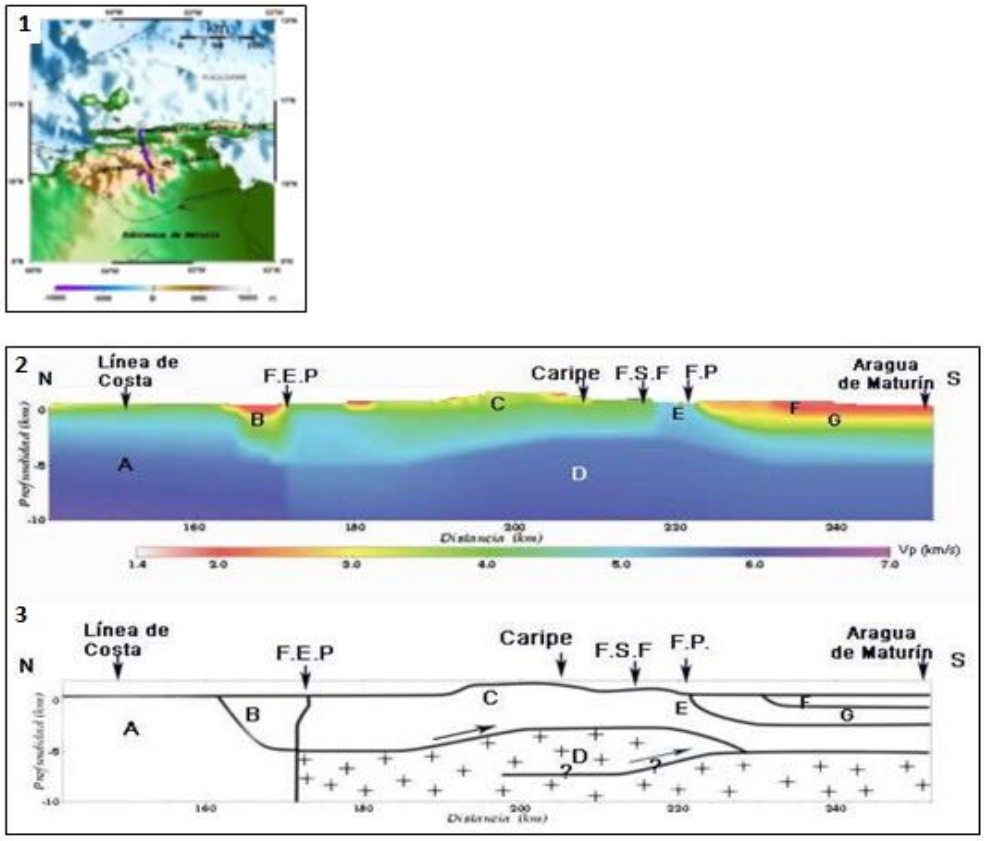

Figure 2.14. (1) Location of the seismic profile. (2) Velocity model with the identification of the structures where: A: Igneous-metamorphic complex Araya-Paria, B: Cariaco Basin; C: passive margin and / or Jurassic (?) of the Serranía Del Interior, D: pre-Cretaceous basement deformed and thickened below the Serranía Del Interior, E: Pirital Thrust (high velocity area, observed only in velocity model), F and G: Unconsolidated and consolidated sediment of the Maturín Basin, respectively; surface location of F.E.P: El Pilar Fault; FSF: San Francisco Fault, FP: Pirital fault. (3) Structural interpretation of the velocity model with thrust in the basement and faults dipping toward the north (from Liuzzi et al., 2006).

The El Pilar Fault

The El Pilar Fault is a 350 km long right-lateral strike-slip fault and is considered to be the most important seismogenic fault in north-eastern Venezuela and Trinidad and (Audemard et al., 2002) (Figure 2.11). This active fault began its activity possibly from Late Miocene and is considered by many authors to be the Caribbean and South American limit which predominantly accommodates the movement between these plates (Pindell et al., 2005; Ysaccis, 1997; Reinoza et al., 2015). To the north of the fault, Mesozoic metamorphic rocks are exposed and these are juxtaposed against the Mesozoic sedimentary rocks of the Serranía Del Interior Range in the south (Duerto, 2007). The El Pilar Fault connects to the San Sebastían and Boconó faults to the west (Gonzalez de Juana et al., 1980; Passalacqua et al., 1995; Audemard et al., 2005). It is well defined on the surface by the morphological depressions of the Cariaco and Paria Gulfs (Audemard et al., 2005).

GPS-based geodetic data show that the present day E-W Caribbean plate movement relative to South America is ~20 mm/y along right-lateral strike-slip faults in Venezuela and Trinidad (Mann et al., 2011; Weber et al., 2001, Perez et al., 2001). In Venezuela, this movement is concentrated in the El Pilar Fault as shown by recent GPS studies (Jouanne et al., 2011; Reinoza et al., 2015). However, Audemard (2005) reported that the slip rate of the El Pilar Fault is on the order of ~10 mm/y. Reconstructions of the Southern Caribbean boundary indicate that ~55 km of strike-slip displacement has accumulated along this major fault system since Pleistocene (Audemard, 2002).

Studies of the seismic event location of the Cariaco earthquake of 1997 established different dips along the El Pilar Fault (Baumbach et al., 2004). To the west of the fault a north dipping fault can be observed. At the center (64° W) the fault shows a vertical dip and to the east, it shows dipping toward the south. Recently, Reinoza et al. (2015) carried out modeling based on a Global Navigation Satellite System (GNSS) and GPS observation in order to constrain the velocity field and the slip rate along the El Pilar Fault. This study suggests an asymmetric velocity field on both sides of the fault (west and east) and a slip distribution model showing that a 40 to 50% of the slip is locked due to the significant creep along the upper part of the fault.

The Urica Fault

The Urica Fault is a NW-SE ~107 km long right-lateral strike-slip fault that marks the western limit of the Serranía Del Interior (Figure 2.11). This fault developed during the Miocene (Di Croce et al., 1995) or it had been inherited from a pre-existing rift of Cambrian age (Duerto, 2007). Audemard et al. (2006) proposed that the Urica Fault is one of the synthetic Riedel shears derived from the major right-lateral strike-slip fault system related to the interaction between the Caribbean and South America plates.

The Urica Fault western trace is hidden due to the limited exposure of the fault and poor quality seismic data. However, structural analyses in the Barcelona Bay show that the Urica Fault may continue as a major southerly dipping normal fault (Ysaccis, 2002; Duerto 2007). The southern trace is related to the thrusts developed between the Monagas Fold and Thrust Belt and the deformation front that limits to the south. Also, differences in shortening have been observed on both sides of the fault: to the east, the shortening is between 30% and 40% while to the west, it is less than 3% (Campos et al., 1988).

The San Francisco Fault

This right-lateral fault NW-SE oriented exhibits 18-40 km of offset (Chaplet, 2002). It starts in the Gulf of Cariaco to the north and then follows to eastward where is oriented E-W until disappearing beneath the Plio-Quaternary series in the northern area of the city of Maturín (Rossi, 1958; Duerto, 2007) (Figure 2.11). The San Francisco Fault separates the SDI into the Bergantín Block to the west and the Caripe Block to the east with an average displacement of 18 km between the blocks (Rosales,1972). Audemard et al. (2006) considers this active fault to be a synthetic Riedel shear derived from the major right-lateral El Pilar strike-slip fault. Vivas et al. (1985) suggest that due to changes in stress orientation, the southeast end of the fault turns into a thrust, as in the case of the Los Bajos fault in the Trinidad south.

2.2.2. The Monagas Fold and Thrust Belt (MFTB)

This province forms the transition from the uplifted and strongly shortened SDI to the Maturín foreland basin (Jácome et al., 2003) (Figure 2.11 and Figure 2.15). The compression in this province thrusted and folded the pre-Cretaceous to Tertiary rocks. Upper Miocene to Pliocene-Pleistocene sequence onlaps on to the emerging fold belt (Jácome et al., 2003). The tectonics in the MFTB allowed burying the structures forming the main petroleum targets in the area (Roure et al., 2003; Parra et al., 2011).

The Pirital and Furrial are the main thrusts and these have different decollement levels associated with two deformation stages occurred during the SDI emplacement: The first stage involves shallow intra-Cretaceous to Tertiary decollements and deep pre-Cretaceous decollements (Roure et al., 2003). The second stage reactivates deeper pre-Cretaceous structures (Jácome et al., 2003). Parra et al. (2011) estimate for the MFTB area a total shortening between 43 and 59 km that increase eastward.

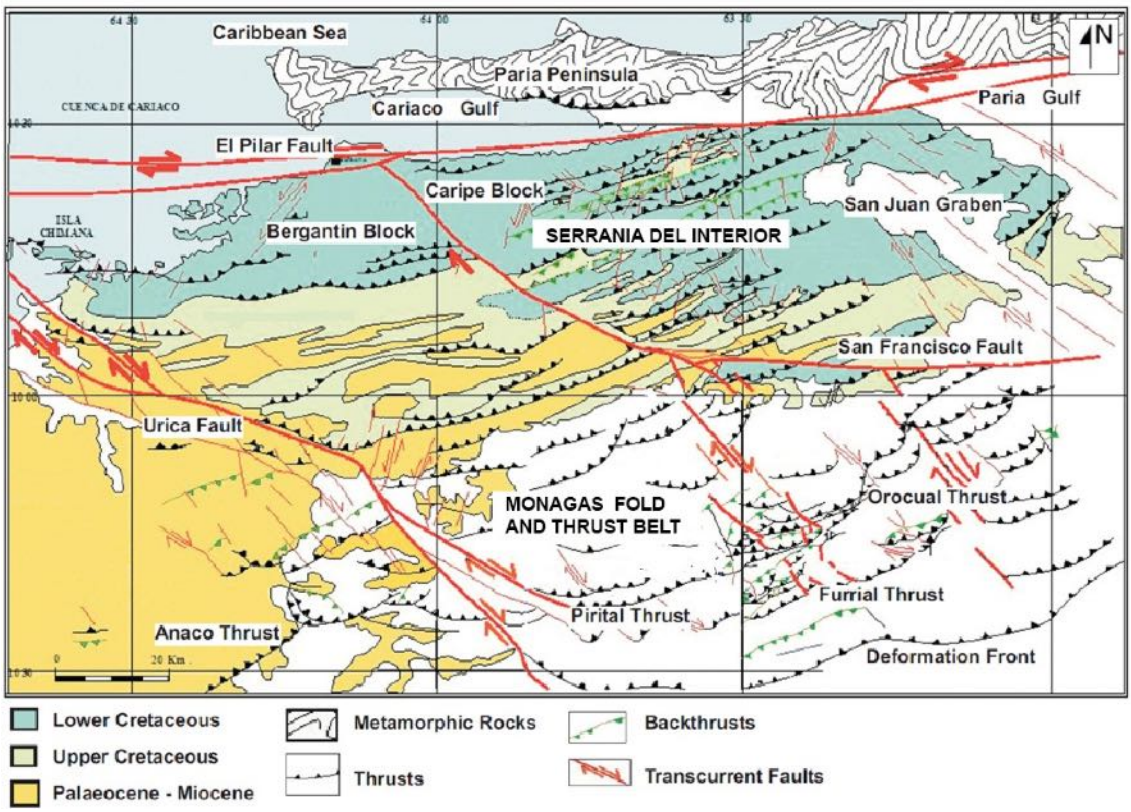

Figure 2.15. Structural map of the SDI and MFTB (modified from Bosset and Gou, 2004).

In order to constrain and understand the kinematic evolution and the petroleum system of the MFTB, Roure et al. (2003) developed quantitative models based on 2D cross section, thermal, pressure and fluid flow data. Then, Parra et al. (2011) proposed a regional structural model that takes the major along-strike variations in structural style and shortening into account. Additionally, they used thermal data including new wells, new 3D seismic data and structural forward modeling. This model at approximately 20, 16 and 11 My explains the Pirital and Furrial Thrust evolution. It shows that the Pirital Thrust activity began during the Late Oligocene-Early Miocene time causing deformation of the area (Figure 2.16a). Then, during the Early Miocene the Furrial Thrust and most of the thrusts were activated (Figure 2.16b). During the Middle Miocene (about 11 Ma), the Pirital Thrust developed an out-of-sequence stage which changed its geometry and increased its velocity (Figure 2.16c). The Pirital and Furrial thrusts seem to still be active but the slip of these thrusts seems to be less since the Late Miocene.

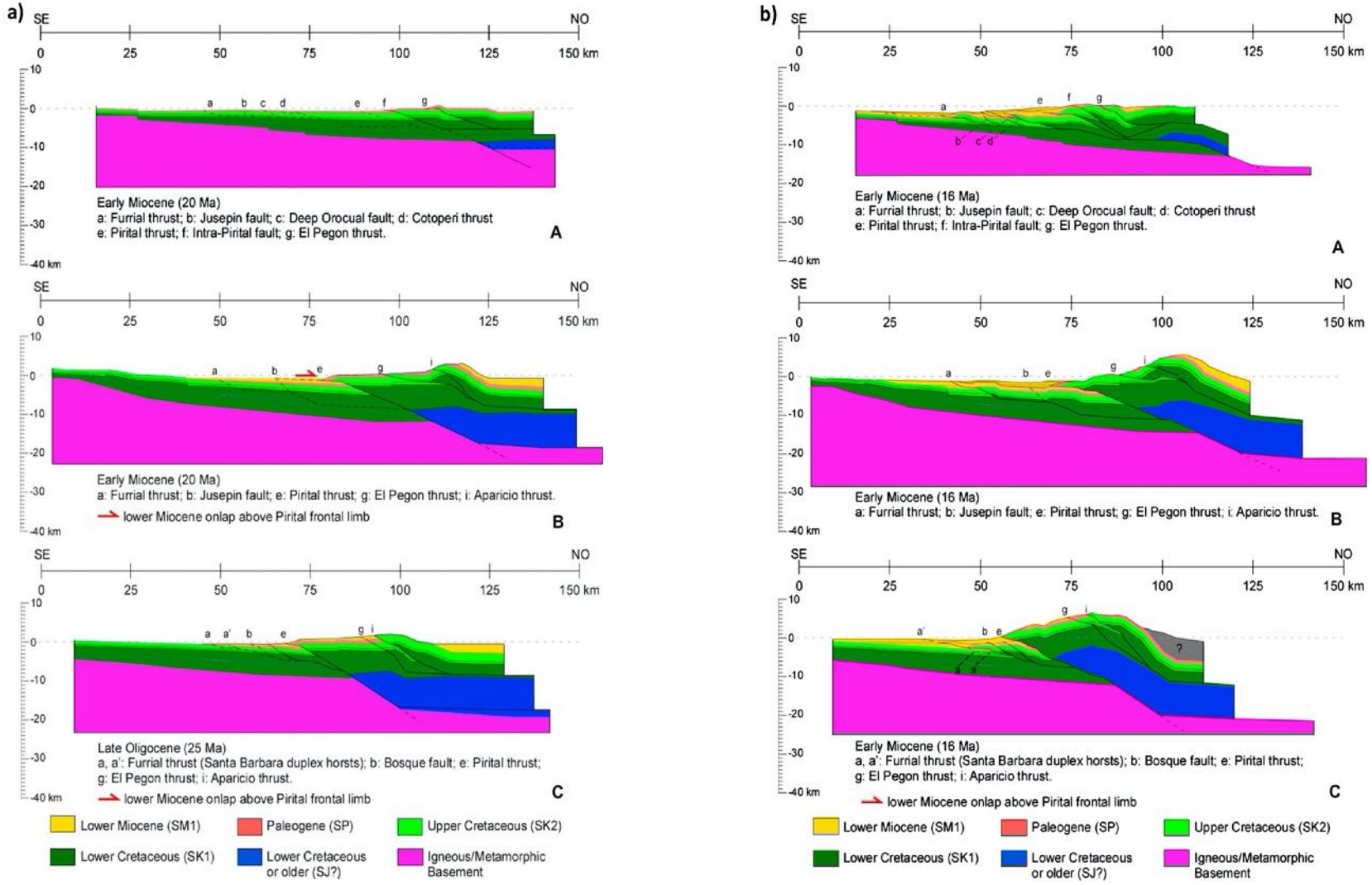

Figure 2.16. Forward modeling configuration at about 20 Ma (a), 16 Ma (b) and 11 Ma (c) in the Monagas Fold and Thrust Belt (MFTB). A. Furrial section (east of the study area). B. Carito section (center of the study area). C. Santa Bárbara section (west of the study area) (from Parra et al., 2011).

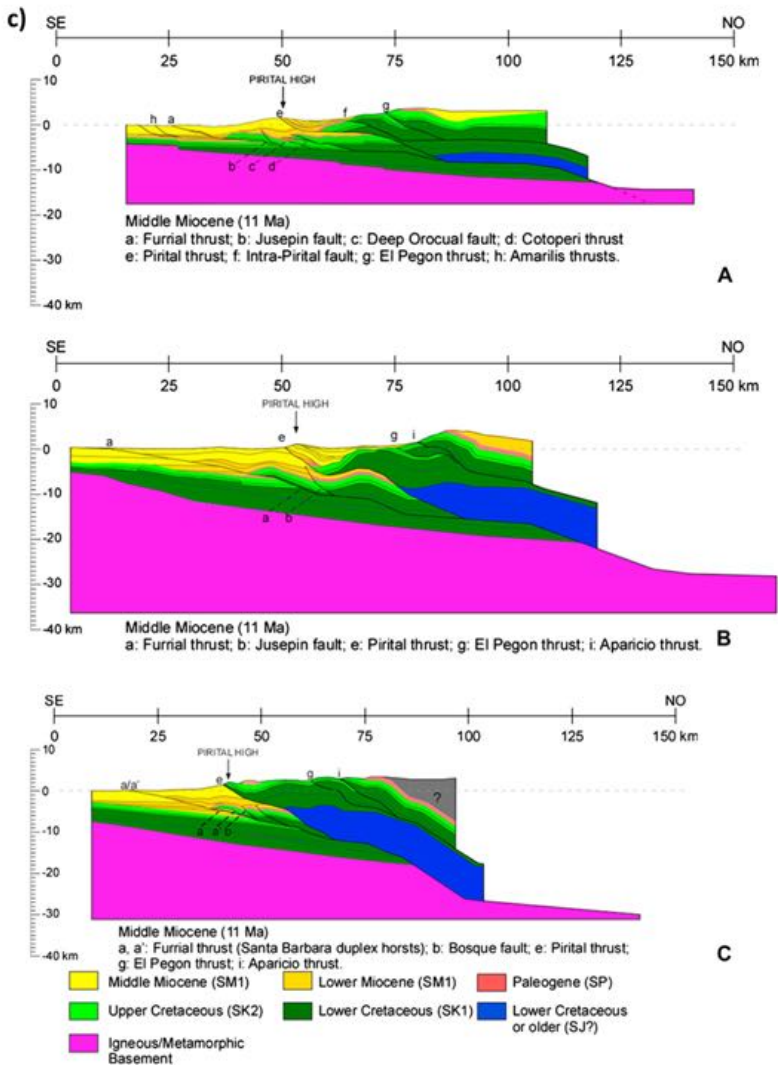

Figure 2.16. (continued)

The Pirital Thrust

This thrust located in the MFTB begins in the Urica Fault (to the west of the MFTB) and continues to the east to reach the San Francisco Fault (Rod, 1959) (Figure 2.11 and Figure 2.15). It runs sub-parallel to the SDI range and is considered by some authors to be the southern boundary of the SDI (Parnaud et al., 1995; Giraldo et al., 2000; Duerto, 2007).

The Pirital Thrust detaches on pre-Cretaceous rocks and reaches up to 80 km of shortening (Parnaud et al., 1995). The orientation of the fault (NE-SW) differs with respect to the overall E-W trend of the thrust system, possibly indicating an out-of-sequence event (Parnaud et al., 1995; Parra et al., 2011). Di Croce (1995) estimated for this thrust a horizontal displacement of ~20-30 km and a vertical displacement ~4-5 km. Parra et al. (2011) consider that the Pirital thrust sheet marks an abrupt change in sediment thickness that could have been controlled by

earlier normal faults. The deformation in the basin started by the activation of this thrust during Late Oligocene-Early Miocene period, which seems to be diachronous from west to east. Later, during the Middle Miocene, the Pirital Thrust developed a frontal high-angle ramp and an out-of-sequence phase (Parra et al., 2011). The frontal Pirital Thrust sheet rotated above this ramp creating the Pirital High, which controlled the sedimentation from the Late Miocene to Pliocene–Pleistocene (Salazar et al., 2011).

The Furrial Thrust

Márquez et al. (2003) define the Furrial Thrust within the fault-bend fold structures that mainly involves Paleo-Cretaceous units. This thrust has a slip of ~17-20 km an its back limb is longer than the front limb (Figure 2.11). Toward the east side, it shows a section approximate of 1.5 km which involves Lower Miocene to Upper Cretaceous units. In the central part of the Furrial Thrust section reaches 2.5 km from Lower Miocene to Upper-Lower Cretaceous (Parra et al., 2011). On the southern, the frontal structure of this thrust is defined by an anticline that involves from Mate Miocene to Pliocene–Pleistocene units. The configuration of this thrust varies along-strike being more complex towards the west (Parra et al., 2011).

2.2.3. The Maturín Foreland Basin

The Maturín Basin is located in Eastern Venezuela between the latitudes 9°N and 10°N. This basin formed in the Neogene as a consequence of the continental load generated by the SDI. To the west, this is limited by the Guárico Basin, to the east by the Atlantic Ocean, to the north by the deformation front and to the south by the Orinoco River (Figure 2.11).

The Maturín Basin consists of 7 to 12 km of Miocene-Pleistocene sediments deposited from different sources: the SDI to the north, the Guyana shield to the south and the El Baul Arch to the west (Jácome et al., 2003; Sánchez et al., 2011).

2.3. Tectonostratigraphic Evolution of the MFTB and Maturín Foreland Basin

The geodynamic evolution of the Eastern Venezuelan Basin can be defined by four major tectonic phases (Eva et al., 1989, Parnaud et al.,1995): 1. The Paleozoic Pre-rift phase, 2. The Jurassic rifting phase, 3. The Cretaceous-Paleogene passive margin phase and 4. The Neogene and Quaternary active margin phase.

The change from continental rifting to passive margin and from passive margin to foreland basin result in the formation of unconformity surfaces, sedimentary sequences, changes in depositional environments and the migration of the basins through time (Duerto, 2007).

2.3.1. The Pre-rift Phase (Paleozoic)

This megasequence was developed before the extension (pre-extensional phase) and that took place during the Paleozoic. The lithotypes are sedimentary, meta-igneous and meta-sedimentary rocks of the Precambrian and Paleozoic ages (Feo Codecido et al., 1984). This phase is associated with the Hato Viejo and Carrizal formations, both of Early Cambrian age and deposited in a continental environment (Figure 2.17).

The Hato Viejo Formation is composed of medium- to coarse-grained arkosic-quarzitic sandstones with an average thickness of 100 m. The Carrizal Formation reports thickness of 650 m and is composed of massive greenish argillites and variable thickness silts intercalated with beds of sandstones or pebbly conglomerate (LEV, 1997; Gonzalez de Juana et al.,1980).

2.3.2. The Rifting Phase (Jurassic)

The Pangea break-up phase and subsequent divergence of the North and South American plates formed the extensive phase that developed grabens such as the Espino Graben (Pindell and Dewey, 1982; Summa et al., 2003), creating an oceanic crust in the Tethys Caribbean domain and also a regional unconformity. This phase is associated with the La Quinta Formation developed in a continental environment and is present in the western part of the basin (Hedberg, 1950 in Parnaud et al., 1995) (Figure 2.17).

2.3.3. The Passive Margin Phase (Cretaceous-Paleogene)

This phase developed between the Cretaceous and Paleogene due to the subsidence of the South American north margin was mainly controlled by sea level changes during the Cretaceous (DiCroce, 1995). Several lithological formations in the Eastern Venezuelan basin indicate different transgressive phases. The first transgressive phase is represented by the Barranquín, El Cantil and Chimana Formations (Lower Cretaceous). The second phase is represented by the Querecual, San Antonio and San Juan formations (Upper Cretaceous) (Santiago et al., 2004). The final transgression is represented by the Vidoño, Caratas, Los Jabillos, Areo and Naricual formations during the Paleogene-Lower Oligocene (Parra et al., 2011) (Figure 2.17).

2.3.4. The Active Margin Phase (Upper Oligocene – Recent)

The oblique collision between the Caribbean and South American plates produced the active margin in the northern part of the Maturín basin, developing the MFTB. During the upper Oligocene-Early Miocene, the basin reached the maximum deepening represented by marine shales of the Carapita Formation (Duerto, 2007). The top of this sequence is represented by an unconformity that indicates a sub-aerial erosion episode (Parra et al., 2011). During the Late Miocene the deformation in the area formed the Pirital High creating two depocenters, the La Pica sub-basin to the south and the Morichito basin to the north (Parra, et al., 2011).

The La Pica Formation was deposited in the shallow marine environment in the La Pica sub-basin. This is unconformable with the Carapita and Las Piedras formations. It is composed of gray brackish to marine shales and silty shales with a maximum reported thickness of 2000 m (Gonzalez de Juana et al., 1980; LEV, 1997). The 1600-m thickness of the Morichito Formation was deposited to the north of the Pirital High (in the Morichito sub-basin). It is composed of alluvial fan deposits (conglomerates, sandstones and siltstones) (Figure 2.17).

Finally, during the Pliocene-Pleistocene, the Maturín Basin was filled by continental sediments of the Las Piedras and Mesa Formations due to an important subsidence phase in the basin. Jácome et al. (2003) related this subsidence not only to the thrust loading but mainly to the subduction of the South American lithospheric mantle beneath the Caribbean plate.

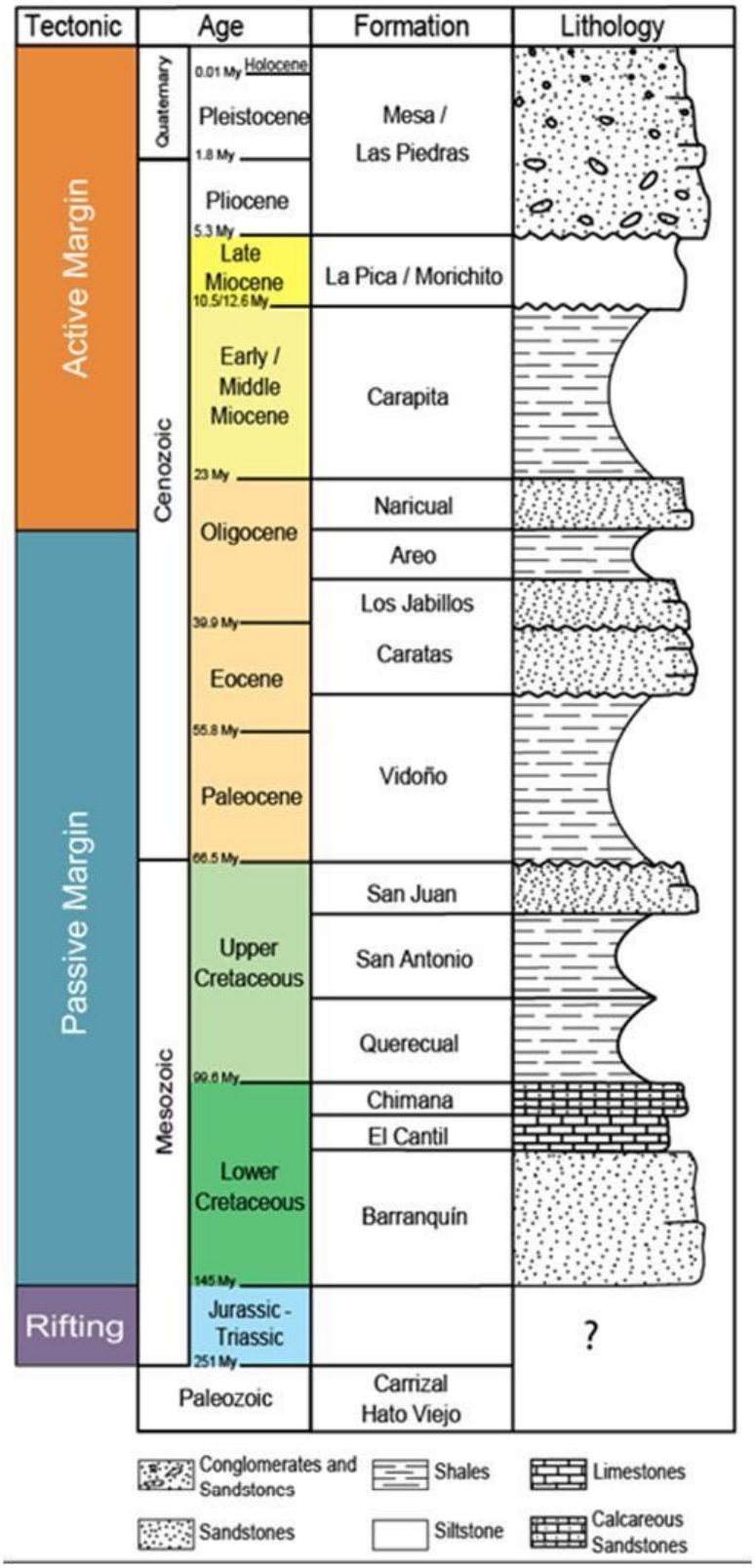

Figure 2.17. Stratigraphic chart of the Maturín Foreland Basin.

2.4. Neotectonics in the Northeastern Venezuelan Basin

The neotectonic activity along Northern Venezuela is controlled by the direct interaction of Caribbean-South America plate boundary. The resulting tectonics structures are concentrated along strips and belts (Singer and Audemard, 1997). The major belt mountain in Venezuela is represented by central north-aligned mountain ranges such as: to the west, by the Mérida Andes Mountains, in the north-central part by the Coast Range and to the northeast by the Serranía Del Interior Range (Audemard et al., 2006) (Figure 2.18).

The GPS data from Weber et al. (2001) show that the movement vector of the Caribbean plate with respect to the Central Range of Trinidad has a direction of N086º ± 2º, and N084º ± 2ºE with respect to South America (Pérez et al., 2001). Both movement vectors suggest an almost pure wrenching movement with a slight transtension in the Eastern Venezuela (Audemard et al., 2006). More recently, GPS studies carried out by Jouanne et al. (2011) on both sides of the El Pilar Fault suggest that at the present, the El Pilar Fault concentrates the relative displacement between the Caribbean and South America plates, characterized by a pure dextral strike-slip and an insignificant shortening across the Serranía del Interior thrusts (Figure 2.19). However, Audemard et al. (2006) suggest that the main geodynamic process of the major strike-slip fault system is wrenching but a compressive component is always present showing the partitioning mechanics. The current expression of this compression component is shown by uplift and important positive relief features present in part of the Eastern Venezuelan Coast and Interior Ranges.

The seismicity in Venezuela is concentrated in the Mountain Ranges (Merida Andes, Coast Range and The Serranía Del Interior Range) and in the major right-lateral strike-slip active fault system (Boconó, San Sebastían and The Pilar faults). This shows that the plate boundary is tectonically active and is distributed within the wrenching faults and mobile belts (Audemard and Romero,1993; Audemard, 2002). Figure 2.20 shows the instrumental seismicity distribution in Venezuela. Generally the seismicity is small to moderate in magnitude (Mw < 3.9). In the Eastern Venezuela the seismicity is mainly concentrated around the El Pilar Fault reaching earthquakes > 5 in magnitude. The seismicity in the SDI is mainly concentrated around the Urica and San Francisco right-lateral strike-slip faults. In the MFTB the seismicity is less frequent and has a smaller magnitude than the SDI. However, some events are mainly focalized on the thrust in the area.

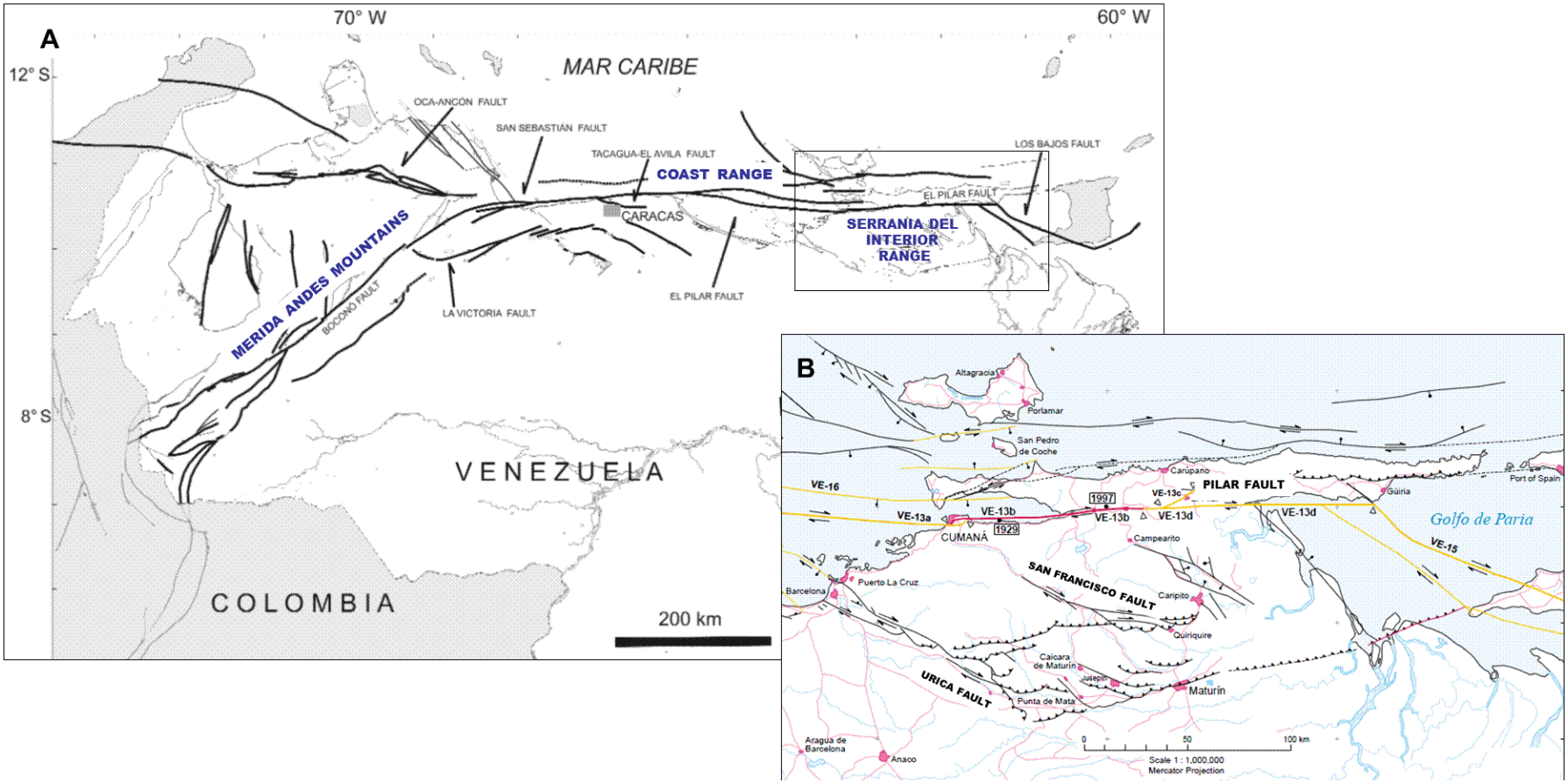

Figure 2.18. Map A: Major Belts Mountains and Quaternary faults of Venezuela. Map B: Quaternary faults in Eastern Venezuelan (VE-13 El Pilar Fault, VE-15 Los Bajos fault, VE-16 San Sebastián fault) (modified from Audemard et al., 2000).

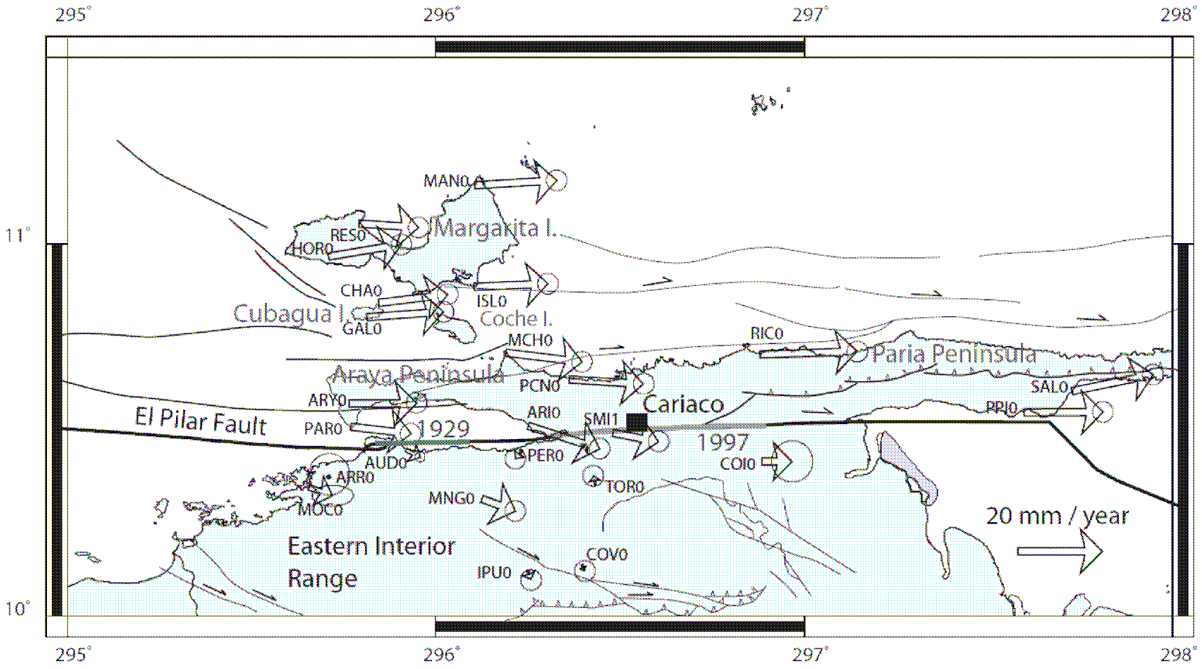

Figure 2.19. Active faults in Eastern Venezuela. Arrows indicates velocities expressed in the South America plate reference frame (from Jouanne et al., 2011).

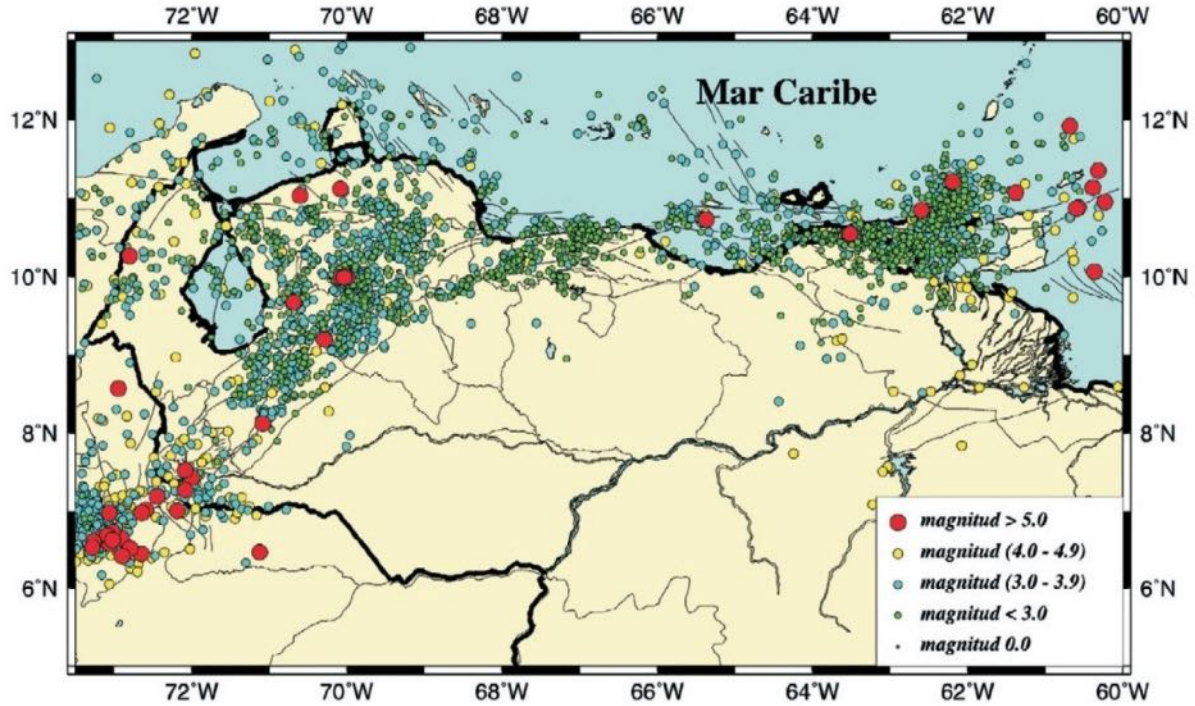

Figure 2.20. Map of the instrumental seismicity in Venezuela (from FUNVISIS webpage).

CHAPTER 3. GEOMORPHOLOGICAL SIGNATURE OF THE PLEISTOCENE THIN-SKINNED TECTONICS IN THE MONAGAS FOLD AND THRUST BELT

3.1. Introduction

Active faulting and recent deformations in the Monagas Fold-and Thrust Belt (MFTB) are less emblematic than the on-going activity along the El Pilar Fault that accommodated the main slip between the South American and Caribbean plates. Satellite imagery in this area is poorly informative and the resolution of DEM is often strongly affected by forests. A preliminary study of the Pleistocene deformation of the area was initiated in 2002 by Roberto Wagner within the framework of an undergraduate study (Wagner, 2004) that mainly focused on the Jusepín area. In this study, river terrace remnants were mapped in the foothill of the SDI and in the Northern Maturín Basin. However, these terraces were not dated which motivated the continuation of the geomorphological investigations in this thesis. We extended the investigation area to the region between the Urica and San Francisco faults (Figure 3.1). Based on drainage network analysis, DEM image analysis, fieldwork observations and ^{10}Be and ^{26}Al dating of the deformed remnant alluvial deposits allowed the quantification of uplift rates above the thrusts. Finally, a recent geodynamic model in MFTB is proposed.

3.2. Physiographic Setting of the Study Area

This area comprises the Serranía Del Interior (SDI) foothills and the southern deformation front. It is limited to the west by the Urica Fault and to the east by the city of Maturín (Figure 3.1). The topographic slope gently decreases from the north-west (480 m) to the south-eastern border of the area where the heights range is between 50 and 80 m (Figure 3.2). To the west, near the Urica Fault, in the La Mesa de Capacho-Sabana del Frasco the topography reaches 250 m and stands about 100 m above the eastern part of the study area. The topography nearest the foothills of the SDI between the cities of San Felix and Quiriquire is higher (between 400 to 300 m) than the domain located around the cities of Furrial, Jusepín and Punta de Mata (between 200 to 100 m) and the Mesa de Macagua more to the south.

Zinck and Urriola (1970) described the area as a group of hills and plateaus gently inclined towards the southeast with an average slope of about 1-2%. The top of the hills is rounded and hillside slopes are gentle. Erosion and tectonics have created the typical landscape of

the area. The great peneplains were cut by regressive erosion and shaped by tectonic uplift.

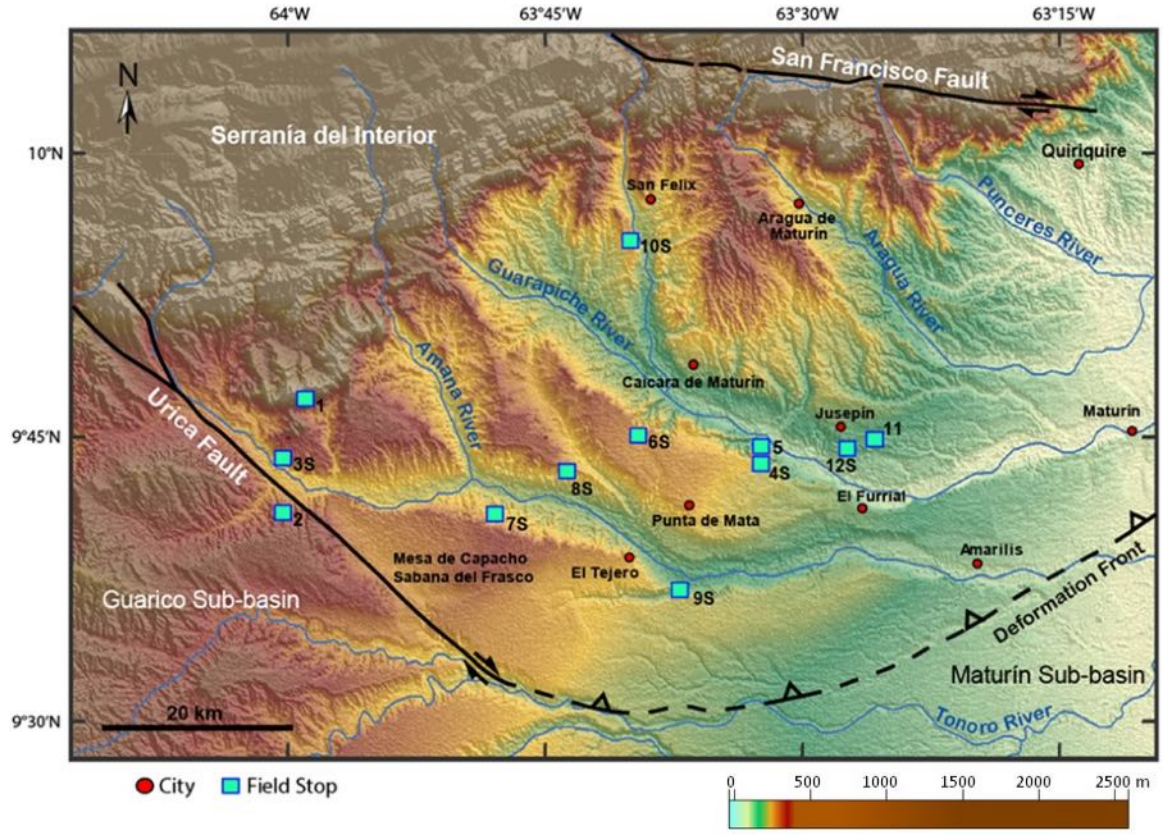

Figure 3.1. Shaded relief of the study area with field stops.

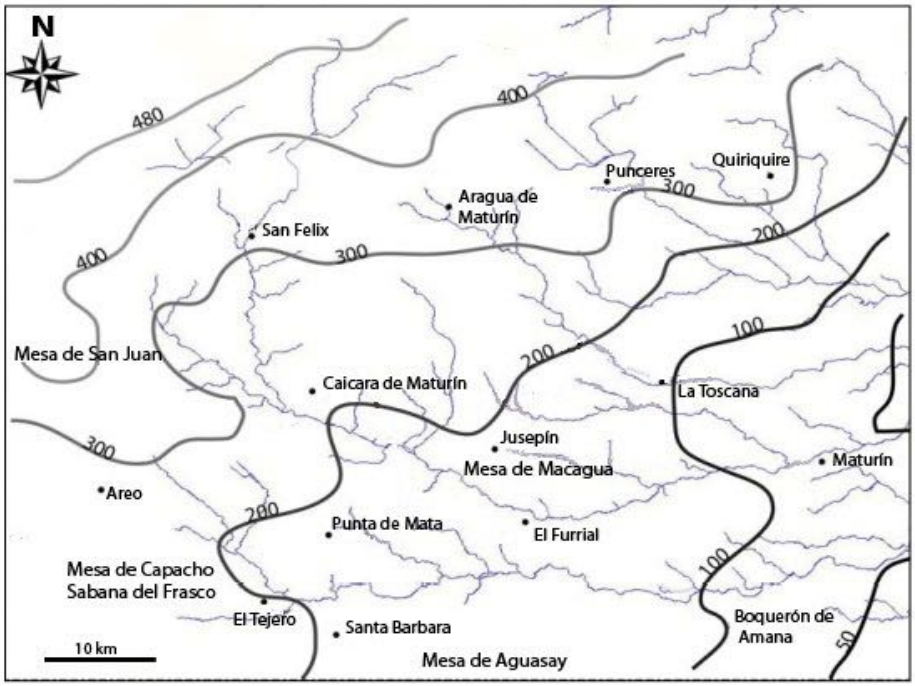

Figure 3.2. Height distribution in the Northern Maturín Sub-basin (modified from Wagner 2004).

The MFTB is drained by two main rivers, the Amana River and the Guarapiche River (Figure 3.1). They are part of San Juan River catchment and have their origin in the SDI, specifically in the Turimiquire mountain system at ~1100 m in elevation. The catchment relief is varied, from the SDI Range with mountains between 2595 m to 1200 m a.s.l, up to the Llanos Orientales peniplains with heights between 20 y 100 m a.s.l**.** The drainage is mainly dendritic around the hills (Figure 3.3).

In the MFTB, the course of rivers is controlled by tectonics. The upper reach of the Amana River flows N-S in the SDI mountains. At the Tarragona Ridge (350 m a.s.l) near the Urica Fault (Figure 3.3), the Amana River changes its course abruptly from N-S to SE direction when it cross cuts the Tarragona thrust. Farther to the east (~150 m a.s.l), the river changes its course once again from SE to E direction between the Punta de Mata and Amarilis ridges. It joins the San Juan River to the east and then to the Atlantic Ocean at ~120 km from the study area. The Amana River elevation varies between 90m and 60 m between the cities of El Tejero and El Furrial, respectively. The source of the Guarapiche River is located in the SDI mountains where it also flows N-S. Arriving of the MFTB, it bends SE along the Punta de Mata Ridge (210 m a.s.l). Towards the southeast, the course of the river changes to an east direction around the Jusepín Ridge. Like the Amana River, the Guarapiche River continues flowing eastward to join the San Juan River. The Guarapiche River entrenched the topographic plane deeply. From an elevation of 150 m at the foot of the SDI, the river reaches 70 m at the city of El Furrial and 35 m at the city of Maturín (Figure 3.3).

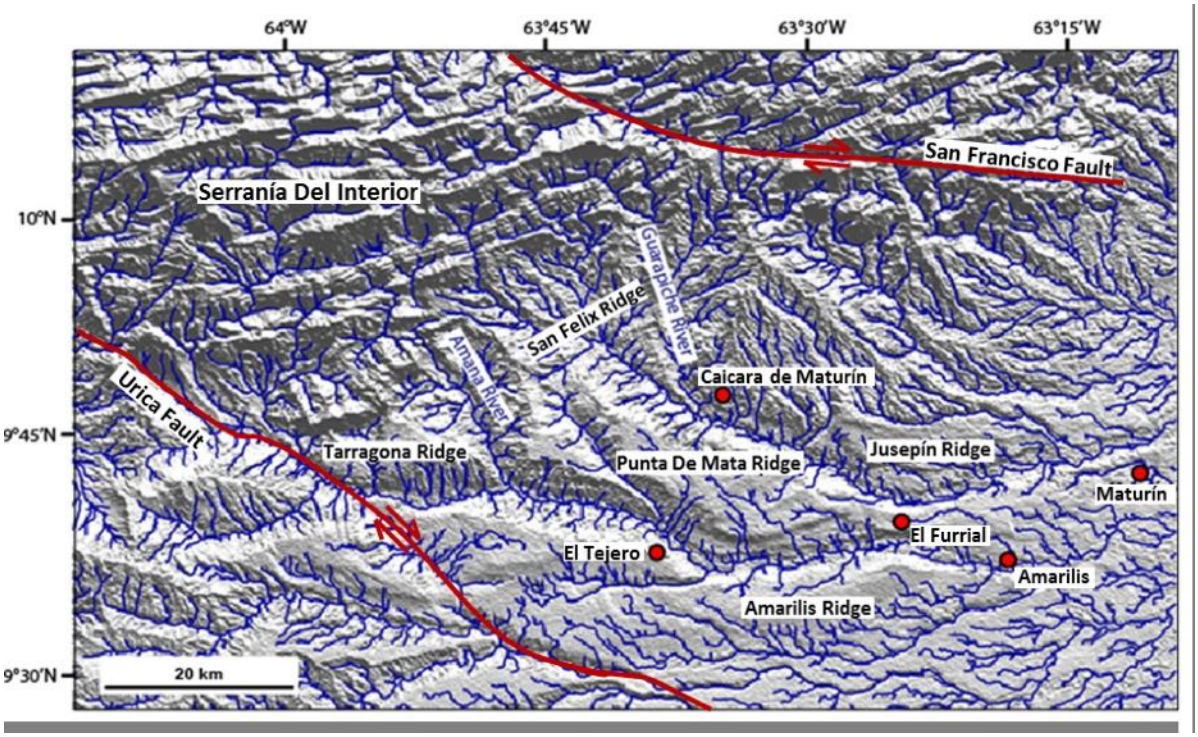

Figure 3.3. Drainage network in the MFTB.

The region is capped by the La Mesa Formation which is composed of silico-clastic coarse sands, gravels with very hard ferruginous cement, red almost black conglomerates, yellowish-white sands and red-purple sands. This formation also contains discontinuous lenses of sandy clay and silts (Gonzalez de Juana et al., 1980; LEV, 1997). The thickness is highly variable, but generally decreases from north to south, due to changes in the fluvial-deltaic sedimentation; and increases from west to east due to the advance of deltaic sediments (González de Juana et al., 1980) (see a more detailed description in CHAPTER 2). The formation has been considered to be of Pleistocene age based on the transitional relation with the Pliocene Las Piedras Formation (Zinck and Urriola, 1970; LEV, 1997).

3.3. Geomorphological Markers of the Quaternary Deformation

The tectonic geomorphology focuses on the link between relief and deformation. This interplay works at several scales of space and time and the use of the appropriate morphotectonic markers is fundamental for identifying the acting tectonic process. For example, a few hundred kilometers of rivers would be appropriate to investigate lithospheric deformations such as buckling or bending.

Most frequently, the morphotectonic markers studied are the river terraces and alluvial fans. These markers allow quantifying the relief formation and degradation rates using data from structural geology, relief morphology and surface geometry. The morphotectonic markers such as tilting, faulting and folding are studied herein as an expression of the tectonic activity. For example, the dating of the river terraces allowed identifying the maximum age of the tectonic deformation and discussing the recent tectonic regime.

The growth of the current deformation front of the SDI acting throughout reverse fault propagation folding in the pre Middle-Miocene units is explored here. For this reason, fluvial remnant terraces are used in this research as deformation markers.

- **River Terraces**

This type of terraces is formed by rivers. Without deformation, terrace remnants are stepped or buried above/under the current river but remains parallel to it. River terraces can also be the remnant of an abandoned flood plain or valley floor produced during a fluvial erosion state or deposition. River terraces studies are one of the fundamental research methods used as morphotectonic markers to record the recent movements of active faults and folds occurring on the mainland (Jain, 2003).

River terraces can be classified in three types according to the fluvial dynamics, morphology and the thickness of the alluvial deposits (Figure 3.4):

- Strath terraces resulting from an incision process and is characterized by a sub horizontal erosional base, carved either into bedrock or soft and poorly consolidated sediments. The strath is covered by a thin alluvial sediments layer ≤ 5 m (Guzmán, 2014).

- Fill terraces formed by thick deposition of alluvial sediment above the substratum during an aggradation episode.

- Fill-cut terraces formed by erosion after alluvial sediments are deposited above the sub-stratum. This type of terrace is formed below the fill terraces.

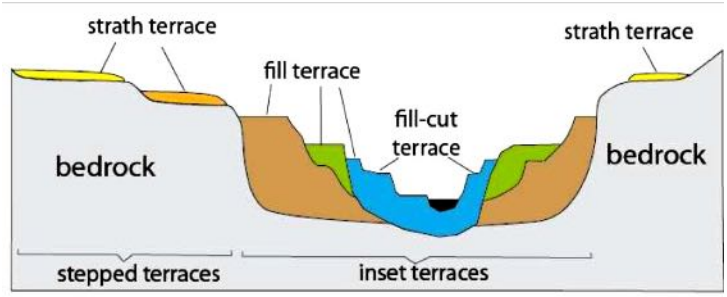

Figure 3.4. Schematic cross-section through a river valley showing geometric differences between strath, fill and fill-cut terraces. An idealized complex of stepped and inset terraces is also shown (from Guzman, 2014)

Zinck and Urriola (1970) recognized four river terrace levels (from Q_0 to Q_3 in an upward direction) along the Guarapiche River (Figure 3.3 and Figure 3.5). These authors found dissymmetric grabens characterized by staggered step series. These grabens are bounded by scarps of 5-10 m high. In the Tonoro River (southern boundary of the study area) three terrace levels were observed. These terrace level numbers continue decreasing southward up to 1 or 2 levels.

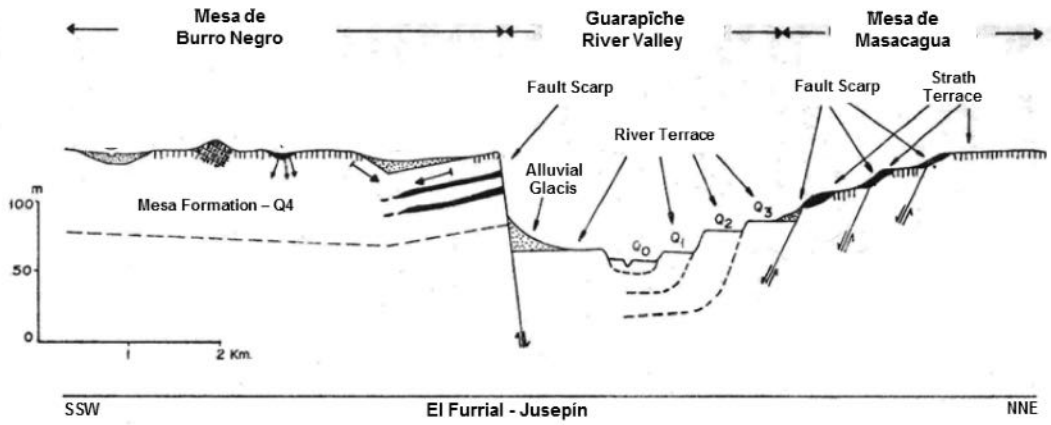

Figure 3.5. Schematic cross-section in the Guarapiche River valley (See location of the river in Figure 3.3) (modified from Zinck and Urriola, 1970).

To the north of the city of Jusepín, Wagner (2004) mapped othe river terraces across the Jusepín thrust. He observed three and four stepped terrace levels that he interpreted as fold-related (Figure 3.6). Based on SRTM DEM, stepping of the highest terrace reaches 20 m high above the current river level.

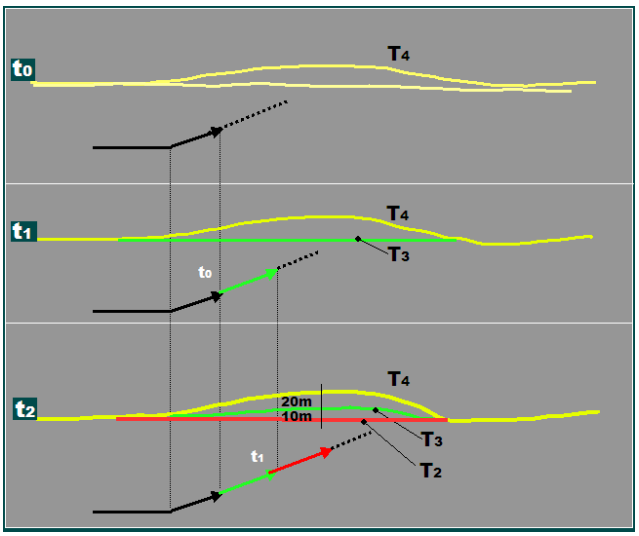

Figure 3.6. Schematic cross-section of the terrace evolution above the Jusepín thrust. Note that the first terrace (T_4) has a larger incision than the most recent ones (T_2, T_3) (from Wagner, 2004).

3.4. Methodology

The morphotectonic analysis was carried out in order to identify deformation and alteration of river terraces and drainage patterns as evidence of the Quaternary tectonic activity. These deformations are expressed by surface uplift, tilting, folding and faulting of river terraces. Similarly, these deformations disturb the drainage pattern. In this thesis, we focused on finding evidences for these deformations in the river terraces and in the drainage network. Finally, dating of the terraces was performed to demonstrate their Quaternary origin and to calculate the deformation rate in the area.

The methodology developed to carry out the morphotectonic analysis consisted of three stages: The first stage, topographic analysis, focused on SRTM DEM images, topographic profiles, topographical and geological maps, drainage network, etc. The second stage consisted of fieldwork and the third stage of dating and quantification of the recent deformation (Figure 3.7).

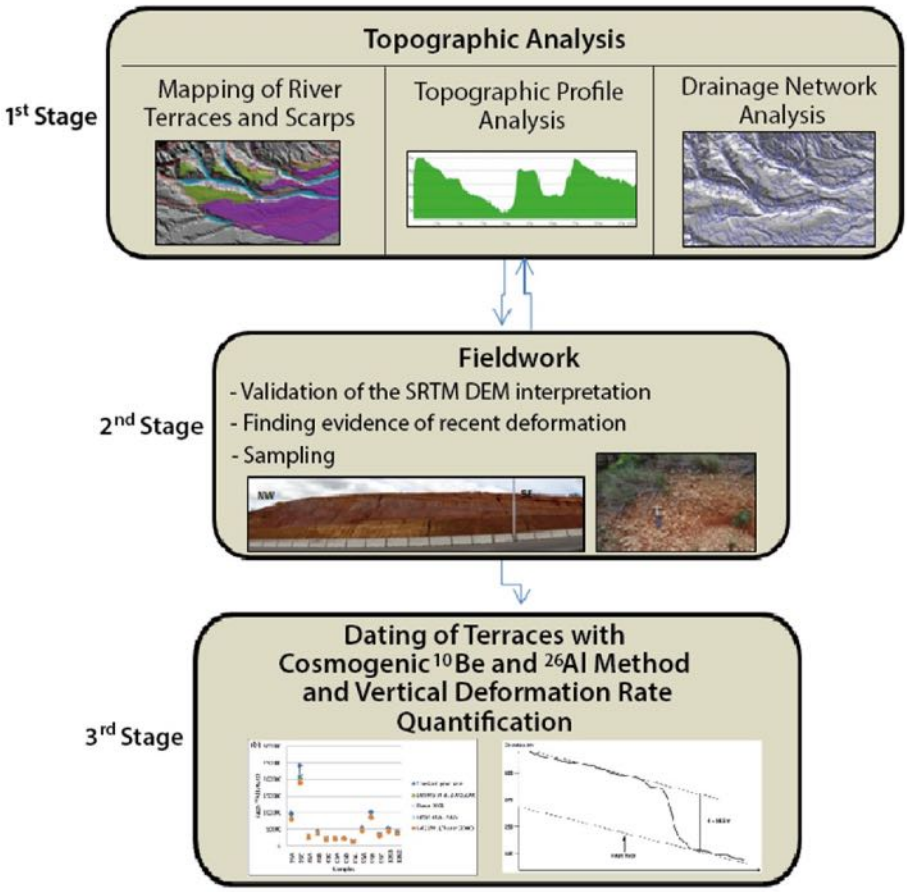

Figure 3.7. Scheme showing the general methodology for the morphotectonic analysis performed in this study.

3.4.1. Morphotectonic Analysis

Topographic Analysis (1st Stage)

The stage was realized with the data and the techniques described as follows:

- Digital elevation model (DEM) interpretation: This stage aims to identify evidence of deformation using the DEM. We focus on topographic scarps, slope and drainage anomalies as expressions of vertical displacements of the topographics on the surface. Drainage morphology was also analyzed in order to find potential deviations in the river courses. Finally, a map of potential deformations indices was elaborated on the SRTM DEM image. According to Farr et al. (2007), the spatial resolution is 90 m and the absolute vertical resolution is between 10 and 16 m (Figure 3.1).

- Topographic profiles extracted from DEM: This stage consisted of carrying out topographic profiles extracted from DEM across the topographic anomalies identified in

the previous stage. These profiles allow identifying relief discontinuity such as: folding, faulting, tilting, abrupt changes of the slopes, among others, that may be related to tectonics. Also, this stage was very useful in determining the road map in the field and the structures to sample.

- Extraction and analysis of the drainage network from DEM: The drainage network extraction was performed using Global Mapper software version 10.0. The aim was to identify perturbations and deviations of the river network which are very sensitive to tectonic disturbances. The drainage network was extracted in the entire study area and also in some specific zones around the Jusepín zone in order to observe the changes of the stream in detail.

Fieldwork (2nd Stage)

Fieldwork is an indispensable step in validating the interpretations made from the DEM. Also, fieldwork gives access to the lithology rock types, weathering and to the features of small scale like faults and fractures. Alternatively, this step allowed us to sample the outcrop in order to date the morphological markers (see 3rd step). In order to carry out these observations 12 stops were made (Figure 3.1).

To summarize, the specific objectives of the fieldwork were:

- Validate the morpho-structural model obtained from DEM: many objects may present morphological traces on the satellite image and on DEM comparable to tectonic deformations. These objects are often man-made (roads, channels, among others) and need to be recognized in the field.

- Specify the location of scarps observed on the images: The elevation value given by DEM is the average value of one pixel. This is an uncertainty related to the pixel dimension. Furthermore, the calculations of slopes that help to identify the scarps, is performed on at least two pixels. This calculation method way doubles the minimum uncertainty in the real position of the scarps.

- Identify objects of smaller dimensions than the vertical planar and altitudinal resolution of the DEM: The DEM used in this study has a resolution of 90 m, therefore, structures < 90 m are invisible in this image. Similarly, breaks on the surface (scarps)

associated with fault emergence with a height lower than the vertical resolution (10 to 16 m), will not be visible.

- Date the terraces with the cosmogenic ^{10}Be and ^{26}Al method: This method allows surface dating. The occurrence of the deformation postdates the shaping of the dated surface. By measuring the exposition time of the rock to sunlight, the date of surface shaping is obtained. The method involves sampling quartz-containing rocks on the ground surface.

River Terraces Dating and Vertical Deformation Quantification (3rd Stage)

The third stage consists of dating terraces using the ^{10}Be and ^{26}Al method and then calculating the uplift rate. Cosmogenic nuclide dating allows estimating the exposure time (ages) of surfaces to the sunlight within a period comprised of thousands to hundreds of thousands of years (Nishiizumi et al.,1986; Klein et al., 1986). This covers the period of recent surfaces formation such as terraces and alluvial fans. The dating method is presented in section 3.4.2.

Crustal movements may deform the surface and are generally associated with vertical displacements whose measurements allow quantification of deformation rates. The vertical displacement is expressed by scarps in topography and tilting of deposits. In active tectonic studies, this vertical offset is calculated measuring the average topographic distance between the foot-wall and hanging-wall slope envelopes (Regard et al., 2005, Carretier et al., 2009) (Figure 3.8). Then, the uplift rate is the vertical offset divided by the age of the surface:

$$V_z \approx \frac{H}{t}$$

where, V_z is the vertical deformation (mm/y), H is the topographic distance between the foot-wall and hanging-wall slope envelopes and t is the age obtained by ^{10}Be and ^{26}Al dating.

3.4.2. Dating of River Terraces using ^{10}Be and ^{26}Al Method

General Principles

Cosmogenic ^{10}Be is produced in the atmosphere by spallation reactions owing to the impact of cosmic rays on the nitrogen and the oxygen. This production is on the order of 10^3 times faster than the average rate in rocks (Gosse and Phillips, 2001). Also, ^{10}Be is produced by

spallation reactions directly from oxygen in the matrix of the rock minerals exposed in the first meters of the Earth's crust and to a lesser extent from heavier elements such as Mg, Al, Si, and Ca (Vassallo, 2006; Masarik, 2002; Kober et al., 2005) (Figure 3.9). At sea level, the production rate in quartz is about 4.5 atoms $g^{-1}y^{-1}$ and decreases rapidly with the depth below the ground surface (Balco et al., 2008). Reactions within the atmosphere decrease the cosmic rays abundance towards the Earth's surface: in turn, the production rate increases with elevation.

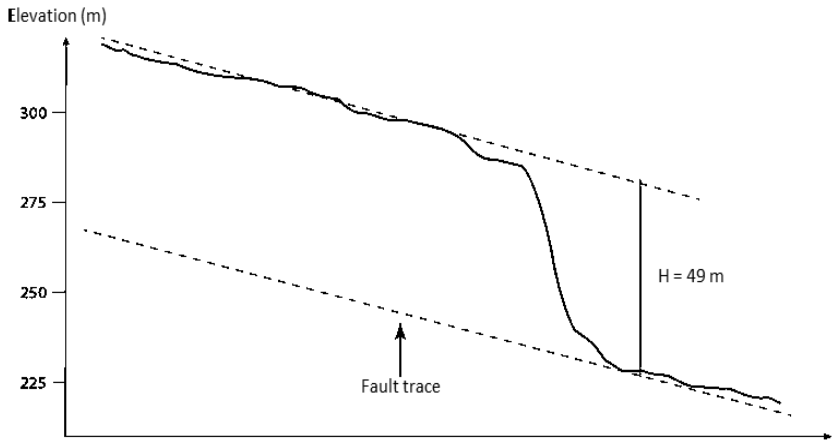

Figure 3.8. Topographic profile across the Tarragona scarp extracted from DEM. The scarp height reaches 49 m. Due to its location above the seismic trace of the Tarragona Thrust (black arrow) this scarp is assumed to be of tectonic origin.

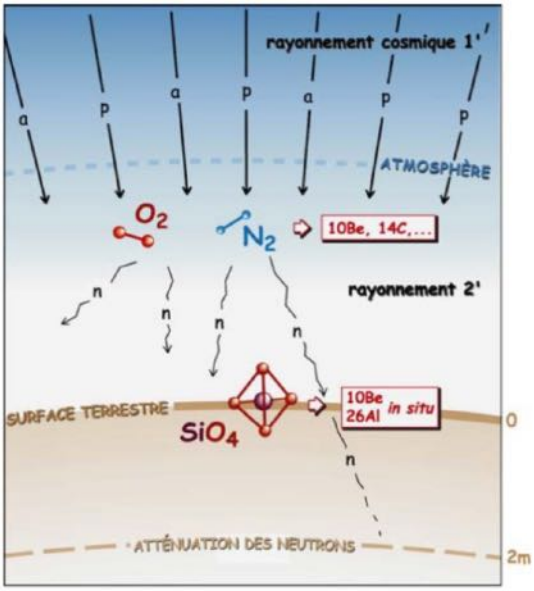

Figure 3.9. Scheme showing the process of ^{10}Be production by cosmic rays in the first meters of the Earth's crust (from Vassallo, 2006).

In crustal rocks such as quartz, ^{26}Al is mainly produced by spallation reactions from ^{27}Al and Si (Masarik, 2002). The production rate in quartz is about 30 atoms $g^{-1}a^{-1}$ and decreases

rapidly with depth in the subsurface (Balco et al., 2008).

In quartz, ^{10}Be and ^{26}Al are produced proportionally from cosmic rays. The production ratio is about P(^{26}Al) = k P(^{10}Be), k ~6.75. In contrast, ^{26}Al radioactive decay is faster than that of ^{10}Be (half-lives are $T_{1/2}$ ^{26}Al = 0.73 Ma and $T_{1/2}$ ^{10}Be =1.36 Ma). The ^{10}Be and ^{26}Al couple is used regularly to constrain complex histories by comparing their relative abundances (Braucher et al., 2000; Granger and Muzikar, 2001) and by comparing the ages provided for each of them (Braucher et al., 2000).

The relation between the alluvial surface ages given by the ^{10}Be and ^{26}Al dating method, can lead to three possible scenarios (Granger & Muzicar, 2001; Messager, 2010; Regard, personal communication):

- If the age obtained from ^{10}Be and ^{26}Al are similar indicates that the rock has a simple depositional history on the terrace from which it was removed.

- If the age obtained from ^{26}Al is less than that obtained from ^{10}Be (^{26}Al age < 10Be age) indicates a long and complex depositional history with at least one episode of burial which may also comprise storage, exhumation and remobilization of the material.

- If the age obtained from ^{10}Be is less than that obtained from ^{26}Al (^{10}Be age < ^{26}Al age), there must be an error in the age calculation due to the production relation (^{26}Al = ~6.75 ^{10}Be).

The cosmogenic nuclide production rates also depend on the magnetic field intensity which varies according to the latitude (Lal, 1991; Stone, 2000) (Figure 3.10). This intensity determines the cosmic ray flux produced in the rock minerals. This dependence, coupled with the dissipation of the cosmic radiation within the Earth's atmosphere due to altitude is the major reason for observing latitudinal and altitudinal variability in cosmogenic nuclide production rates (Braucher, 1998). This surface production rate (P_0) is well known for the mineral quartz as a function of the altitude and latitude (Lal, 1991; Stone, 2000; Dunai, 2010).

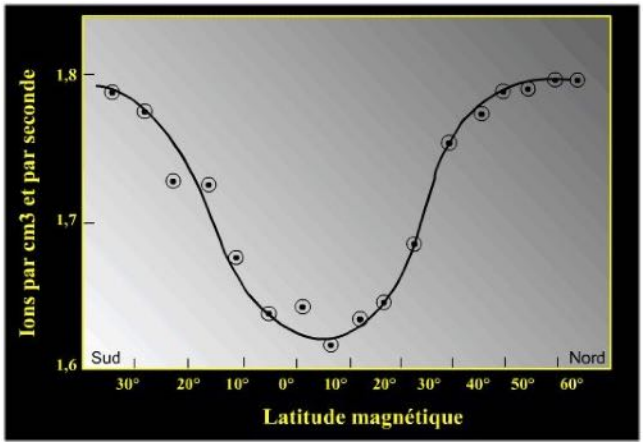

Figure 3.10. Ion production variations per second with respect to latitude (from Siame, 2004).

Different models are currently used to calculate the production rate such as: Desilets et al. (2006); Dunai (2001), Lifton et al. (2005), Lal (1991) and Stone (2000). Following, the model of Lal (1991) is used as an example in order to explain the production rate equations.

The production rate (P_0) is expressed by the polynomial of Lal (1991) (Equation 3.1):

$$P_0\,(L, z) = a(L) + b(L)z + c(L)z^2 + d(L)z^3 \tag{3.1}$$

where, L is the geomagnetic latitude, a,b,c,d are coefficients as a function of L and z is the site altitude in km.

At greater depths from the Earth's surfaces, the in situ ^{10}Be production rate decreases according to the absorption of the cosmic rays by the material traversed. This causes an exponential decay of the production with respect to the depth from the surface (Siame, 2004; Braucher et al., 2003; Vassallo, 2006). This evolution of the cosmogenic nuclide production rate $P_{(x)}$ as a function of the depth (x) and of the density of the material traversed (ρ) is given by the Equation 3.2:

$$P_{(x)} = P_0 \times e^{(-\rho x/\Lambda)} \tag{3.2}$$

where, $P_{(x)}$ is expressed in atom/g/y, P_0 is the surface production rate, x is expressed in cm, ρ is the density of the material traversed (g/cm^3) and Λ is the particle attenuation length (g/cm^2). The particle attenuation length in neutrons is ~150 g/cm^2, for slow muons is ~1500 g/cm^2 and for fast muons, ~5300 g/cm^2 (e.g. Braucher et al., 2003).

Moreover, the cosmogenic nuclide concentration increases with the exposure time but

decreases due to radioactive decay and to erosion. A steady-state between the production and the losses can be reached (Lal, 1991). Figure 3.11 also indicates that the top-left area in the graph cannot be explained: this constitutes a forbidden area. For a given concentration (y axis) the first time-compatible curve reached (in increasing x direction) is the zero-erosion curve. Consequently, assuming a simple exposure history and negligible erosion (ε=0), the exposure time (t_{min}) can be calculated using the Equation 3.3:

$$t_{min} = -\frac{1}{\lambda} \times \mathrm{Ln}\left(1 - \frac{\lambda C}{P_0}\right) \quad (3.3)$$

where, λ is the radioactive decay constant of ^{10}Be or ^{26}Al and C is the ^{10}Be or ^{26}Al concentration.

When the steady state has not been reached, cosmogenic nuclides are useful for dating surfaces. On the contrary, when it has been reached, cosmogenic nuclides give information on denudation rates: they can be calculated by Equation 3.4 (Braucher et al., 2000)

$$\varepsilon_{max} = \left(\frac{P_0}{C_{(0,\infty)}} - \lambda\right) \times \Lambda \quad (3.4)$$

where, $C_{(0,\infty)}$ is the ^{10}Be (or ^{26}Al) concentration at steady-state balance. Figure 3.11 illustrates that a concentration $C_{(0,\infty)}$ can be reached for lower erosion rates (if not at steady state) but not for higher erosion rates, thus giving a maximum estimate of erosion rate. Typical surfaces at steady state are either surfaces with low denudation rates (cratonic surfaces for example; Beauvais and Chardon, 2013) or actively eroding surfaces like mountains (F.von Blanckenburg, 2005).

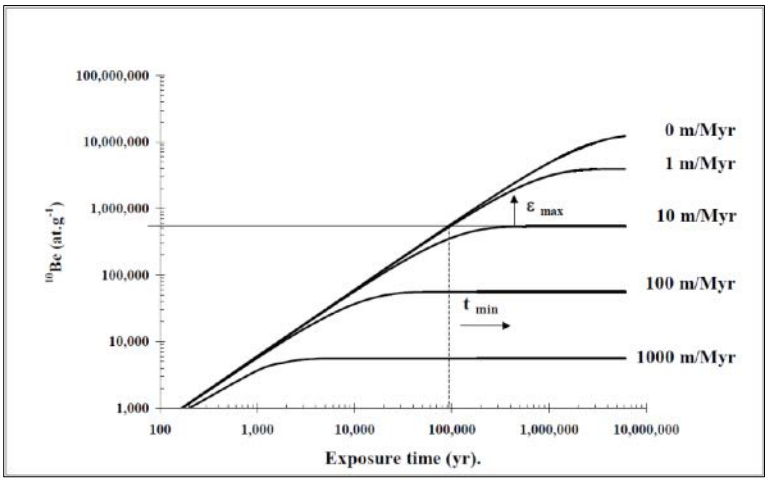

Figure 3.11. Theoretical evolution of ^{10}Be concentration with exposure time for different erosion rates (from Braucher et al., 2000).

Another important aspect that affects the cosmogenic nuclides concentration is burial. When the environmental changes bury minerals previously to their exposure a la surface (eroding), the cosmogenic nuclides balance changes. There is no additional decrease by erosion, but production is less and can be negligible if burial depth is more than 10 m; on the contrary, the radioactive decay is enhanced (Braucher et al., 2000).

^{26}Al and ^{10}Be Ratio

The ^{26}Al and ^{10}Be ratio is a relation that can be used to understand complex histories and the mechanisms involved during the evolution of the surface analysed (Lal, 1991; Nishiizumi et al., 1991; Granger and Muzikar, 2001)

The significantly different radioactive decay constants of these two cosmogenic nuclides imply that in the case of any surface (whether or not at steady state), the ratio vs. nuclide concentration curves envolve closely toward a ‘‘steady erosion curve” (Figure 3.12). In the case where the rock has been exposed for a given time (t) and erosion rates equal zero (ε = 0), ^{26}Al/^{10}Be ratio is expressed by Equation 3.5 (Braucher et al., 2000):

$$\frac{C_{26(0,t)}}{C_{10(0,t)}} = \frac{P_{26}\lambda_{10}}{P_{10}\lambda_{26}} \frac{1-e^{-\lambda 10 t}}{1-e^{-\lambda 26 t}} \quad (3.5)$$

If the case corresponds to finite erosion and an infinite exposure time, the ratio is expressed by Equation 3.6:

$$\frac{C_{26(\varepsilon,\infty)}}{C_{10(\varepsilon,\infty)}} = \frac{P_{26}}{P_{10}} \frac{\lambda_{10}+\frac{\varepsilon}{\Lambda_n}}{\lambda_{26}+\frac{\varepsilon}{\Lambda_n}} \quad (3.6)$$

If a rock that has been exposed is then buried and shielded from the cosmic rays, the ^{26}Al and ^{10}Be concentration decreases due to the radioactive decay. This indicates complex histories of exposure and burial.

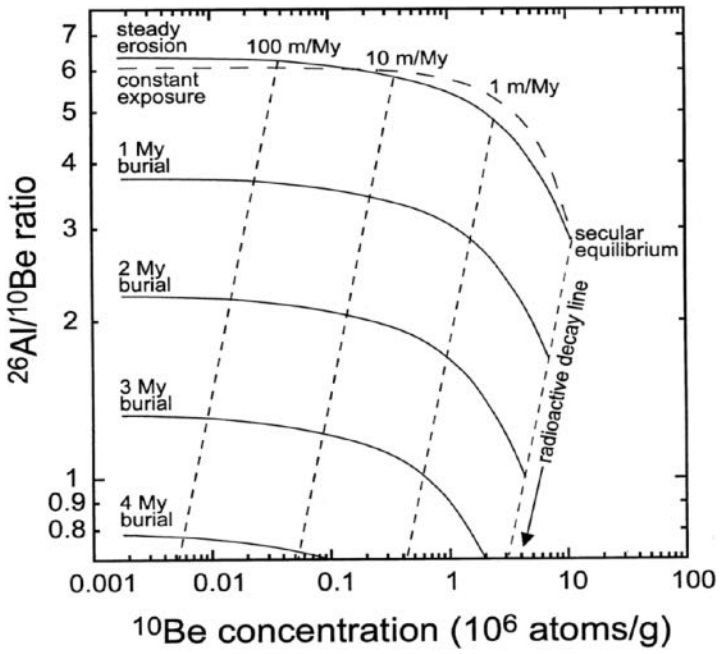

Figure 3.12. $^{26}Al/^{10}Be$ ratio vs ^{10}Be concentration in sediments. Quartz grains with no burial history should plot between the "constant exposure" and "steady erosion" lines. Note that muonic production causes these two lines to cross. For sediment that is buried and completely shielded from cosmic rays, the $^{26}Al/^{10}Be$ ratio decreases along a line parallel to the dashed "radioactive decay line". Million-year isochrons are shown for sediment burial following steady erosion (from Granger and Musikar, 2001)

Surface Sampling for ^{10}Be and ^{26}Al Dating Method

In this study, in situ ^{10}Be and ^{26}Al method was used for dating quaternary surfaces. Cosmogenic ^{10}Be and ^{26}Al are used mainly in quartz (SiO_2) which can be found in a wide range of geological settings (Dunai, 2011). Additionally, quartz is resistant to erosion and has a tight crystal structure that minimizes diffusion and contamination by meteoric ^{10}Be. The main targets for ^{10}Be production in quartz are ^{16}O and ^{28}Si whereas for ^{26}Al production the only one is ^{28}Si (Braucher, 1998).

There are two techniques for alluvial formation sampling: surface sampling and depth-profile sampling. The technique to use depends primarily on the field conditions and sampling time. Five different terraces geographically distributed in the study area were sampled and dated. Only surface sampling was made on the MFTB terraces due to time and equipment limitation in the field.

The rocks sampled are mainly formed by quartz and embedded within the surface terrace, in flat areas and distant from escarpments and landslides. Also, the rocks sampled must have similar size and shape and characteristics and must not be fractured or weathered (Figure

3.13). These sampling conditions are necessary to avoid taking rocks that could have been transported and/or eroded from neighboring areas, thus assuring that they were deposited on the surface sampled. Five or six rocks from each terrace were taken in order to discriminate complex exposure histories better.

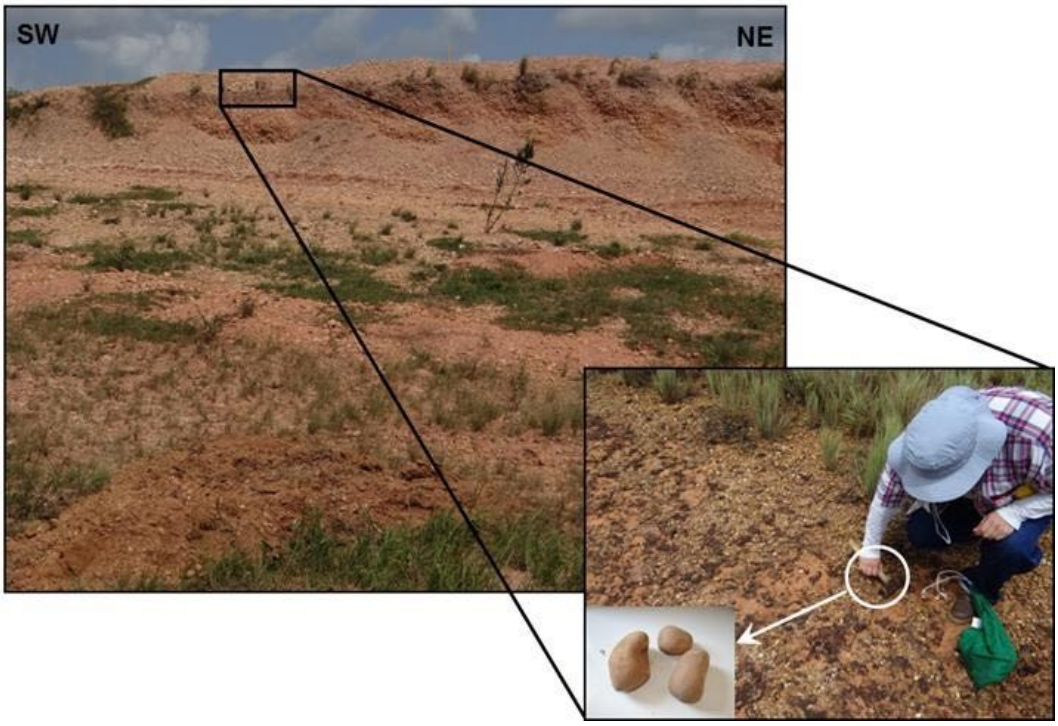

Figure 3.13. Example of the terrace sampled in site 11S in the Jusepín zone (above). Quartzite rock sample embedded in the surface terrace (bottom).

3.5. Morphologic Signature of the Quaternary Deformations in the MFTB

In this thesis, the morphotectonic analysis is integrated with the study of 11 sites of which 8 have been sampled (3S, 4S, 6S, 7S, 8S, 9S, 10S and 12S) and five sites (3S, 4S, 6S, 9S and 12S) were dated by the ^{10}Be and ^{26}Al method (Figure 3.14). These sites were chosen taking into account the ridges observed in DEM and the main fault zones identified in previous studies carried out in the area. The observations were divided into five zones. From the mountain front to the foreland, these zones are: Tarragona (to the west), San Felix (to the north), Punta de Mata (in the central part), Jusepín (to the east) and Amarilis (to the south).

3.5.1. Surface Deformation in the San Felix Zone (Site 10S)

The San Felix zone is located in the north central part of the study area at the border with the SDI (Figure 3.14). Here, a ridge of 30 km long SW-NE direction named by us San Felix Ridge is associated with the San Felix Thrust interpreted in SRTM DEM image (Figure 3.15a). Its maximum elevation reaches 300 m to the east and decreases progressively to

175 m to the southwest (Figure 3.15c). The ridge is limited to the south by two scarps. The NW scarp (km 2 in Figure 3.15b) is 25 m high and the SE scarp is 15 m high (km 4 in Figure 3.15b). The northernmost one follows the trace of the San Felix thrust.

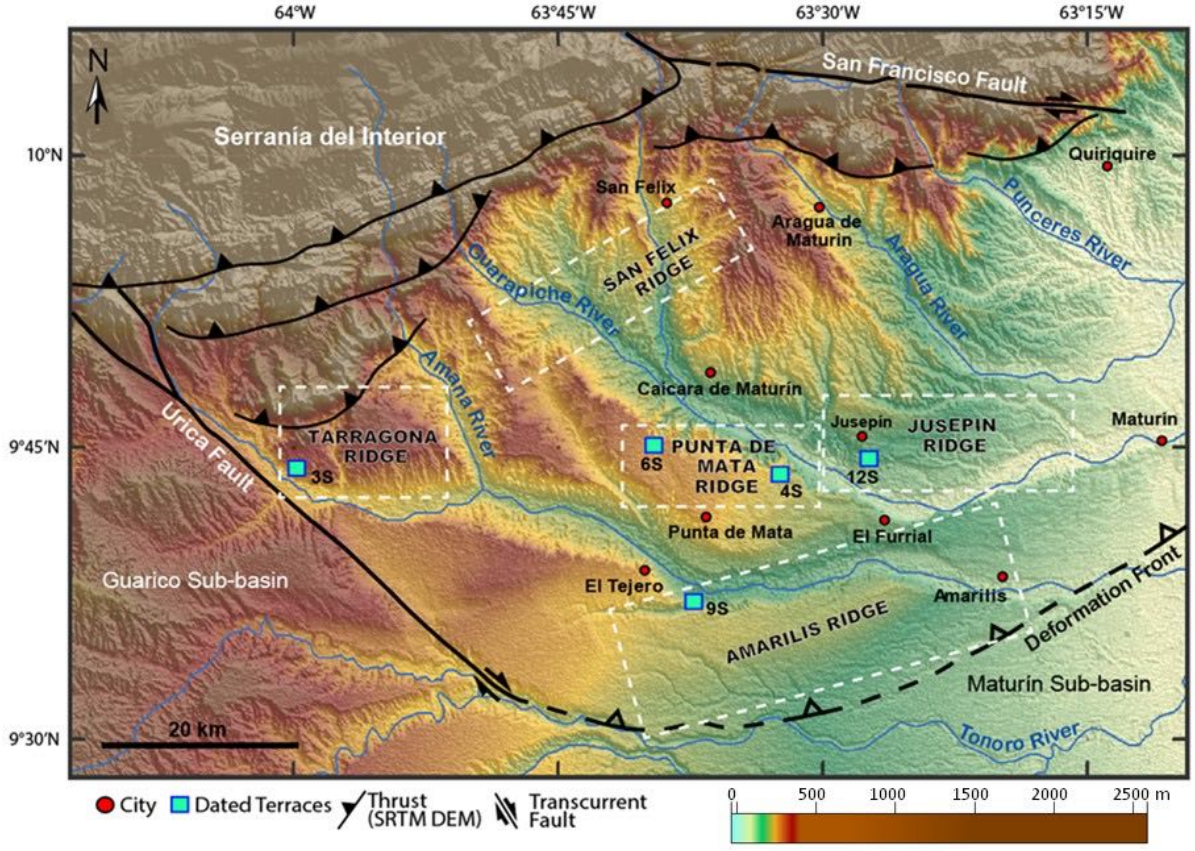

Figure 3.14. SRTM DEM showing the ridges and the dated terraces observed in MFTB.

Figure 3.16 shows the terraces of the Guarapiche River immediately upstream from the San Felix Thrust (orange square in Figure 3.15 for location) where the alluvial plain is wide. Five terrace levels are observed in the landscape. The lower terraces (T1 to T3) are currently cultivated whereas the uppermost T4 and T5 are covered by forest. The stepping of these levels shows an entrenchment of the river in the hanging-wall of the San Felix thrust.

Terraces T1 to T3 dip gently to the south, remaining parallel to the river current (T0), but the oldest T4 and T5 terraces dip to the north. We interpret this tilt as the consequence of the San Felix Thrust activity during and after the shaping of T4 and T5. This explains why the younger T4 level appears less back-tilted than T5. The thrust does not seem active after shaping T3.

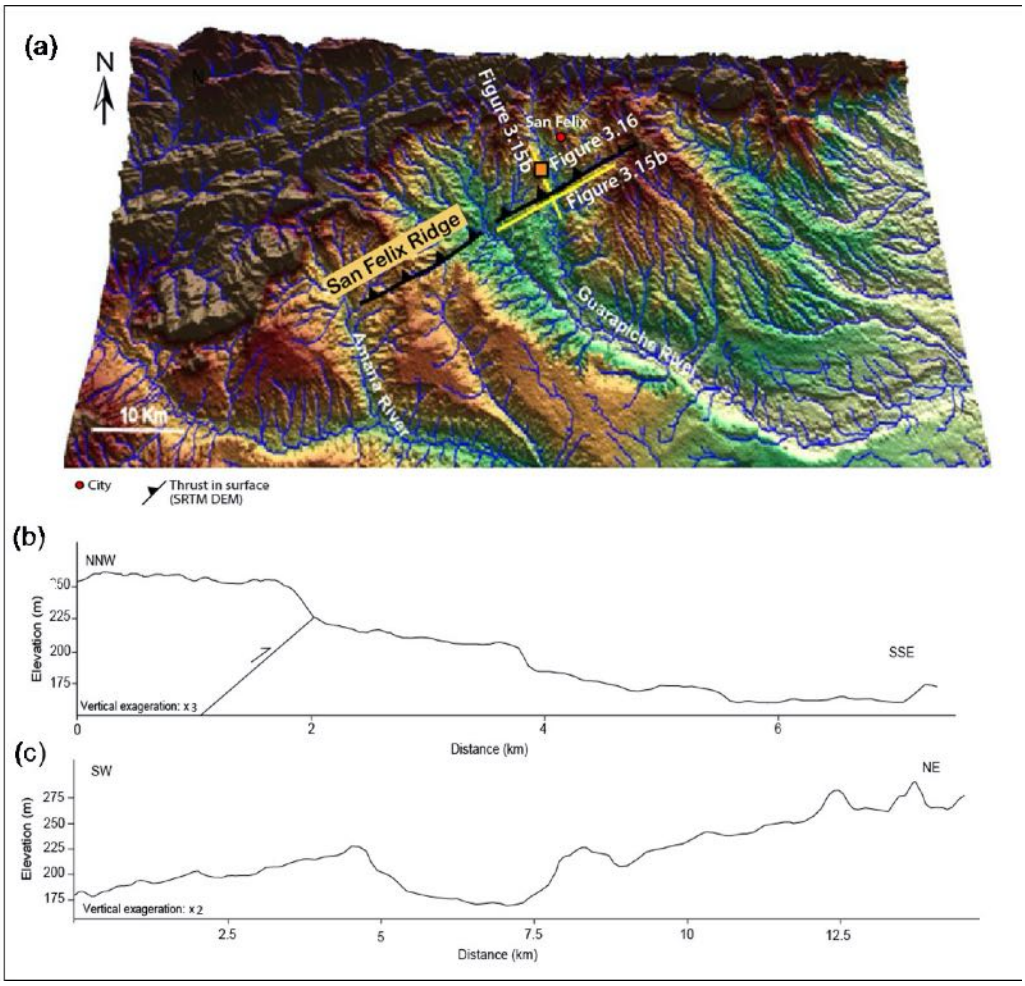

Figure 3.15. (a) 3D-view of the San Felix Ridge extracted from shaded DEM image (b) Topographic profile across the thrust, showing the two structural scarps (km 2 and 4). (c) The topographic profile along strike of the ridge shows that its elevation decreases to the west.

The Tarragona Ridge is located against the Urica Fault to the west of the MFTB and to the north of the Tarragona thrust. This ridge is 3 km wide and 9 km long in an EW direction and reaches 375 m in elevation (Figure 3.17a). Its gentle slope to the south (0,8°) corresponds to the deposition slope of the foothill. The ridge is asymmetric and limited to the south by a high scarp of 30 ± 5 m aligned to the trace of the Tarragona thrust. This uncertainty of 5 m is not linked to the resolution of the DEM which is difficult to evaluate, it is linked to the lateral variation of the scarp height. As stated above, the absolute resolution of the SRTM DEM is lower than 16 m. That is why it is interpreted as a tectonic scarp (Figure 3.17b). To the west, the scarp bends northward to become parallel to the Urica Fault. At the base of the scarp, the course of the Amana River has been forced to follow the thrust scarp due to the deformation that constrained the river.

Figure 3.16. Remnant terraces of the Guarapiche River near the San Felix Ridge. Note that T4 is back tilted to the north in the hanging-wall of the San Felix thrust. T1, T2 and T3 remain parallel to the river (T0) showing that the thrust is not still active. (Picture taken from site 10S)

3.5.2. Surface Deformation in the Tarragona Zone (Site 3S)

A terrace remnant in the Tarragona Ridge was identified in the field (green square in Figure 3.17a). The outcrop is topped by a ~0.5 m-thick alluvial layer made of small pebbles (a few cm) and coarse sands. The terrace dips strongly (>15°) towards the SW. Under the alluvium layer, a yellowish siltstone layer lays above a greenish one.

Figure 3.18 shows that the greenish silts at the right (NE) have been displaced and placed in contact with the yellowish silts at the left (SW). This displacement suggests the presence of a reverse fault (~10° north dipping) that displaced the siltstones and tilted the overlain alluvium layer. This reverse fault can be interpreted as a surface faulting associated with the Tarragona thrust.

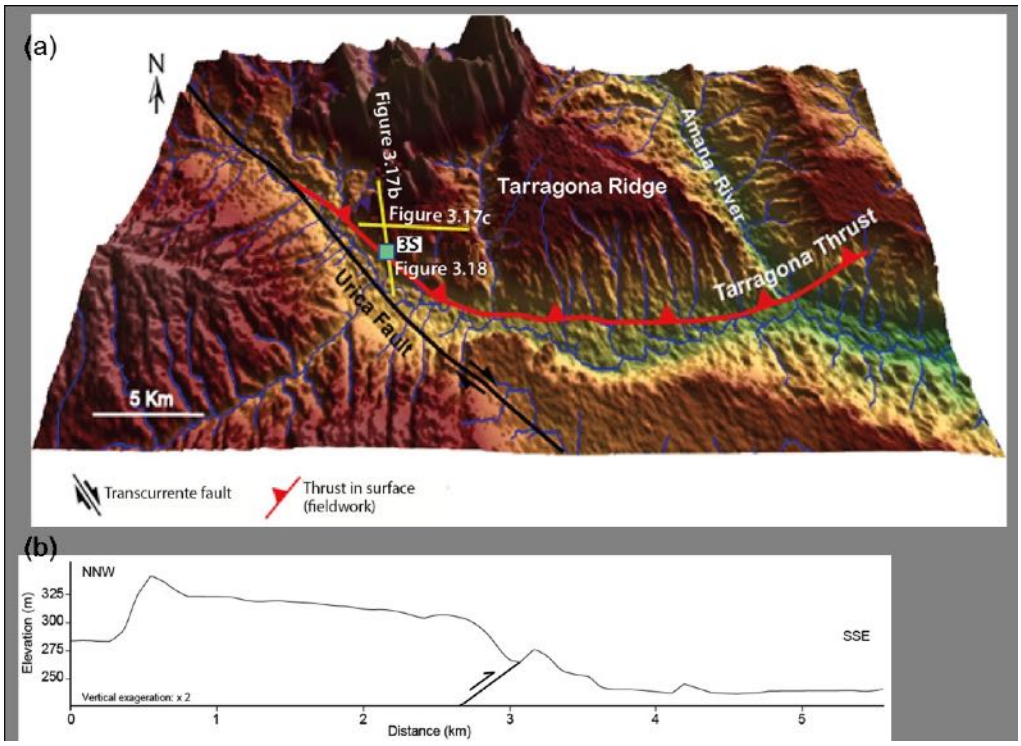

Figure 3.17. (a) 3D-view of the Tarragona Ridge (shaded SRTM DEM). (b) Topographic profile across the Tarragona Ridge showing the tectonic scarp associated with the Tarragona thrust.

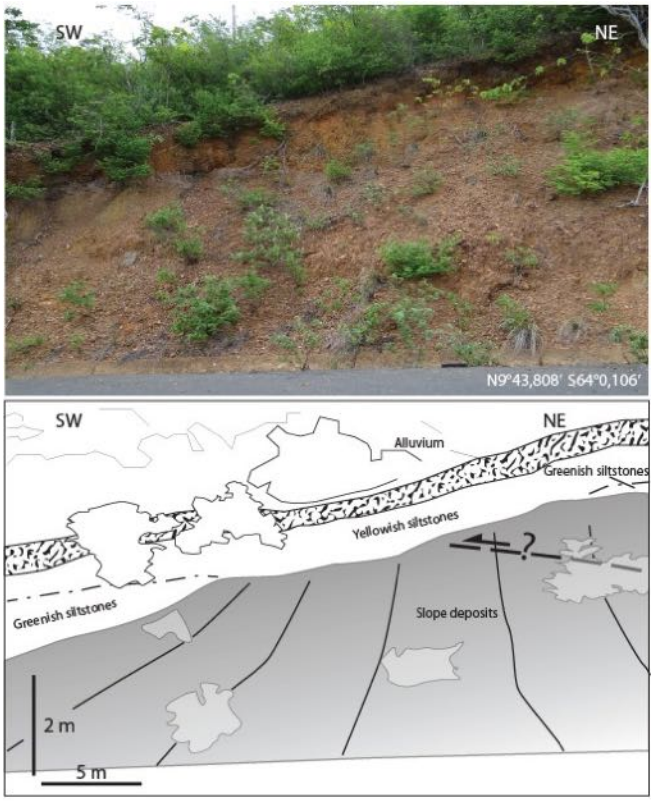

Figure 3.18. Reverse surface faulting associated with the Tarragona thrust. Outcrop photo (top) and its interpretation (bottom).The contact between yellowish and greenish siltstones shows a gently north-dipping reverse fault that tilted the upper alluvium layer.

3.5.3. Surface Deformation in the Jusepín Zone (Site 11 and 12S)

The Jusepín Ridge is located to the east of the MFTB, The ridge has a length of 28 km and an approximately E-W trend (Figure 3.19a and b). It is overprinted to a mean regional slope of ~1.25°. Its mean elevation is 120 m a.s.l. The greater heights are located to the north (180 m a.s.l.) and decreases towards the south (50 m a.s.l). The elevation decreases eastward along strike (Figure 3.19c). A 3D-view and a NW-SE topographic profile show two slope-breaks (Figure 3.19a). Another slope-break to the west (Figure 3.19a) is not cross-cut by the topographic profile in Figure 3.19b. These three slope-breaks were interpreted as fault scarps because they correspond to faults located in geological maps or to thrusts observed in seismic profiles. The asymmetry of scarp and topography also discards the possibility of erosional scarps.

The medium scarp reaches here 10 m (km 2.5 in Figure 3.19b). Figure 3.20 shows its morphological trace in the field. It is easily followed along an approximately E-W trend for over 15 km. The ridge is associated with the Jusepín Thrust which strongly forced the drainage. Regionally, the upper reaches of the Guarapiche River flow across the SDI in N-S

direction. Then, the lower reaches of the river flow downstream in a NW-SE direction. Once again, in the Jusepín zone, the Guarapiche River drainage network changes its course abruptly to a W-E direction parallel to the Jusepín Ridge.

More locally, Figure 3.21 shows the change in direction of the flow along the southern border of the Jusepín Ridge. The drainage pattern visible on the hanging-wall block is characterized by short and deep stream incisions along tributary creeks located at the toe of the scarp, and by long antecedent streams that cross-cut the whole structure. This indicates a morphological asymmetry typical of an active folding. Wagner (2004) studied the stepping of remnant terraces across the structure to illustrate the ongoing activity of the Jusepín thrust.

Evidence of active reverse folding is shown in the field along the thrust located to the south-west of the Jusepín Ridge (Figure 3.19a). The E-W scarp associated with this structure is 5 km long and 10 m high. An asymmetric local drainage pattern also developed around it, suggesting ongoing activity. A natural trench in its middle part (site 11, Figure 3.22a) shows that yellow silts and clays are topped by alluvial deposits. These alluviums are folded (8 m of amplitude) and the relief is here a structural surface (Figure 3.22a). A few hundred meters in front of that structure (site 12S, Figure 3.22b), another fold is observed in alluvium. Its amplitude is only 5 ± 1 meters and the asymmetry of folding shows a north verging fold. Pebbles of site 12S for dating were sampled.

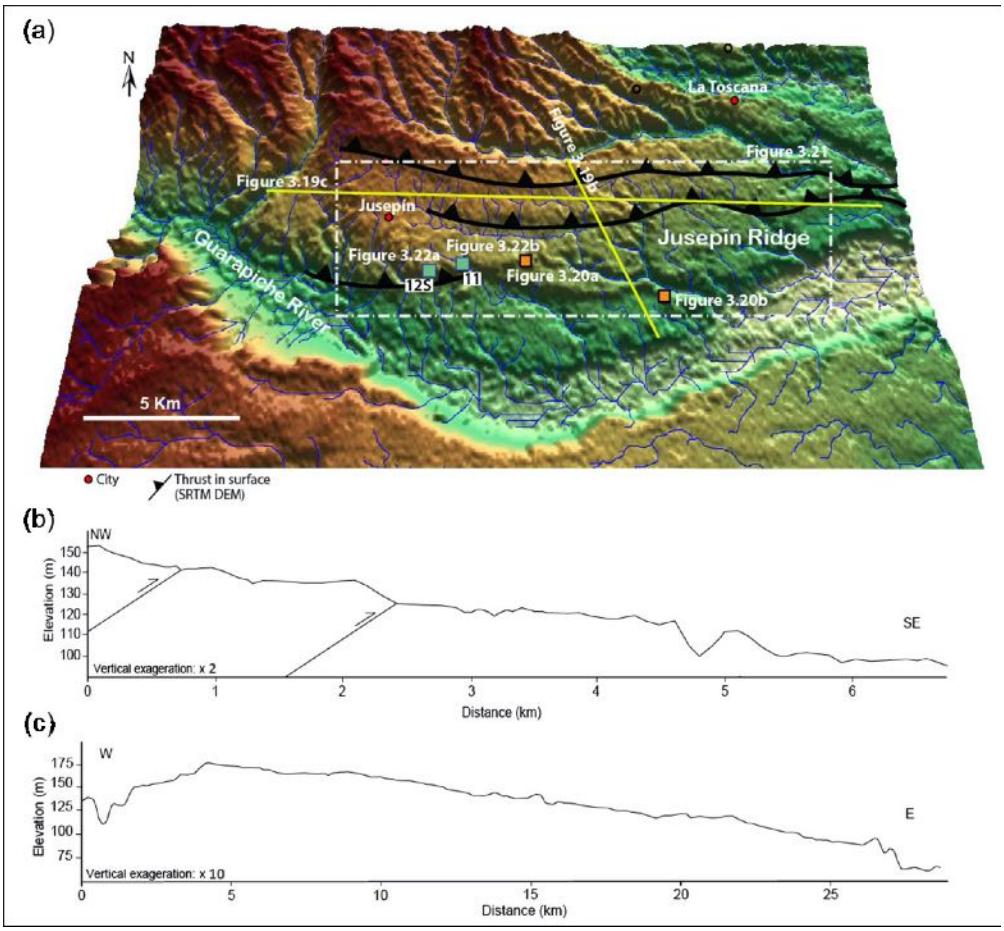

Figure 3.19 (a) 3D-view of the Jusepín Ridge (SRTM DEM). The white box is the location of the drainage network extracted from DEM image (Figure 3.21). The orange squares show the location of Figure 3.20 and Figure 3.22.

Figure 3.20. Morphological trace of the Jusepín thrust. The road clearly underlines its trace (a). We can follow it laterally in the field. White arrows point out the scarp (Location in Figure 3.19a).

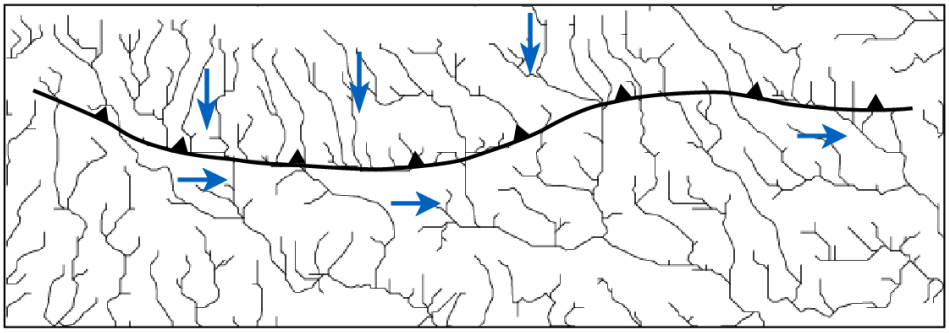

Figure 3.21. Drainage network around the Jusepín Thrust extracted from SRTM DEM. Tectonic forcing deviated the river flow to the east. Blue arrows indicate that the course of the river changes after crossing the thrust (Location in Figure 3.19a).

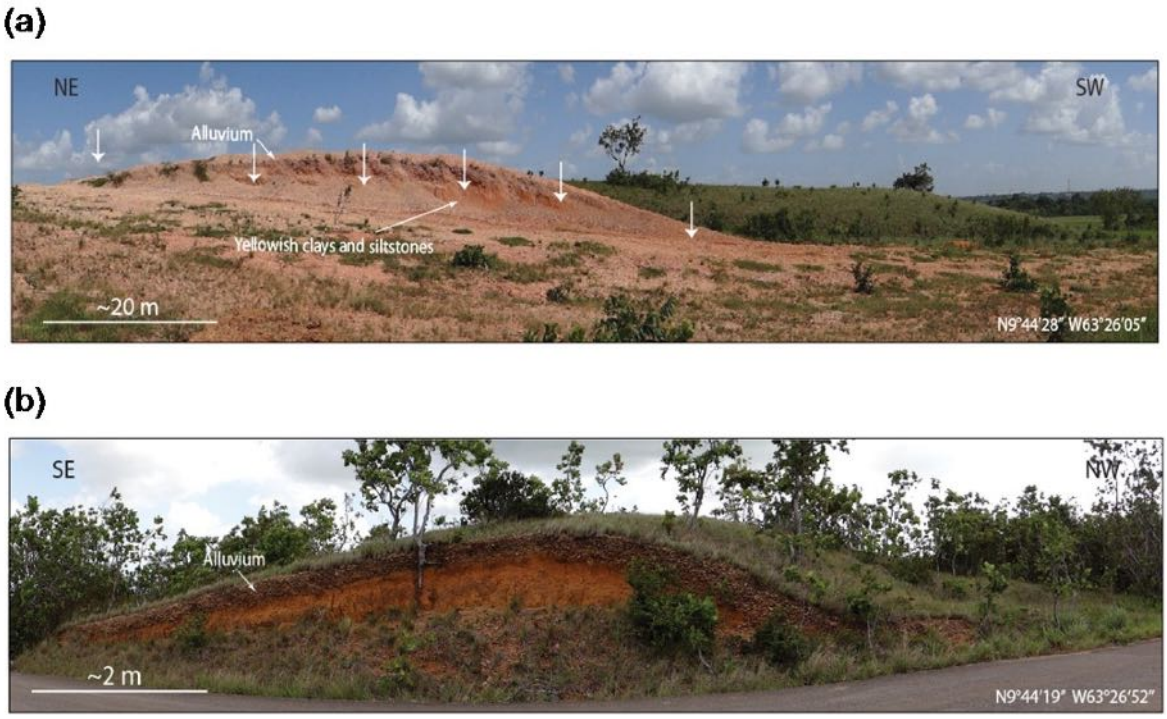

Figure 3.22. Tilted and folded river terraces observed in fieldwork. a) Terrace T11 located at site 11. White arrows point out the folded and tilted alluvium layer towards the SW. b) Terrace 12S located at site 12S. Note the tilting and folding of the alluvium layer. (Location in Figure 3.19a).

3.5.4. Surface Deformation in the Punta de Mata Zone (Site 5, 4S and 6S)

The Punta de Mata Ridge is located in the central part of the study area (Figure 3.14 and Figure 3.23a). As with other ridges, it is limited to the south by a strong scarp with a vertical offset of 105 ± 10 m (Figure 3.23b). The Punta de Mata Ridge is 25 km long and trends approximately NE-SW. It reaches 290 m high and decreases to the east where it has an average height of only 130 m (Figure 3.23c). The Amana River cross-cuts the ridge and then follows it to the east.

In the field, to the north of the Punta de Mata, an abnormal contact is observed between horizontal red and yellowish clays, siltstones at the bottom, and at the top bluish clays, silts and pebbles of ~25° south-dipping (Figure 3.24). This contact could be the trace of a reverse fault. Above these bluish siltstones in the hanging-wall of the fault, another yellowish layer was observed which could be the uplifted continuity of the yellowish basal unit observed in the foot-wall. This could depict a vertical offset of a few meters. The thickness of this yellow layer decreases from 1.5 m to zero meters to the NW, i.e., toward the fault trace. So it shows a taper and dip of layers increasing downward which suggests growth strata geometry. Above this unit, another red layer similar to the red one observed above the yellow one in the foot-wall also displays growth strata. These growth strata indicate the progressive uplift above the reverse fault. The outcrop is topped by alluvial deposits sampled for dating.

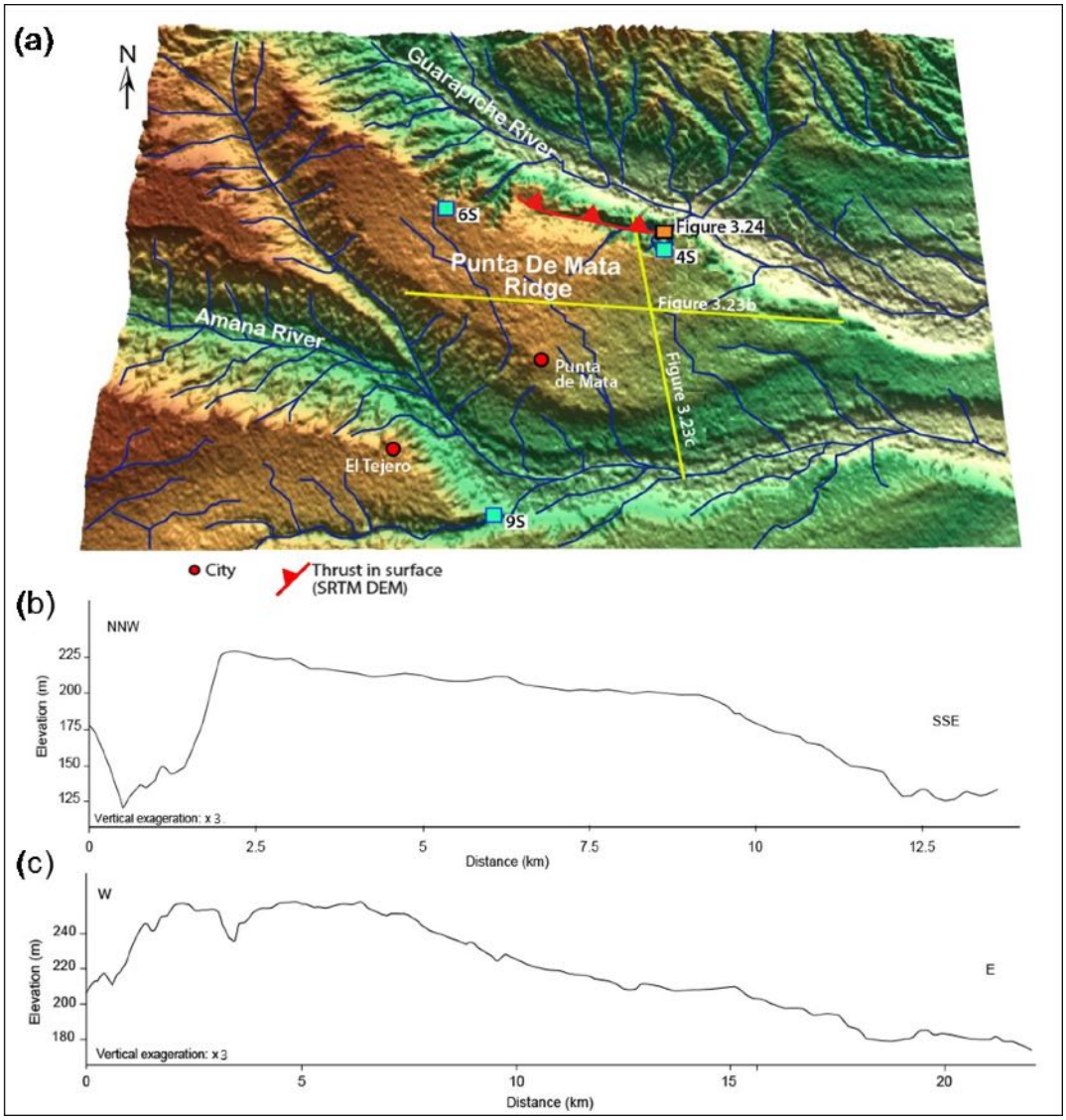

Figure 3.23. (a) 3D-view of the Punta de Mata Ridge (SRTM DEM). (b) Topographic profile across the ridge shows a scarp (km 11 in this figure). (c) Topographic profile along the structure shows decreasing heights from west to east.

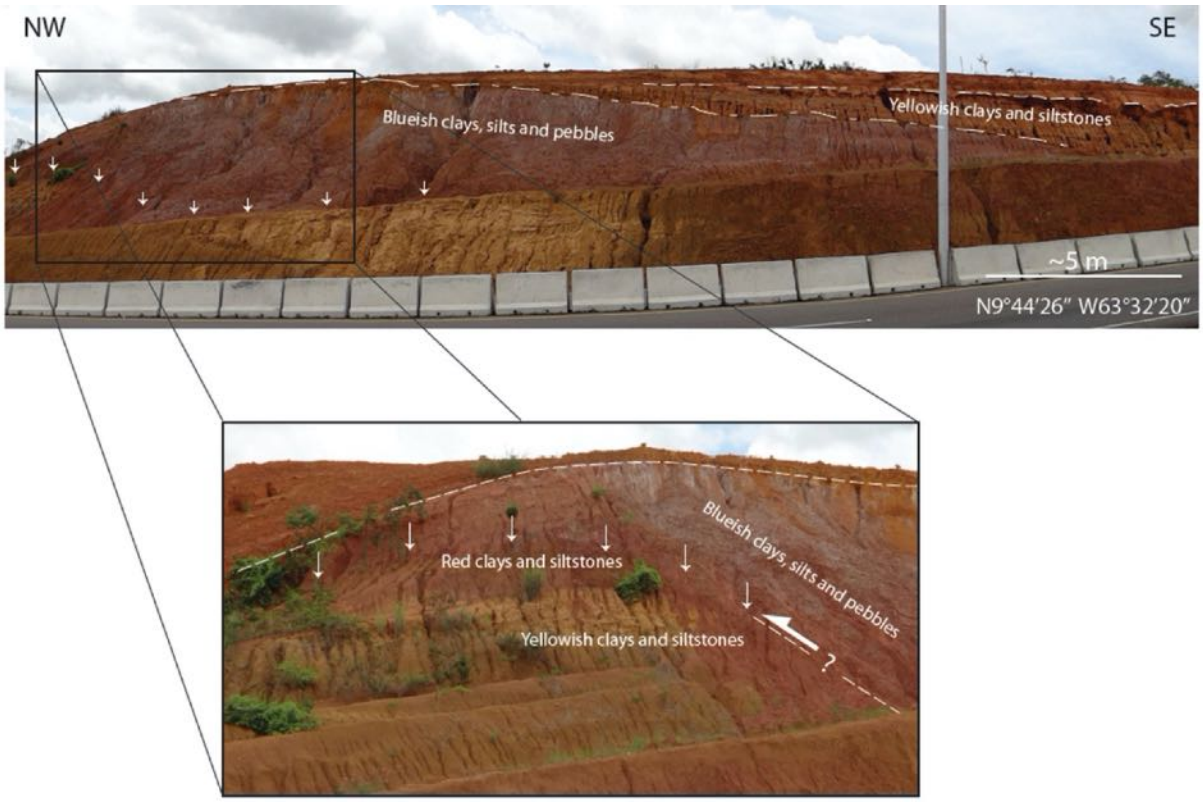

Figure 3.24. Terrace T4S in the Punta de Mata zone (a) Outcrop picture (b) Interpreted picture showing the possible reverse fault trace (arrows) that places the bluish clays, silts and pebbles layer in contact with the red clays, siltstone and yellowish clays basal layer.

3.5.5. Surface Deformation in the Amarilis Zone (Site 9S)

The Amarilis Ridge is located to the south of the study area (Figure 3.14) with ENE-WSW strike direction (Figure 3.25a). The elevation, along the strike is approximately constant around 200 m and is truncated by the Amana River to the east (km 27 in Figure 3.25c). Its height decreases from north (~200 m) to south (~70 m) (Figure 3.25b). The relief of the ridge corresponds to a flexure of the topographic surface. Deformations in the field were not observed, to date this folding an alluvial terrace (T9S) was sampled to the northwest of the Amarilis zone, on the left bank of the Amana River. DEM shows that the Amarilis Ridge marks the southern limit of the deformation front in the MFTB.

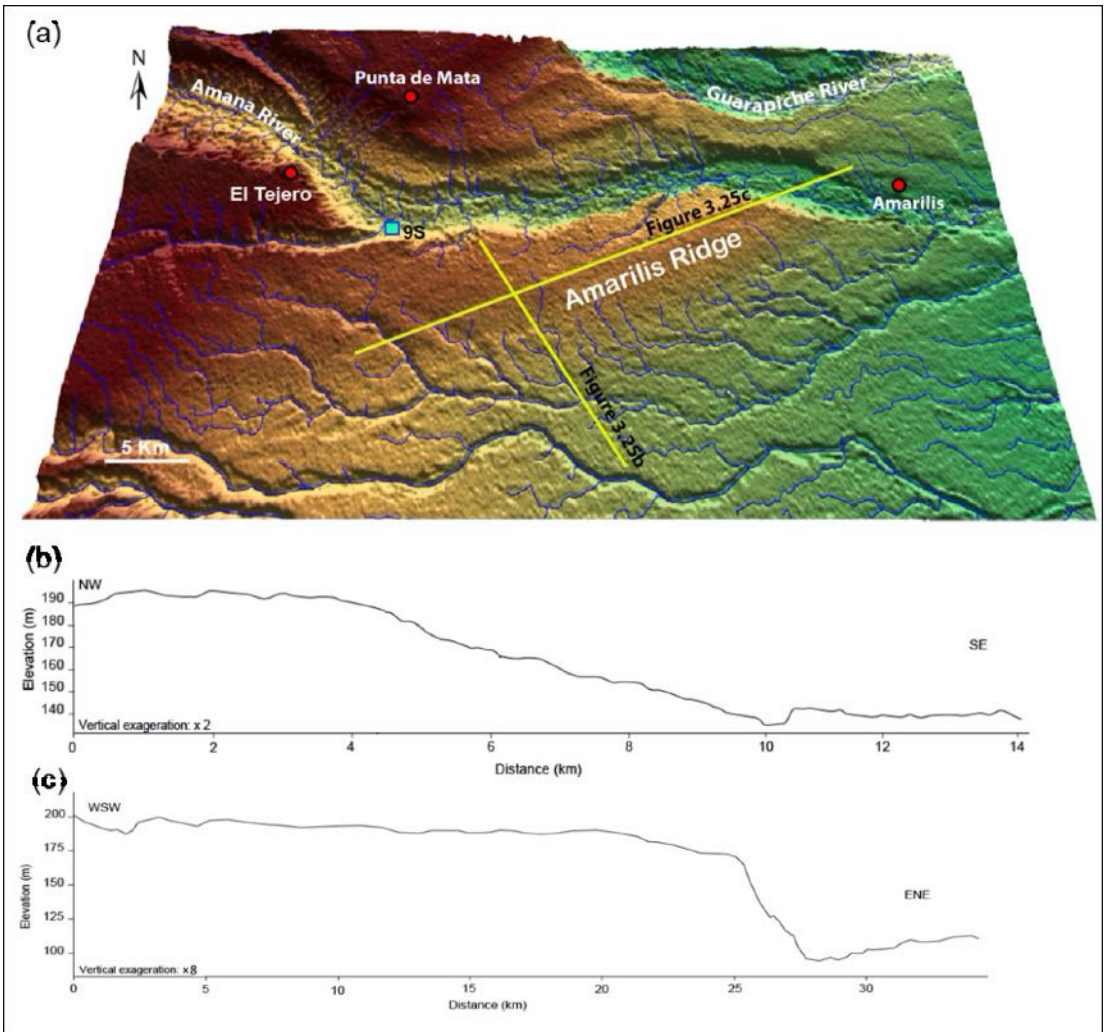

Figure 3.25. (a) 3-D view of the Amarilis Ridge (SRTM DEM). (b,c) Topographic profiles across the Amarilis Ridge.

3.6. Age Calculations Results

The age calculations were performed on the terraces sampled in the fieldwork. The dated terraces are uniformly distributed in the study area (3S, 4S, 6S, 9S and 12S) (see Figure 3.14 for location). The ages obtained with the ^{10}Be and ^{26}Al method were calculated as a function of the geographic location, altitude and concentration of each site (Table 3.1)

The estimation of the exposure ages was carried out using the equations of Desilets et al., 2006; Dunai 2001; Lifton et al., 2005 and Lal,1991 / Stone, 2000 (Figure 3.26). However, working with the ages obtained by the Dunai equations was chosen due to their having the least margin of error and being within the average range of the ages obtained by the other equations.

Two or three samples for each terrace were dated with both isotopes (^{10}Be and ^{26}Al). The ages obtained show an important dispersion (Figure 3.26). In every case, the age calculated with ^{26}Al was lower than that calculated with ^{10}Be (e.g. site 12S = 83 ky with the ^{10}Be isotope and 47 ky with the ^{26}Al isotope; Table 3.1). These results indicate a complex depositional history including burial which allowed a decrease in the ^{26}Al concentration with respect to that of ^{10}Be (radioactive decay relation $T_{1/2}$ ^{10}Be =1.36 Ma; $T_{1/2}$ ^{26}Al = 0.73 Ma). This complex history may include storage, burial, exhumation and remobilization stages of the rock.

As a consequence, the total concentration of the ^{10}Be and ^{26}Al isotopes in a sample with a complex history is the sum of two components (Equations 3.7 and 3.8). The first component is the concentration of cosmogenic nuclides in the before being sedimented onto the terrace: this is called inheritance. The ratio between ^{26}Al and ^{10}Be inheritances does not necessarily reflect the production ratio “k” (section 3.4.2). The second component is the one we are looking to evaluate: it corresponds to the cosmogenic nuclide concentrations produced in the terrace from the time of its formation.

$$^{10}Be_{\text{total concentration}} = {}^{10}Be_{\text{inheritance (rock)}} + {}^{10}Be_{\text{terrace}} \quad (3.7)$$

$$^{26}Al_{\text{total concentration}} = {}^{26}Al_{\text{inheritance (rock)}} + {}^{26}Al_{\text{terrace}} \quad (3.8)$$

In the case of the terraces in the MFTB, the ratio between ^{26}Al and ^{10}Be concentrations is lower than k, i.e., ^{26}Al data reflect less inheritance. Consequently, the ages obtained by ^{26}Al concentrations are closer to the real age of the terrace and can be treated as upper bounds for terrace ages. For this reason, the ages obtained with the ^{26}Al concentration were taken as the reference ages for this study. In some cases, the various ^{26}Al ages obtained for the same terrace are scattered (e.g. sample 3SA = 207 ky and sample 3SC = 87 ky, both samples in site 3S; Table 3.1). Following the above mentioned consideration, the minimum ^{26}Al age reflects the lesser inheritance and therefore is closer to the terrace age (and its upper bound).

Table 3.1. ^{10}Be and ^{26}Al results calculated by Dunai (2001) equations.

Site	Sample	Latitude (N)	Longitude (E)	Altitude (m)	^{10}Be concentration (10^5 at/g)	^{26}Al concentration (10^5 at/g)	^{10}Be age (ky)	^{26}Al age (ky)	^{26}Al / ^{10}Be ratio (at/g)
3S	3SA	9°43'48"	64°00'07"	287	3.7 ± 0.1	20.5 ± 0.6	103.0 ± 12.9	87.2 ± 11.1	5.5 ± 0.3
	3SC				9.4 ± 0.3	47.8 ± 1.6	267.2 ± 34.7	207.2 ± 28.1	5.1 ± 0.2
4S	4SA	9°44'14"	63°32'20"	204	2.4 ± 0.1	6.0 ± 0.4	71.7 ± 11	28.0 ± 3.9	2.5 ± 0.2
	4SB				1.9 ± 0.1	8.8 ± 0.6	55.7 ± 8.9	39.1 ± 5.3	4.6 ± 0.3
	4SC				1.0 ± 0.1	4.2 ± 0.5	29.6 ± 4.0	19.8 ± 3.3	4.3 ± 0.6
6S	6SA	9°45'03"	63°39'23"	265	0.8 ± 0.0	4.7 ± 0.4	25.1 ± 3.2	21.5 ± 3.1	5.6 ± 0.5
	6SB				1.0 ± 0.1	4.9 ± 0.3	30.1 ± 3.9	22.4 ± 3.0	4.8 ± 0.4
	6SC				0.5 ± 0.0	3.0 ± 0.3	15.8 ± 2.1	14.0 ± 2.2	5.9 ± 0.7
9S	9SA	9°36'42"	63°36'52"	175	3.9 ± 0.1	11.0 ± 0.7	114.7± 14.4	48.6 ± 6.6	2.8 ± 0.2
	9SB				6.3± 0.2	20.0 ± 0.8	189.5 ± 24.2	92.6 ± 12.0	3.2 ± 0.2
	9SC				2.0 ± 0.1	6.8 ± 0.5	60.2 ± 7.5	32.1 ± 4.5	3.4 ± 0.3
12S	12SB	9°36'42"	63°36'52"	95	2.6 ± 0.1	10.0 ± 0.7	82.6 ± 10.3	47.0 ± 6.5	3.9 ± 0.3
	12SC				2.1 ± 0.1	8.0 ± 0.4	65.0 ± 8.2	38.8 ± 5.1	3.9 ± 0.3

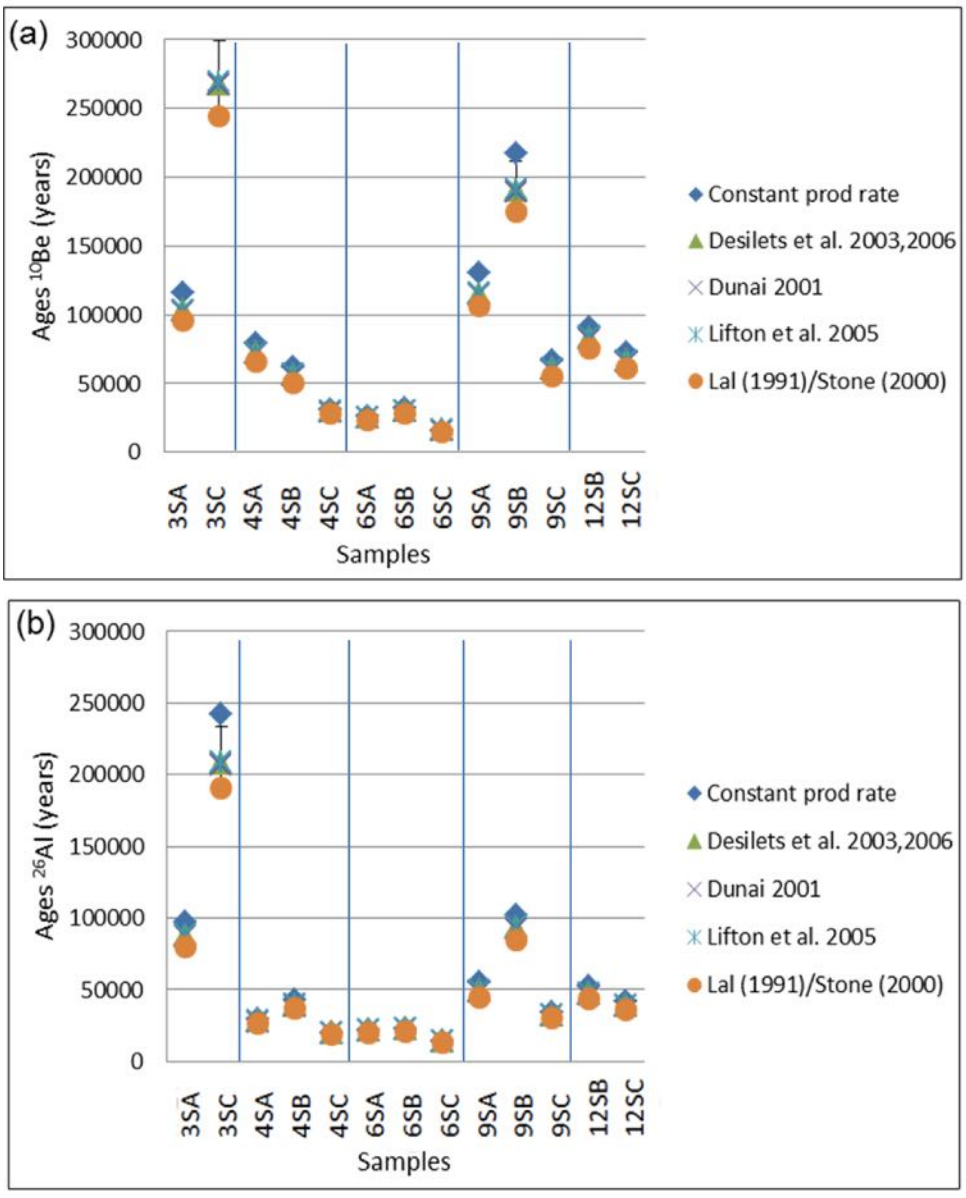

Figure 3.26. (a) Ages calculated by ^{10}Be (b) Ages calculated by ^{26}Al. For both isotopes the age calculation was performed using different equations (Desilets et al., 2006; Dunai 2001, Lifton et al., 2005 and Lal, 1991/Stone, 2000).

The discrepancy between ^{26}Al and ^{10}Be ages comes from inheritance, itself being due to a burial episode. For a sample taken at depth (in a cave for example), a plot ^{26}Al/^{10}Be vs ^{10}Be concentration is useful using curves for different burial durations. The concentration results reflect two episodes, burial followed by re-exposure at terrace surface (Figure 3.27). As a consequence, the burial duration evaluation is a minimum estimate. This plot (Figure 3.27) indicates that every sample collected has experienced a burial duration of at least a couple of hundred thousand years, and clearly more than 1 My for some of them (4SA, 9SA, 9SB, 9SC, 12SB, 12SC).

In order to constrain the terrace ages, we investigated the possible sample histories through time. For this, a history in three phases was assumed (Table 3.2):

1st Phase. The rock was exhumed to an initial erosion rate (e) and at an initial production (P_alt) calculated according to the upstream average altitude of ~1200 m (average altitude of the SDI mountains).

2nd Phase. The rock was transported from the mountain and stored within of an alluvial formation (e.g. thick conglomerate of the Mesa/Las Piedras Formation of Plio-Pleistocene age) to a significant depth (z > 10m; we took z = 100 m in calculations) and during a storage time (burial) ranging ~0-5.3 My. The burial time (T) assumed for the model must be in the the Mesa/Las Piedras Formation age range. We propose here that during burial, the $^{26}Al/^{10}Be$ ratio decreases following radioactive decay.

3rd Phase. Finally, the rock was abruptly removed from the alluvial formation (Mesa/Las Piedras) as a result of incision by the river and/or tectonic movements and re-deposited on the terrace sampled.

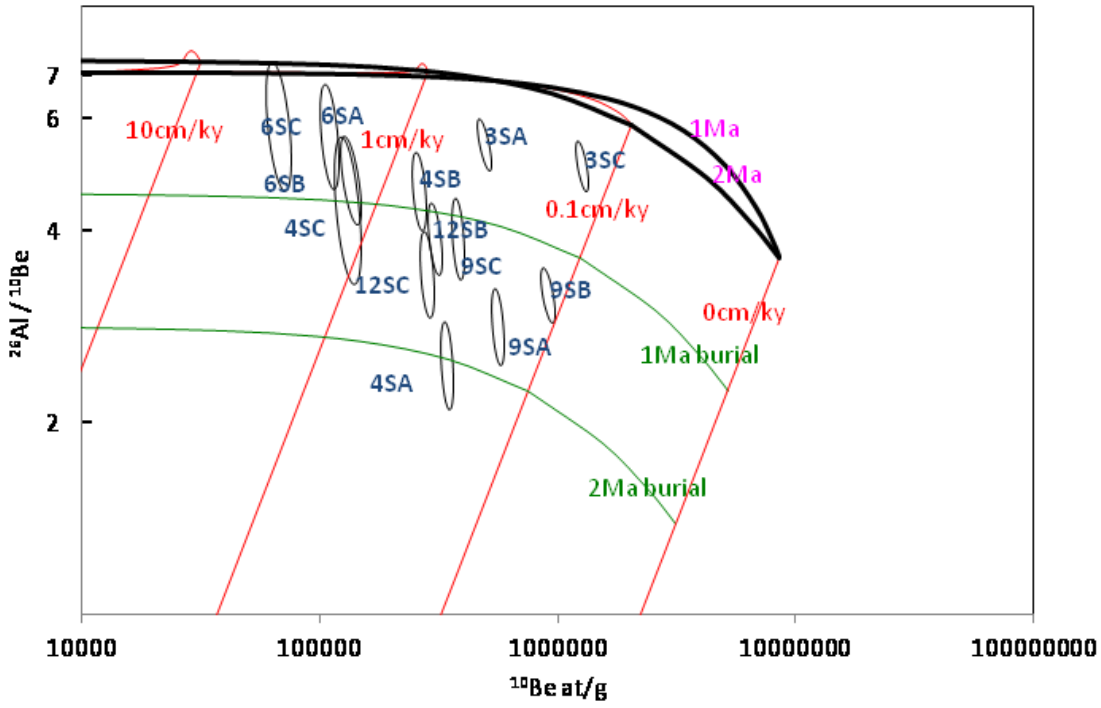

Figure 3.27. 'Banana' of ^{26}Al and ^{10}Be concentrations for the terraces sampled (from Vermesch, 2007). Bold lines represent the concentration of superficial samples (one is for erosion only, the other for exposure only). Most samples are below the bold lines which indicate a complex history with an integrated storage period. This graph does not take into account the sample history after burial when exposed at the terrace surface, whose main effect is an increase in $^{26}Al/^{10}Be$.

Table 3.2. Parameters used in the model to constrain the ages obtained from ^{10}Be and ^{26}Al analysis.

Parameter	Phase	Scale Variation
Initial erosion rate (e)	1st	0 to 2.10^{-4} m/y
Production at exhumation site (Pz_alt)	1st	3 to 15 at/g/y (ref 6.3 at/g/y)
Burial time (storage) (T)	2nd	0 to 5.3 My [Mesa/Las Piedras Fm. Age, between 0 to 5.3 My]
Burial depth (z)	2nd	Set a 100 m
Terrace age (Θ)	3rd	0 to100 ky
Terrace erosion rate (e')	3rd	10-4 m/y to 3.10^{-6} m/a

The original output of our investigations is illustrated in Figure 3.28. In general, the evolution model shows initial erosion rates of at least 5.10^{-6} m/y for all samples. Samples 3SC, 9SA and 9SB show the lowest initial erosion rates (below of 10^{-5} m/y). In contrast, the samples 6SA, 6SB and 6SC (located to the left of the diagram) require a quicker initial erosion rate (sometimes exceeding 10^{-4} m/y) and samples 3SA, 4SA, 4SB, 4SC, 9SC, 12SB, 12SB and 12SC require an initial erosion rates between 10^{-4} m/y to 10^{-5} m/y. Roughly, the eastern area (sites 4, 6 and 12) shows higher initial erosion rates (10^{-5} m/y to $>10^{-4}$ m/y) than the western samples (sites 3 to 9, 5.10^{-6} to 3.10^{-5} m/y); this reflects either a zoning of the mountain range erosion or elevation (affecting production rates) during the Pliocene. This diagram also shows that the evolution of samples 4SA, 9SC, 9SA, 9SB, 12SB and 12SB can be explained by a burial time between 1 to 2 My. Samples 3SA, 3SC, 6SA and 6SC can be related to a history of a moderate burial time of ~500 ky.

Knowing that the samples have a history with a maximum burial time of 2 My, two additional evolution time models were calculated in order to constrain the ages obtained by the dating methods: a model for a burial time limit between 1 and 2 My (Figure 3.29a) and a model for a burial time limit of 1 My (Figure 3.29b).

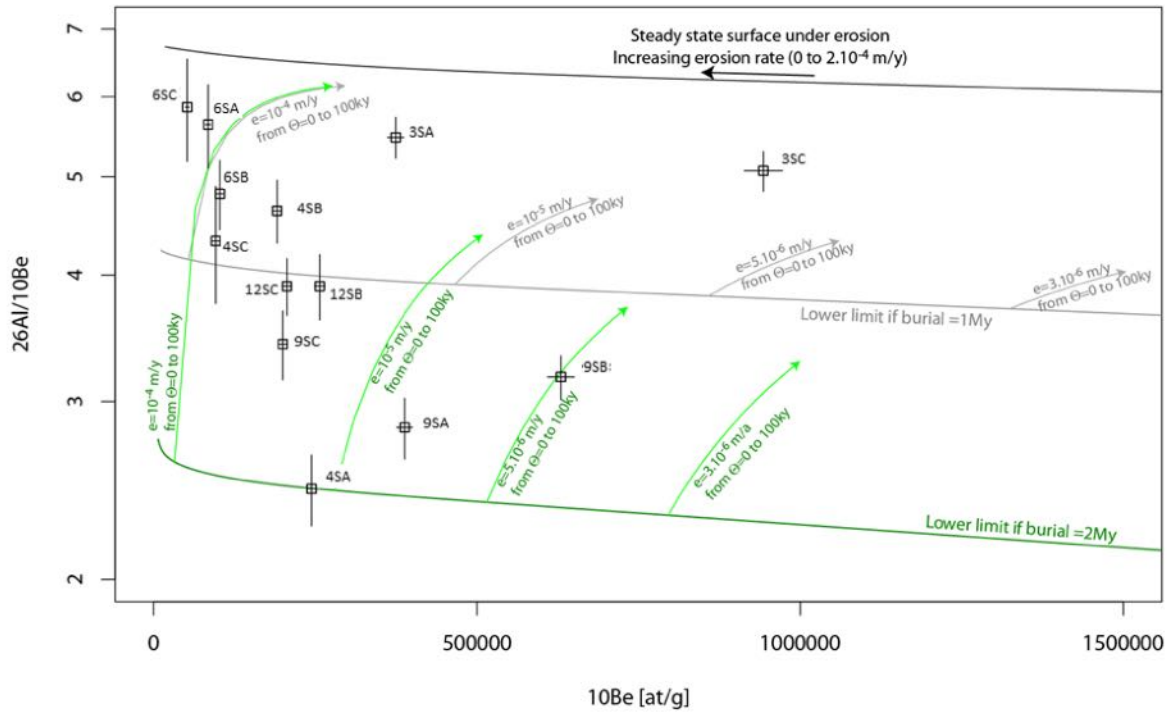

Figure 3.28. Sample evolution model. The samples are eroded at a given erosion rate and then buried: they follow the grey (1 My-burial) or green (2 My-burial) curves. Then, the samples are brought to the surface of the terrace where they are exposed to cosmic rays. While on the terrace, they follow the paths described by arrows (the arrow length corresponds to terrace exposure durations between 0 and 100 ky). It is important to notice that for high initial erosion rates (left part of diagram) after burial, the sample concentration is low but during re-exposure, this concentration comes back quickly reaches the constant exposure curve (top curve). Two examples in the graph (Figure 3.29): (sample 9SB) if we postulate a burial of 2 My, this sample needs 40 ky of exposure to explain its ^{26}Al and ^{10}Be content; it originates from a mountain eroding at a rate of 5.10^{-6} m/y (sample 12SB) this sample concentration can be explained by a 1My-burial without further exposure or by a 2My-burial followed by a 30 ky exposure; in both case, the initial erosion rate is not very different from $2\text{-}3.10^{-5}$ m/y.

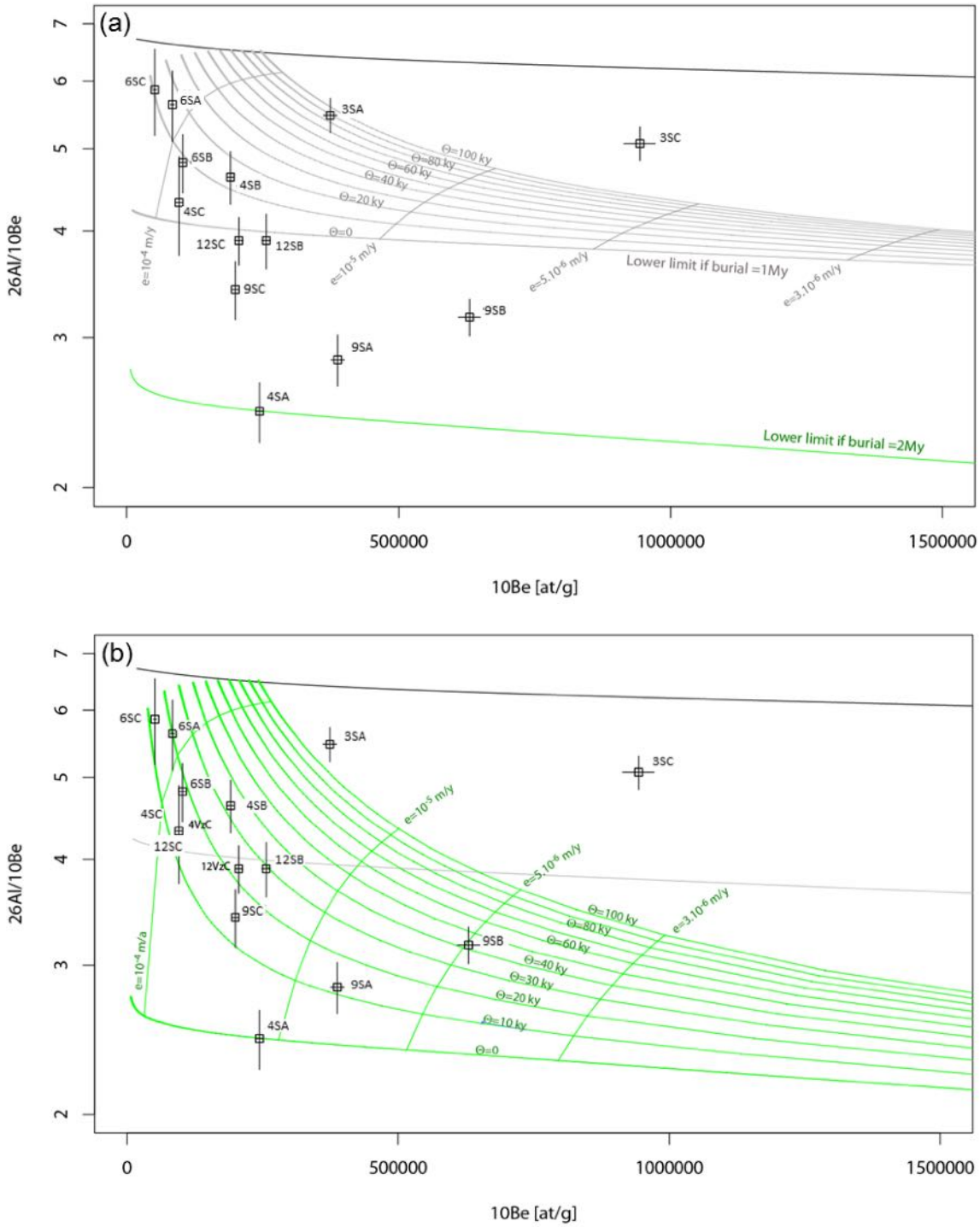

Figure 3.29. Evolution model through time for samples stored between 1 My (a) and 2 My (b). The curves display expected cosmogenic nuclides concentrations for a final stay (Θ) between 0 and 100 ky at the terrace surface.

The main conclusions from these studies at each site are described according to Figure 3.29:

- Site 3S: Samples 3SA and 3SC can be related to a moderate burial duration of ~500 ky and then re-exhumation. For a burial time limit of 1 My, this site shows ages between ~90 ky (3SA) and > 100 ky (3SC). This moderate burial did not last long enough to significantly remove the inheritance and thus the only thing that can be

concluded is that the maximum terrace age is given by ^{26}Al, around 87 ky; we cannot rule out that this terrace possibly being much lower. Finally, for sample 3S an age of ~90 ky was taken.

- Site 4S: The exposure age is similar in both scenarios. For sample 4SB the calculated exposure age is between ~10 and 30 ky and for sample 4SC between ~10 ky and ~15 ky. The burial time for both samples is between ~500 ky and ~1 My. By contrast, a longer burial time (between 1 My and 2 My) is necessary to explain sample 4SA.

- Site 6S: Samples 6SA, 6SB, 6SC have the highest initial erosion rates of ~10^{-4} m/y, a burial time < 1 My and exposure ages between ~10 and 20 ky. However, the age obtained by ^{26}Al data indicates that this terrace cannot be older than 14 ky (Table 3.1). Moreover, sample 6SC indicates a similar age derived from ^{10}Be and ^{26}Al. Therefore, the inheritance is probably low and the terrace age close to an ^{26}Al exposure age of 14 ± 5 ky.

- Site 9S: This site shows a burial time greater than ~1 My and an initial erosion rate between 10^{-4} and 5.10^{-6} m/y. The exposure ages for this terrace are between ~15 and 40 ky (Figure 3.29b).

- Sites 12S: The history of this site can only be explained by a burial time greater than ~1 My with an initial erosion rate between 10^{-4} and 10^{-5} m/y. Exposure ages between ~20 and 30 ky were calculated.

For sites 4S, 9S and 12S, we explored several scenarios summarized in Table 3.3, in order to cross the constraints obtained from the other samples of the same site and from the burial time limit of 5 My, the age of the Mesa/Las Piedras Formation. Indeed, this is the only formation than could have lodged and buried the samples for a duration time between 0 and 5 My, because longer burial durations would have removed most of the ^{10}Be and ^{26}Al.

Table 3.3. Age calculation of the terraces (per sample) obtained for burial times from 0 to 5 My; the sign "-" indicates impossible scenarios. According to our conclusions, possible scenarios are bold-faced, impossible ones are in italics.

Burial Time (My)			**0**	**0.5**	**1**	**1.5**	**2**	**3**	**4**	**5**
Site	**Sample**	**^{26}Al age (ky)**	**Terrace Age Calculated as a Function of the Burial Time (ky)**							
4S	4SA	28	-	-	-	-	**0**	**15**	**15**	**15**
	4SB	39	-	-	**15**	26	33	40	42	45
	4SC	20	-	-	**3**	**10**	**13**	**16**	20	20
9S	9SA	49	-	-	-	-	**13**	**27**	42	34
	9SB	93	-	-	-	**9**	32	52	>> 50	
	9SC	32	-	-	-	**5**	**15**	**24**	**25**	**25**
12S	12SB	47	-	-	-	**18**	**30**	40	40	41
	12SC	39	-	-	-	**15**	**23**	**24**	**33**	**35**

According to Table 3.3 it can conclude that:

- Terrace 4S: its exposure age cannot be greater than 15 ky (constrained by 4SA). We take an uncertainty of 5 ky, typical of 4S (Table 3.1). Exposure age 4S < 15 ky ± 5 ky and burial time between 1 and 5 My (Table 3.4).

- Terrace 9S. Its exposure age cannot exceed 25 ky ± 5 ky (constrained by 9SC, similar uncertainty as for 4S). Burial durations are between 1.5 and 5 My (Table 3.4).

- Similarly, an exposure age for 12S < 35 ky ± 5 ky and burial time between 1.5 and 5 My (constrained by 12SC) (Table 3.4)

Other initial production rates were not tested. It can be suggested, rather qualitatively that a change in the initial erosion rate weakly affects the assessment of terrace age: a higher initial erosion rate decreases the terrace age.

Table 3.4. Final results obtained in the ^{10}Be and ^{26}Al analysis carried out at each terrace sampled in the MFTB.

Site	Terrace	Latitude (N)	Longitude (E)	Altitude (m)	Estimated Age (ky)
3S	T3S	9°43'48"	64°00'07"	287	≤ 90 ± 5
4S	T4S	9°44'14"	63°32'20"	204	≤ 15 ± 5
6S	T6S	9°45'03''	63°39'23''	265	≤ 14 ± 5
9S	T9S	9°36'42''	63°36'52''	175	≤ 25 ± 5
12S	12SB	9°36'42''	63°36'52''	95	≤ 35 ± 5

3.7. Vertical Deformation Quantification

This was estimated dividing the vertical offset observed in the deformed terraces by the calculated exposure age of each one as calculated by ^{10}Be and ^{26}Al dating. In all cases, it was assumed that the vertical offset has been produced after exposure of the terrace. Vertical deformation rates were calculated for the terraces where visible deformation was observed in fieldwork (T4S located in the Punta de Mata zone and T12S located in the Jusepín zone) and on the terraces that show folding or scarps in DEM (T3S located in the Tarragona zone and T9S located in Amarilis zone).

For the remaining T3S terrace located in the Tarragona zone and T9S located in the Amarilis zone, the vertical offsets were estimated from the topographic profiles extracted from SRTM DEM. Based on an estimated vertical offset of 30 ± 5 m for T3S and a maximum of 90 ky for exposure age, a minimum vertical deformation rate of ~0.3 ± 0.3 mm/y was calculated. For terrace T9S, a vertical offset of 15 ± 5 m was estimated, and with the exposure age of 25 ky a vertical deformation rate of ~0.6 ± 0.3 mm/y was calculated (Table 3.5).

In the Jusepín zone, the vertical deformation rate was quantified using the fold surface observed on T12S where the bottom of the fold (to the north) allowed an in situ estimation for the vertical offset of ~3.5 m (Figure 3.23). This yields a vertical deformation rate of 0.1 ± 0.06 mm/y. Similarly, in the Punta de Mata zone, with a vertical offset of ~1.7 m observed in situ on the TS4 (Figure 3.24) a minimum vertical deformation rate of 0.1 ± 0.06 mm/y was estimated (Table 3.5).

Table 3.5. Vertical deformation rates calculated from terrace ages obtained by ^{10}Be and ^{26}Al analysis.

Site	Terrace	Vertical offset (m)	Maximum exposure age (ky)	Minimum vertical deformation rate (mm/y)
3S (Tarragona zone)	T3S	30 ± 5	90 ± 5	0.3 ± 0.3
4S (Pirital zone)	T4S	1.7 ± 1	15± 5	0.1± 0.06
9S (Amarilis zone)	T9S	15 ± 2	25± 5	0.6 ± 0.3
12S (Jusepín zone)	T12S	3.5 ± 1	35 ± 5	0.1 ± 0.06

3.8. Discussion

The first morphological observations in the Maturín Foreland Basin were carried out by Zinck and Urriola in the 1970s. They described the main morphological features present in the area such as the rivers terraces, hills, plateau, slope directions, river origins, grabens and faults, among others. Then in the 2000s, these observations were taken up again with main focus on the cartography of the river terraces located to the northeast and the determination of active thrusts in the Serranía Del Interior foothills through geomorphological evidence (Singer et al., 1998; Audemard et al., 2002; Wagner, 2004). The vertical deformation rate in surface calculated in this study provides new data to the previous geomorphological studies carried out in the area.

The present study focused on five surface structures where identified morphotectonic markers were identified as: deformed surfaces, river terraces, alluvial deposits folded on the tops of some terraces, deviation of the drainage network and the presence of strong fault scarps. From the internal to the external domains of the MFTB, these structures are the San Felix, Tarragona, Punta de Mata, Jusepín and Amarilis Ridges. The exposure age for the terraces located in the San Felix zone was not calculated due to problems in accessing to the zone.

The most internal ridges (Tarragona and San Felix ridges) are higher (300 to 250 m a.s.l) than those located to the south, the Amarilis and Jusepín ridges (220 to 120 m a.s.l). These differences in height suggest that the tectonic activity has been greatest and/or has lasted longer to the NNW than to SSE of the MFTB. Additionally, the heights of all the ridges observed in the different zones decrease towards the SSE which is additional evidence to propose that the tectonic movements in the NNW are stronger and gradually decrease towards the SSE of the MFTB.

The analysis of the terrace ages obtained by the ^{10}Be and ^{26}Al method supports this complex evolution. Indeed, it suggests that the rocks sampled on the terraces had a possible inherited cosmogenic nuclides concentration before being placed and stored within the terrace. The rocks were probably transported from the Cretaceous formations exposed in the SDI until being deposited in the foothills and the foredeep of the Maturín Basin in the Mesa/Las Piedras Formation. In this Plio-Pleistocene age formation, the rocks were buried, stored and finally re-exhumed during the terrace formation.

According to the ^{10}Be and ^{26}Al dating results, all the terraces were exposed during the Late Pleistocene (the oldest 90 ky at T3S and the most recent 15 ky at T4S) (Figure 3.30). Additionally, these river terraces showed one or more deformation markers such as: strong slopes, tilting, folded surfaces and faulting, indicating that the tectonics in the area was active even after they were exposed to the surface.

With respect to the calculated vertical deformation rate, it observed that the greatest rates are observed in the zones near the Urica Fault (Tarragona Ridge (T3S) = 0.33 ± 0.06 mm/y and Amarilis Ridge (T9S) = 0.6 ± 0.2 mm/y), decreasing to the east as it becomes more distant from the Urica Fault (Pirital zone (T4S) and Jusepín zone (T12S) = ~0.1 mm/y). This indicates that the Urica Fault activity can possibly be influencing the vertical deformation rate variation in the MFTB (Figure 3.30).

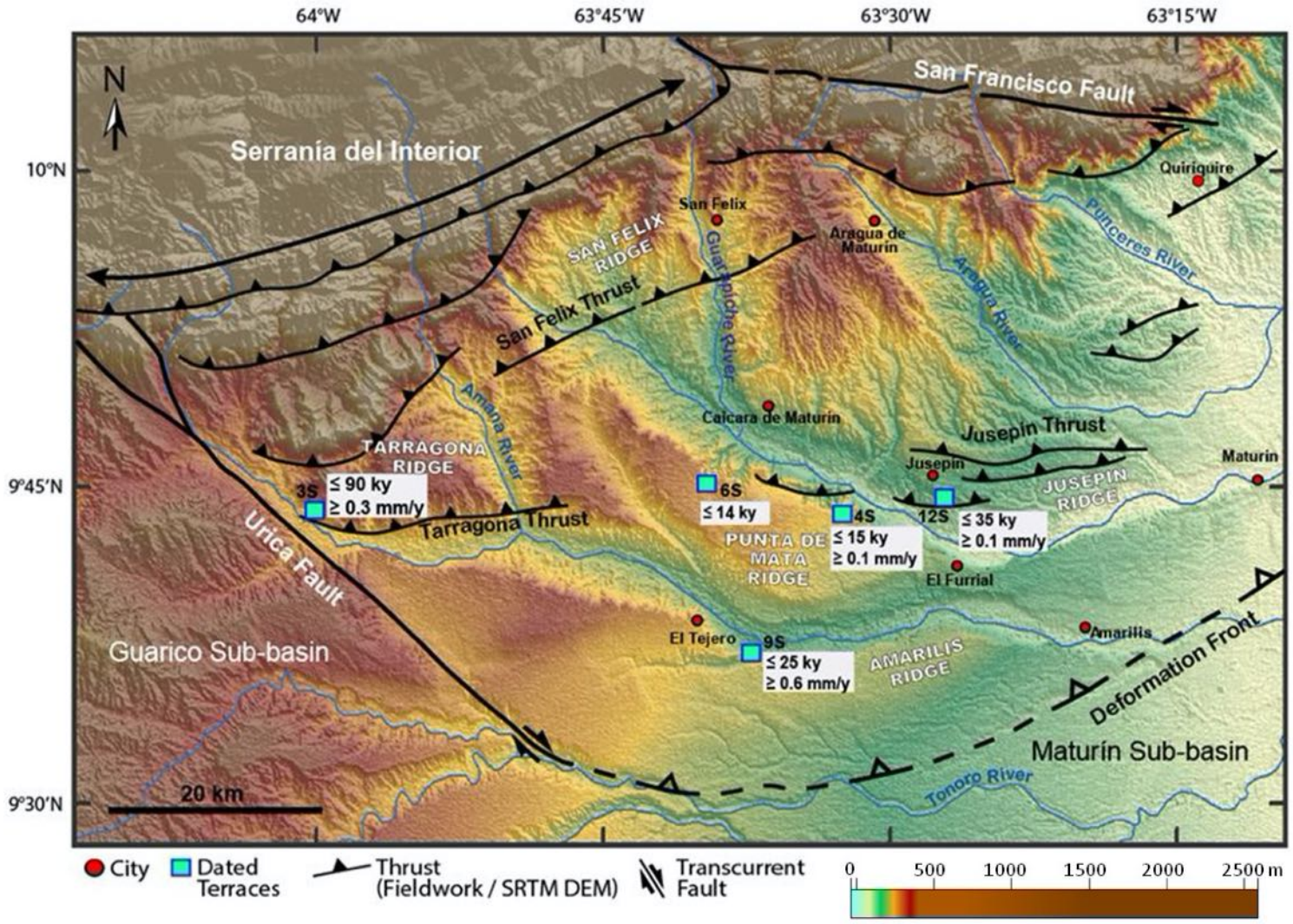

Figure 3.30. SRTM DEM of the MFTB showing the calculated terrace age according to the ^{10}Be and ^{26}Al analysis, the estimated vertical deformation rate and the direction changes of the rivers flowing in the area.

CHAPTER 4. SEISMIC INTERPRETATION IN MONAGAS FOLD AND THRUST BELT

4.1. Introduction

The Monagas Fold and Thrust Belt (MFTB) is located between the Serranía Del Interior (SDI) foothills and the northern edge of the Maturín foreland sub-basin (see location map in CHAPTER 1, Figure 1.1) The Pirital and Furrial thrusts are the two mains faults responsible for the most of the shortening in the area. The MFTB has been studied in detail for more than 40 years, motivated by hydrocarbon exploration in the Cretaceous and Tertiary units. However, the Plio-Quaternary levels in seismic lines have not been studied in detail. Thanks to the fieldwork research and DEM images analysis, surface deformations in the area were observed (see CHAPTER 4) and these could be related to the deep structures.

Following, we present a summary of the different superficial structures identified during fieldwork and geomorphologic studies (see CHAPTER 3). Figure 4.1 shows the map location of these structures in MFTB.

1) To the northwest of MFTB, in the Tarragona zone, a ridge that we named “Tarragona Ridge” was identified. This is possibly affected by a reverse faulting. The top surface shows a deformed quaternary alluvium layer.

2) In the central part of MFTB, at the Punta de Mata zone, a ridge of ~5 m of height and ~25 m long was observed (Punta de Mata Ridge). This ridge is possibly formed by a back-thrust. The yellowish clays and siltstones layers of the ridge show onlap geometry.

3) In the San Felix zone, to the north, four levels of terraces, product of the recent deformation on the San Felix Ridge were observed.

4) To the northeast, in the Jusepín zone, several tilted terraces and folded quaternary alluvium layers on the Jusepín Ridge were observed.

5) To the south, in the Amarilis zone, DEM image shows a NE-SW ridge named by us Amarilis Ridge, which marks the superficial limit of the deformation in the MFTB.

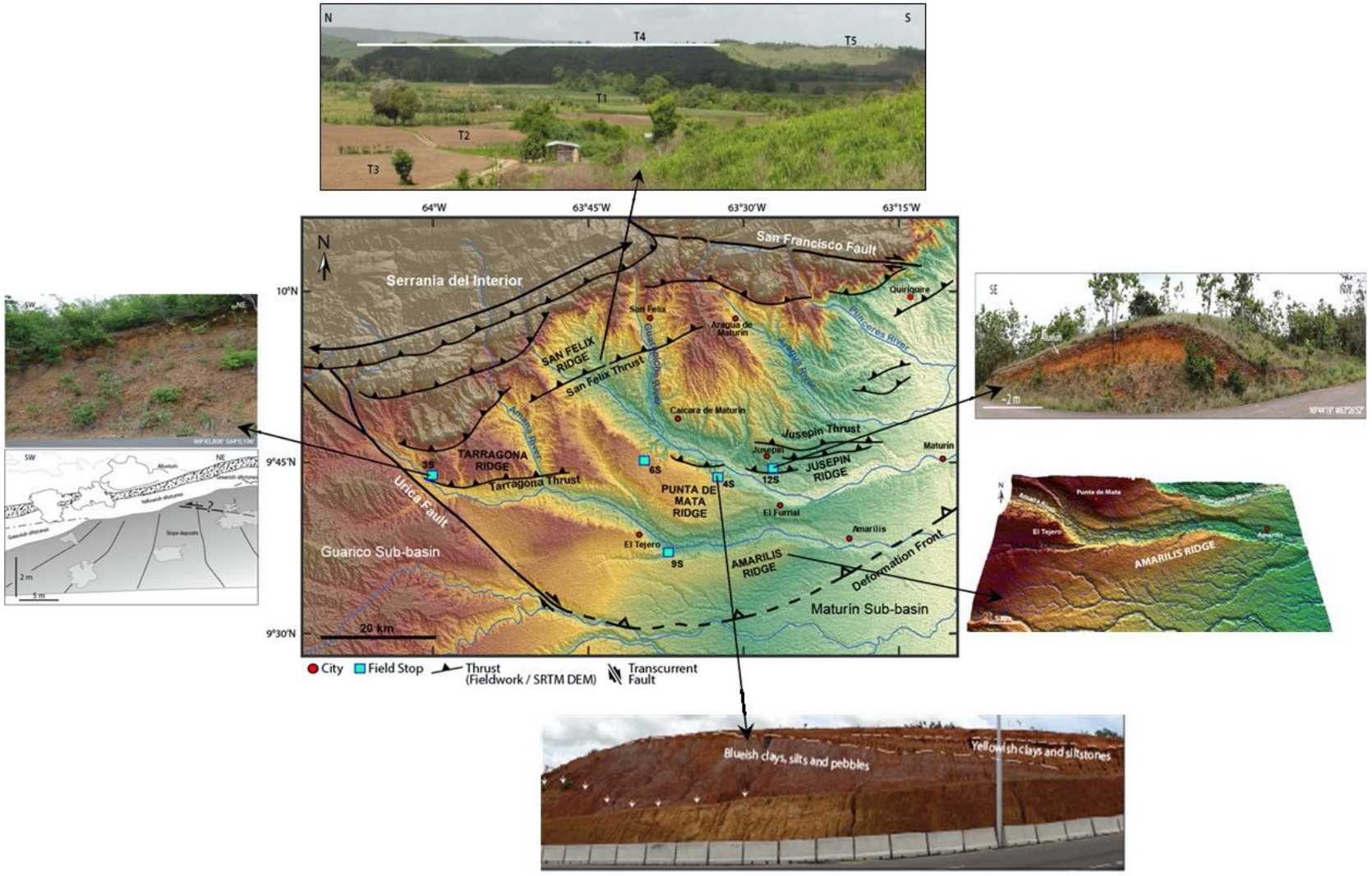

Figure 4.1. Superficial structures showing evidence of recent deformation in MFTB. These observations came from geomorphological analysis and fieldwork (see CHAPTER 3).

In order to determine if a relation between superficial deformations (Plio-Quaternary levels) and deep structures (Cretaceous-Tertiary rocks) exists, the structural interpretation of 2D and 3D seismic profiles was carried out. The interpretation was performed from the Cretaceous to the Plio-Pleistocene levels, focusing on the Tarragona, Pirital and Furrial thrusts, the Amarilis Backthrust and the Pirital, Amarilis and Jusepín highs, which are vertically related to the superficial structures.

This chapter is organized as follows: 1) methodology and database; 2) a review of the seismic stratigraphic markers of the MFTB; 3) interpretation of the seismic lines and description of the structures identified; 4) presentation and interpretation of subsurface structural and isochron maps in depth from seismic interpretation.

4.2. Methodology

The seismic and well database used in this chapter was provided by Petróleos de Venezuela (PDVSA Intevep). PDVSA facilities were used to carry out the interpretation. For the 2D seismic interpretation Openworks 2003 Landmark™ software was used and for the 3D seismic, the Petrel™ 2010-Schlumberger software suite. The loading of the database was realized by PDVSA technical staff. Then, the location of the seismic, wells and stratigraphic wells tops was verified with respect to the coordinate system of the area (Figure 4.2).

The seismic interpretation focuses on stratigraphic markers and structures such as: unconformities, lithological contrast, structural highs, thrust and faults, among others. All these generally have a good reflectivity which allowed a good match between geological tops and seismic horizons.

2D seismic interpretation was performed in different zones of the area. In this chapter, only the 2D line located above the superficial structure of the Tarragona High (M1 seismic line) is shown. The other lines shown in this chapter are of the 3D seismic which covers the rest of the superficial structures observed in the geomorphological study (see CHAPTER 3)

The first stage of the 3D seismic interpretation was the fault interpretation. The major faults interpreted in the study area were: Tarragona, Pirital, Furrial, Jusepín and Amarilis. The automatic horizon interpretations were carried out by following the stratigraphic tops of the wells and then these horizons were adjusted manually. Finally, the intersection between the faults and the horizons was performed in order to build the 3D structural model (Figure 4.2).

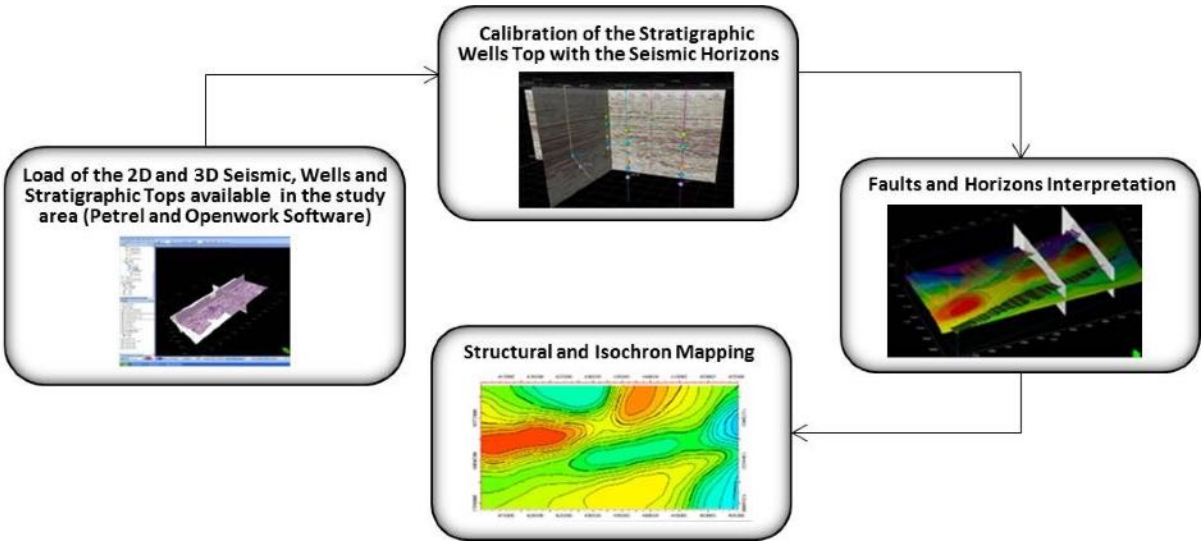

Figure 4.2. Methodology used for the seismic interpretation.

4.3. Database

1200 km of 2D seismic in time and 980 km^2 of 3D seismic data in depth were interpreted (Figure 4.3). The 2D seismic profiles come from different surveys acquired by PDVSA between 1975 and 1999. The 3D seismic cube was acquired in 1998. The 3D seismic cube interpreted in this work was migrated in depth in 2003 by PDVSA Intevep which improved the quality and the definition of the structures.

12 wells were used to calibrate the seismic profiles and to follow stratigraphic tops provided from the PDVSA team that currently works on the area. The stratigraphic data and time-depth tables were validated from PDVSA internal reports.

The quality of seismic data may be affected by different factors such as: acquisition and processing techniques, complex structural geology, anisotropy of the lithological formations, presence of hydrocarbons, faults and thrusts, among others. In the MFTB the seismic quality varies according to the seismic surveys. In general, the quality is bad to regular because this area is characterized by high dip structures, overlapping thrusts, high-angle reverse faults, chaotic reflections associated with the gas chimneys; all these factors affecting the resolution of the seismic image. Several quality patterns were associated with:

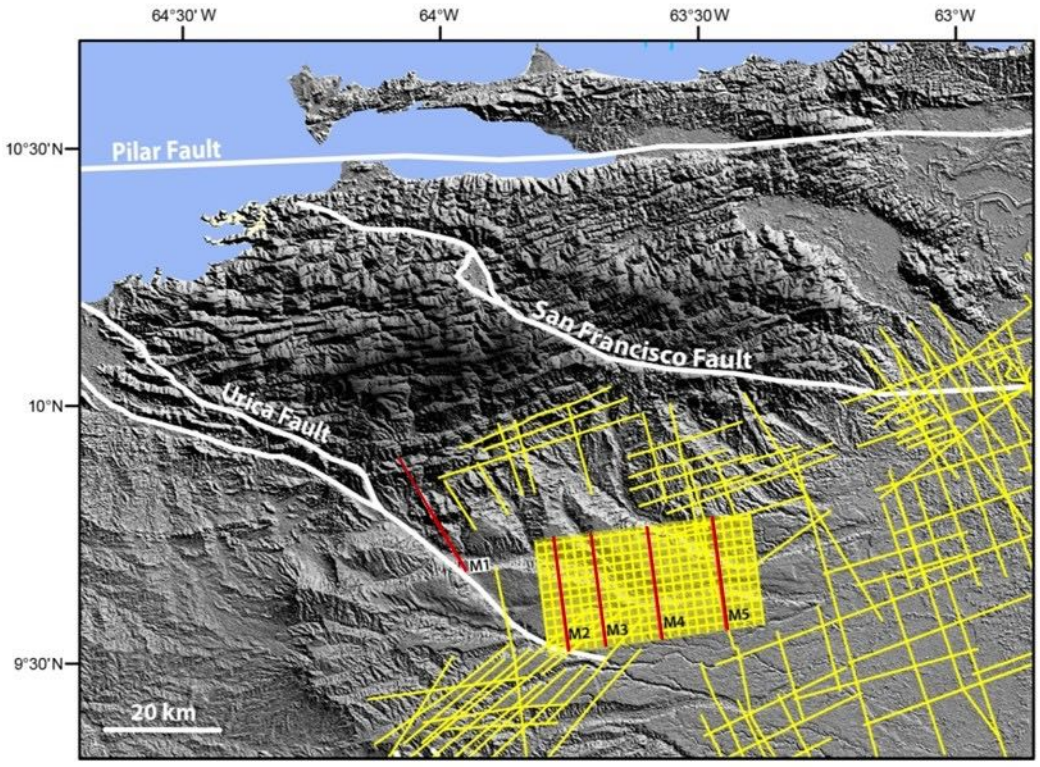

Figure 4.3. Seismic lines interpreted in the area. The yellow lines represent the seismic lines available in the area; the red lines are seismic lines shown in this chapter.

- Geological Structures: In foothills areas such as the SDI, the geological structures are characterized by thrusting, deep seated, structures with high dip (e.g. The Tarragona zone) (Figure 4.4a). The presence of mud diapirs as for example in the Maturín foredeep, produce discontinuous seismic reflectors and low signal-to-noise ratio (Figure 4.4b). In areas with shallow and simple dip structures such as the Plio-Pleistocene sequences, the seismic quality is from regular to good with strong and continuous seismic reflectors that are easy to follow (Figure 4.4c).

- Sedimentation and Stratigraphy: Heterogeneous sequences, formed by layer intercalation of different lithologies produce impedance contrast that results in good seismic reflectors. On the contrary, if the sedimentation is homogeneous the seismic reflectors are rather chaotic and discontinuous. A good example in the MFTB area is the marine shale of the Carapita Formation, which has traditionally been interpreted as chaotic shale masses due to a high sedimentation rate and a rapid deepening experimented by the basin during the Miocene (Duerto, 2007; Parra et al., 2011). It produces chaotic reflection patterns with discontinuous reflectors and low signal-to–noise ratio (Figure 4.4d). However, Duerto (2007) interpreted this sequence and proposed a shale tectonic model in this area.

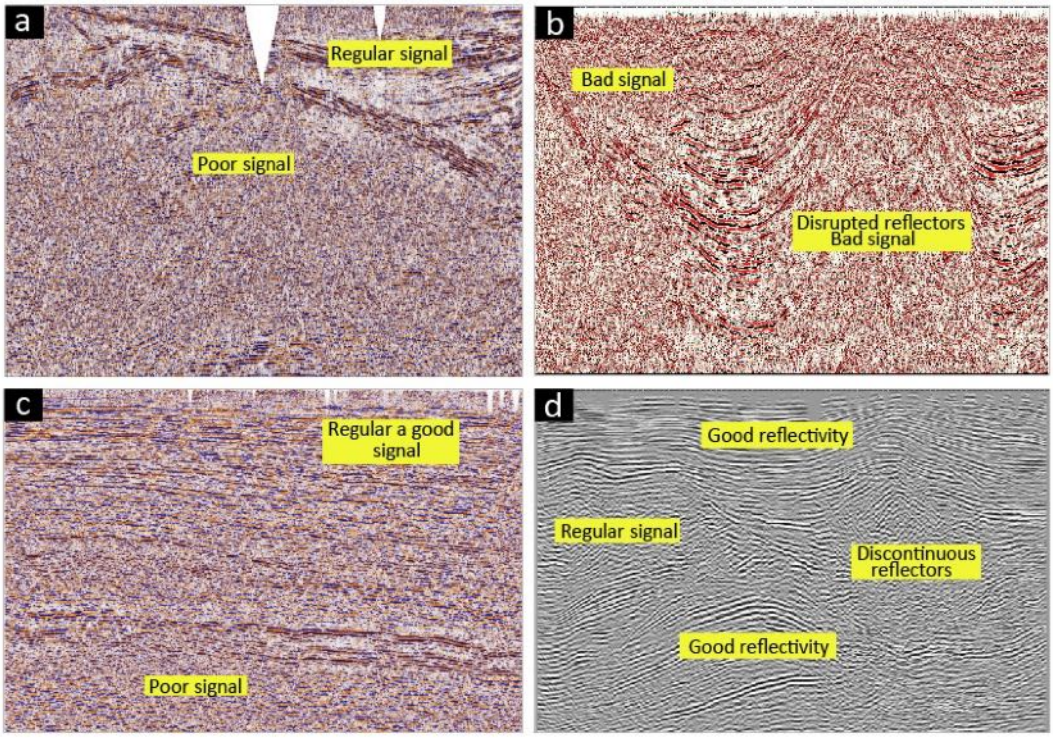

Figure 4.4. Seismic line examples of different 2D and 3D seismic surveys. a) 2D seismic acquired in 1985. Note the poor signal below the continuous reflectors due to the thrust present in the Serranía Del Interior foothill b) 2D seismic acquired in 1990 in the Maturín foredeep. Seismic reflectors are disrupted by mud diapirs present in the area. c) 2D seismic acquired in 1996 to the south of the deformation limit (forebulge). Note the continuous and parallel reflectors. d) 3D seismic acquired in 2003 in the MFTB. Observe the good reflectivity in the upper reflectors and discontinuous reflectors in the shales of the Carapita Formation

4.4. Seismic Stratigraphic Markers in the MFTB

The seismic profiles have a maximum recorded length of 5 sec. (~10 km), which allows identifying the markers from the Cretaceous to the Pleistocene. The stratigraphic markers were divided in two main periods: The pre-Middle Miocene and the post-Middle Miocene separated by the Middle Miocene Unconformity (MMU). This unconformity represents the upper limit of the thrust belt developed in the basin. Above this unconformity, gentle growth folds are developed in Late Miocene and Plio-Pleistocene units (Figure 4.5).

In the pre-Middle Miocene period, three different phases were identified according to impedance contrast and seismic reflectors continuity. The first and oldest phase has regular continuity of the reflectors and good contrast of impedance due to intercalations of limestone, sandstone and shale units. This phase is represented by the Cretaceous units (Barranquín, El Cantil, Chimana, Querecual, San Antonio and San Juan Formations). The second phase (above the oldest zone) shows the Oligocene-Paleocene units with good continuity of the reflectors and good contrast of impedance. The third and youngest phase below the MMU is

represented by the Early-Middle Miocene shale units (Carapita Formation). There, the seismic image shows many lateral variations, bad impedance contrast and very bad continuity of the reflectors which are cut by faults (Figure 4.5).

In the post-Middle Miocene period two phases were identified. The first phase shows good impedance contrast but the continuity of reflector is not good. This phase is constituted by the siltstone unit of the Late Miocene (Morichito/La Pica Formation). Finally the youngest phase identified in the seismic image is represented by the Mesa/Las Piedras Formation of the Plio-Pleistocene age which is constituted by conglomerates and sandstone rocks. Here, the reflectors have a good continuity and an impedance contrast higher than in the Late Miocene unit (Figure 4.5).

The seismic study in this thesis is focused on the Plio-Pleistocene units, this being the youngest unit deposited in the basin and therefore its top is the present-day topography where the recent deformations were observed in the fieldwork. This unit represents the shallow-marine to continental fill of the Maturín Basin due to the southeastward migration of the Serranía Del Interior Thrust Belt (Jácome et al., 2003). Based on biostratigraphic information, Gamma Ray (GR) and Spontaneous Potential (SP) curves, Di Croce (1995) proposed three depositional sequences within the Plio-Pleistocene units which are bounded by SB-5.5, SB-4.2, SB-3.8 and SB-3.0. The thickness of these sequences varies considerably and pinches out to the south and to the west of the Maturín foreland fold belt. More recently, Duerto (2010) defined three different growth strata within the same unit with ages of Lower Pliocene, Upper Pliocene and Pleistocene ages as a consequence of the growth folds.

4.5. Interpreted Seismic Lines

Based on the seismic data quality, on the majors deep structures possibly related to the superficial structures observed in fieldwork (CHAPTER 3) and on seismic stratigraphic markers recognized in the MFTB (section 4.3 in this chapter), four horizons were interpreted. From bottom to top, the seismic horizons interpreted were: Top of Paleocene-Oligocene (in the hanging wall and in the foot-wall of the Furrial thrust), Middle Miocene unconformity (MMU), Late Miocene unconformity (LMU) and one horizon in Intra Plio-Pleistocene units (Mesa/Las Piedras Formation).The main faults interpreted were: the Pirital, Jusepín, Furrial and Amarilis faults. Each horizon and fault is described in the M1, M2, M3, M4 and M5 seismic lines (Figure 4.6).

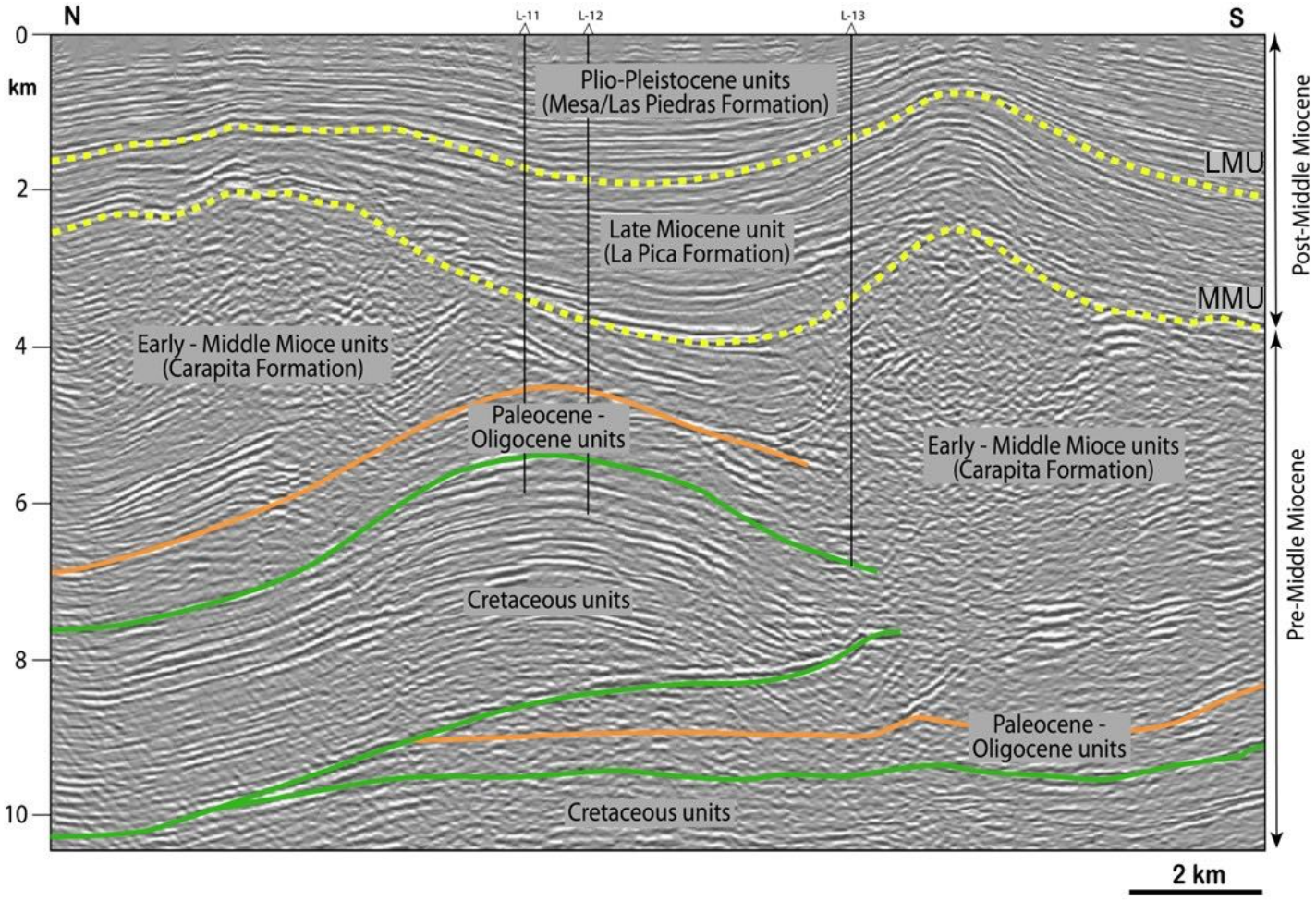

Figure 4.5. Seismic line of the 3D seismic cube showing the stratigraphy markers recognized in the interpretation of the MFTB (to the left). Tectonostratigraphic chart of the MFTB (to the right).

The lines are oriented N-S and are almost perpendicular to the superficial structures identified in the fieldwork. These lines presented from west to east in order to show the development of the faults and the structures along the MFTB.

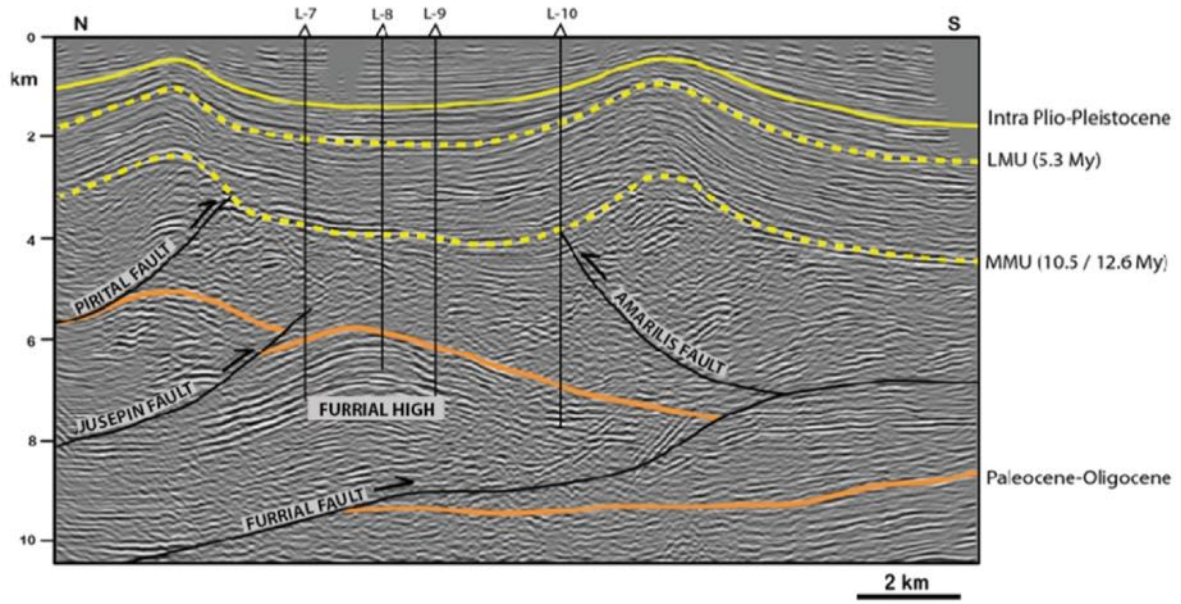

Figure 4.6. Seismic horizons and faults interpreted in the MFTB.

The configuration of the major faults can be appreciated in the 3D seismic cube. The Pirital, Furrial and Jusepín faults, respectively, can be observed. These faults have been extensively studied and their geometry is constrained by wells and cross sections (Roure et al., 2003; Cobos, 2005; Duerto, 2009; Parra et al., 2011). From west to east, the north-dipping of the Pirital fault at ~7 km depth can be observed. This fault is segmented thus forming a fault system. To the east of the study area, the Jusepín fault can be appreciated. This fault shows ~20°- 30° north-dipping. The deepest fault is the Furrial fault (>10 km). This fault shows ~25° north-dipping and is continuous through the 3D block (Figure 4.7). To the east, the Amarilis Backthrust can be observed. This backthrust was developed from the Furrial thrust. It shows ~35° south dipping and reach ~8 km in depth.

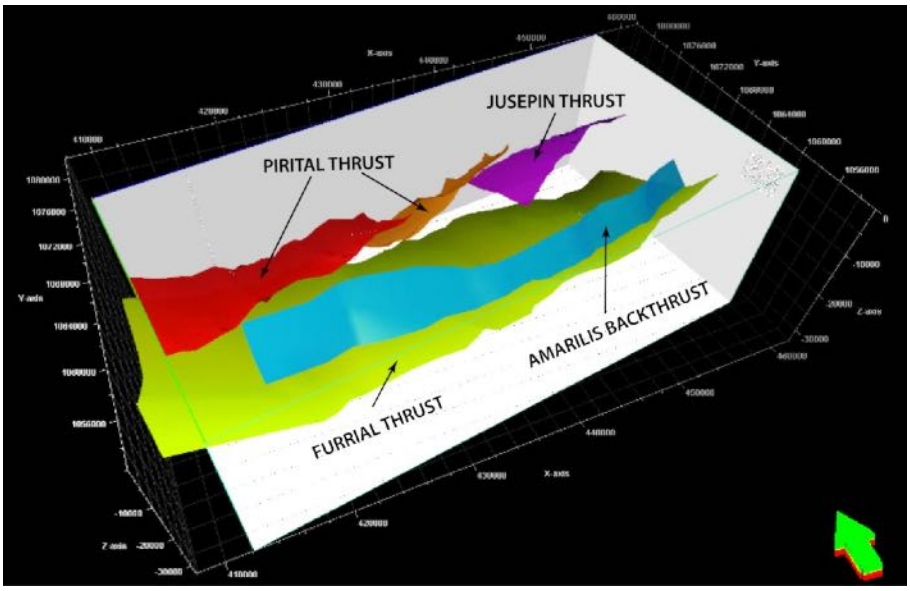

Figure 4.7. Geometry of the deep-seated thrusts within the 3D cube.

4.5.1. M1 Seismic Line

Located to the east of the Urica Fault (Figure 4.3), this 22 km long seismic line shows a section of the SDI foothills characterized by a thrust belt. Three structures at different depths can be identified. The deepest structure is formed by two thrust sheets with south vergence and 30° north-dipping, exhibiting Cretaceous to Paleo-Oligocene rocks. The Tarragona Thrust is the main thrust present in this section and is located above the thrust sheets. This thrust involves pre-Cretaceous (Jurassic?) to Paleo-Oligocene rocks with a possible detachment in pre-Cretaceous rocks. The thrust sheet associated has an estimated thickness of ~7 km with southerly vergence and a 20° dip towards the north (Figure 4.8).

Above the Tarragona thrust sheet, there is an anticline named Tarragona High. This is composed of Early-Middle Miocene unit (Carapita Formation). This shallow anticline reaches the surface through compression and uplifting generated by the Tarragona thrust. The Late Miocene and Plio-Pleistocene sequences onlap this shallow anticline.

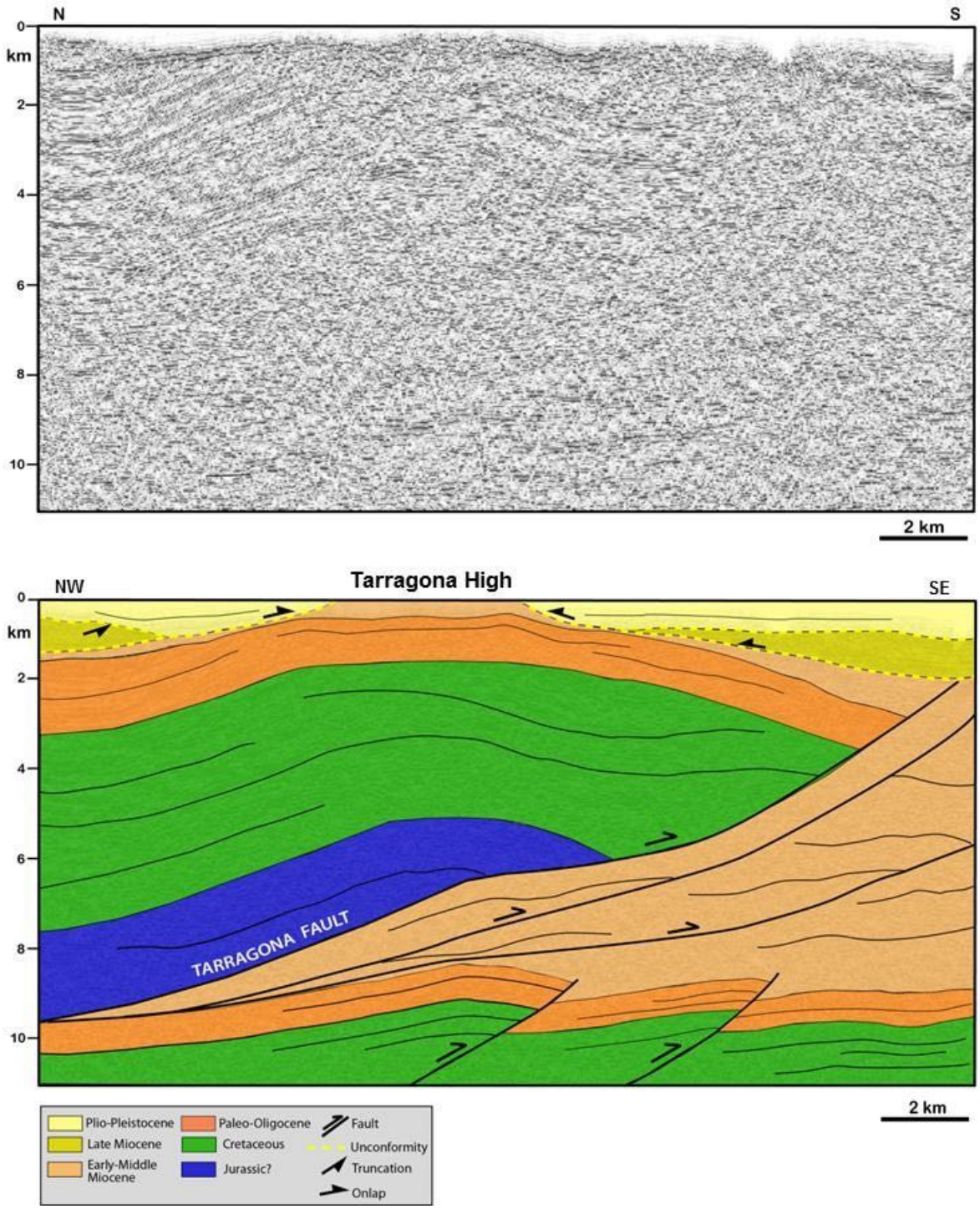

Figure 4.8. M1 seismic line on Tarragona zone. Location of the seismic line in Figure 4.3.

4.5.2. M2 Seismic Line

M2 seismic line is an N-S section of the 3D seismic in the Punta de Mata zone (Figure 4.3). Here, the Pirital High, the Pirital and Furrial thrusts can be observed (Figure 4.9).

The Furrial Thrust is located at the bottom of the seismic line and shows 20° north-dipping

transporting towards the south ~4 km of Cretaceous to Paleo-Oligocene units. Above the Furrial Thrust, the Pirital Thrust is located. This shows 15° north-dipping and transports ~3.5 km of pre-Cretaceous to Paleo-Oligocene units towards the south. The thrust sheet associated to the Pirital Thrust is in contact with Early-Middle Miocene units which are also displaced and folded by this thrust forming a shallow anticline called Pirital High.

The overlaying layer composed of Late Miocene unit changes in thickness on each side of the Pirital High. The La Pica Formation was deposited on the southern flank of this high. It shows onlap termination towards the structure, indicating that the uplifting was active at the time of the sedimentation (syn-tectonic deposits). On the northern flank, Late Miocene unit is represented by the Morichito Formation, which filled a mini basin developed by the strong thrusting of the underlying structures. Here, this unit is thicker than its counterpart in the southern flank and shows truncation in the top represented by the regional MMU. This unconformity indicates active uplifting and an erosive episode developed in the northern part of the basin before the deposition of the Plio-Pleistocene units.

The Mesa/Las Piedras Formation of Plio-Pleistocene age, represents the final stage of deposition in the Maturín Basin. In the seismic lines, Late Miocene to Plio-Pleistocene units shows onlap termination on both sides of the Pirital High with deposits becoming thinner towards the fold limbs. This strata geometry indicates that the active uplifting in the area exceeds the sedimentation rate.

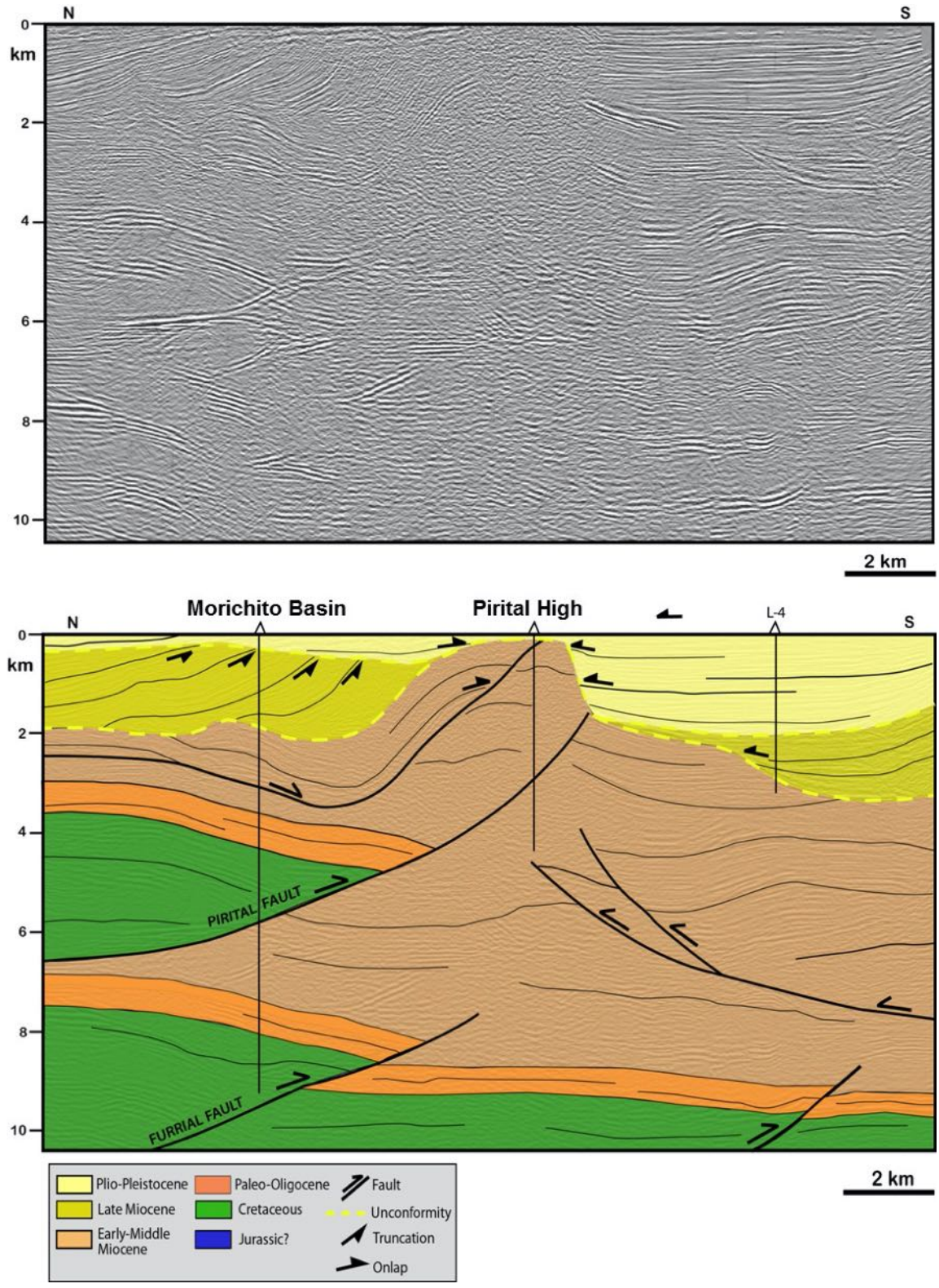

Figure 4.9. M2 seismic line in the Punta de Mata zone. Location of the seismic line in Figure 4.3.

4.5.3. M3 Seismic Line

This N-S profile is located to the east of the M2 seismic line (Figure 4.3). The M3 seismic line shows the evolution toward the east of the same structures interpreted in the M2 line: the Pirital and Furrial thrusts and the Pirital High (Figure 4.10).

In this profile, as the Furrial Thrust increases its development towards the south showing ~12° north-dipping and possible detachment level in the Paleo-Oligocene units can be observed. The Pirital Thrust sheet has a thickness of 2.5 km and the Paleo-Oligocene units are eroded coming into contact with the Early-Middle Miocene unit (Carapita Formation). Within the Carapita Formation, were developed detachment levels and thrusts that affected this unit and the post-Middle Miocene sequences.

As was observed in the M2 seismic line, the Late Miocene to Pliocene-Pleistocene units onlap the emerging Pirital High and are gently folded by active thrusting in the deep structures. The geometry of MMU and LMU indicates that MMU has been eroded. The uplift between the base of LMU to the north of Pirital High and its counterpart to the south is likely the expression of a thrust lying within the Carapita Formation according to our interpretation.

4.5.4. M4 Seismic Line

This N-S line shows the advance of the Furrial Thrust towards the south and as the Pirital high located in the north limit of the seismic line begins to disappear in this same direction. To the south, there is another structural high called Amarilis (Figure 4.11).

The Furrial Thrust exhibits similar geometry as observed in the M3 seismic line. Note that the fault cut-off is in the same location through the entire 3D seismic cube. In the M4 line, the Amarilis Backthrust shows 35° south-dipping. The associated thrust sheet is composed of ~3.6 km of Early-Miocene unit (Carapita Formation). The Late Miocene to Plio-Pleistocene units above the Amarilis Backthrust display growth strata geometry. Also, these units were folded, forming the Amarilis High which is the shallower structure that can be seen in this profile.

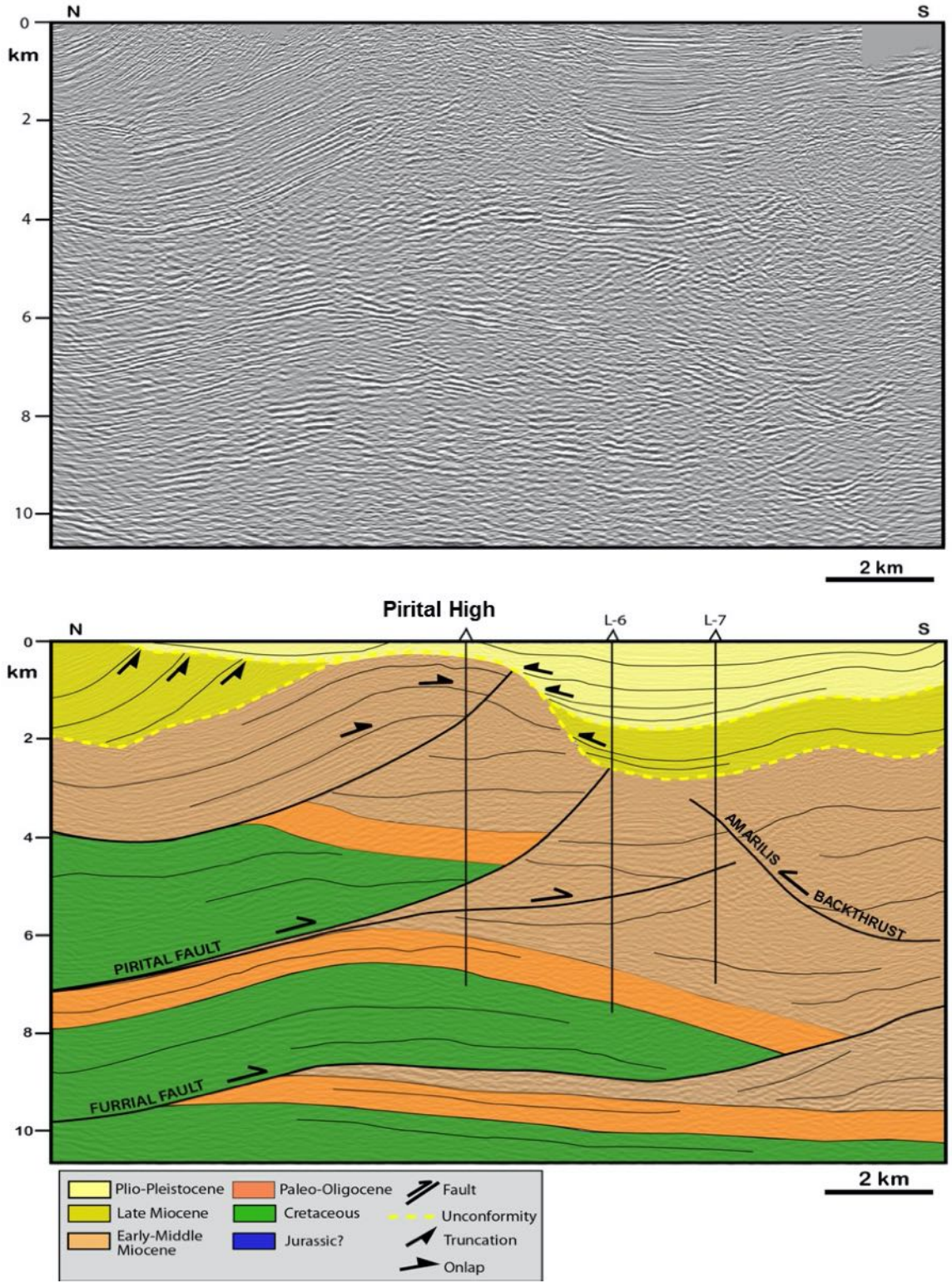

Figure 4.10. M3 seismic line. Location of the seismic line in Figure 4.3.

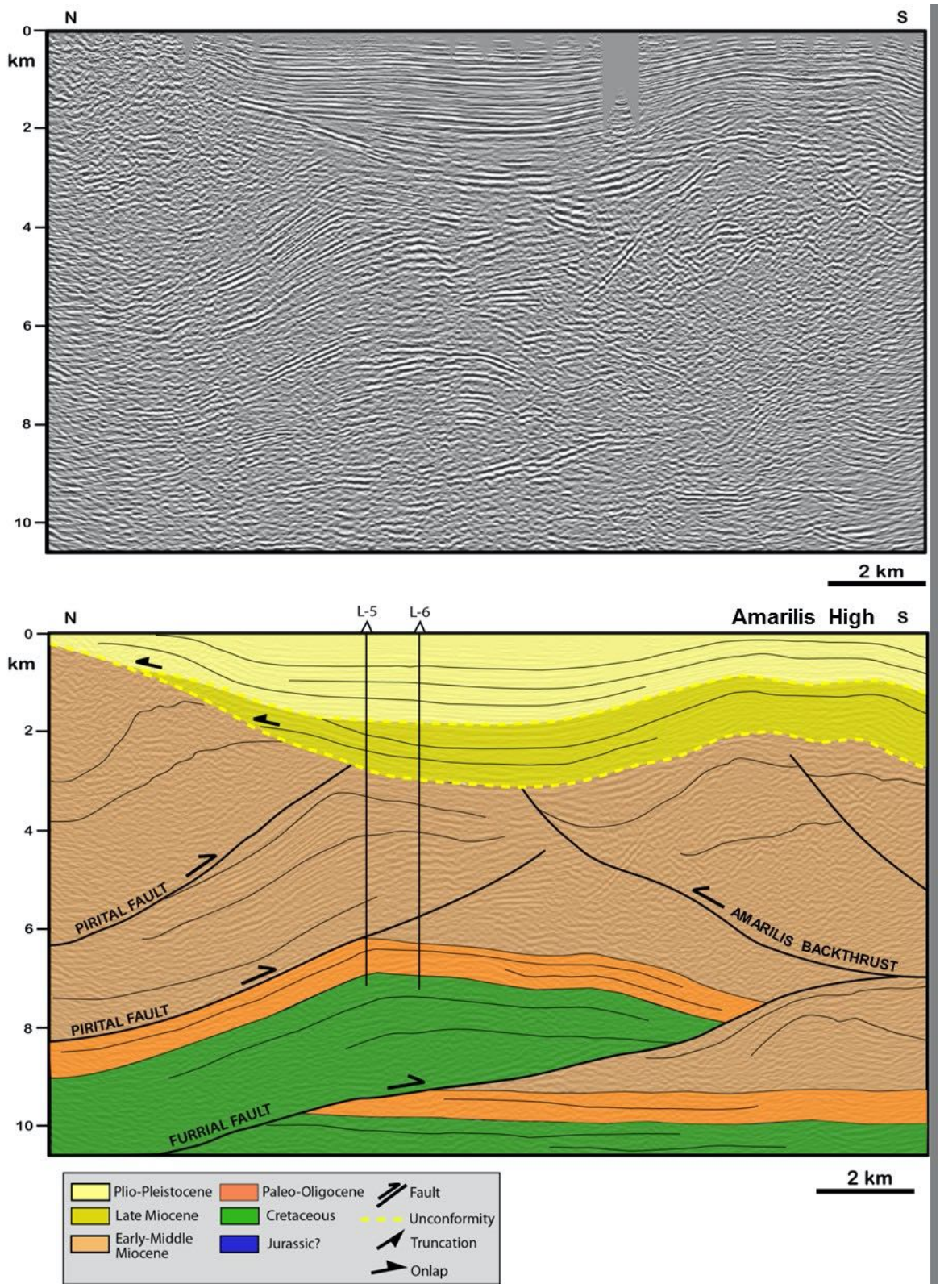

Figure 4.11. M4 seismic line. Location of the seismic line in Figure 4.3.

4.5.5. M5 Seismic Line

This is the most eastern seismic line interpreted in this study (Figure 4.3). The configuration of the Furrial and Pirital thrusts at the eastern limit of 3D block can be observed. The Furrial and Pirital thrusts are still present as in previous lines located to the west. However, in this line, the tip end of the Pirital Thrust dies out progressively from west to east. Also, can be observed another thrust developed as a lateral evolution of the Pirital Thrust and has been named the Jusepín Thrust (Figure 4.12).

To the north of the seismic line, the thrust sheet associated with the Pirital Thrust has a south vergence and is composed of 2.2 km thick of Early-Middle Miocene unit. The activity of this thrust like the Amarilis Backthrust are gently folding the overlying Late Miocene and Plio-Pleistocene layers forming a structural high. This high has been named Jusepín High. However, the crests of the structural highs developed in the Late Miocene to Plio-Pleistocene sequences are located a little further north than the crests of the structures developed in the Early-Middle Miocene unit.

4.6. Structural Depth Maps

In this section, the structural depth maps from the different horizons interpreted in the 3D block are presented.

4.6.1. Structural Depth Map from the Intra Plio-Pleistocene Units

The structural depth map for the Intra-Pleistocene shows the shallow configuration of the Pirital, Amarilis y Jusepín highs (Figure 4.13).To the northwest of the 3D block, the Pirital High is 35 km long and shows a N60E strike. The height varies between -750 m and -300 m. To the north of the high, is present the Morichito Basin developed as a consequence of the Pirital High uplifting. This mini-basin reaches a depth >750 m. The Jusepín High developed in the NE of the 3D block along a N70E strike, reaching a height of ~- 450 m.

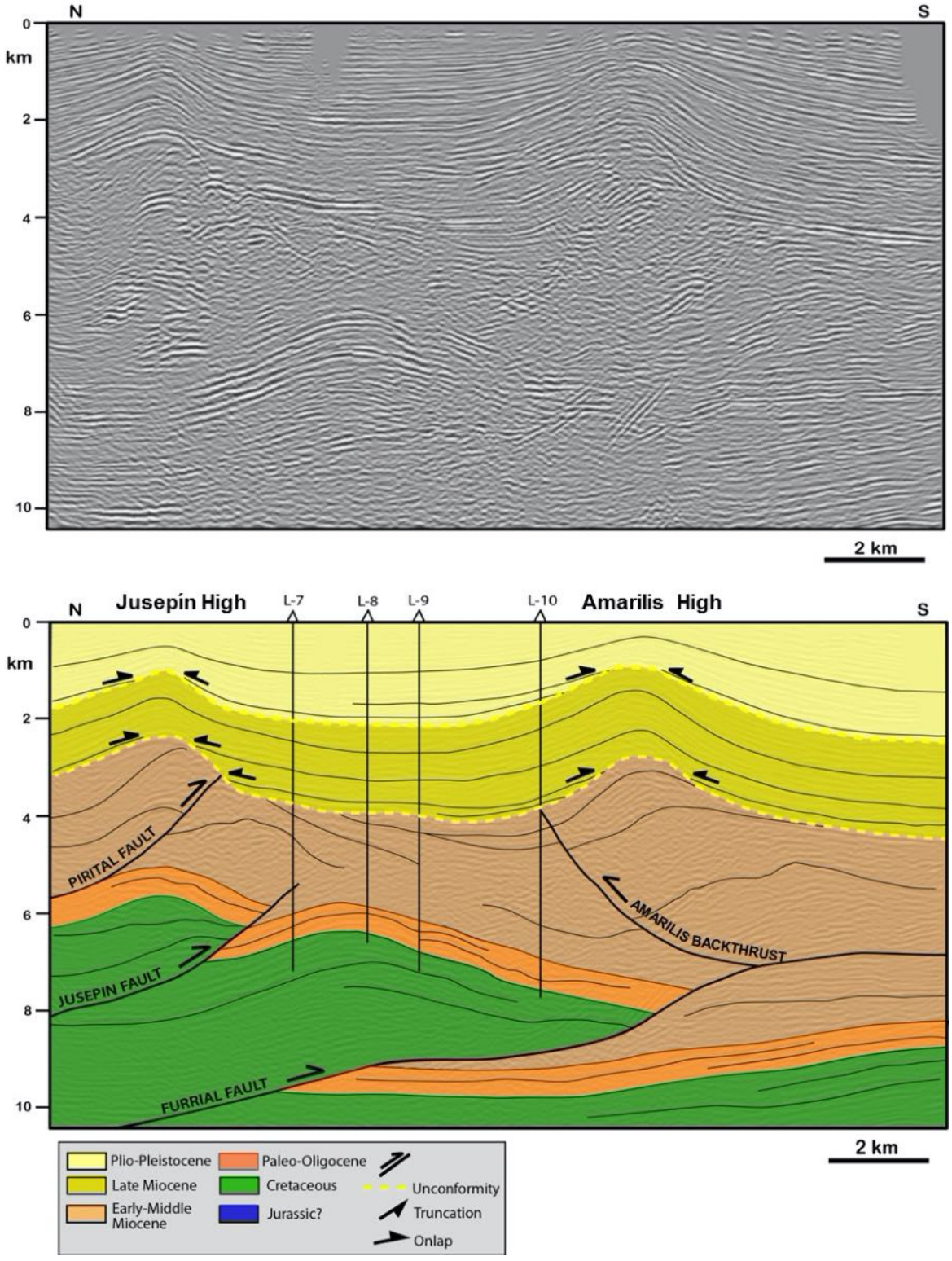

Figure 4.12. M5 seismic line in the Jusepín and Amarilis zones. Location of the seismic line in Figure 4.3.

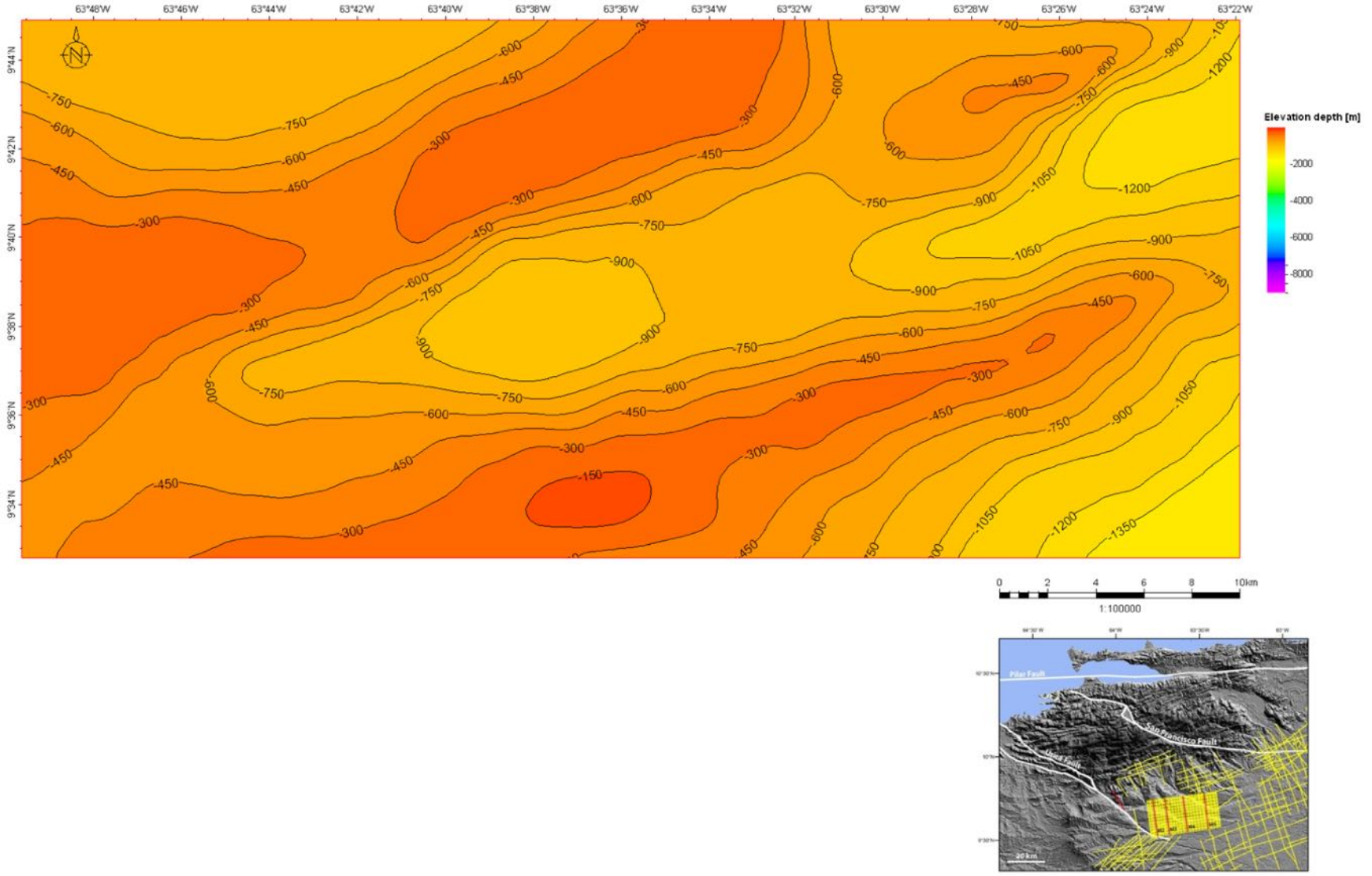

Figure 4.13. Structural depth map from the Intra Plio-Pleistocene units.

4.6.2. Structural Depth Map from the Late Miocene Unconformity (LMU)

This depth map shows the same three structures described in the previous map (the Pirital, Jusepín and Amarilis highs). In this level, to the west, the Pirital High shows a N65E strike direction and is ~24 km long and ~7 km wide. Towards the north, changes to a N35E strike direction. The height varies between -1000 and -600 m (see north central part of the map). The Morichito Basin dips towards the north reaching a depth of -2000 m (Figure 4.14).

The Jusepín High has a maximum height of ~ -800 m. To the south, the Amarilis High reaches a maximum height of -400 m. The basin formed between the Pirital and Amarilis highs, reaches ~ -1200 m in depth.

4.6.3. Structural Depth Map from the Middle Miocene Unconformity (MMU)

The MMU is the top of the pre-Middle Miocene units and the base of the post-Middle Miocene units (Figure 4.4). At this level, the Pirital High has a maximum height of -300 m, with two orientations: N85E to the west of the 3D block, and N55E in the central part.

The Jusepín High is not too clear in this map. The Amarilis High reaches its maximum depth at ~ -2000 m. Similarly, in the northwest, the Morichito basin reaches its maximum depth of ~ -3500 m (Figure 4.15).

4.6.4. Structural Depth Map from the Paleocene-Oligocene Units (El Furrial hanging-wall)

The structural map from the Paleocene-Oligocene units defines the top of the Furrial Thrust sheet, which is one of the major thrusts present in the area. This thrust sheet has an average height of ~ -3600 m and shows an almost E-W trend, being more inclined to the east (N65E strike direction). Three structural highs compose the Furrial Thrust sheet where are located the most important oil targets in the MFTB (Figure 4.16).

4.6.5. Structural Depth Map from the Paleocene-Oligocene Units (El Furrial foot-wall)

This map shows the general NE-SW trend of the basin. The basin is deeper to the northwest reaching ~ -9000 m. Towards south is shallower with depths between ~ -6000 m and -6500 m (Figure 4.17).

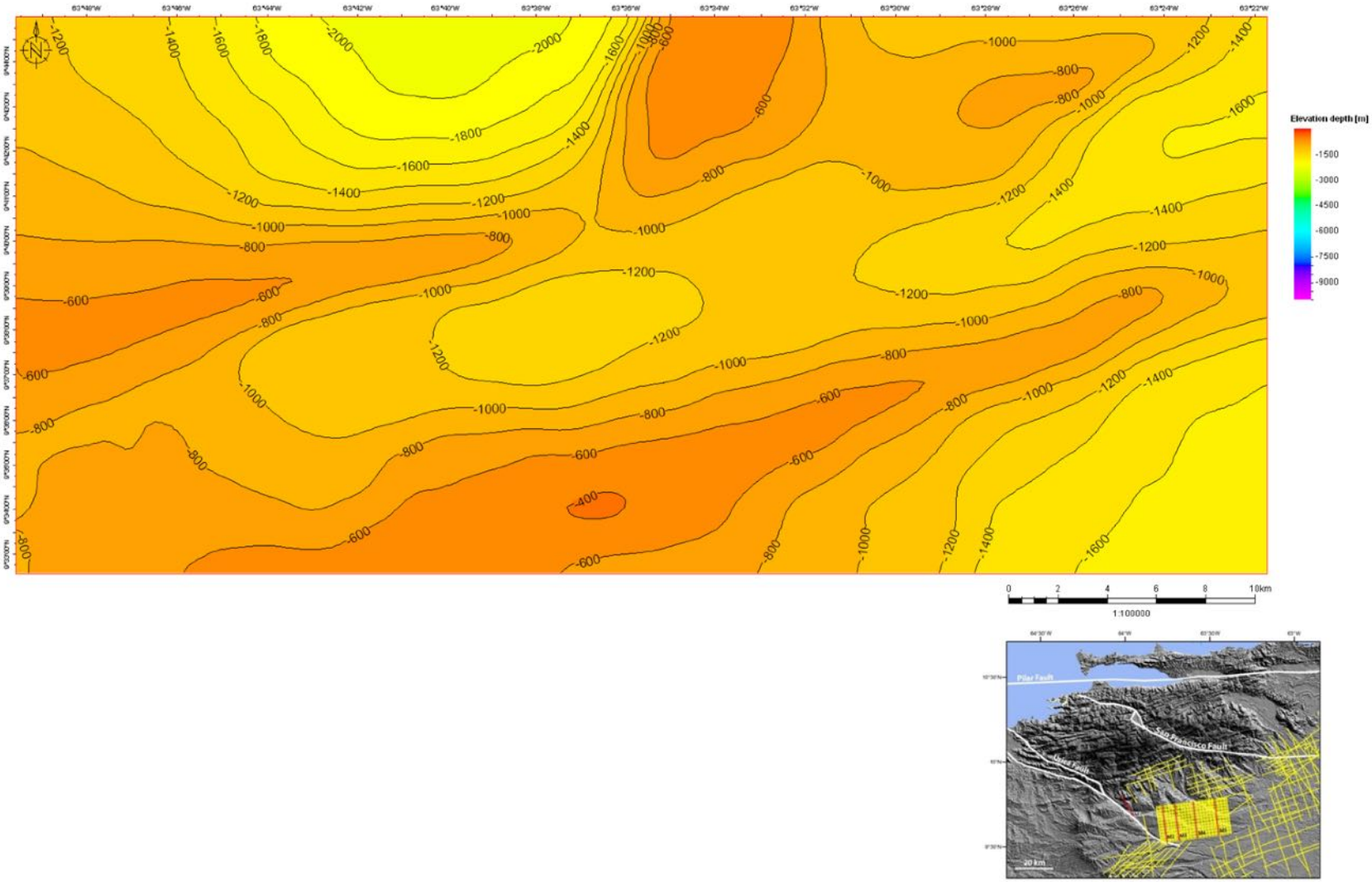

Figure 4.14. Structural depth map from the Late Miocene Unconformity (LMU)

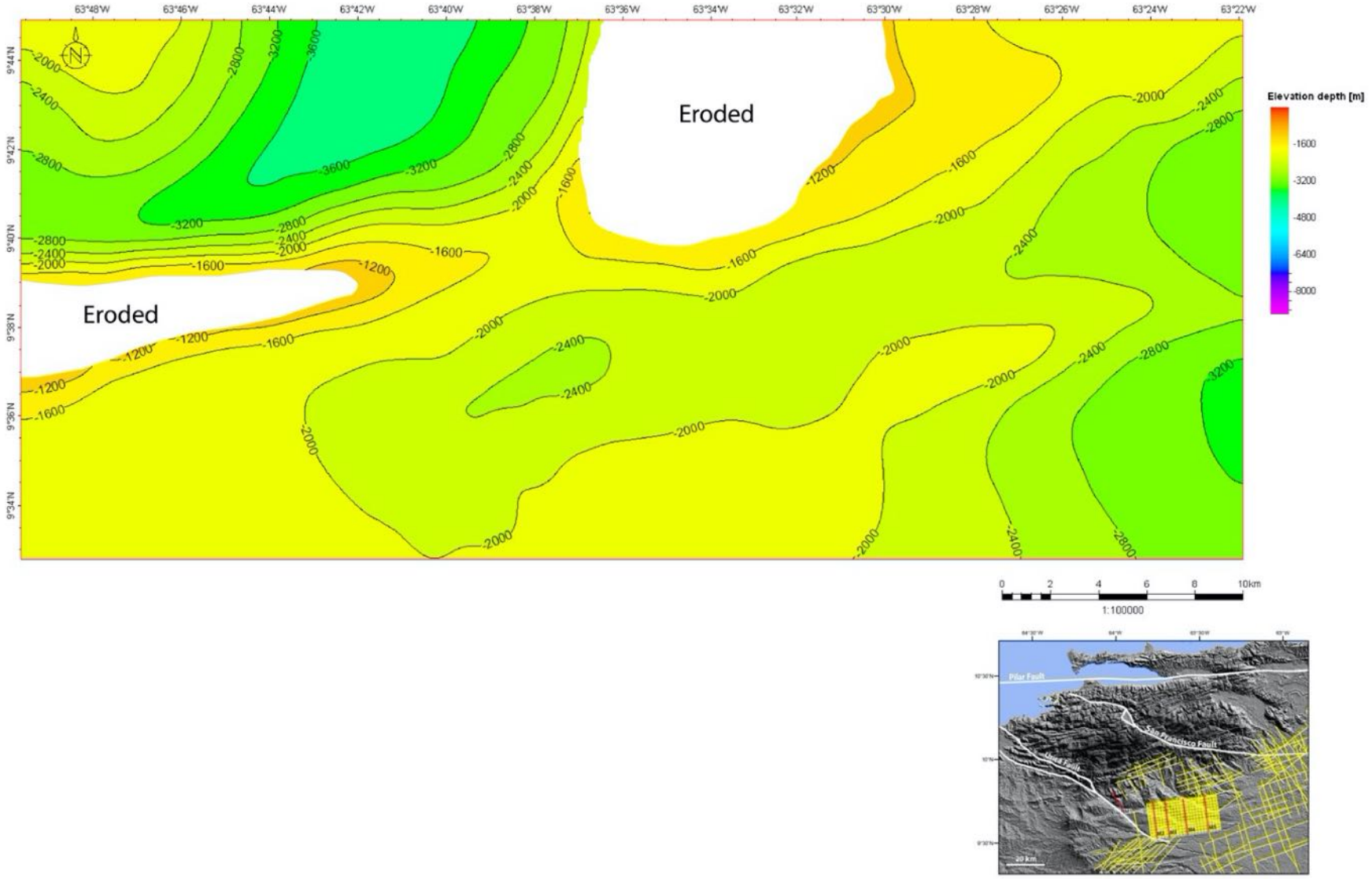

Figure 4.15. Structural depth map from the Middle Miocene Unconformity (MMU)

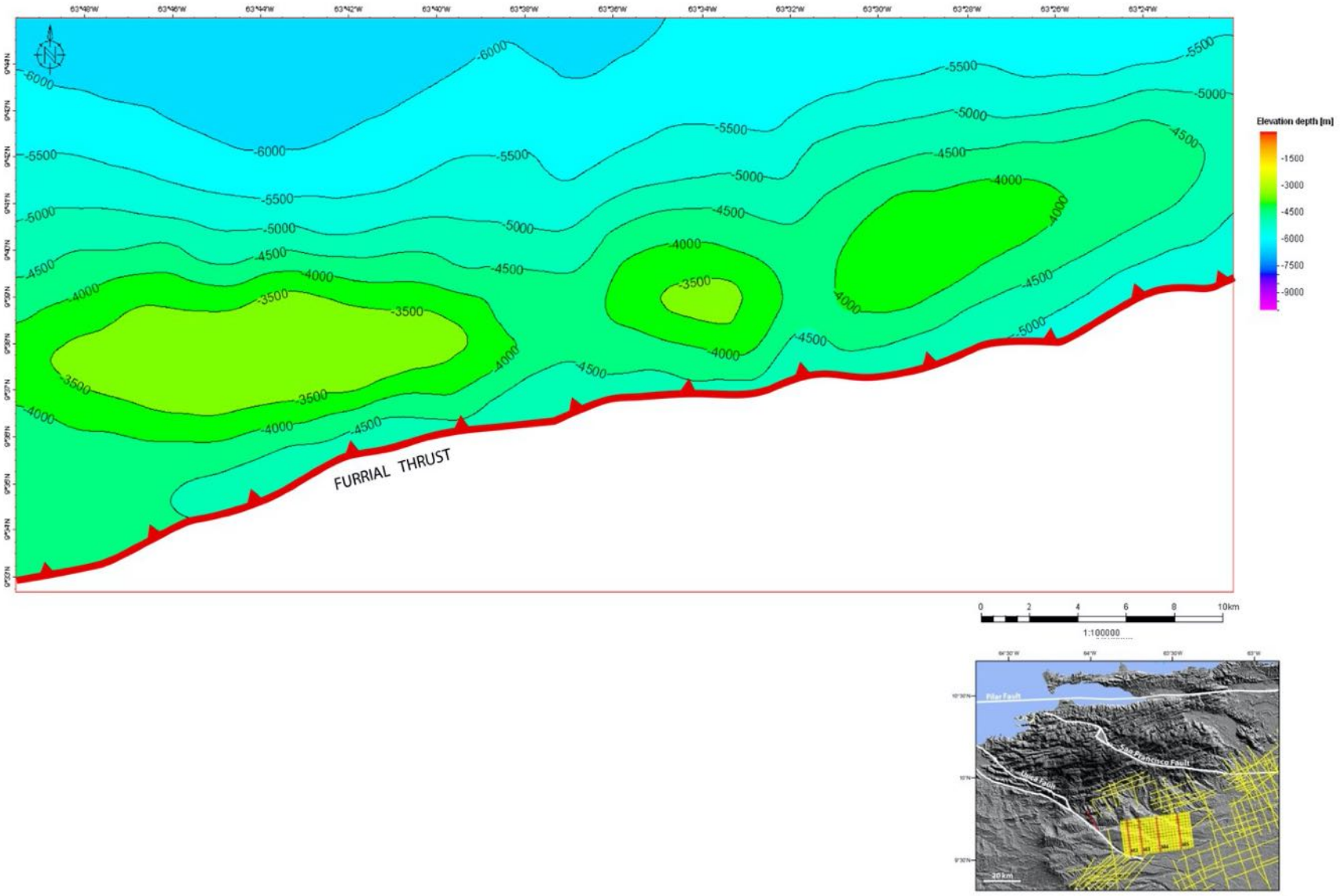

Figure 4.16. Structural depth map from the Paleocene-Oligocene units (Furrial hanging-wall).

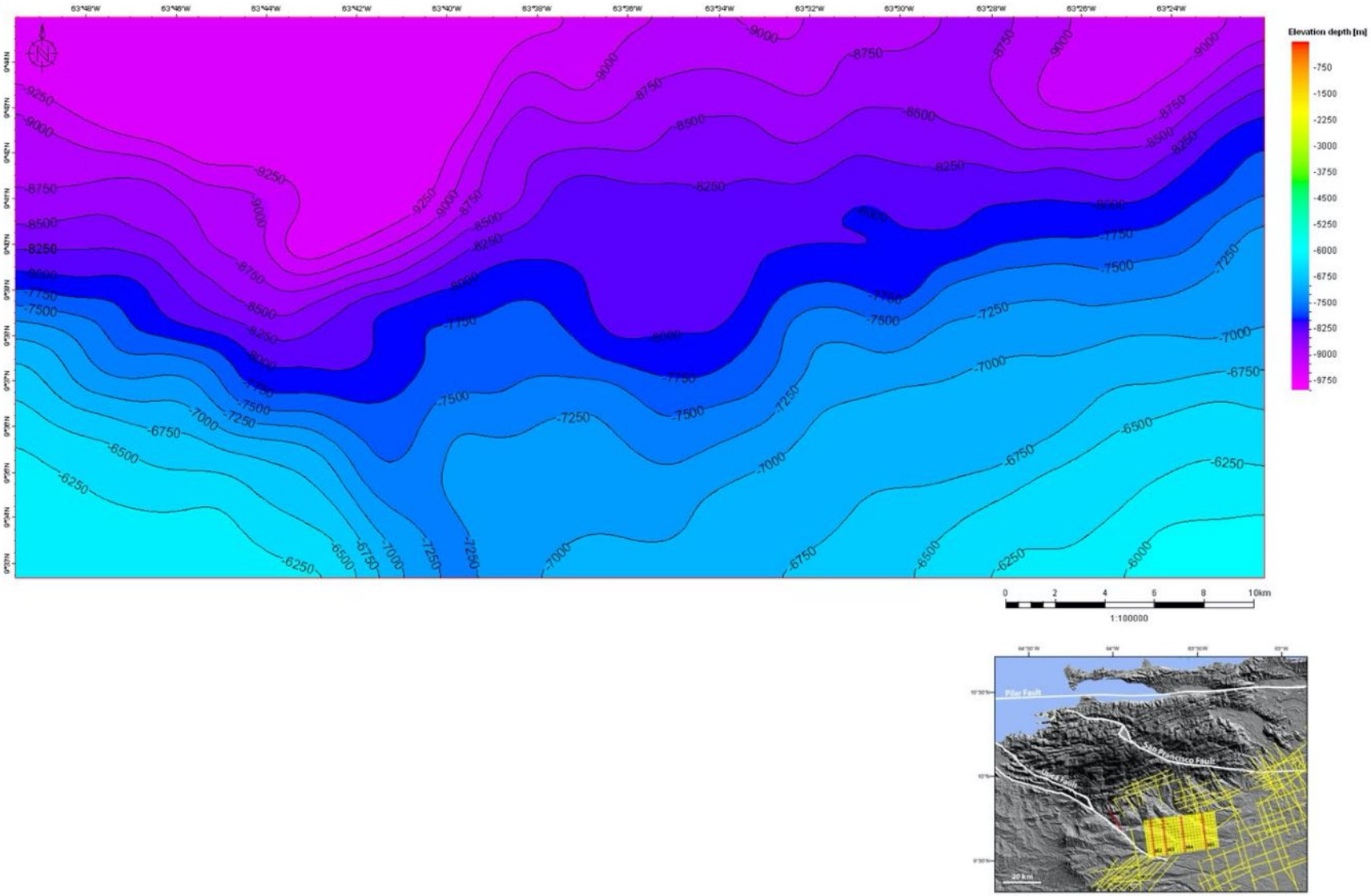

Figure 4.17. Structural depth map from the Paleocene-Oligocene units (Furrial foot-wall).

4.7. Isochron-depth Thickness Maps from the post-Middle Miocene Units

The post-MMU units display growth strata geometry and hence, their thicknesses are controlled by the active tectonic in the area. The isochron map aims at illustrating the thickness variation on the different structures identified in the structural maps.

The isochron map between MMU and LMU shows thickness variation on both sides of the Pirital High (west side of the map) (Figure 4.18). To the northeast of the Pirital High the thickness reaches ~2100 m, decreasing towards the high to 0 m (onlap termination). To the southwest, the thickness is smaller compared to the north, between -600 m and -900 m. Here, the thicknesses also decrease to zero towards the Pirital High.

To the northeast of the 3D block, thicknesses are higher and increase towards the east with ranges between 600 m and 1800 m (thicker eastward sequence). To the south, in the Amarilis High, the thickness shows a slight variation between 900-1200 m.

The isochron map obtained from the upper levels (between LMU to the Plio-Pleistocene top units) shows greater thicknesses to the north of the Pirital High which vary between 450-150 m (Figure 4.19). As in the lower level, the thickness decreases towards the structural high. Also, the thickness decreases towards the Amarillis High (onlap termination) varying between 150-300 m. In general, in this sequence, thicknesses increase towards the southeast and northeast of the area reaching 1050m and 900 m, respectively.

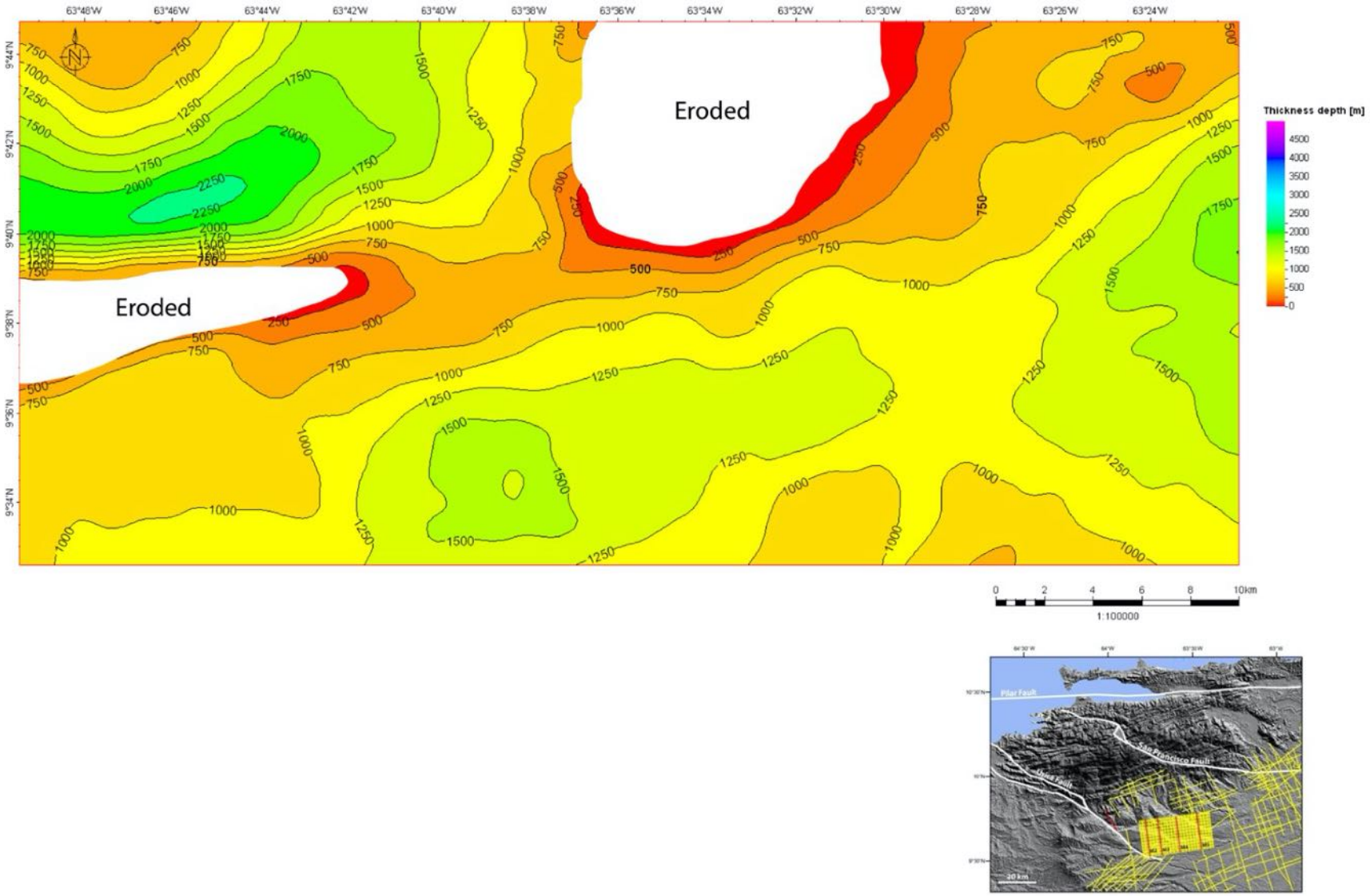

Figure 4.18. Isochron depth map between MMU and LMU unconformities.

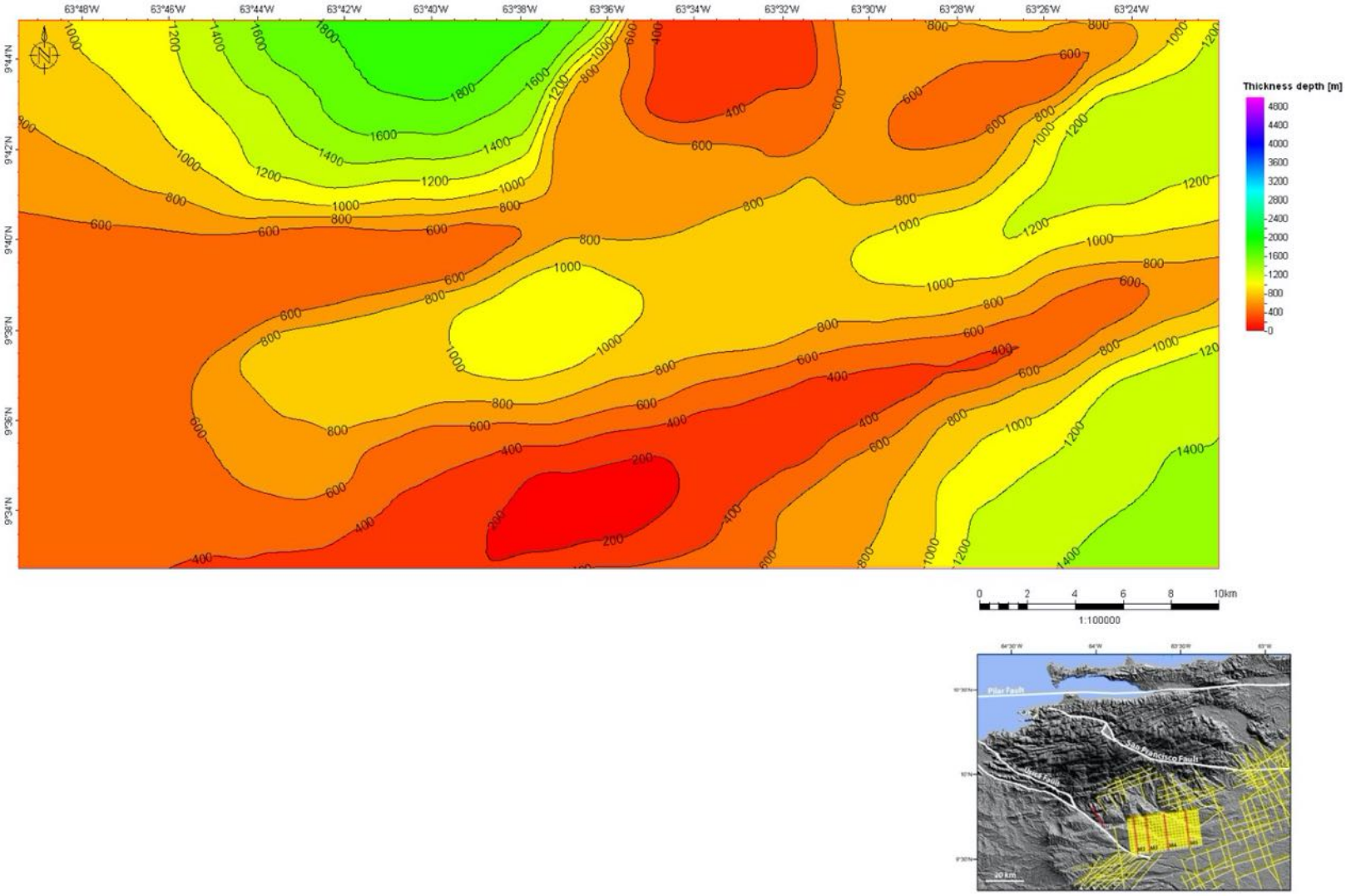

Figure 4.19. Isochron depth between LMU unconformity to Plio-Pleistocene top unit.

4.8. Discussion

The analysis of 2D section M1 and M2 to M5 3D sections provides a better comprehension of the post-Middle Miocene deformation in the MFTB. One of the key observations of this study is the mapping of the MMU (10 My) and the LMU (5.3 My) and the growth strata geometry identified. These unconformities folded indicate that in MFTB have occurred different episodes of compression and exposition which also controlled the sediments deposition reflect in growth strata geometry (Figure 4.20).

The structural depth maps show several structures developed which vary from northwest to southeast in the study area (Figure 4.13 to Figure 4.17). Isochron depth maps between the MMU and the LMU and between LMU and Plio-Pleistocene units indicate strong variations in the thickness from the west to the east (Figure 4.18 and Figure 4.19).

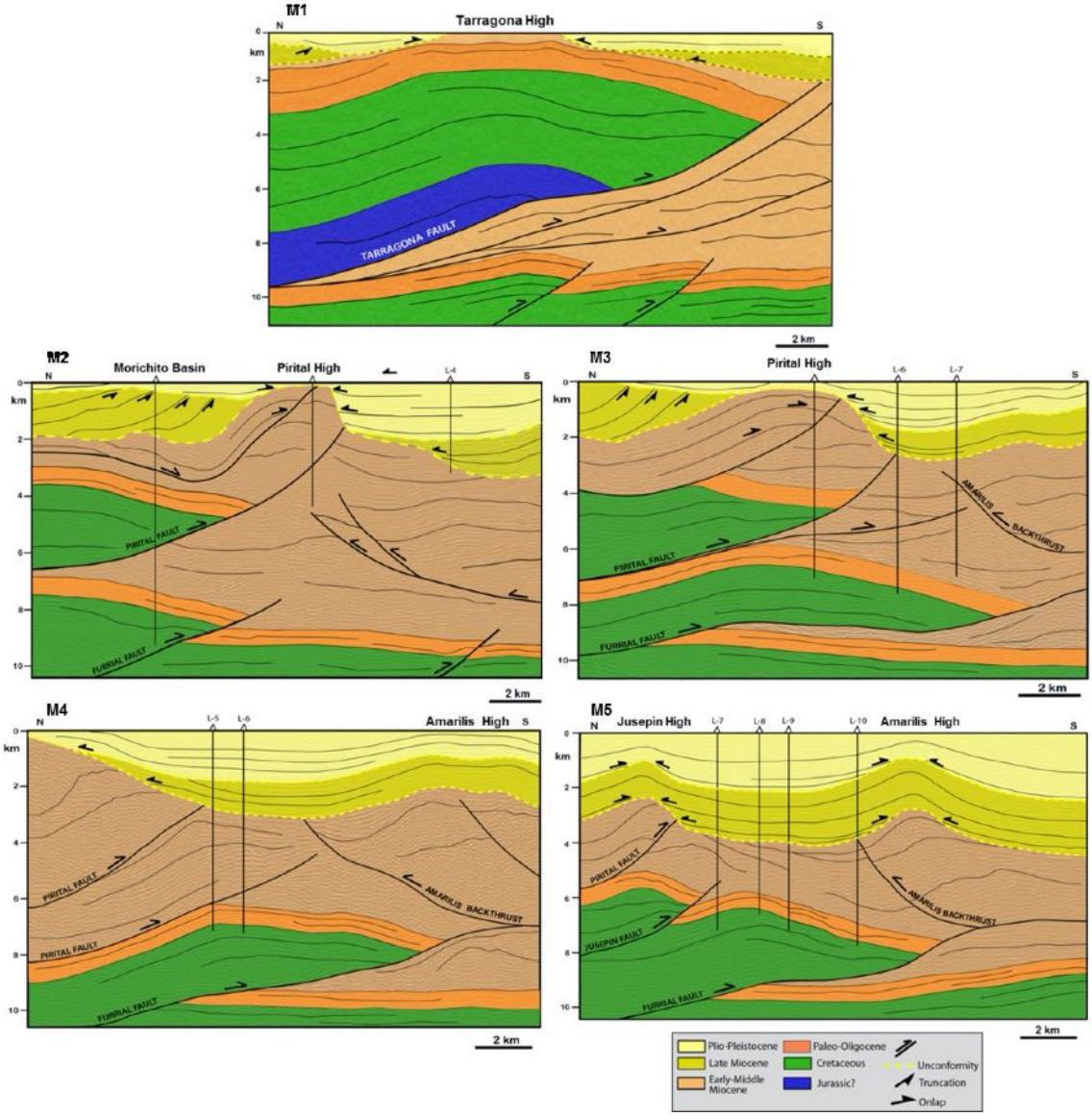

Figure 4.20. M1, M2, M3, M4 and M5 seismic lines interpreted in MFTB.

Growth Strata Pattern in the Monagas Fold and Thrust Belt

The units deposited during deformation around a growing fold are called growth strata or syntectonic strata (Suppe, 1992; McClay, 2004; Shaw et al., 2005). The age of these stratigraphic intervals gives the timing of deformation. Two main factors define the geometry of the growth strata: the folding mechanics (kink band migration and limb rotation) and the relation between the uplift and sedimentation rates.

The growth strata pattern according to the sediment-to-uplift ratio can be identified in seismic lines. If the sedimentation rate is greater than the uplift rate, the sediments deposited are thinner towards the structural high and are frequently folded in the limbs of the structure (Figure 4.21). In contrast, if the uplift rate is greater than the sedimentation rate, the growth strata generally show onlap and become thinner towards the structural high and are folded in one or both limbs of the structure (Shaw et al., 2005) (Figure 4.21).

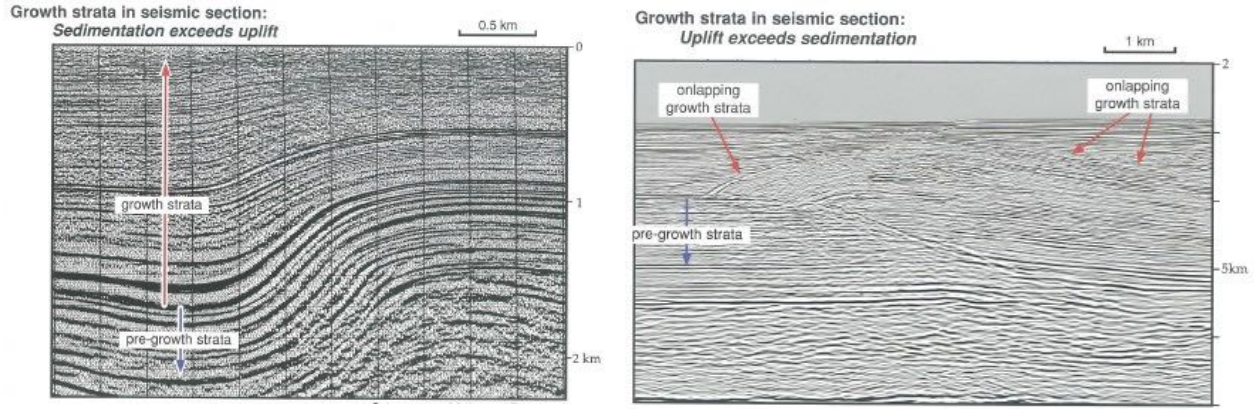

Figure 4.21. Common patterns of growth strata in fault-related folds identified in seismic reflection images. Sedimentation exceeds uplift (left). Uplift exceeds sedimentation (right) (from Shaw et al., 2005).

Growth strata provide information on kinematics and mechanisms of folding according to the patterns of the deformation shown above fold limbs. In contractional fault-related folds, two folding mechanic modes are typically developed: kink-band migration and limb rotation

In a kink-band migration mechanism, the fold limbs widen amplifying the fold while keeping a fixed dip (Suppe & Medwedeff, 1990; Suppe et al., 1992). The axial surface is active due to uplifting and thus the geometry of the material deposited is controlled in the fold limb. This mechanism does not show fanning growth geometries in the syn-kinematic sediments (Duerto, 2007). Another important factor is the relation between sedimentation and uplifting

rates. Where the sedimentation rate is greater (Figure 4.22), the strata deposited into the fold limb are folded through the synclinal axis. The dip of the folded growth strata is the same as the fold limb in the pre-growth strata. The fold limbs of the younger horizons become narrower than do older horizons, thus fold limbs are narrowing as they rise forming kink bands in growth strata. If the sedimentation rate is lower than the sedimentation rate, folding creates a gentle fold scarp in the active axial surface. Then, continuous deposits onlap this fold scarp generating pinch-out termination above the fold limb (Shaw et al., 2005).

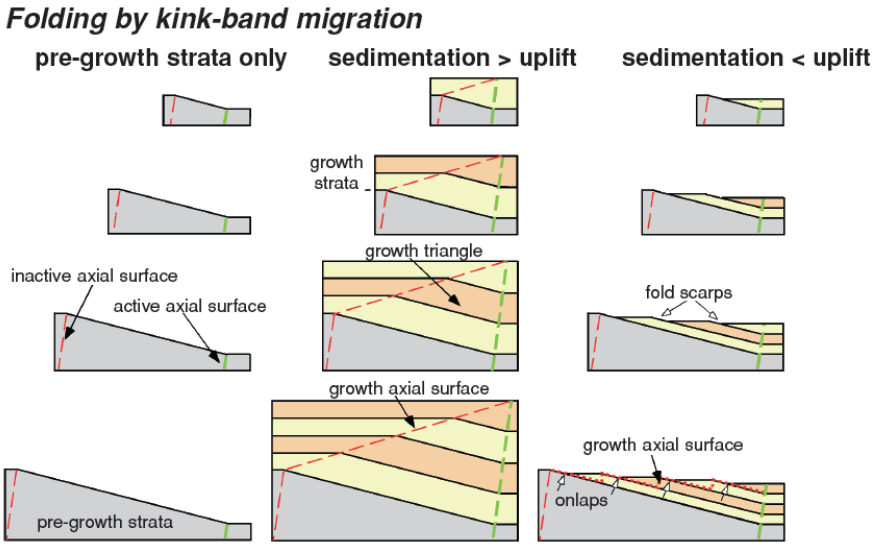

Figure 4.22. Kink-band migration mechanism in contractional fault-related folds (from Shaw et al., 2005).

In limb rotation mechanism with inactive axial surfaces, the folding augmentation increases the dip of the fold limb (Figure 4.23). This mechanism shows progressive fanning of growth strata as the fold grows (Poblet et al., 1997; Duerto, 2007). Where the sedimentation rate is greater than the uplifting rate, strata rotate at the same time that folds increase and thus staying constant the fold limb width. In the case where the sedimentation rate is lower than the uplifting rate growth strata onlap the fold limb (Shaw et al., 2005).

The seismic image interpreted in the MFTB shows that sedimentary deposits from the Late Miocene to Pleistocene age were folded and have growth strata geometry with respect to the structural highs identified in the area. The dips of these growth horizons are steeper in the oldest growth strata, showing a progressive fanning of the limbs dip. This geometry is the main characteristic of the limb rotation mechanism in contractional fault-related folds described previously. Additionally, these growth strata onlap the Pirital and Tarragona highs to the north and the Amarilis and Jusepín highs to the southeast, evidence that the uplifting rate exceeds the sedimentation rate (Figure 4.24).

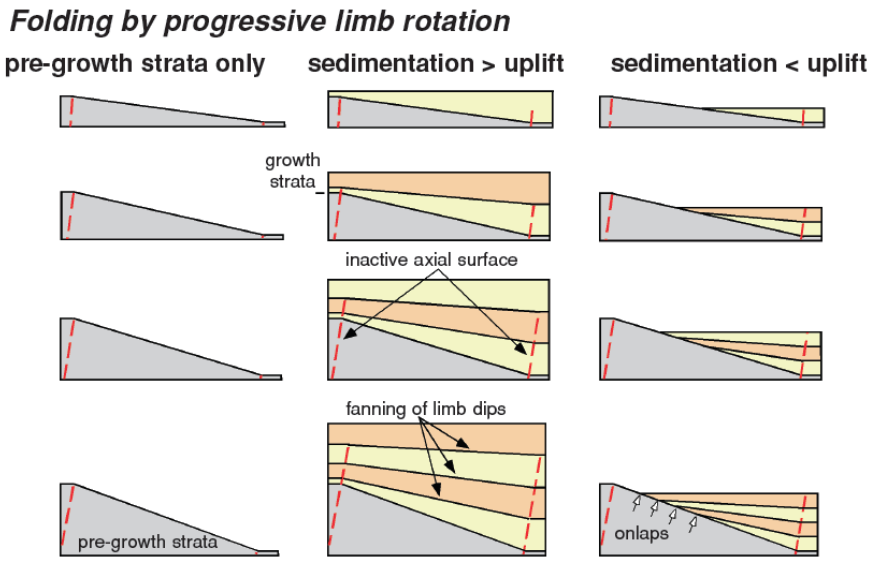

Figure 4.23. Limb rotation migration mechanism in contractional fault-related folds (from Shaw et al., 2005).

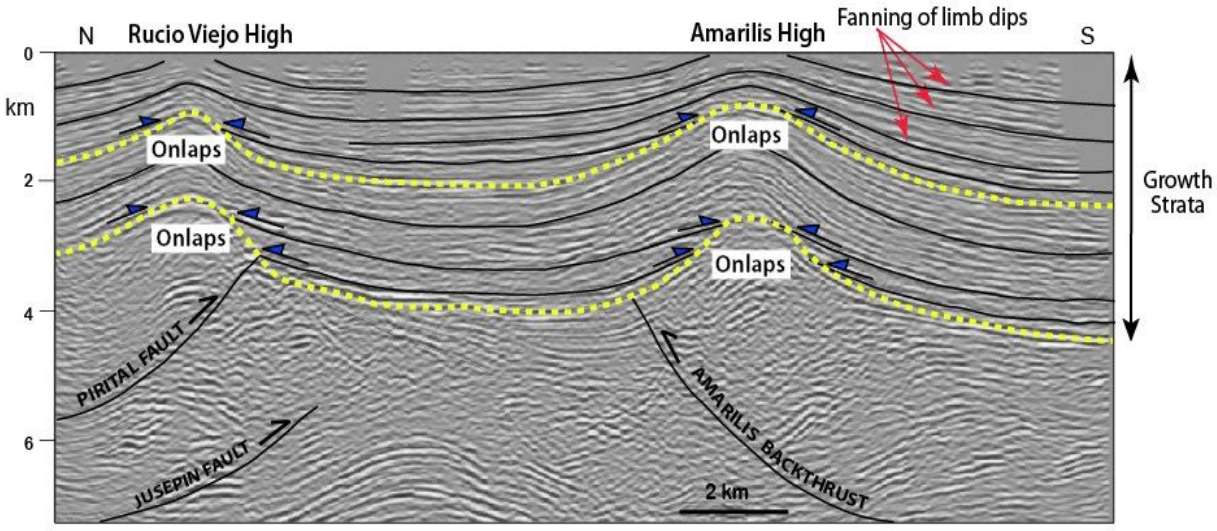

Figure 4.24. 3D seismic line in the MFTB showing the growth strata configuration in the area.

Seismic Signature in Monagas Fold and Thrust Belt

Four mainly deep structures were identified in seismic lines and related to the superficial deformation studied in the geomorphology chapter (CHAPTER 3) (Figure 4.25):

The Tarragona High (M1 Seismic Line)

Located to the northwest of the study area, in the foothill of the Serranía Del Interior, the Tarragona High is an anticline formed by Early-Middle Miocene shale units (Carapita Formation) that reaches the surface according to the seismic image. The southward

propagation of the Tarragona Thrust deformed the Pre-Cretaceous to Paleo-Oligocene units with likely detachment level in Pre-Cretaceous units. Seismic interpretation suggests that the Tarragona Thrust was reactivated during an out-of-sequence period, uplifting and deforming the shale units. The reactivation of this thrust generated the Tarragona High. Additionally, this out of sequence thrusting period controlled the deposition in the area. For that reason; the late Miocene to Plio-Pleistocene units display growth strata geometry (onlap relation against Tarragona High) indicating that the compression was active at the time of the sedimentation.

The expression on the surface of the Tarragona High was observed in DEM image by a ridge of ~350 m high and a N80E strike direction (Figure 2.17, CHAPTER 2). Additionally, in the fieldwork, in the same place, an outcrop composed of shale of the Carapita Formation was observed (Figure 3.1, site S3). This outcrop is affected by a thrust with south vergence that places yellowish shale in contact with greenish shale. The top of the outcrop is defined by an alluvium layer folded. The alluvium deformed in the top of the outcrop is evidence of the active deformation in the area.

The Pirital High (M2, M3, M4 Seismic Lines)

The structural depth map of the MMU shows that the Pirital Thrust affected strongly this unconformity and the post-Middle Miocene units. As with the Tarragona Thrust, the Pirital thrust was assumed to have been reactivated during an out sequence period, uplifting and deforming the shale unit, thus forming the Pirital High. In the area covered by the 3D block, this high does not reach the surface. However, in fieldwork, to the north of the M4 seismic line (Punta de Mata zone, site S6, see CHAPTER 3) a ridge ~5 m high and ~25 m long was observed. This ridge is affected by a backthrust of north vergence and is located above the Pirital High interpreted in the seismic depth line. Accordingly, this ridge is suggested to be a surface expression of the Pirital High interpreted in depth, indicating that the compression system is still active (Figure 4.9 to Figure 4.11).

Additionally, in the seismic lines, the Late Miocene to Plio-Pleistocene units shows onlap termination on both sides of the Pirital High (as in the Tarragona High). This onlap termination defines growth strata geometry. In the Pirital Ridge observed in field (site S6, see CHAPTER 3) this growth strata geometry was also found where yellowish clays and siltstones onlap the ridge.

The presence of the growth strata geometry (in depth and surface), the Late Miocene to Plio-Pleistocene units folded, and the ridges observed in field are evidence once again of the active deformation in the study area.

The Jusepín High (M5 Seismic Line)

The Pirital Thrust system is expressed in the M5 seismic line through a thrust with 30° north dipping located in the southeast of the study area. This thrust of south vergence displaces and deforms the shale of the Carapita Formation. Above, the Late Miocene to Plio-Pleistocene units have growth strata geometry and are also being uplifted and gently folded generating the Jusepín High (Figure 4.13 and Figure 4.19).

On the surface, from DEM image, several south vergence thrusts were identified just above the Jusepín High in depth. These superficial thrusts tilt and deform the alluvial terraces observed in the fieldwork (Figure 3.1 and CHAPTER 3).

The Amarilis High (M4, M5 Seismic Lines)

The north verging Amarilis Backthrust was observed to the south of the 3D block. This is associated with the southward limit of the Furrial thrust. The thrust sheet associated with the Amarilis Backthrust is composed of Early Miocene units with a thickness of 3.6 km. As in the Jusepín High, the Late Miocene to Plio-Pleistocene deposits have growth strata geometry, product of the active uplifting. These units are also being folded and uplifted, thus having formed the Amarilis High, which is the most southerly anticline in the MFTB.

From surface observation (including DEM analysis), the Amarilis High is the ridge that marks the deformation limit to the south of the study area. The ridge is related vertically to the Amarilis High identified in the seismic lines and is 19 km long, 6.5 km wide and reaches 200 m in height.

Shortening in the Plio-Pleistocene Units

The seismic lines interpreted show that the post-Middle Miocene units are more deformed to the west of the MFTB. This is shown by the large Tarragona (M1 seismic line) and Pirital (M2 and M3 seismic lines) thrusts which are more developed to the west of the area. The seismic lines show that the deformation is progressively attenuated towards the east where for example the expression of the Pirital High decreases until it disappears. The M4 and M5

seismic lines located to the east of the 3D block show that the folds and shortening in the Plio-Pleistocene units are smaller with respect to the seismic lines located to the west. The shortening is mainly caused by the Tarragona (to the west), Pirital (in the center part) and Furrial thrusts and by the Amarilis Backthrust (to the south).

The comparison between MMU and LMU shows that the post-Middle Miocene deformation in the MFTB occurred differently to the NW to the SE of the area. To the NW, the M1 seismic line shows that the MMU truncates the units below. This unconformity have been slightly folded and tilted before the LMU due to the Tarragona Thrust activity. Then, a higher deformation occurred creating the LMU which truncated the Late Miocene unit. This unconformity is folded which shows an important post-LMU deformation.

Toward the east, in the M2 and M3 seismic lines the geometry of The MMU and LMU unconformities reflects the Middle Miocene Pirital out-of-sequence thrusting. This event formed the Pirital High and the MMU. The ramp created by this thrust formed the Morichito piggyback basin to the north of the high. Also, this event produced the difference in thickness between the post-Middle Miocene deposits to the north and to the south of the high. The difference in depth of the LMU to the north and south of the high shows that the deformation was higher in the post-LMU.

Further east, in the M4 and M5 seismic lines, the MMU and LMU geometries show a different configuration with respect to the lines to the west (M2 and M3). Here, even though the growth strata and the onlaps against the Jusepín and Amarilis highs show that the deformation have been continued since the post-Middle Miocene, the layers and unconformities have been folded symmetrically.

The broad geometry of the LMU and MMU suggests that most of the convergence of the Plio-Pleistocene units took place post-LMU. For this reason, we calculate the shortening of the LMU. From west to east, we obtained a minimum shortening of ~1.3 km in the M1 seismic line, ~1 km in the M2 and M3 seismic lines, ~0.7 km in the M4 seismic line and ~0.5 km in the M5 seismic line (Figure 4.25). Figure 4.26 shows the shortening percentage in each seismic line with respect to its length (Table 4.1). The shortening reaches 6% near the Urica Fault (M1 seismic line) and toward the east, it decreases to 3% (M5 seismic line).

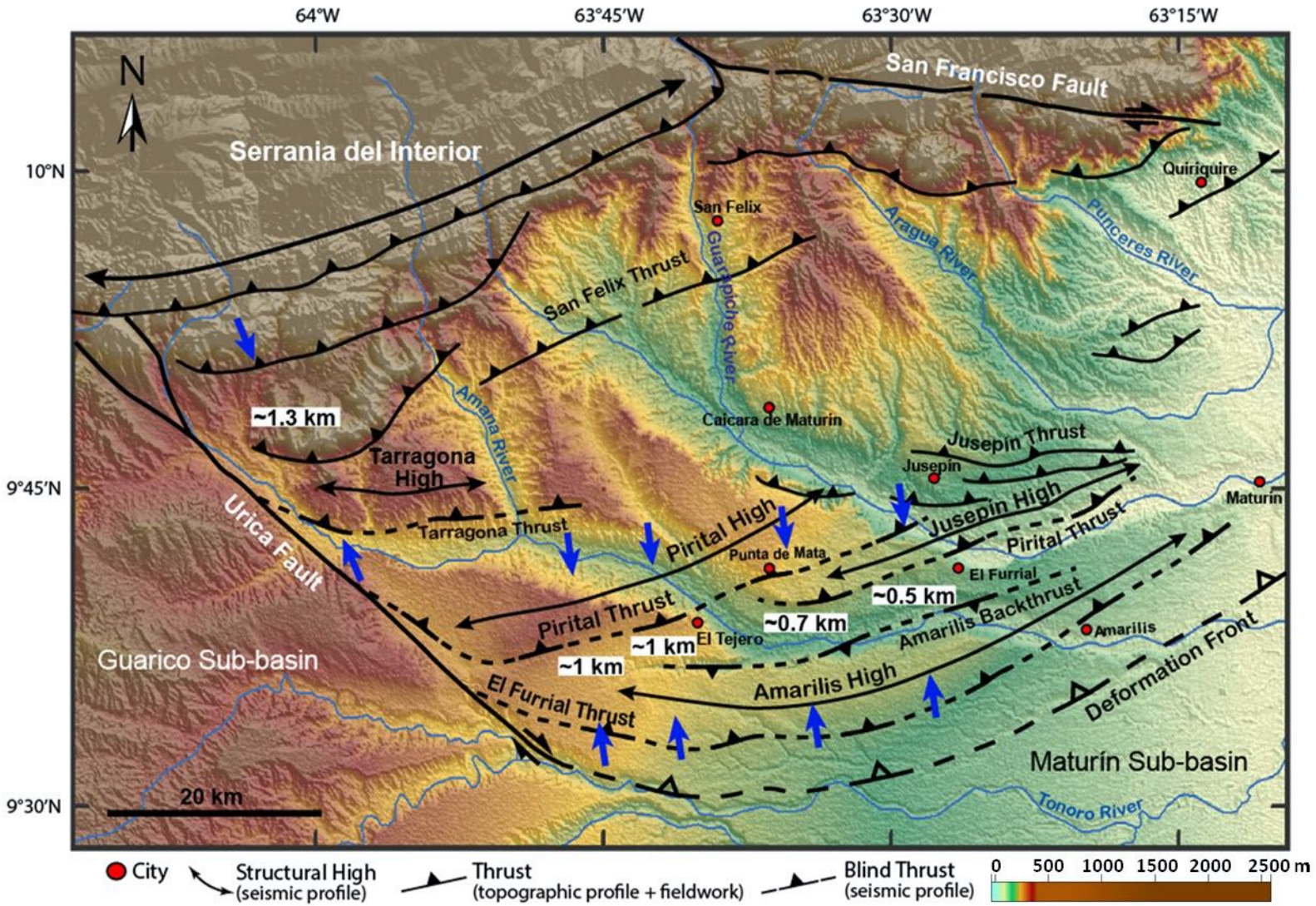

Figure 4.25. DEM image of the MFTB showing the thrusts and structural highs interpreted (from seismic lines, fieldwork and DEM image) and the shortening in km. calculated in this study from the Plio-Pleistocene units.

Table 4.1. Shortening percentage of Plio-Pleistocene units with respect to seismic line length.

Seismic line	Shortening (km)	Seismic line length (km)	Shortening (%)
M1	1.3	22	6
M2	1.0	20	5
M3	1.0	20	5
M4	0.7	20	4
M5	0.5	20	3

Uplift Rates in Plio-Pleistocene Units

Based on seismic lines interpreted in this work, we estimate the uplift rates in the Plio-Pleistocene units using the LMU geometry (Figure 4.26). For this purpose, we assume that 5.3 My ago, the LMU was sub-horizontal. The uplift rate is then an average for the last 5.3 My. Then, this uplift rate can be compared to the uplift rate obtained from cosmogenic nuclides data.

As seen above, the uplift is mainly caused by the activity of the Tarragona, Pirital and Furrial thrusts and the Amarilis Backthrust.

Along the M1 seismic line, the LMU is folded and eroded to the north (Figure 4.8). Assuming the extension of the eroded part, a vertical offset of ~1.5 km is estimated. This yields an uplift rate of ~0.3 mm/y.

Along the M2 and M3 seismic lines, the LMU horizon is deeper to the south than to the north (Figure 4.9 and Figure 4.10). The offset between the LMU horizons is related to the Pirital Thrust which is dipping to the north. The vertical offset for M2 is of ~1.9 km which yields an uplift rate of ~0.4 mm/y. For M3, a vertical offset of 1.7 km is estimated yielding an uplift rate of ~0.3 mm/y.

Along the M4 line, the LMU was folded and partly eroded to the north of the cross section (Figure 4.11). The vertical offset observed is ~1.6 km which yields an uplift rate of 0.3 mm/y.

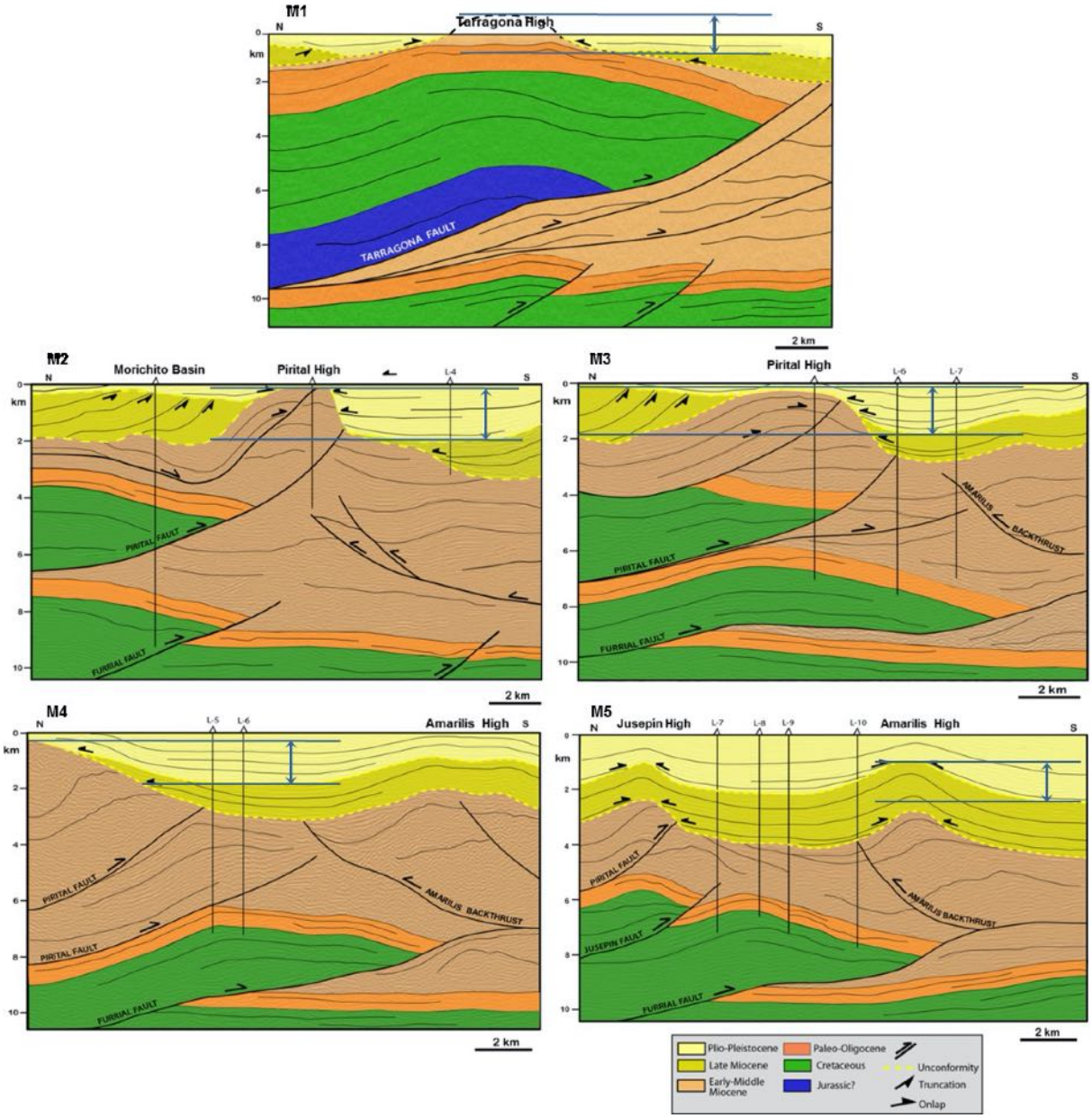

Figure 4.26. Seismic lines. Horizontal blue lines show the vertical offset estimated for the LMU to calculate the post-LMU uplift rates.

Along the M5 line, the LMU and MMU are equally folded, suggesting that most of the folding to the south took place after the LMU. The estimated vertical offset is ~1.5 km, yielding an uplift rate of ~0.3 mm/y (Table 4.2).

Table 4.2. Uplift rates calculated in Plio-Pleistocene units from seismic lines interpretation.

Seismic line	LMU vertical offset (km)	LMU age (My)	Uplift rate (mm/y)
M1	1.5 ±	5.3	~0.3
M2	1.9 ±	5.3	~0.4
M3	1.7 ±	5.3	~0.3
M4	1.6 ±	5.3	~0.3
M5	1.5 ±	5.3	~0.3

The Figure 4.27 shows the shortening ratio and the uplift rate in the Plio-Pleistocene units with respect to the distance between the seismic line and the Urica Fault. The uplift rate is in general constant (~0.3 mm/y), except in the M2 line where the uplift rate is slightly higher (0.4 mm/y). This is because in this line the greatest expression of the Pirital High can be observed and therefore the higher vertical offset of the LMU. An average Plio-Pleistocene uplift rate ≤ 0.4 mm/y for the last 5 My is estimated in the MFTB. In contrast, the shortening is higher to the west (6%) and to the east decreases as it becomes more distant from the Urica Fault (3%). This suggests a close relation between the neotectonics of the MFTB and the Urica Fault activity. This aspect will be developed in the CHAPTER 6.

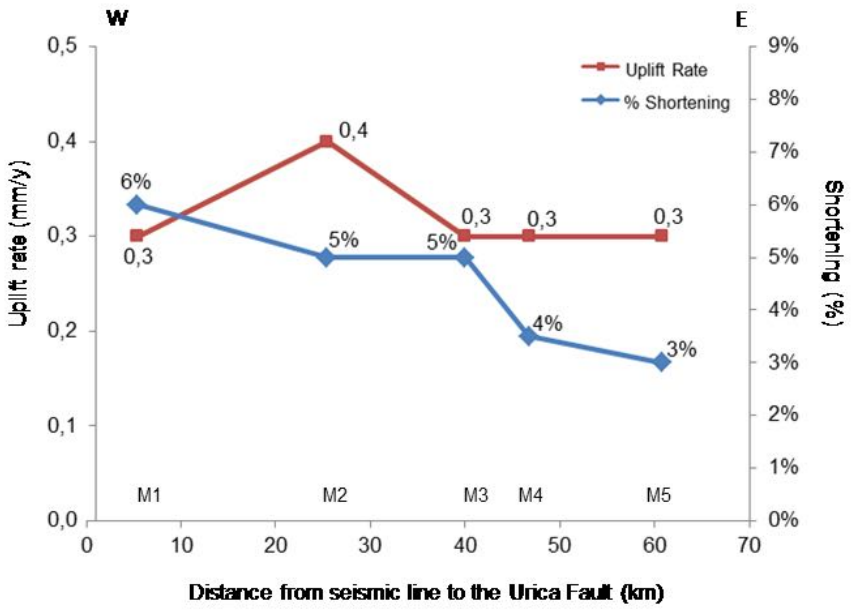

Figure 4.27. Shortening and uplift rate calculated in the Plio-Pleistocene unit of the MFTB.

Shortening and Uplift Rate Analysis

The analysis of 2D seismic line M1 and 3D seismic lines provides additional information for the understanding of the neotectonics in the MFTB. In particular, the deformation sequence

and the post-LMU shortening ratio suggest that the Urica Fault is playing a role in the location of the active tectonics. The post-LMU deformation is stronger near the Urica Fault with a significant attenuation as it becomes more distant from this fault. The post-LMU shortening ratio decreases from NW (6%) to SE (3%) (Figure 4.28).

The post-LMU uplift rate on the order of 0.3 mm/y is comparable to the vertical deformation rate derived from cosmogenic nuclides data within the statistical uncertainty (see CHAPTER 3). In the general discussion (CHAPTER 6), we will develop a conceptual model to explain the role of the Urica Fault.

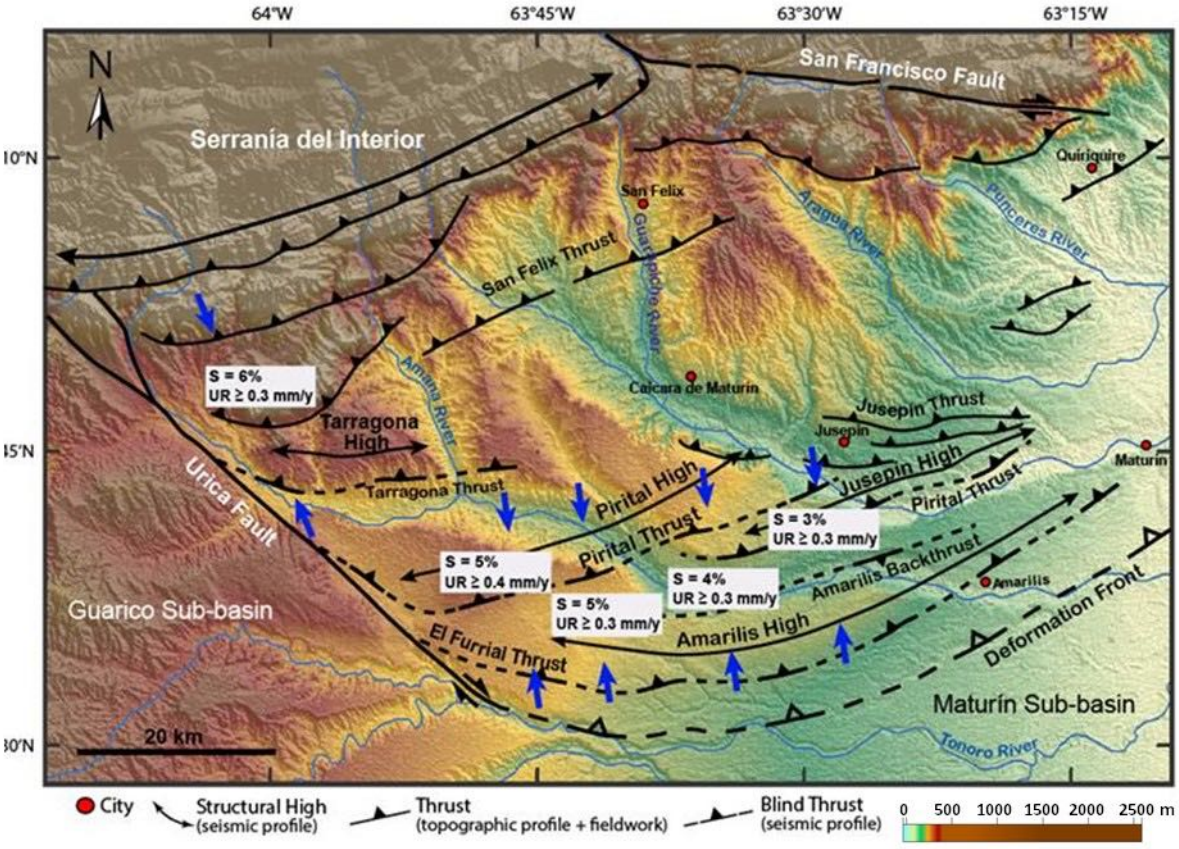

Figure 4.28. DEM image of the MFTB showing the thrusts and structural highs interpreted in this study from the seismic lines, fieldwork and DEM image. Shortening (S) and uplift rate (UR) calculated in the Plio-Pleistocene units from seismic lines.

CHAPTER 5. PALEOMAGNETISM IN THE SERRANÍA DEL INTERIOR

5.1. Introduction

Almost all rocks have the ability to record the characteristics of the magnetic field existing at the time of their formation or later. This has made the study of the history of the Earth's magnetic field called paleomagnetism, possible.

On the other hand, reading the recorded fossil magnetism in rocks sheds light on the structural and tectonic evolution and makes the study of the magnetic field variation in terms of intensity and direction, possible.

In the Serranía Del Interior, we use paleomagnetism to detect block rotation along vertical axes. In this area, the large scale strike-slip faults (El Pilar, San Francisco and Urica faults) delineate compartments, where block rotations are likely. In fault and thrust belts, the blocks rotation is generally related to a strike-slip fault regime. Here, some conceptual models of block rotation in dextral strike-slip regime are briefly described (Figure 5.2). The most common model is the "domino-style" system. The domino-shape blocks are compartmentalized and are delineated by sinistral strike-slip faults. Block rotation here is clockwise (Figure 5.1a). At the outcrop scale, "domino blocks" can be observed as for example at site 7Vz (Figure 5.1b). The domino model has been widely used in Betic-Rif Arc, (Platt et al., 2003), San Andres fault, north of Anatolian fault (Piper et al., 1997), among others (e.g. Ron et al., 1984). However, this model assumes a rigid block and implies the development of extensional and compressional areas which were not observed in the field.

Instead of rigid "domino-shaped blocks" with homogenous size (Figure 5.2a) Mckenzie & Jackson (1983) proposed a model of heterogeneous blocks (Figure 5.2b). This model has been successively applied along the San Andres Fault. The magnitude of block rotation is variable between each block.

Authors such as Geissman (1984) emphasize mechanisms which might explain the lack of significant rotation in the case of a strike-slip regime. They propose a partitioning model where only lateral displacement of blocks accommodated the strike-slip movement (Figure 5.2c). Finally, Garfunkel (1989) proposes that counterclockwise block rotation might occur if "Riedel" faults are developed (Figure 5.2d).

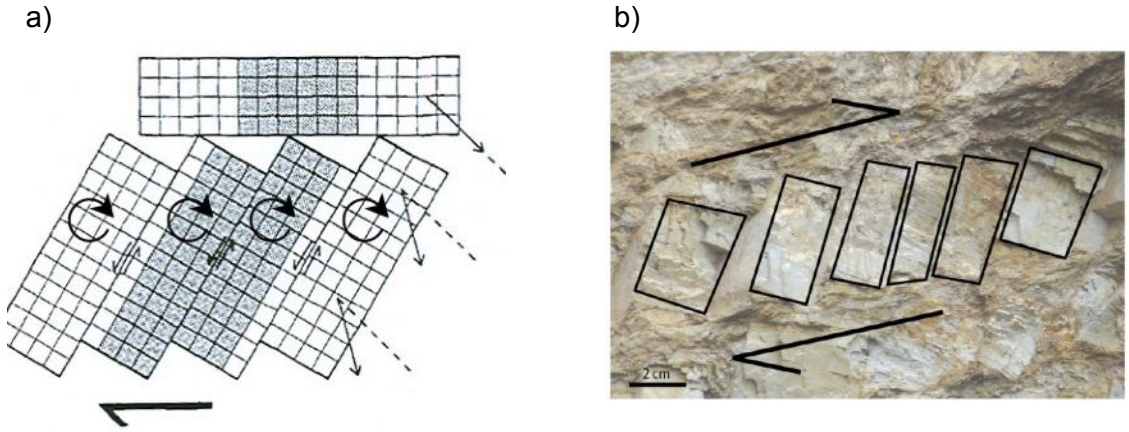

Figure 5.1. Block rotation model on a shear zone (dextral strike-slip fault) with “domino” effect. (a) Conceptual model according to Nelson and Jones, 1987 (b) Picture taken in site 7Vz in the Serranía Del Interior showing domino model at centimeter scale.

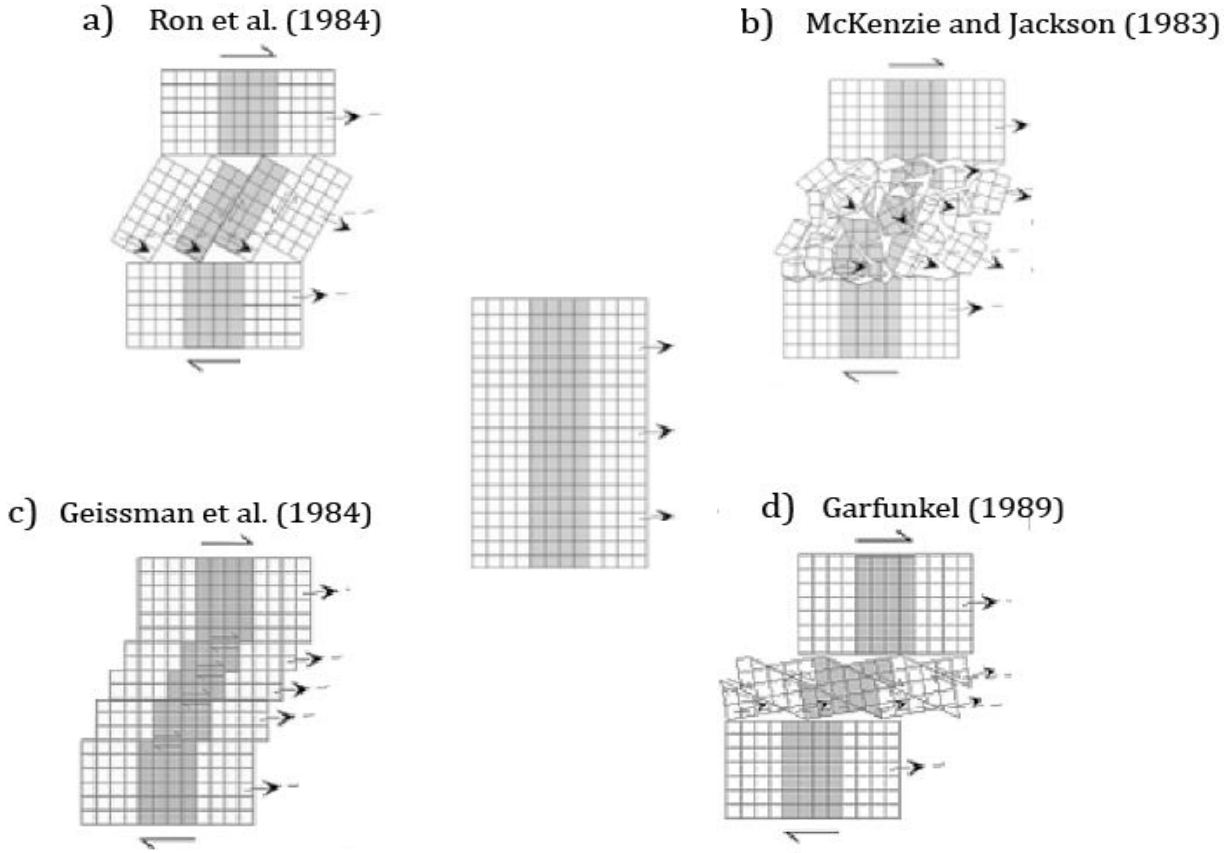

Figure 5.2. Conceptual blocks rotation models on a shear zone in a strike-slip fault.

From this enumeration of different systems, it appears that the size of blocks, the identification of strike-slip faults, and the possible strain partitioning are critical to understanding the block rotation. Canerot et al. (2005), among many others, proposed a conceptual strain model with strain partitioning and strain distribution (Figure 5.3). In this case, the fault-parallel component of the strain is accommodated through movement of the main strike-slip fault. The fault-normal component is absorbed by the blocks producing folds

whose axes would be parallel to the wrench fault (Figure 5.3a). However, it is possible that strain is distributed on the entire area (blocks and on either side of the strike-slip fault), leading to oblique folds with respect to the wrenching fault (Figure 5.3b). Oblique folds with respect to the orientation of the wrenching system are then an additional observation for the understanding of block rotations.

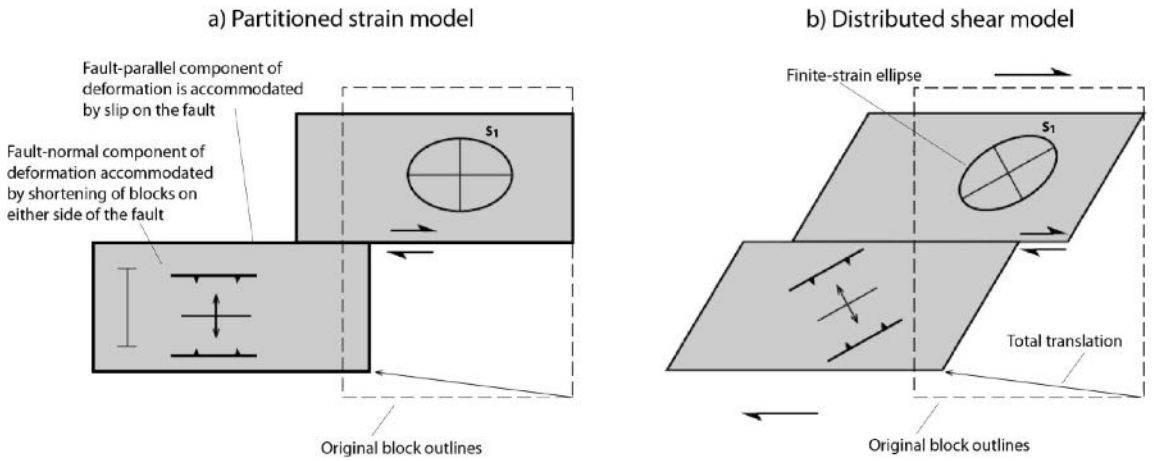

Figure 5.3. Models of a strike-slip system in transpression a) Partitioned strain model. The orientation of the finite-strain ellipse in blocks remains constant due to the strain partitioning. b) Distributed shear model. In this case, the finite-strain ellipse rotates through time due to the strain distributed on the whole area (modified from Canerot et al., 2005).

The location of sites with respect to the faults is also of importance. At the tip end of a strike-slip fault where thrusting is commonly observed, Cunningham et al. (2003) proposed a model where rotation is expected, for example counterclokwise in the example shown in Figure 5.4. In this model, the shortening along the strike increases near the fault (S_A) and dicreases as it becomes more distant from the strike-slip fault (S_B).

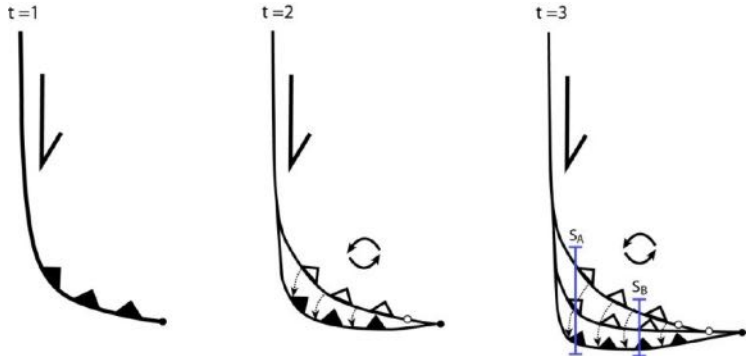

Figure 5.4. Block rotations at the termination zones for dextral strike-slip faults through time (t=1 to t=3). Terminal thrust propagation is in direction of strike-slip displacement which causes counterclockwise rotation of thrust block. Note that the magnitude of the shortening is greater near the strike-slip fault (S_A) and lower as it becomes more distant from the fault (S_B) (modified from Cunningham, 2003).

5.2. Basic Elements of Paleomagnetism

Following, the basic concepts useful to understand the paleomagnetism are presented. The reader is invited, however, to consult classical manuals for further information on this technique.

5.2.1. Geomagnetism

Earth's Magnetic Field (EMF)

The EMF can be of external or internal origin. The magnetic field of external origin is created by solar wind that produces a stream of electrically charged particles emitted by the sun (Lowrie, 2007). The magnetic field of internal origin (of interest to paleomagnetists) is generated by convection currents in the outer liquid core of the Earth composed of iron, nickel and unknown lighter components. The energy produced by this convection is probably due to cooling of the core and to the buoyancy of the iron/nickel outer liquid core caused by freezing out of the inner pure iron core (Tauxe, 2009).

The EMF is a vector defined by magnitude (intensity) and direction. The intensity is measured in units named tesla (T) and its maximum intensity is reached near the magnetic poles. The intensity of EMF is about ~10^{-5} T (Lowrie, 2007).

The direction of the geomagnetic field vector H on the Earth surface is decomposed in several components (Figure 5.5). The vertical component $\mathrm{H_v}$ is defined as positive downward given by Eq. 5.1.

$$\mathrm{H_v} = \mathrm{H'} \sin \mathrm{I}\, \mathrm{H_v} = \mathrm{H'} \sin \mathrm{I} \tag{5.1}$$

where, $\mathrm{H'}$ is the magnitude of H and I is the inclination defined as the angle of H from the horizontal. I varies from -90° to +90°.

The horizontal component $\mathrm{H_h}$ is given by Eq. 5.2.

$$\mathrm{H_h} = \mathrm{H'} \cos \mathrm{I} \tag{5.2}$$

$\mathrm{H_h}$ is a combination of North and East components, given by Eq. 5.3 and 5.4 respectively.

$$\mathrm{H_N} = \mathrm{H'} \cos \mathrm{I} \cos \mathrm{D} \tag{5.3}$$

$$H_E = H' \cos I \sin D \tag{5.4}$$

where, D is the declination, defined as the angle between the geographic north and the magnetic north (Figure 5.5). This angle varies from 0° to 360°, with positive clockwise movement.

The parameters I and D describe the geomagnetic field direction.

If the components are known, the total intensity field is expressed by Eq. 5.5.

$$H = \sqrt{H_N^2 + H_E^2 + H_V^2} \tag{5.5}$$

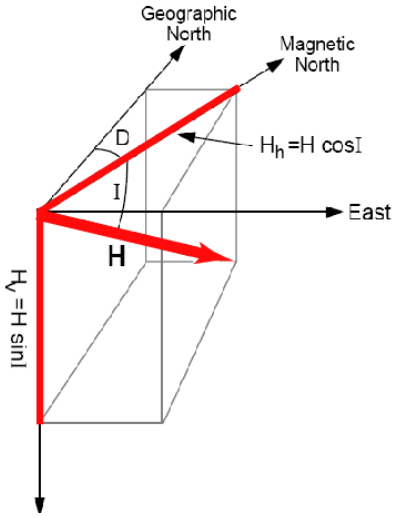

Figure 5.5. Description of the magnetic field direction. The total magnetic field vector H can be broken into (1) a vertical component, $Hv=H\ sinI$ and (2) a horizontal component, $Hh=HcosI$; inclination (I) is the vertical angle (=dip) between the horizontal and H; declination (D) is the azimuthal angle between the horizontal component of $H(=Hh)$ and the geographic north; the component of the magnetic field in the geographic north direction is $HcosIcosD$; the east component is $HcosIsinD$ (modified from Butler, 1998).

Geocentric Axial Dipole (GAD) Model

A large portion of the EMF (~90%) is a dipole with its axis slightly oblique to the Earth's rotation axis. The present geomagnetic field polarity is normal (the North magnetic pole is located near the South geographic pole) but this can change to reverse polarity (the North magnetic pole is located near the North geographic pole) (Lowrie, 2007). It has been demonstrated that the dipole nature of EMF was true for a geological time. When averaging out the secular variation (~2 ka), the dipole is aligned to the Earth's rotation axis. This is the

Geocentric Axial Dipole (GAD).

A model consist of placing with a single magnetic dipole (M) aligned with the rotation axis in the center of the Earth (Figure 5.6) and is defined by several properties expressed in Eq. 5.6, 5.7 and 5.8 respectively.

$$H_h = \frac{M\cos\lambda}{r_e^3} \tag{5.6}$$

$$H_v = \frac{2M\sin\lambda}{r_e^3} \tag{5.7}$$

$$H = \frac{M}{r_e^3}\sqrt{1 + 3\sin^2\lambda} \tag{5.8}$$

The geographic latitude λ ranges from -90° at the south geographic pole to +90° at the north geographic pole; the mean Earth radius is r_e, the magnetic field directions at the Earth's surface produced by the geocentric axial dipole are represented as arrows where the lengths show the increase in the magnetic field strength from equator to poles (Figure 5.6). The inclination of the field can be defined by Eq. 5.9.

$$\tan I = \left(\frac{H_v}{H_h}\right) = \left(\frac{2\sin\lambda}{\cos\lambda}\right) = 2\tan\lambda \tag{5.9}$$

H_v and H_h are the vertical and horizontal components of the magnetic field, respectively. D is zero everywhere for a geocentric axial dipole. The Inclination (I) increases from -90° at the geographic South Pole to +90° at the geographic North Pole. The lines of latitude (λ) are parallel to the lines of equal inclination (I), for that reason, the relation between them is basic to understand many of the tectonic and paleogeographic applications of the paleomagnetism.

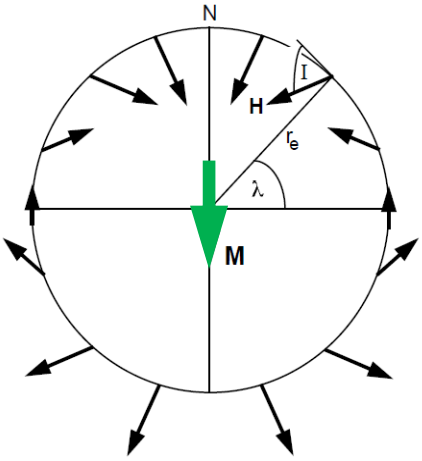

Figure 5.6. Geocentric axial dipole model (modified from Butler, 1998)

Apparent Polar Wander Paths (APWP)

The APWP is a time sequence of the paleomagnetic poles that records the tectonic plate orientations from a particular continent assuming a dipolar geomagnetic field (Irving, 1979). A paleomagnetic poles set of different geologic ages are represented in a single diagram. The paleomagnetic poles for the Neogene are located near the present geographic pole and for older geologic times, are generally located on a circuitous path away from the geographic pole (Butler, 2004).

The major portion of apparent polar wander is due to lithospheric plate movements carrying continents over the Earth's surface. Plotting this movement is useful for knowing the velocities, directions and kinematics of the plates through time (May and Butler, 1986) (Figure 5.7).

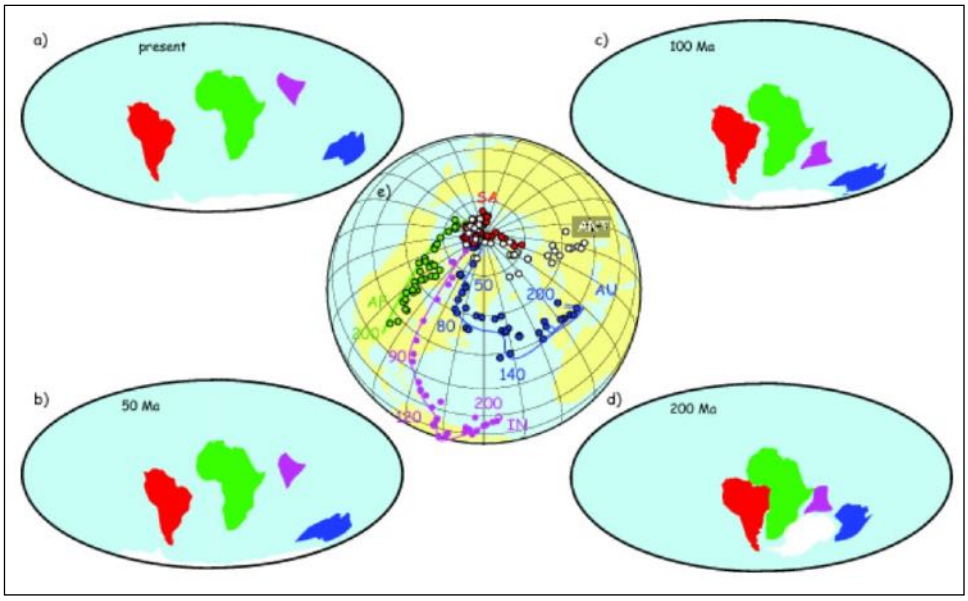

Figure 5.7. Map of continental reconstruction a) Present, b) 50 Ma. c) 100 Ma. d) 200 Ma. e) Poles and APWP for various continents for the last 200 Ma. Paleomagnetic poles from the synthetic APWP constructed by Besse & Courtillot (2002) (modified from Tauxe, 2014).

The APWP for South America shows very little polar wander. The continent has basically remained in the same position with respect to the geographic poles in the last 200 My and most poles have latitudes higher than 80°. Nevertheless, the path shows several features, such as a track from 200 to 180 My, a change in direction near 180 My, a some movement from 180 to 130-140 My and from 50 My to the present, but basically has not had any polar wandering (Besse & Courtillot, 2002) (Figure 5.8).

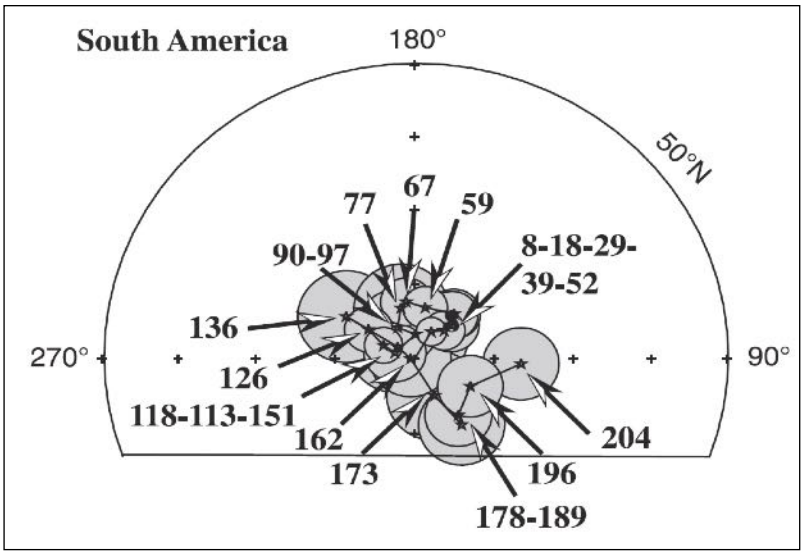

Figure 5.8. South American synthetic APWPs. Each pole corresponds to a mean pole computed using a 20 My sliding window. Equal-area projection. Ages are in Ma; the values shown are the current mean ages derived from the data in the appropriate window (modified from Besse & Courtillot, 2002).

5.2.2. Rock Magnetization

The magnetism can be explained as a pair of magnetic charges generating a magnetic dipole moment defined as magnetic moment M, according to Eq. 5.10.

$$\mathrm{M} = \mathrm{m}\,\mathrm{l} \tag{5.10}$$

where, m is the magnitude of the charge of both magnetic charges and l is the infinitesimal distance vector separating the positive and negative charges.

The magnetic moment in a magnetic field cannot be measured directly, but it is possible to measure the alignment torque Γ on a magnetic dipole moment in the magnetic field, given by Eq. 5.11.

$$[\Gamma] = [\mathrm{M}\,\mathrm{x}\,\mathrm{H}] = \mathrm{MH}\sin\theta\hat{\Gamma} \tag{5.11}$$

where H is the magnetic field, θ is the angle between M and H, $\hat{\Gamma}$ is the unit vector parallel to Γ.

A magnetic moment aligns with the magnetic field in the same way that the compass aligns with the horizontal component of the geomagnetic field resulting in magnetic azimuth or magnetic North.

The magnetization J is the net magnetic moment per unit volume. Magnetization of a material with a particular volume is calculated by the sum vector of magnetic moments divided by the volume of material containing magnetic moments, expressed in Eq. 5.12

$$\vec{J} = \frac{\sum_i \overrightarrow{M_i}}{\text{volume}} \tag{5.12}$$

where, M_i is the constituent magnetic moment.

The magnetization can be induced or remanent. When a material is exposed to a magnetic field H, it acquires an induced magnetization J_i, which is related to H through the magnetic susceptibility χ of the material, expressed in Eq. 5.13.

$$\overrightarrow{J_I} = \chi \overrightarrow{H} \tag{5.13}$$

χ is the capability of the substance to magnetize. Moreover, a material submitted to an induced magnetization by present magnetic fields may also have a remanent magnetization, J_r, produced by ancient magnetic fields that acted on the material and were recorded, too.

5.2.3. Magnetic Minerals

In a paleomagnetic study is important to know how the magnetic remanent was imprinted in the rock and when the rock acquired the magnetization.

The influence of a magnetic field on a mineral produces magnetic behavior that can be distinguished on the basis of magnetic susceptibility such as: diamagnetism, paramagnetism, ferromagnetism (Figure 5.9). In diamagnetic materials, the susceptibility is negative and small due to the induced magnetization that develops in an direction opposite to the applied magnetic field (Figure 5.9a). Diamagnetism is universal, and all minerals have a diamagnetic component. Paramagnetic materials have a positive and low susceptibility due to induced magnetization in the same direction to the applied magnetic field (Figure 5.9b). Finally, ferromagnetic materials are characterized by high positive susceptibilities and a remanent magnetization J_r (Lowrie, 2007; Tauxe, 2014) (Figure 5.9c).

When a ferromagnetic mineral is submitted to a magnetic field, it acquires a resulting magnetization constituted by two components: the induced magnetization and the remanent magnetization. The induced magnetization (J_s) is generated by the applied magnetic field at saturation and removed when the field is reduced to zero. The remanent magnetization or

remanence (J_r) is the residual magnetization remaining in the absence of a magnetic field (Figure 5.9c).

In ferromagnetism (lato sensu) the atomic magnetic moments react in unison with the magnetic field producing strong magnetic behavior (Lowrie, 2007). Also, in this kind of materials electronic interactions occur between neighboring spins which allow the magnetization to persist in the absence of an applied field giving rise to remanent magnetization. The remanent magnetization can be present in a mineral below the Curie temperature, which depends on the mineral considered (Lowrie, 2007).

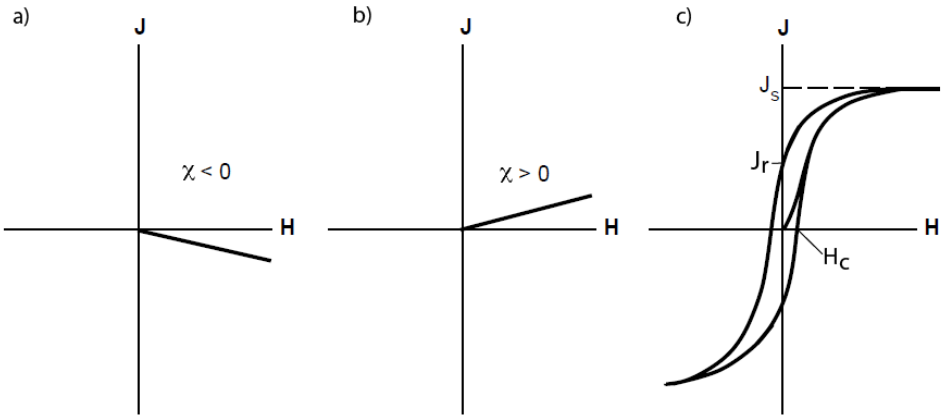

Figure 5.9. Magnetic behaviors. Magnetization J vs. magnetic field H. χ is the susceptibility ; $\mathbf{J_s}$ the magnetization at saturation; J_r is the remanent magnetization and H_c (bulk coercitive force) is the opposite magnetic field to drive J back to zero (modified from Butler, 1998).

According to the spin arrangements, ferromagnetism (lato sensu) can be: antiferromagnetism or ferrimagnetism. In ferromagnetism all the spins are parallel. In antiferromagnetism the spins are antiparallel. In ferrimagnetism the spins are of a different magnitude at antiparallel (Figure 5.10).

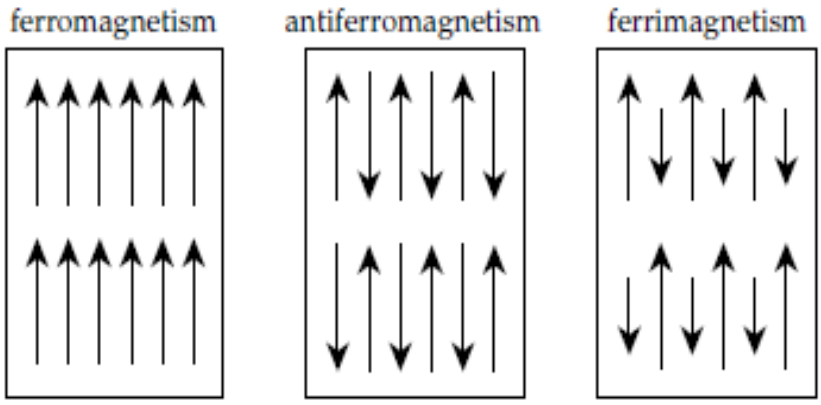

Figure 5.10. Exchange couplings for (a) ferromagnetic, (b) antiferromagnetic, and (**c**) ferromagnetic materials. The net magnetization for ferromagnetic material is shown at right; the net magnetization of antiferromagnetic material is zero (modified after Lowrie, 2007).

The most common magnetic minerals present in sedimentary rocks and the Curie or Néel temperature associated with each are shown in Table 5.1.

Table 5.1. Magnetic minerals in sediments and its transition temperatures (Modified from Tauxe, 2014).

Magnetic Mineral	Temperature
Magnetite (Fe_3O_4)	Curie temperature = 580°C Dunlop and Özdemir (1997)
Maghemite (γFe_2O_3)	Curie temperature = 590-675°C Dunlop and Özdemir (1997)
Hematite (αFe_2O_3)	Néel temperature = 675°C O'Reilly (1994)
Goethite (αFeOOH)	Néel temperature: 70 → 125°C O'Reilly (1994)
Pyrrhotite (Fe_7S_8)	Curie temperature = ~270-325°C Dekkers (1988 – 1989)
Greigite (Fe_3S_4)	Max. unblocking temperature = ~330°C Roberts (1995)

5.2.4. NRM in Sedimentary Rocks

The Natural Remanent Magnetization (NRM) is controlled by the geomagnetic field, which is present from the formation time of the rock until the present day. In sedimentary rocks, the NRM is a combination of several components acquired during the processes occurred in the history of the rock.

The component acquired during the rock formation process is called "primary NRM" and the component acquired during processes after rock formation is referred to as "secondary NRM". This secondary component can over impose partially or completely the primary NRM (Table 5.2). The total NRM is expressed by:

$$\text{NRM} = \text{primary NRM} + \text{secondary NRM}$$

Processes of Remanence Acquisition in Sedimentary Rocks

Following, the description of the main mechanisms of remanence acquisition in sedimentary rocks (Table 5.2).

Table 5.2. Different types of NRM and associated processes (Modified from Kars, 2012)

Type of NRM	Process
Detrital Remanent Magnetization (DRM)	Deposition of magnetic grains
Chemical Remanent Magnetization (CRM)	Growth (alteration) of magnetic grains
Viscous Remanent Magnetization (VRM)	Long-term time exposure to magnetic field.
Thermoviscous Remanent magnetization (TVRM)	Combination of moderate heating below Curie or Néel temperature and time exposure
Isothermal Remanent Magnetization (IRM)	Lightning strikes, exposure to large magnetic field

Detrital Remanent Magnetization (DRM): In sedimentary rocks, the primary NRM is generally related to DRM. This is acquired during deposition, accumulation and lithification of sedimentary rocks containing detrital ferromagnetic minerals (Butler, 2004). DRM is of considerable importance, as it is synchronous with sediment deposition. For that reason, DRM is used for dating sediments (magnetostratigraphy). Generally, the dominant detrital ferromagnetic mineral is magnetite. However, it has been known for two decades that anoxic and euxinic environments contribute to alteration and dissolution of iron oxides due to bacterial activity (e.g. Roberts et al., 2012). For depth < 200 m, formation of greigite (Fe_3S_4) might add an additional component to the putative DRM, but it can be still considered as a 'primary' NRM.

DRM can be a very complex process because the physicochemical conditions vary during sedimentation. The ferromagnetic grain will align with the magnetic field direction during deposition but the viscosity of water and inertia of the grain will disrupt the orientation. Other important parameters that control or change the DRM magnetization direction are the grain size (coarse grains result in a more chaotic magnetization), the nature of the current (turbulent or laminar) and the salinity of the water (Figure 5.11)

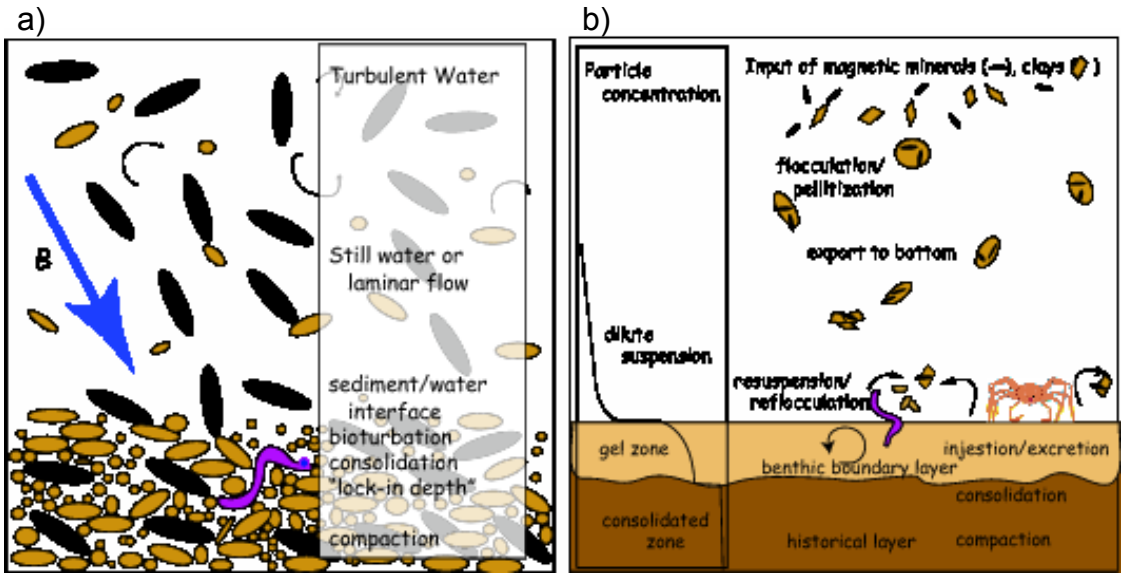

Figure 5.11. Representation of physicochemical processes affecting the deposition of sedimentary particles and their magnetization. (a) freshwater environment (b) marine environment (from Tauxe, 2014).

Chemical Remanent Magnetization (CRM): CRM is acquired during chemical changes in a magnetizing field that produce the growth of ferromagnetic grains below the Curie temperature. This process is very common in sedimentary rocks from fold and thrust belt (e.g. Cairanne, 2003). CRM is responsible for partial to total overprint of the primary NRM (e.g. Kars et al., 2012). Some pervasive remagnetization is identified worldwide such as those occurring during the long 40 My reverse Permian chrome (named as Kiaman overprint) or the long normal chrome during the Cretaceous. There is considerable work about the CRM and extensive remagnetization (Stacey & Banerjee, 1974; Thellier, 1976; O'Reilly, 1984; Dunlop & Özdemir, 1997). To explain the pervasive nature of remagnetization in claystone rocks, Aubourg et al. (2012) proposed that magnetic minerals formed all along the burial processes relating to this model. In the Serranía Del Interior, rocks are essentially unmetamorphosed except in some localities where pencil cleavage is observed. In this context, and sticking to the model of Aubourg et al. (2012), a CRM carried by neoformed magnetite is possible (Figure 5.12).

Viscous Remanent Magnetization (VRM): VRM is acquired during long exposure of the rock to the action of a geomagnetic field. This is typically recorded between present day and 0.78 Ma; which correspond to the Bruhnes normal chrone. This VRM is generally associated with coarse magnetic minerals, and by extension, with coarse sediments (sandstones to conglomerates). Also, VRM can be related to ultra-fine magnetic minerals that are in superparamagnetic state (SP). Generally this magnetization is undesirable noise. (Butler, 2004)

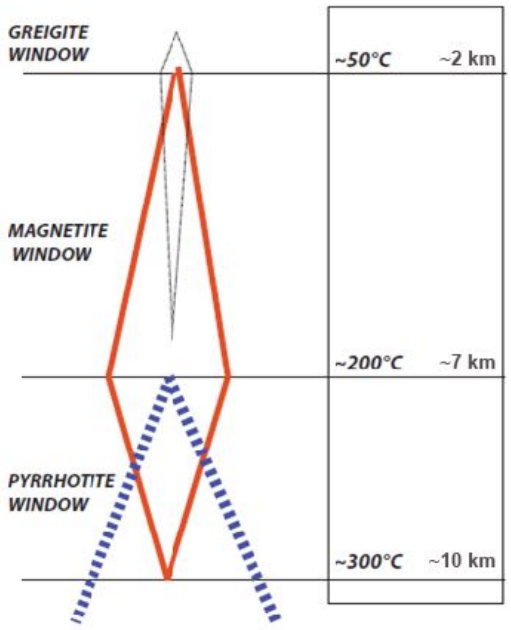

Figure 5.12. Burial models for the formation of magnetic mineral claystones. The central box represents a sedimentary column from the surface to 10 km deep. On the left, the concentration of neoformed magnetic mineral is indicated. Burial temperature is calculated using a thermal gradient of 30°/km (modified from Aubourg et al., 2012).

Thermoviscous Remanent Magnetization (TVRM): TVRM is also a predominant secondary component in sediments. TVRM is acquired by exposure of the rock to elevated temperatures and for long periods of time as occurs during deep burial. In the laboratory, the rock must be heated in a zero field to high temperature for a period of time sufficient to erase this remanence (Tauxe, 2014). According to the laboratory experiment, the last grains that acquired the remanence are the last to be demagnetized, since they require higher temperatures to be removed (Kars, 2012).

Isothermal Remanent Magnetization (IRM): This is acquired during short-term exposure to strong magnetizing fields at constant temperature only if grains have a coercive force smaller than the applied field (Butler, 2004). In practice, this is triggered by lightning processes. A modest magnetic cleaning at 20 mT is generally sufficient to remove this component.

5.2.5. Magnetic Cleaning

The NRM is in essence the sum of several components. These components can be: low-stability or high-stability component. The high-stability component is commonly defined to as the Characteristic Remanent Magnetization (ChRM) which is inferred to be primary NRM. However, not always a ChRM is a primary NMR (Buttler, 2004). On the other hand, the low-

stability components are generally assumed as a secondary NRM which are easily removed by demagnetization technique. The low-stability components can hide the ChRM. The aim of making the magnetic cleaning using demagnetization procedures is erased the low-stability components and thus isolate the high-stability component (ChRM). To clean these up, the most common techniques are the AF demagnetization and the thermal demagnetization.

Alternating-Field Demagnetization Technique (AF)

AF technique consists of applying an AF oscillating magnetic field to the sample rock in a null magnetic field environment. Generally, waveform of the magnetic field applied is a sinusoid of frequency commonly of 400 Hz with a linear decrease in amplitude and in time (Butler, 2004) (Figure 5.13). The intensity of the alternative field applied is progressively higher until a maximum of 100 mT is reached, but sometimes total demagnetization is not achieved because some ferromagnetic minerals as hematite have a very high coercivity (goethite, hematite for example).

During the demagnetizing process, AF instruments rotate the samples in three directions in order to demagnetize in sequence all the axes during a single processing, using an apparatus called tumbler.

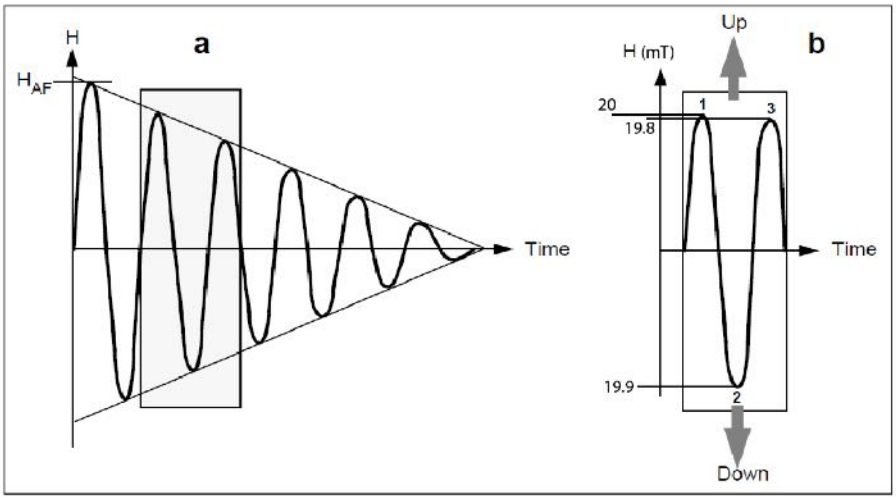

Figure 5.13. Schematic representation of alternating-field demagnetization. (a) Generalized waveform of magnetic field used in AF demagnetization showing magnetic field versus time. The maximum amplitude of the magnetic field (=peak field) is H_{AF}; the stippled region is amplified in part (b). (b) Detailed examination of a portion of the AF waveform. Two successive peaks and an intervening trough of the magnetic field are shown as a function of time; the peak field at point 1 is 20 mT; the peak field at point 2 is -19.9 mT; the peak field at point 3 is 19.8 mT. (modified from Butler, 2004).

Thermal Demagnetization Technique

Thermal demagnetization allows obtaining the relation between relaxation time and temperature of the grains in a rock. This technique involves heating samples to an elevated temperature below the Curie temperature and then these are cooled in a room to zero magnetic field to prevent samples acquiring a new magnetization during the process. After each heating-cooling step, the magnetization of the samples is measured. Each heating step can demagnetize the magnetic domains with blocking temperature lower than the temperature applied, separating various magnetizations components. Thermal demagnetization provides the unblocking range of temperature Tub where Tub≤TCurie/Néel. Tub is proportional to grain size.

Representation of the Paleomagnetic Data

Following, we explain the different graphs, diagrams, statistical methods and geological tests used for the interpretation of the paleomagnetic cleaning data.

Directional data is generally represented on a stereographic projection. Usually, this graphical representation uses the combination the two hemispheres. Black symbols are plotted in the lower hemisphere and represent normal polarity. Open symbols are plotted in the upper hemisphere, and represent reverse polarity.

To monitor the stepwise demagnetization and calculate the different components, it is useful make an orthogonal plot by combining horizontal and vertical planes. This plot is the Zijderveld diagram (Zijderveld, 1967) (Figure 5.14). This diagram is composed of two orthogonal planes, on which directional (inclination and declination) and intensity information are displayed. The NRM vector can be visualized projected on the plane due to the distance of each data point from the origin and is proportional to the intensity. The demagnetization process generates vectors that are decomposed into their north (N), east (E) and vertical (Down) components. When tracks converge to the origin, the magnetization is stable and it is labeled Characteristic Remanent Magnetization (ChRM). A ChRM is not necessarily a primary NRM.

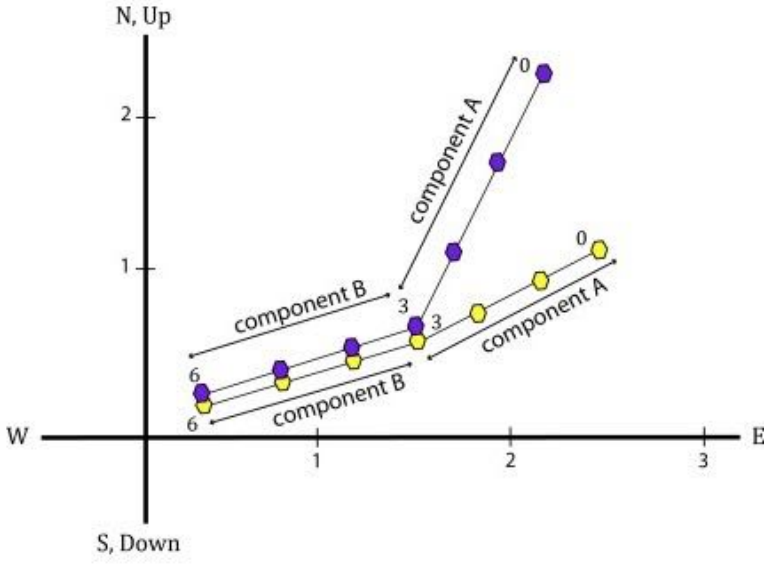

Figure 5.14. Construction of vector component diagram (Zijderveld diagram). Two components A and B are despicted. Component A is described by demagnetization levels of 0 to 3. Component B converges toward the origin, this is a ChRM, and it is described by demagnetization levels of 3 to 6. Yellow polygons indicate vector end points projected onto the horizontal plane; blue polygons indicate vector end points projected onto the vertical plane.

An additional step in the analysis of paleomagnetic data is to calculate the Fisher distribution (Fisher, 1953). This statistic method is a probability density function applicable to many paleomagnetic directional data sets, in order to evaluate the dispersion of unit vectors and calculate mean directions with confidence limits represented by points on a stereographic projection.

The confidence at 95% of the average vector obtained of Fisher distributions is represented by the angle α_{95} (confidence limit) that is a measure of the precision with which the true mean direction has been estimated. This angle represents a 95% probability that the unknown true mean direction lies within α_{95} of the calculated mean (Butler, 1998). α_{95} is given by Eq. 5.14.

$$\alpha_{95} = \frac{140^{\circ}}{\sqrt{KN}} \tag{5.14}$$

The average direction of each site is the average of the directions of each specimen measured. The average direction of each zone is the average directions of each site. The Fisher probability density is represented by Eq. 5.15.

$$P_{dA}(\theta) = \frac{K}{4\pi \sin h(k)} \exp(k \cos\theta) \tag{5.15}$$

where, θ is the angle between the unit vector and the true direction.

The precision parameter K is a measure of the distribution concentration around the true mean direction. The parameter K increases with the grouping of data. Thus, when the parameter K increases, the confidence angle α95 decreases (Figure 5.15).

- For each specimen, we display the components of the NRM obtained of the demagnetization processes onto a Zijderveld diagram and onto the stereographic Wulff projection (Figure 5.16).

- The demagnetization track is projected in Zijderveld diagrams in sample and in geographic direction. To obtain the NRM direction in-situ (geographic) from sample coordinates it is necessary to apply a bedding-tilt correction using the bedding attitude measured in the fieldwork (dip direction-dip).

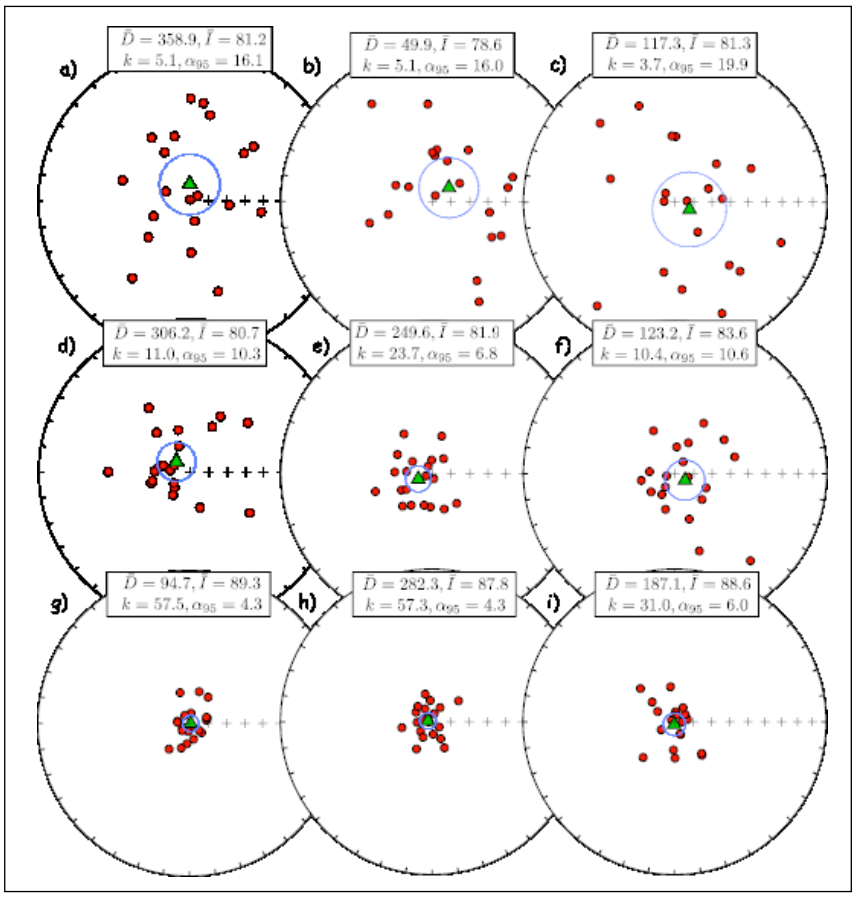

Figure 5.15. Fisher distribution examples with vertical true directions. K=5 (a-c), K=10 (d-f), K=50 (g-i) (from Tauxe, 2014).

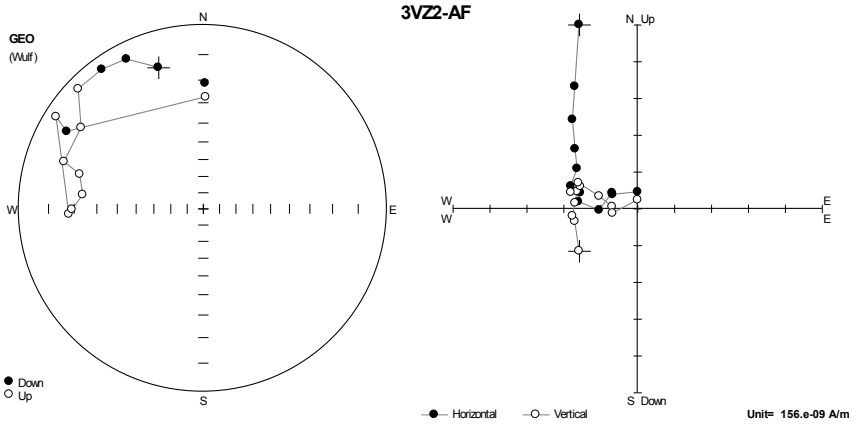

Figure 5.16. Example of AF demagnetization track for specimen 3Vz2 in the Serranía Del Interior. Two components are observed, the first and weaker one being parallel to the present day EMF and the second converging toward the origin. The latter is a ChRM.

5.2.6. The Bedding-Tilt Test

Graham (1949) first defined the use of the “fold test” to date magnetic poles direction using the fold geometry. Since then, considerable work has been done with this fold test.

In practice, it is rather rare to have samples in both limbs of one fold. And even if this sampling scheme is achieved; the way to untilt the fold remains debatable (e.g. Cairanne et al., 2002). The most common situation is to have several folds sampled, and hence, it is more reasonable to speak about a “bedding-tilt test”. At one locality, where only one correction of the bedding (along the strike) can be made, it is generally difficult to judge the scattering of the data. In this case, inclination and declination data must be examined to date the magnetization with respect to folding.

The classical bedding-tilt test consists of estimating the dispersion of the magnetization directions of a layer before and after bedding correction in order to determine the age of a particular set of directions (Figure 5.17). The bedding correction consists of transforming the sample coordinates to geographic coordinates using the strike and dip of the layer sampled and measured during fieldwork. The parameter that measures the dispersion of the paleomagnetic directions is called K. If the parameter K increases after bedding correction (more clustered data), it indicates that the magnetization was likely acquired before tilting, thus representing a positive fold test. If the parameter K decreases (less clustered data) this indicates that the magnetization was likely acquired after tilting, in this case, the test is negative (Tauxe, 1994; Cairanne, 2003; Sonnette, 2012) (Figure 5.18).

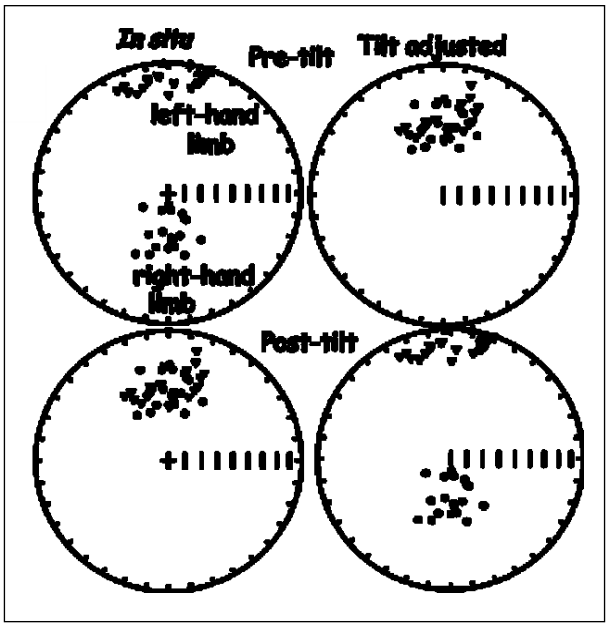

Figure 5.17. Representation of paleomagnetic directions before and after bedding-tilt correction. Top circles shows the case in which clustering of paleomagnetic directions is better after bedding correction indicating that the magnetization was likely acquired pre-folding. Lower circles shows better clustering before bedding correction (in-situ) representing a post-folding acquisition of magnetization.(from Tauxe, 1994)

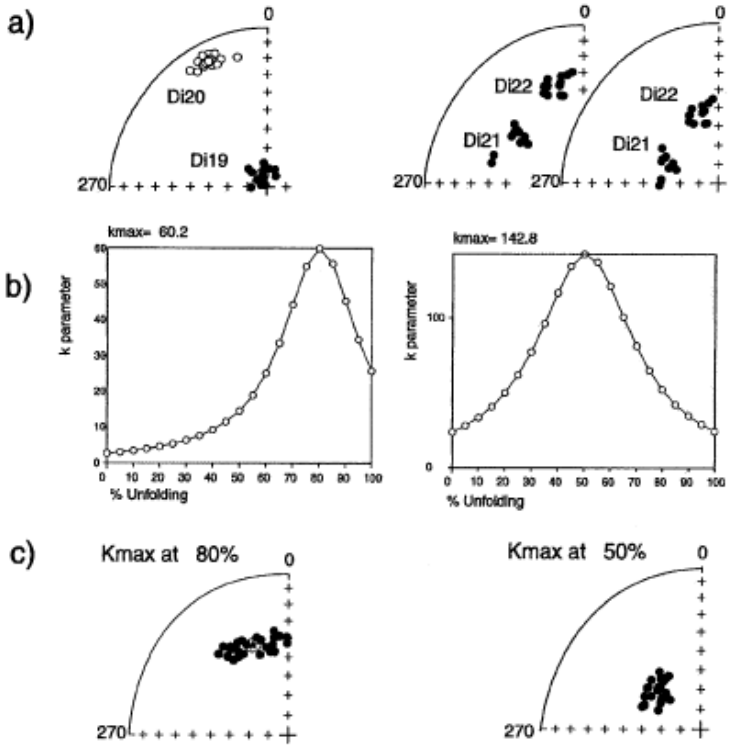

Figure 5.18. Evolution of the parameter K. a) Geographic coordinates. b) Graph of the evolution of the parameter K. c) Percentage of untilting (from Carainne et al., 2002).

Sometimes, the comparison between parameter K before and after bedding correction is not conclusive to determine when the magnetization was acquired. In that case, it is necessary to make the comparison with the expected paleomagnetic direction which will help to define if the magnetization was acquired before or after tilting.

In a fold-and-thrust belt, it is common to observe syn-tilting remagnetization (e.g. Lewchuk et al., 2002). Generally, the syn-tilting remagnetization is related to a short-term or long-term geological event. The short-term geological event is produced during folding and can be produced by orogenic and/or fluid circulation (Rouiver et al., 2012). The long-term geological term is related to burial process (Katz et al., 2000; Cairanne, 2003) (Figure 5.18).

5.2.7. Block Rotation

The paleomagnetism applied to crustal block movements is based on the determination of the calculation of latitudinal movements and rotations with respect to a paleomagnetic pole. The theory used to detect crustal block movements is illustrated in Figure 5.19 showing a meridional cross section of the Earth, which illustrates a paleomagnetic pole (PP), and the expected magnetic field inclinations (stippled arrows) that are located on the surface of the Earth. If a crustal block was magnetized an intermediate latitude and subsequently was moved (angular distance p) to a high latitude, the observed inclination of paleomagnetism in this crustal block will be less than the expected inclination at its new location. Thus, the movement towards a paleomagnetic pole (latitudinal movement) produces flattening of inclination shown by the angle (F) (Butler, 1998) (Figure 5.19a).

When a crustal block rotation occurs in the vertical axis within its boundary, it produced a little or no significant latitudinal movement. The vertical axis rotation produces a rotation angle (R) of the observed declination from the expected declination which originally would have pointed toward the paleomagnetic pole PP (Figure 5.19b).

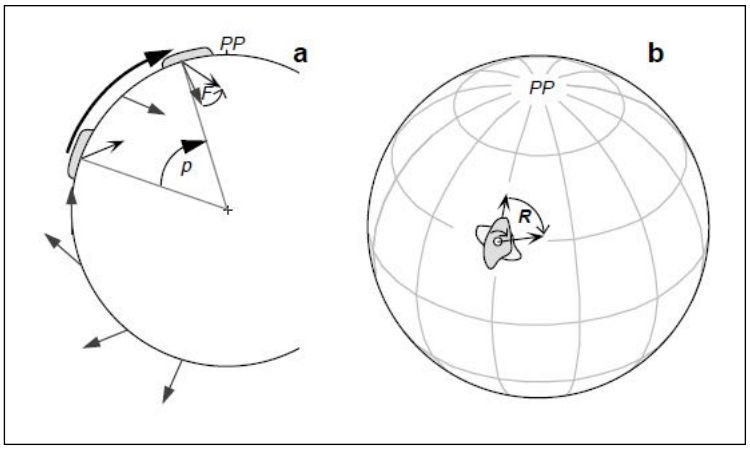

Figure 5.19. Paleomagnetic directions resulting from crustal rock movements due to tectonic movements. a) Meridional cross section. b) Rotation of the paleomagnetic declination by tectonic rotation about a vertical axis internal to the crustal block (from Butler, 2004).

To determine the vertical rotation, it is necessary to compare the paleomagnetic poles to the expected poles provided by APW curves.

Figure 5.20 illustrates the direction-space approach method (Beck et al., 1986) to calculate the movement of a block. The expected paleomagnetic direction (I_x, D_x) compared with the observed paleomagnetic direction (I_o, D_o) is calculated by Eq. 5.16 and 5.17.

$$F = I_x - I_o \tag{5.16}$$

$$R = D_o - D_x \tag{5.17}$$

where, F is the inclination flattening and R, is the rotation of the declination. R is positive if D_o is clockwise of D_x.

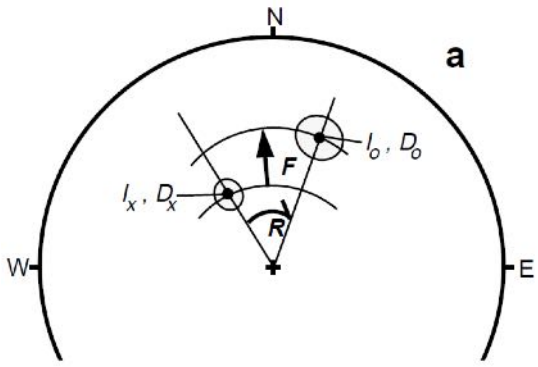

Figure 5.20. Direction-space analysis. Expected direction with inclination I_x and declination D_x compared to an observed paleomagnetic direction with inclination I_o and declination D_o. The observed declination is clockwise from the expected declination by the rotation angle R (from Butler, 2004).

5.3. Remagnetization in Fold and Thrust Belt

In sedimentary rocks, the primary NRM is considered of detritical origin (DRM). When the rock is submitted to other processes after formation, secondary NRM components known as remagnetization can be added to the NRM primary. During geological processes (e.g. the orogenesis), parameters such as temperature, time, sediment alteration, pressure, magnetic field and chemicals can remagnetized a rock at different times in its history. Figure 5.21 shows how the geomagnetic field record in the sediments is affected by these earth filters resulting in the current NRM.

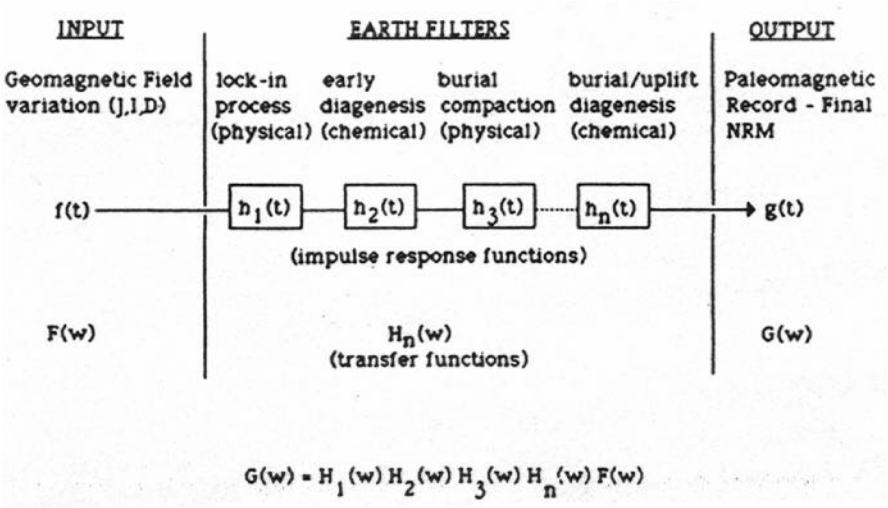

Figure 5.21. Scheme of NRM acquisition and subsequent changes in sedimentary rocks (from Lund & Karlin 1990)

The main secondary remanent magnetizations that sedimentary rocks may acquire during their history are VRM, TVRM, CRM and IRM. These can be acquired as a consequence of superficial alterations, karstification, lateritization and oxidation (Gehring and Heller, 1989; Keller and Gehring, 1992). Also, during the sedimentary processes as: slumping, bioturbation, dolomitization and diagenesis (Elmore et al., 1993; Xu et al., 1998). Following, the way in which each secondary NRM is related to the sedimentary rocks processes is described:

The long term exposure of a rock can gradually unlock the its magnetization of the rock and it can acquire VRM (Figure 5.22a). Also, the temperature increase unlocks the magnetic moments of the grains whose relaxation time is less or equal to the duration of the heating action, i.e., an instantaneous heating time reorients the grains only if the unblocking temperature is less or equal than the applied temperature. This remagnetization is called TVRM and is present during burial processes (Cairanne, 2003) (Figure 5.22b).

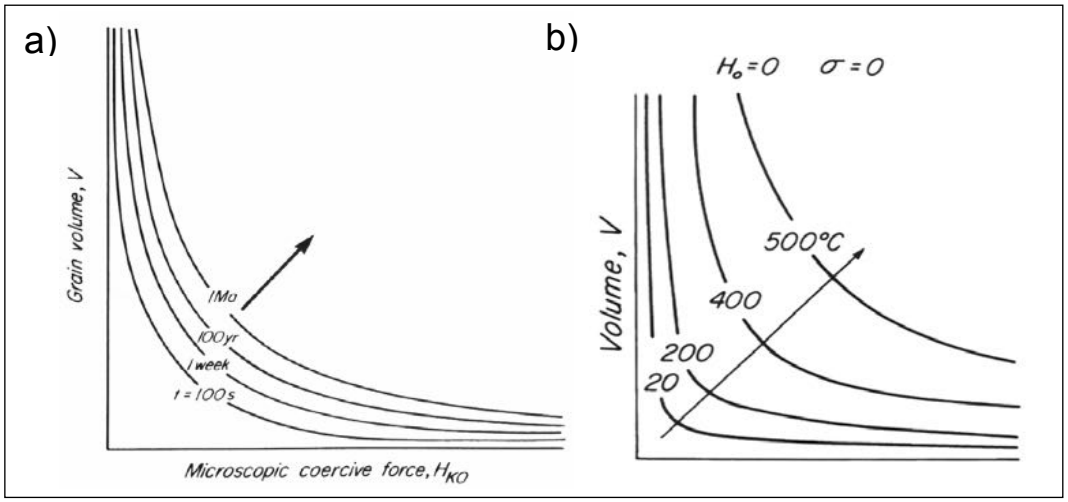

Figure 5.22. a) Time effect (Dunlop & Özdemir, 1997). b) Temperature effect (Dunlop et al.,1969) on the magnetization stability of a group of single-domain grains. Note as the time and the temperature move the hyperbola according to Néel's bisector.

At different moments of the sedimentary rock history, chemical changes may form ferromagnetic minerals in a magnetizing field below their blocking temperatures acquiring CRM. To consider CRM as a secondary magnetization, it must be acquired long after deposition and its stability is independent of the acquisition process and only dependent on the grain volume (Dunlop et Özdemir, 1997).

Ferromagnetic minerals are affected by chemical reactions such as:

- Precipitation of a ferromagnetic mineral from solution: In this case CRM accurately records the direction of the magnetic field.

- Alteration of the preexisting mineral (possibly also ferromagnetic) to a ferromagnetic mineral: If the alteration produces a change in the chrystal structure (e.g. magnetite to hematite) the CRM acquired records the magnetic field direction during alteration. But, if the alteration does not produce changes in the chrystal structure, the resulting CRM can record the remanence direction of the original grains (Butler, 2004).

Enkin et al. (2000), proposed the sequence of a chemical remagnetization (CRM) episode caused by fluid circulation associated with the emplacement of a frontal thrust, followed by an episode of partial thermoviscous remagnetization (TVRM) imposed by tectonic burial (Figure 5.23).

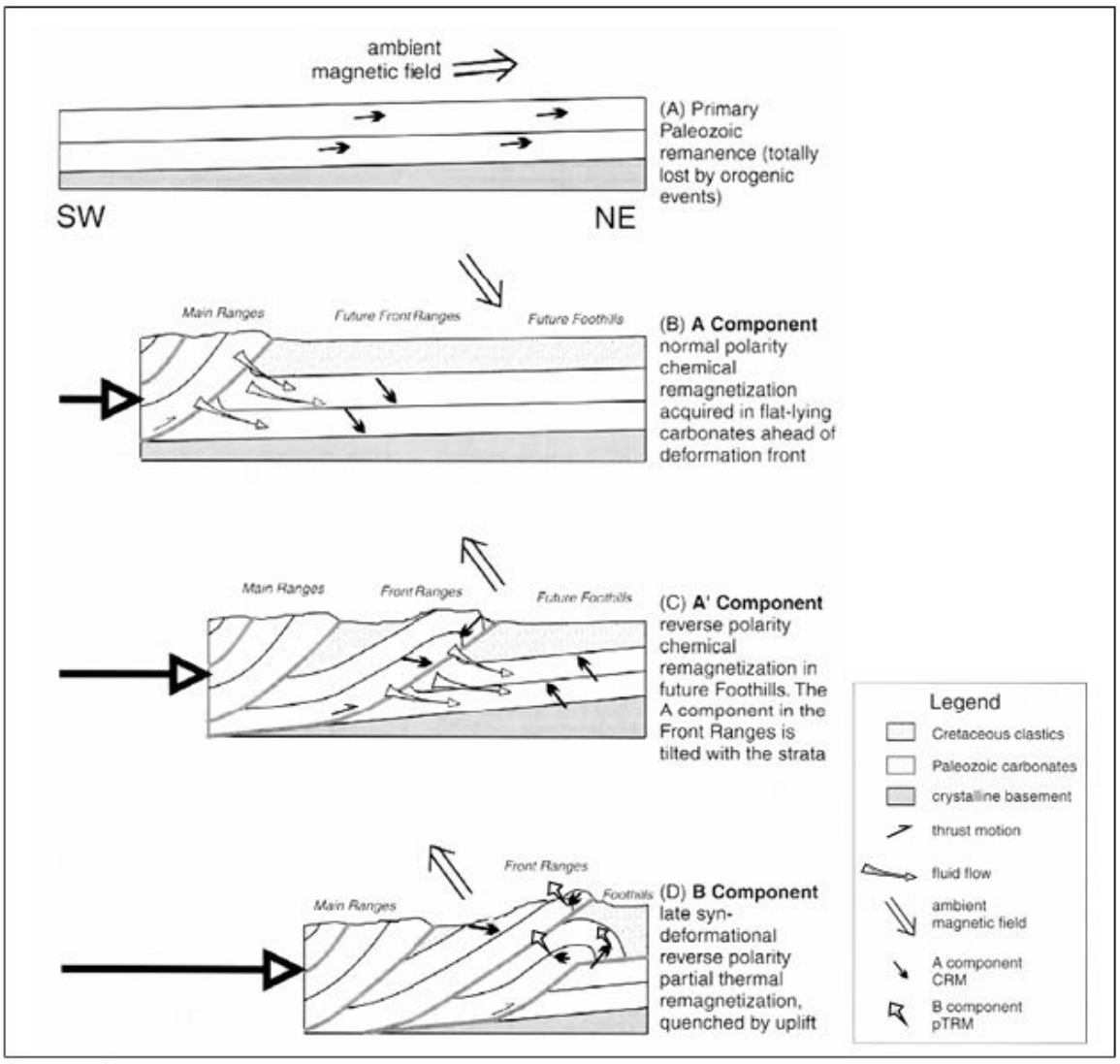

Figure 5.23. Model of chemical and thermoviscous remagnetizations during successive foldings of the Canadian Cordillera (from Enkin et al., 2000).

Several authors have noted that for orogens of Mesozoic and Cenozoic ages, the secondary magnetizations are often synchronous with the folding and are of normal polarity (Moreau et al., 1992; Halim et al., 1998; Aubourg et Chabert-Pelline, 1999; Dinares-Turell and Garcia-Senz, 2000; Kechra et al., 2003).

In an orogenic prism different processes can occur causing the rock remagnetization, such as:

1. Burial (Diagenesis): This process produces the transformation of minerals, such as:

   Smectite to Illite ⟶ Magnetite (Katz et al., 2000; Elmore et al., 2012).

   Pyrite Alteration: Py + Organic Matter ⟶ Magnetite (Brothers et al., 1996)

   Aubourg et al. (2012) proposed a simple pattern of magnetic mineral windows,

resulting from burial processes; the greigite window (sub-surface to ~2 km), magnetite (~2km to ~10 km), pyrrhotite window (>10 km). Note that this model works for clay rocks.

2. Fluid Circulation: Though widely proposed, the hypothesis of fluid circulation rarely explains pervasive remagnetization (e.g. Elmore et al., 2012 and references therein). Recently, Rouvier and Henry (2012) propose that the fluid types (Pb, Zn) of the Mississippi Valley Type (MVT) are responsible for remagnetization in the rock.

3. Strain: Pressure solutions might be responsible for large scale orogenic remagnetization (e.g. Oliva & Urcia et al., 2008).

5.4. Sampling and Laboratory Procedures

5.4.1. Methods

Paleomagnetic Samples

Paleomagnetic samples were drilled in the field using a portable drill with a diamond crown and water cooling system to avoid high increases of the friction temperature. Cylindrical samples 2.5 cm diameter and with a maximum penetration depth of ~10 cm were collected. Then, each sample was oriented in-situ using magnetic and sun compass. Once oriented, the samples were marked and stored. For the sites where blocks were taken, the block (20 cm x 20 cm) was oriented and marked with the compass and finally detached and stored (Figure 5.24), where declination or azimuth is the angle measured in the horizontal plane with respect to the magnetic north and inclination or hade is the angle between the field arrow and the horizontal plane (Figure 5.25).

Figure 5.24. Drilling, orientation in-situ and sample acquisition in the field.

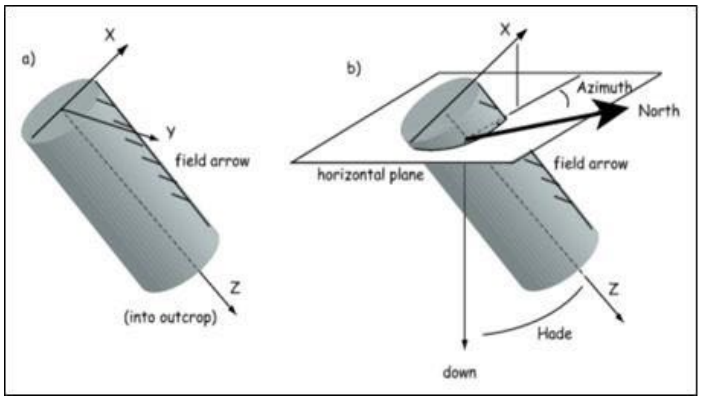

Figure 5.25. Orientation system of sampled collected by portable core drill. a)Orientation core sample in-situ. b)Orientation angles for core sample (from Tauxe, 2009).

Laboratory Analysis

Preparation of samples for paleomagnetic analysis was performed in the laboratories of the University of Pau and the University of Burgos. The thermal and alternating-field demagnetization processes were performed at the University of Provence (CEREGE, France) under the supervision of François Demory, and at the University of Burgos and Centro Nacional de Investigación de la Evolución Humana (CENIEH) in Burgos, Spain, under the supervision of Juan Villalain and José Pares respectively.

Equipment and Instruments

The following equipment was used:

At the University of Provence (CEREGE) (Figure 5.26):

- Auformated AF demagnetizing SQUID 2G.

Figure 5.26. Instrumentation of the paleomagnetism laboratory at the University of Provence (CEREGE), France.

At the University of Burgos (Figure 5.27):

- Superconductor magnetometer 2G-755 with automatic sample holder, alternating fields system and ARM inducer, all automatic and synchronized.

- Helmholtz coil system (6 m^3) self-compensated (in-house design and manufacturing) with automatic power triaxial fluxgate MR-3.

- Thermal demagnetizer TD48-DC (ASC).

The processing of the data obtained from the sample demagnetization in the laboratory was carried out with Remasoft 3.0 software.

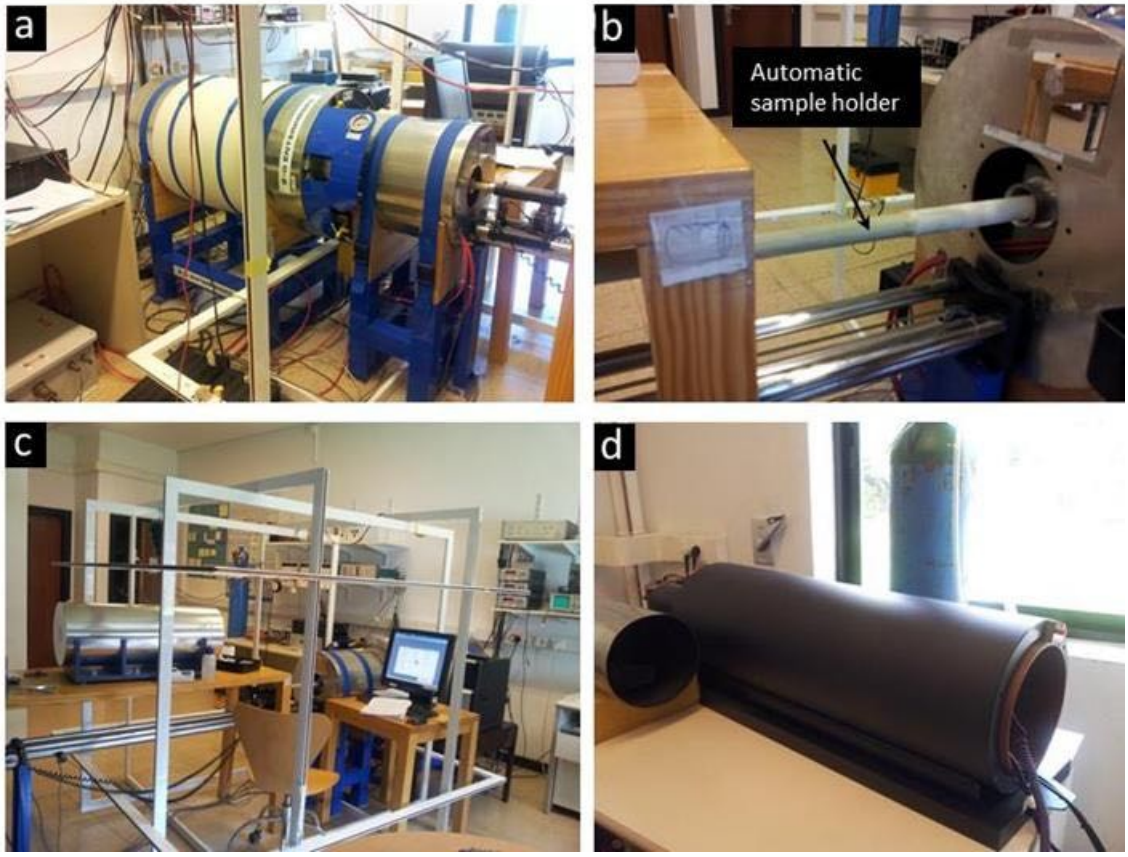

Figure 5.27. Paleomagnetism laboratory instrumentation at the University of Burgos, Spain. a) Superconductor magnetometer 2G b) Automatic sample holder c) Helmholtz coil system d) Thermal demagnetizer TD48-DC (ASC).

Paleomagnetic Measurements

The demagnetization process of the specimens was performed in two stages: the first measurement stage for the drilled samples from sites 1Vz to 11Vz was carried out at the University of Provence, (CEREGE). The second measurement stage was performed at the University of Burgos and at the CENIEH on the oriented blocks taken in the fieldwork (site 12Vz to site 27Vz).

In order to know which of the two methods (AF and Thermal demagnetization) was the most efficient to demagnetize the samples, a pilot test was carried out on 3 or 4 specimens of each site. Subsequently, based on the results, the demagnetization was performed on all samples. The thermal method reached higher demagnetization steps so it was applied to all samples.

Before applying the demagnetization methods, the NRM is measured for each specimen. The protocol followed for the thermal demagnetization specimens consisted of heating every 30°C from 50°C up to 450°C (12 heating steps).

AF demagnetization was carried out by applying progressively higher alternating magnetic fields and measuring the magnetization after each step (5 mT up to 100 mT). In order to achieve uniform demagnetization during the demagnetization process, each specimen is placed in a sample holder capable of rotating in three directions of space (x, y, z planes)

Thermal demagnetization was carried out for most of the samples connected and in some cases combination of the two techniques, first thermal and then AF. In some samples, AF demagnetization only was applied.

Sample Preparation

For the NRM and demagnetization process measurements, the drilled samples were cut in specimens (2.2 cm thick); obtaining one to five standard specimens (Figure 5.28).

The blocks were previously drilled in the laboratory in order to obtain the samples and then, were cut into specimens like the other samples and marked as A, B and C, where A is the top of the sample and D the bottom (Figure 5.29).

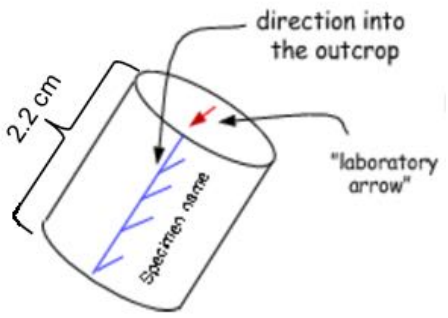

Figure 5.28. Specimen shape and orientation convention for a sample core (from Tauxe, 2009).

Figure 5.29. Drilling, cutting and preparation of the oriented blocks in the laboratory at the University of Burgos, Spain.

5.4.2. Sampling

Samples were taken from a total of 27 sites distributed in the Serranía Del Interior Mountain (Bergatín and Caripe blocks) to the east of the Urica Fault and to east and west of the San Francisco Fault (Figure 5.30). 159 oriented samples and 42 oriented blocks were obtained.

The sites are located according to the position on the regional faults and structures of the Serranía Del Interior and described as follows:

- Sites 1Vz, 2Vz and 27Vz are located near the Urica Fault in the Bergatín block.

- Sites 25Vz and 26Vz are located to the north of the Bergatín block.

- Sites 10Vz, 11Vz, 17Vz, 16Vz and 18Vz, are located in the southeast area of the Bergatín block, near the San Francisco Fault.

- Sites 3Vz, 8Vz and 9Vz, are located in the Caripe block near the San Francisco Fault.

- Sites 4Vz, 23Vz and 24Vz are located to the north of the Caripe block near the El Pilar Fault.

- Sites 5Vz, 7Vz, 6Vz, 22Vz, 21Vz, 20Vz and19Vz are located to the center of the Caripe Block.

- Sites 12Vz, 13Vz, 14Vz and 15Vz are located more eastward at the western edge of the San Juan Graben.

The sampling includes mainly limestone, black shale and calcareous sandstone from the Querecual, San Juan and San Antonio Formations (Upper Cretaceous “Grupo Guayuta”)(15 sites), limestone from the Lower Cretaceous Cantil Formation (7 sites), calcareous sandstone, limestone and black shale from Cantil and Barranquin Formations (Lower Cretaceous “Grupo Sucre”) (4 sites). Finally, black shale from the Paleocene Vidoño Formation (1 site). 15 oriented samples were taken from each one of the 11 sites drilled and 3 or 4 oriented blocks from the others 16 sampled sites (Figure 5.31 and Figure 5.32).

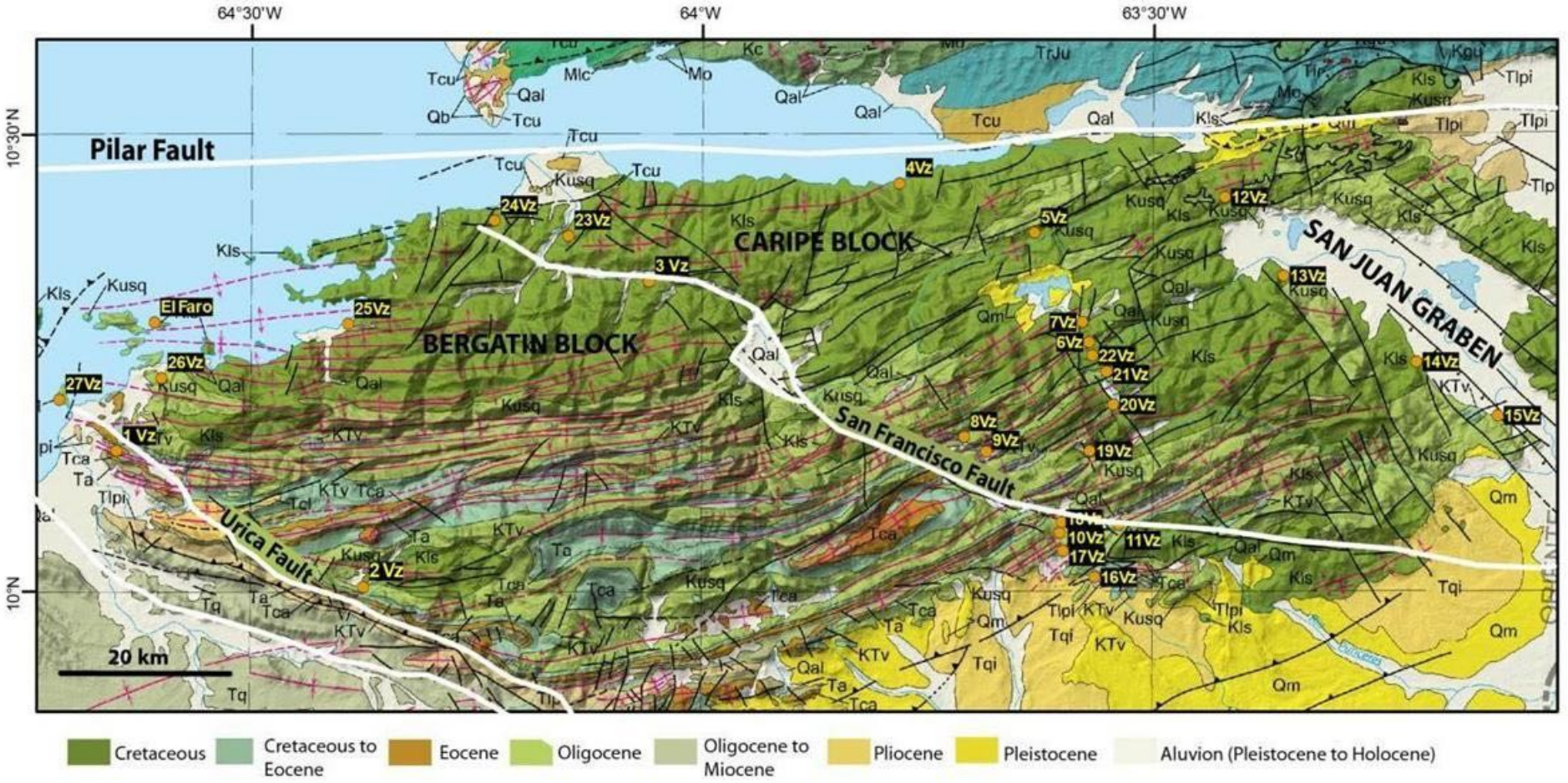

Figure 5.30. Map of the study area with de fieldwork stops in the Serranía Del Interior Mountain (modified from Geological Map of Venezuela) USG, 2005)

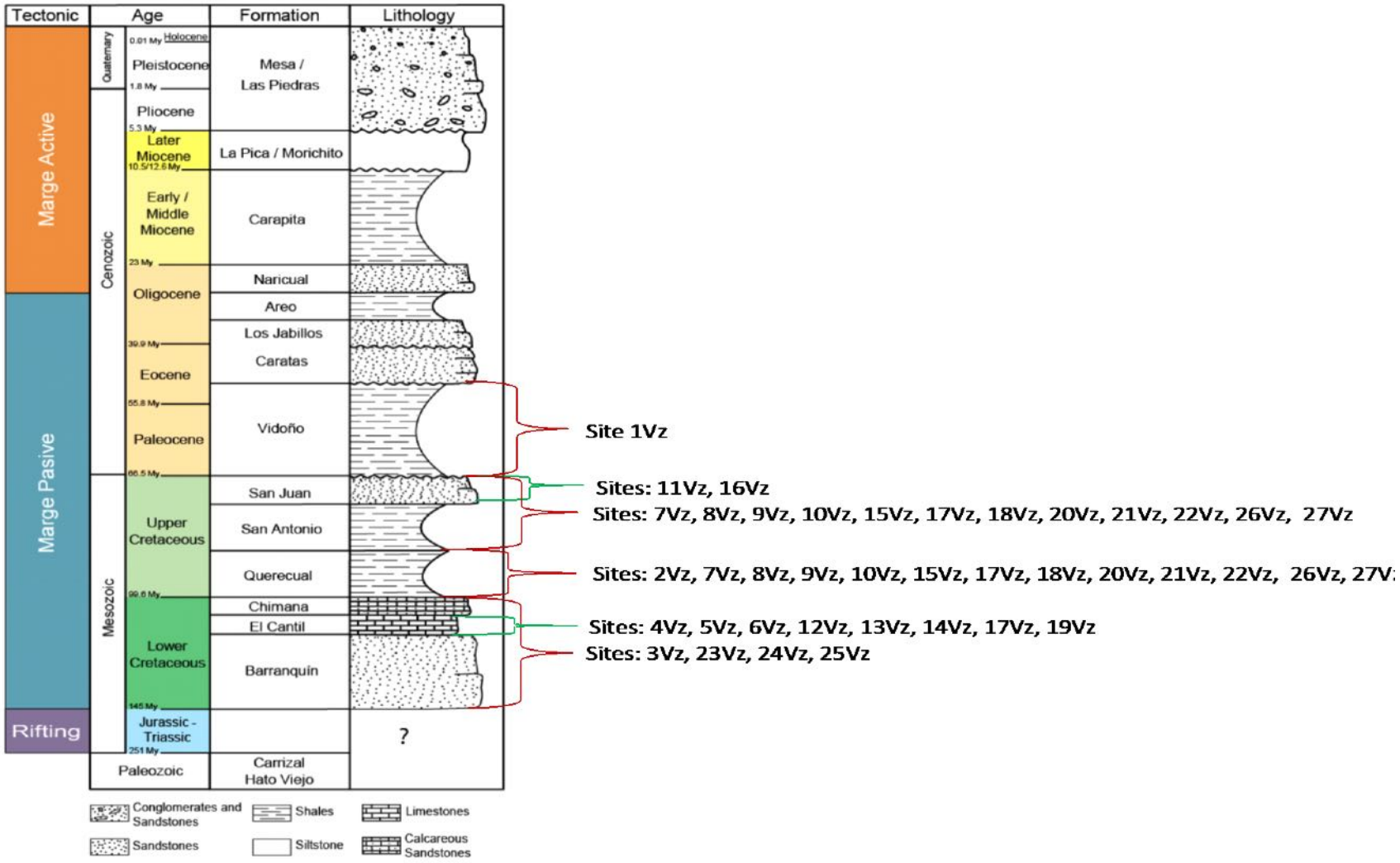

Figure 5.31. Tectonic stratigraphy column with geological formations sampled in the Serranía Del Interior.

Figure 5.32. Examples of formations sampled. a) Vidoño Formation (Site 1Vz). b) Querecual Formation (Site 2Vz). c) Grupo Sucre. Cantil-Barranquín Formation (Site 4Vz). d) Cantil Formation (Site 14Vz). e) Grupo Guayuta. Querecual – San Juan – San Antonio Formations (Site 10Vz). f) San Juan Formation (Site 11Vz)

5.4.3. Paleomagnetic Results

Components could be identified in 92% of the specimens. Figure 5.33 shows representative examples of the results obtained at different sites. Only site 7Vz showed an unstable and uninterpretable demagnetization track. This site was not used for paleomagnetic analysis (Figure 5.34).

The average of the NRM intensity in the rocks is low, between 10^{-6} and 10^{-12} Am^2 / kg.

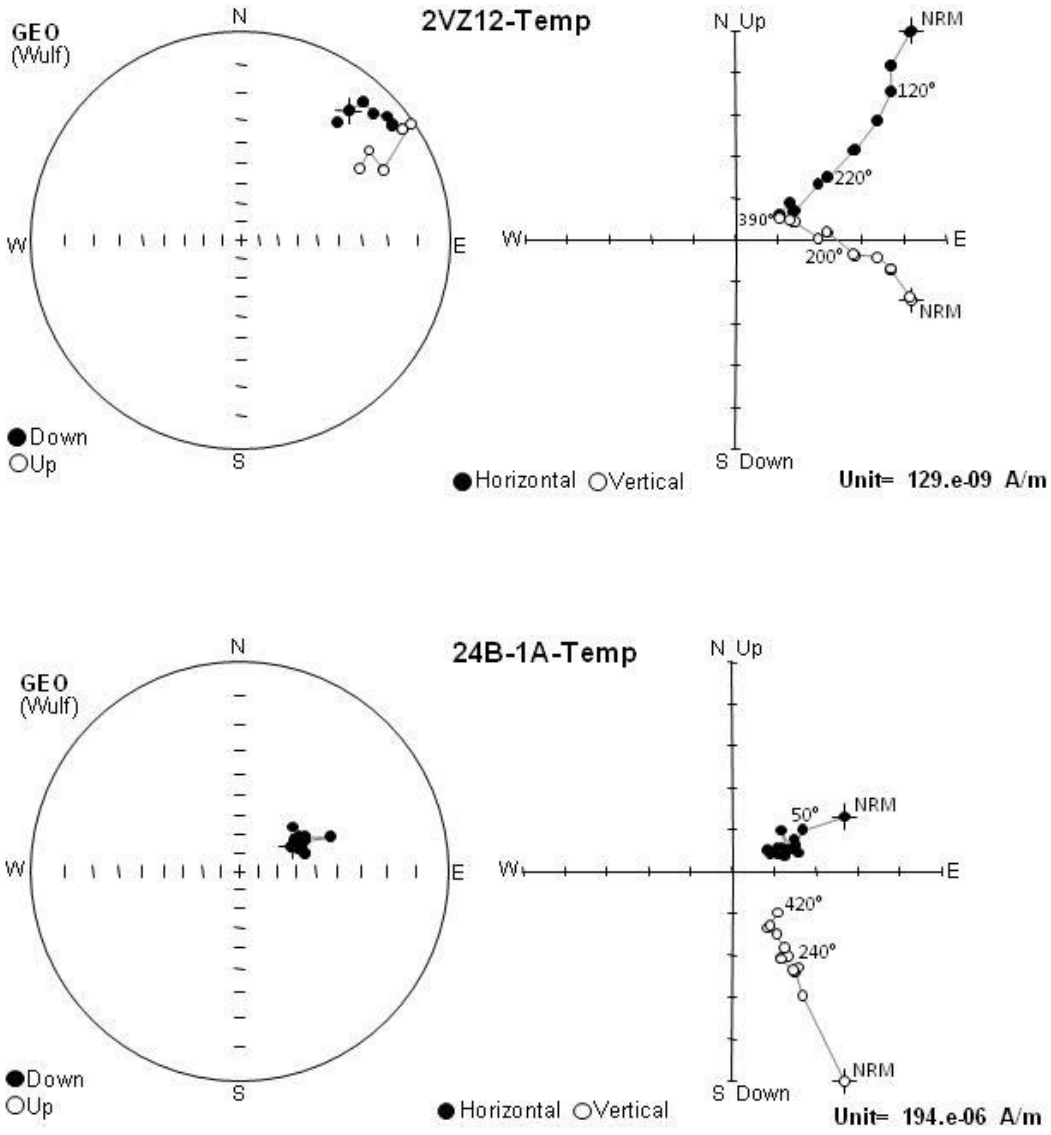

Figure 5.33. Representation of Zjiderveld diagrams and stereographics Wulff projection examples of magnetization directions obtain from the sites sampled in the Serranía Del Interior.

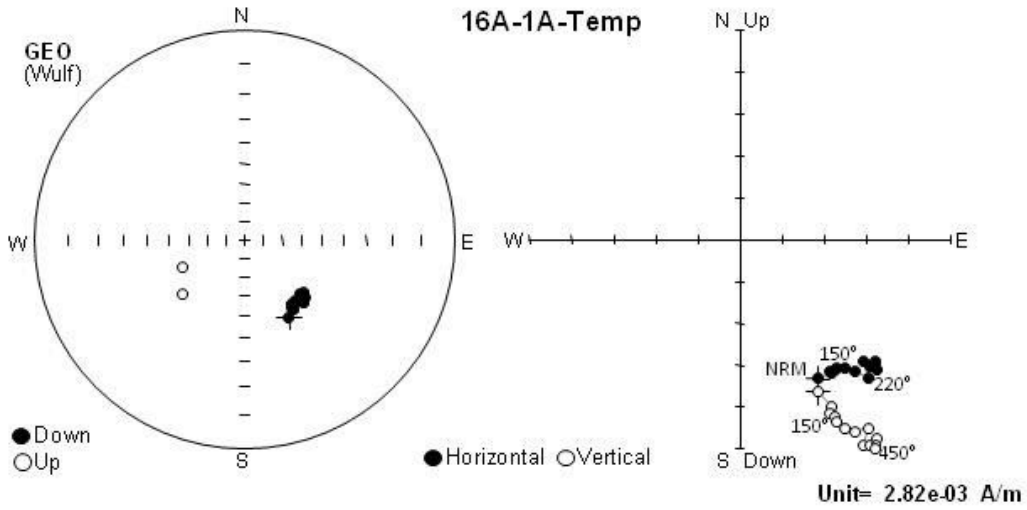

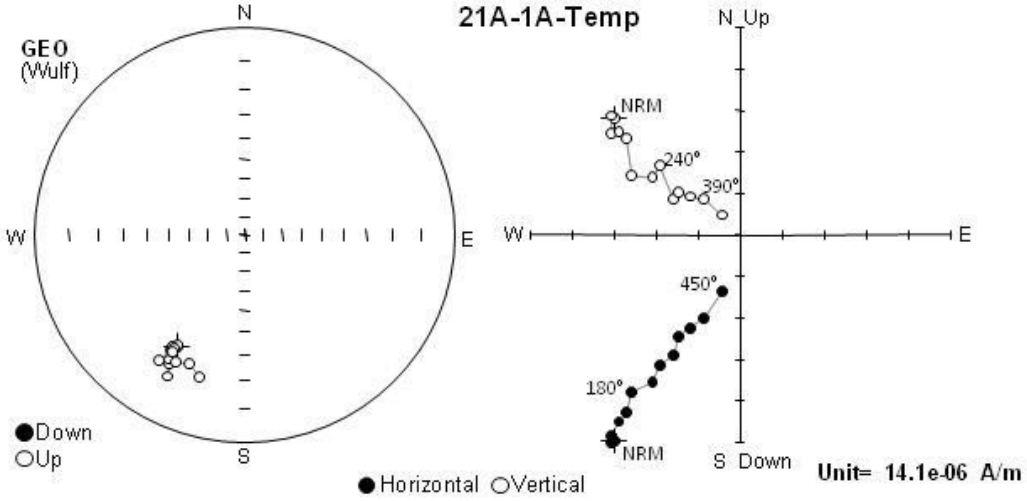

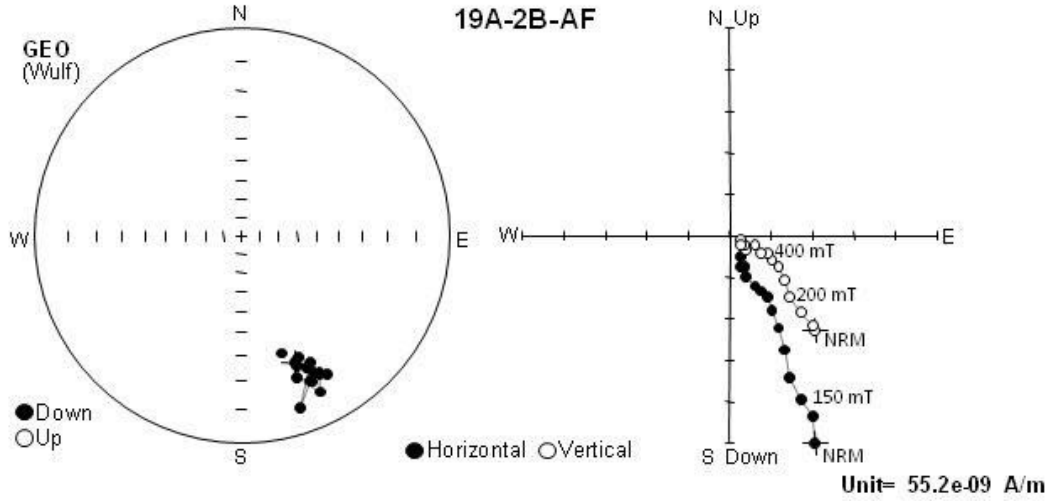

Figure 5.33. (continued)

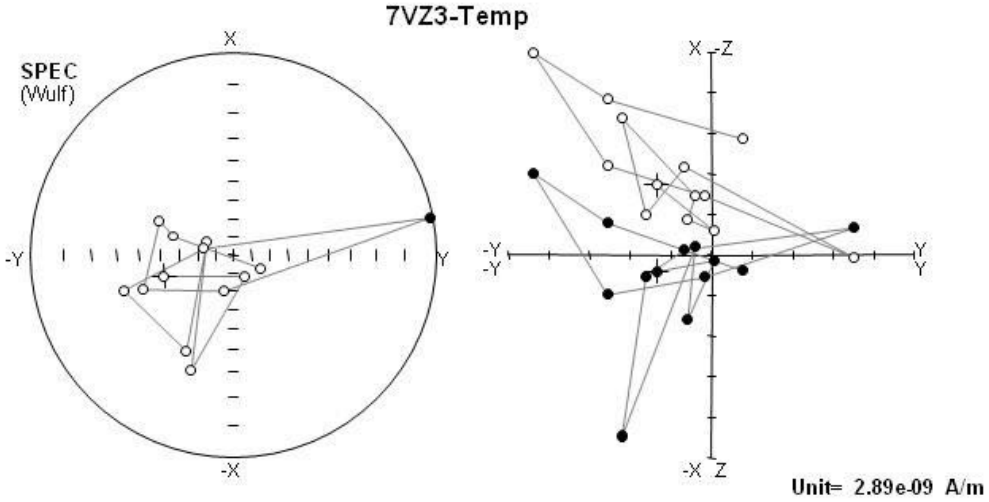

Figure 5.34. Example of one specimen from site 7Vz showing an unstable and uninterpretable demagnetization track.

Two components have been identified:

- The first component named Component A, was generally removed between 100-350°C and between 25-35 mT (Table 5.3). In 23% of the specimens, Component A is aligned with the present geomagnetic field direction, thus in this case it can be interpreted as a viscous remanent magnetism (VRM) (Figure 5.35). In 63% of the specimens, Component A shows vector end points toward the origin (ChRM) (Figure 5.36). The rest of the specimens (14%) display linear segments, but different from the VRM and ChRM.

- The second component named Component B, is present together with Component A. Component B was generally removed between 360-450°C and between 70-100 mT. This component is observed at all sites except at sites 15Vz and 17Vz.

To determine block rotation along vertical axis in the study area, a GAD parallel to the Earth's rotation axis was assumed. The expected $APWP_{0\text{-}10\ My}$ direction (D=2°, I=11°) is near the Earth's rotation axis, thus the magnitude of rotation is directly the declination of the mean component (Figure 5.35). The $APWP_{0\text{-}10\ My}$ was calculated using PALEOMAC software based on the magnetic poles of Besse & Courtillot (2002).

Table 5.3. Paleomagnetic data and results obtained of this study.

Site	Latitude	Longitude	Lithology	All Samples	Samples analyzed	Total Specimen analyzed by each sample	Specimen used in statistic (N)	Specimen used in the final statistic (n)	n/N	Unblocking Temperature °C (CA)	Unblocking Temperature °c (CB)	Unblocking AF mL (CA)	Unblocking AF mL (CB)	Geo				Tecto (Tilt Corr)			
														D	I	k	α95	D	I	k	α95
1Vz	10°09'01"	64°38'49"	Black Shales	15	7	7	7	6	6/7	50-350		50-200	200-1000	24	25	13	19	172	72	15	17
2Vz	09°59'59"	64°22'26"	Limestone & Black shales	14	10	10	10	5	5/10	50-300	200-400	50-220	200-1000	30	30	41	12	163	67	41	12
3Vz	10°20'15"	64°03'31"	sandstone, limestone and intercalated shale	18	11	12	12	7	7/12	100-450	150-300	50-300	50-1000	290	-24	16	15	288	29	16	15
4Vz	10°26'46'	63°46'55"	Limestone	14	10	11	8	5	5/8	120-390	150-420	50-300		355	32	12	22	346	57	12	22
5Vz	10°23'29"	63°37'58"	Limestone	14	13	13	13	5	5/13	100-400	200-450	50-200	200-1000	24	46	33	13	6	-19	33	13
6Vz	10°16'14"	63°34'19"	Limestone	13	12	12	12	10	10/12	100-240	150-450	50-250	200-1000	300	-64	1	61	325	-15,5	1	58
7Vz	10°17'34"	63°34'47"	Limestone and shale	17	5	5	Outcrop in bad condition														
8Vz	10°09'55"	63°42'38"	Limestone and shale	15	12	12	12	3	3/12	100-300	180-450	50-700	200-1000	45	31	15	12	29	13	14	13
9Vz	10°04'58"	63°39'23"	Limestone and shale	12	9	12	12	8	8/12	100-260	220-350	50-300	150-1000	45	31	15	12	29	13	14	13
10Vz	10°04'58"	63°39'23"	Limestone and shale	14	10	10	10	5	5/10	100-420	220-450	50-1000	250-1000	31	28	19	12	11	32	20	12
11Vz	10°04'8"	63°32'22"	Sandstone and shale	14	9	9	9	4	4/9	100-420	200-450	50-300	350-1000	31	28	19	12	11	32	20	12
12Vz	10°25'49"	63°25'20"	Limestone	4	3	7	7	6	6/7	100-240	240-450	50-250	200-1000	156	32	22	13	159	-4,8	22	13
13Vz	10°20'38"	63°21'28"	Limestone	2	2	6	6	4	4/6	50-210	240-450	50-450	300-1000	169	30	32	14	169	-41,8	26	15
14Vz	10°14'57"	63°12'39"	Limestone	3	3	7	Possible fallen block			50-120	100-450	50-250	250-1000								
15Vz	10°11'22"	63°07'15"	Limestone and shale	5	4	8	8	1	1/8	50-420		50-1000		169	30	32	14	169	-41,8	26	15
16Vz	10°00'38.7"	63°33'59.9"	Sandstone and shale	4	4	9	9	4	4/9	50-180	150-450	50-200	250-1000	105	30	5	10	103	37	6	30
17Vz	10°02'23"	63°36'4.9"	Sandstone and shale	1	1	3	3	1	1/3	50-420		50-1000		105	30	5	10	103	37	6	30
18Vz	10°03'34"	63°36'18"	Sandstone and shale	1	1	2	2	1	1/2	50-100	120-390	50-250	300-1000	105	30	5	10	103	37	6	30
19Vz	10°09'02"	63°34'18"	Limestone	4	4	10	10	3		50-150	180-420	50-600	300-1000								
20Vz	10°12'5"	63°32'44"	Marls and limestone	4	4	8	8	2	2/8	50-120	150-450	50-150	200-1000	300	-64	1	61	325	-15,5	1	58
21Vz	10°14'16"	63°33'11"	Sandstone and shale	3	3	6	6	2	2/6	50-450	210-360	100-600	300-700	300	-64	1	61	325	-15,5	1	58
22Vz	10°15'20"	63°35'8"	Sandstone and limestone	3	3	5	5	2	2/5	50-450	100-450	50-200	250-900	300	-64	1	61	325	-15,5	1	58
23Vz	10°23'17"	64°8'51"	Sandstone and limestone	4	4	8	8	4	4/8	50-210	150-420	50-250	200-1000	114	73	7	24	343	37	7	23
24Vz	10°24'17"	64°13'44"	Sandstone and limestone	3	3	6	6	3	3/6	50-120	150-420	50-800		114	73	7	24	343	37	7	23
25Vz	10°17'25"	64°23'27"	Sandstone and limestone	1	1	2	Only 2 samples			50-180	210-420										
26Vz	10°13'50.6"	64°35'51"	Sandstone and limestone	5	5	8	8	6	6/8	50-420	120-420	50-250	250-1000	97	38	5	27	110	43	4	33
27Vz	10°12'25"	64°42'37"	Sandstone and limestone	2	2	4	4	2	2/4	50-240	120-420	50-500	400-1000	97	38	5	27	110	43	4	33

Component A

Component A is present at 9 of the 27 sites sampled (1Vz, 2Vz, 3Vz, 4Vz, 6Vz, 8Vz, 9Vz, 10Vz and 11Vz) and is close to the present magnetic field (Figure 5.30). The magnetization directions are well clustered, in-situ, and yield a site mean direction of D=360°, I=35°, K=42, α_{95}=4°. After bedding correction, the site mean direction is D=1°, I=63°, K=4, α_{95}=15°. The magnetization directions are more dispersed after bedding correction suggesting that this component was acquired post-folding (Figure 5.35). This Component A is interpreted to be a VRM.

Component A identified to be a ChRM is present in 21 of the 27 sites sampled (1Vz, 2Vz, 3Vz, 5Vz, 6Vz, 8Vz, 9Vz, 10Vz, 11Vz, 13Vz, 14Vz, 15Vz, 16Vz, 17Vz, 18Vz, 19Vz, 21Vz, 22Vz, 24Vz, 26Vz and 27Vz). This ChRM has a mixture of normal (85%) and reverse polarity (15%). The directions are more clustered before bedding correction (in-situ) than after (tilted). For this reason, this component is considered to have been recorded post-folding. The site-direction calculation in-situ is D=36°, I=31°, k=10, α_{95}=5° and after bedding correction D=46°, I=41°, k=4, α_{95}=11° (Figure 5.36)

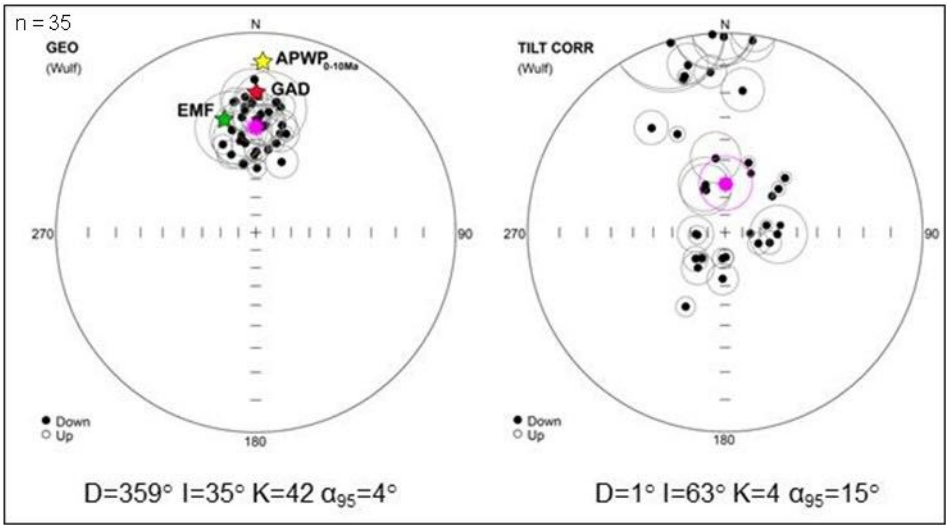

Figure 5.35. Component A (VRM). Stereographic projection in-situ (Geo) and after bedding correction (Tilt Corr). The yellow start represents the expected direction from $APWP_{0\text{-}10\ Ma}$ in the area. The green start represents the EMF (present day dipole) in the area. The red point represents the present Geocentric Axial Dipole (GAD) in the area.

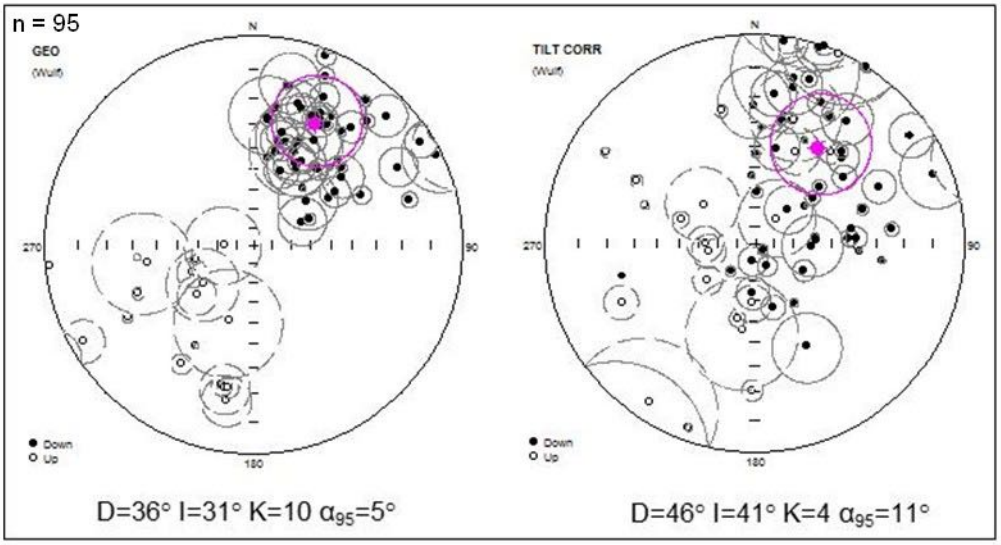

Figure 5.36. Component A (ChRM). Stereographic projection in-situ (Geo) and after bedding correction (Tilt Corr).

Component A (ChRM) and Component B

Where several sites are close, were carried out analyses by zones in order to define site-direction with more data and to observe if the behavior of the magnetization can be affected by local structures in the area. The analyses were done using both components: Component A (different from VRM) and Component B.

East of the Urica Fault (Bergatín Block)

This zone is defined by sites 1Vz, 2Vz, 25Vz, 26Vz and 27Vz and is located in the Bergatín Block of the Serranía Del Interior (Figure 5.30and Figure 5.37).

The first analysis was carried out for the sites 1Vz and 2Vz which are located along the Urica Fault. The site mean direction, in-situ, is D=29°, I=34°, K=22, α_{95}=10° and after bedding correction D=162°, I=61°, K=19, α_{95}=11°. When dealing with the dispersion parameter K, the bedding-tilt test is inconclusive. However, the in-situ declination and inclination are close to the expected direction. This component was interpreted to have been acquired post-folding. In this hypothesis, the observed rotation is clockwise and has a magnitude of R=29°±10° (Figure 5.38)

Figure 5.37. Sampled sites in the East of the Urica Fault (Bergatín Block in the Serranía Del Interior)

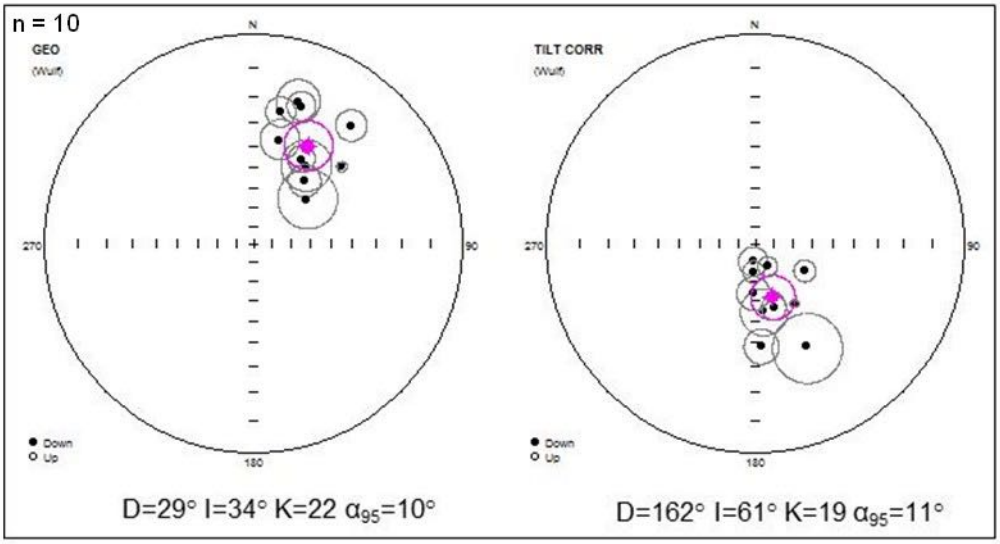

Figure 5.38. Sites 1Vz and 2Vz. Stereographic projection in-situ (Geo) and after bedding correction (Tilt Corr) of Component A (ChRM) and Component B.

Sites 25Vz, 26Vz and 27Vz are located to the north of the Bergatín Block, near the El Pilar Fault. Cleavage in the rocks was observed at site 2Vz and strong weathering in the rocks at site 25Vz (Figure 5.37). The site mean direction, in-situ, is D=95°, I=46°, K=7, α_{95}=19° and after bedding correction D=127°, I=49°, K=5, α_{95}=24°. Analysis of the data shows better

clustering before bedding correction (in-situ) suggesting that magnetization is post-folding. Clockwise rotation of R=95°±19° was observed (Figure 5.39).

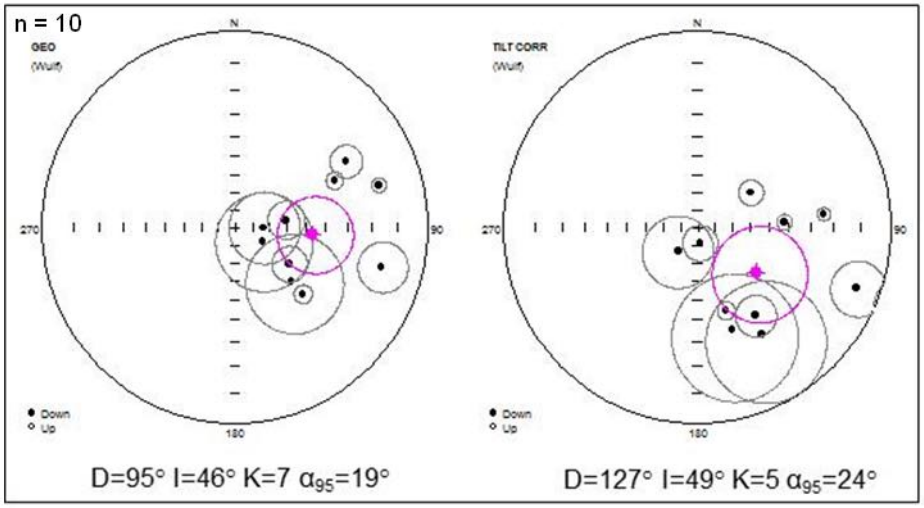

Figure 5.39. Sites 25Vz, 26Vz and 27Vz. Stereographic projection in-situ (Geo) and after bedding correction (Tilt Corr) of Component A (ChRM) and Component B.

Northeast of the San Francisco Fault (Caripe Block)

This zone is represented by sites 3Vz, 23Vz and 24Vz located to the northwest of the Caripe Block, near the San Francisco Fault in the Serranía Del Interior. The rocks at sites 24Vz and 25Vz are moderately weathered (Figure 5.30 and Figure 5.40)

The analyses of components A and B at site 3Vz yield site mean direction (in-situ) of D=294°, I=-21°, k=16, α_{95}=14° and after bedding correction, of D=287°, I=34°, k=16, α_{95}=14°.The bedding-tilt test is inconclusive because only one bedding data set is used and inclination is consistent before and after bedding correction. The rotation observed (in-situ) is R=114°±14° clockwise or after bedding correction R=66°±14° counterclockwise (Figure 5.41)

Sites 23Vz and 24Vz were analyzed together yielding, in-situ, a site mean direction of D=39°, I=68°, K=10, α_{95}=20° and after bedding correction D=347°, I=27°, K=3, α_{95}=42°. Here, the magnetization directions are more clustered before bedding correction (in-situ) indicating that the magnetization was acquired post-folding. However, inclination is by far too steep (I=68°), and it is uncertain to determine block rotation.

Figure 5.40. Sampled sites located to the north of the Bergatín Block (Serranía Del Interior), near the El Pilar Fault.

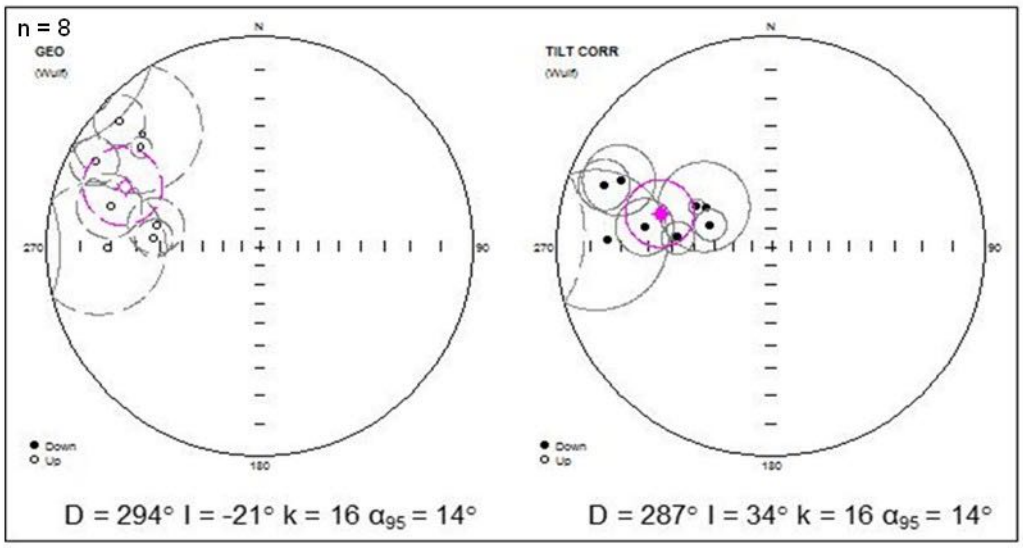

Figure 5.41. Site 3Vz. Stereographic projection in-situ (Geo) and after bedding correction (Tilt) of Component A (ChRM) and Component B.

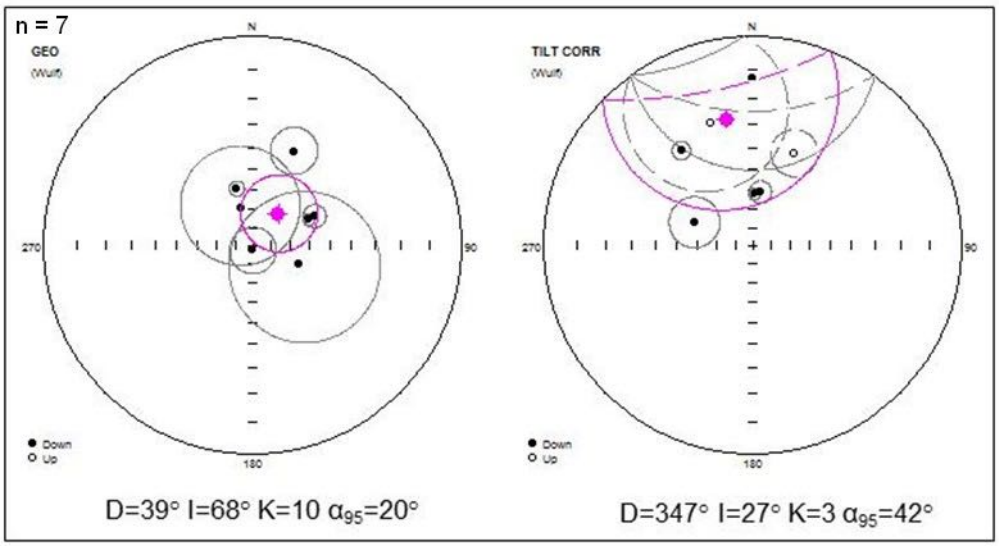

Figure 5.42. Sites 23Vz and 24Vz. Stereographic projection in-situ (Geo) and after bedding correction (Tilt) of Component A (ChRM) and Component B.

South of the San Francisco Fault

This zone is represented by sites 8Vz, 9Vz, 10Vz, 11Vz, 16Vz, 17Vz, and 18Vz to the south of the study area near the San Francisco Fault (Figure 5.30 and Figure 5.43)

The in-situ site mean direction for sites 8Vz and 9Vz located in the Caripe Block is D=37°, I=29°, K=18, α_{95}=11° and after bedding correction D=26°, I=7°, K=17, α_{95}=11°. The bedding-tilt test is not conclusive because the K parameter is the same before and after bedding correction. However, the in-situ inclination (I=29) is close to the expected VRM inclination of 32°, thus this magnetization was interpreted to have been acquired post-folding. Data suggest a clockwise rotation of R=37°±11° (Figure 5.44).

Sites 10Vz, 11Vz, 16Vz, 17Vz and 18Vz are located to the south of the Bergatín Block, close the San Francisco Fault. The calculated in-situ site mean direction is D=32°, I=39°, K=21, α_{95}=10° and after bedding correction D=10°, I=42°, K=21, α_{95}=10°. The tilt test here is inconclusive. A clockwise rotation of R=32°±10° was calculated (Figure 5.45).

Figure 5.43. Sampled sites 8Vz, 9Vz, 10Vz, 11Vz, 16Vz, 17Vz, and 18Vz located near the San Francisco Fault in the Serranía Del Interior.

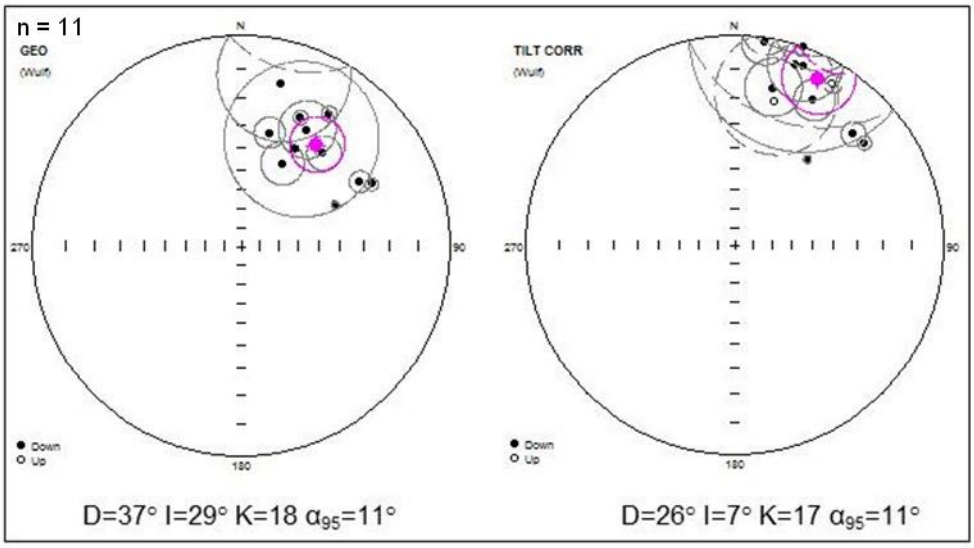

Figure 5.44. Sites 8Vz and 9Vz. Stereographic projection in-situ (Geo) and after bedding correction (Tilt) of Component A (ChRM) and Component B.

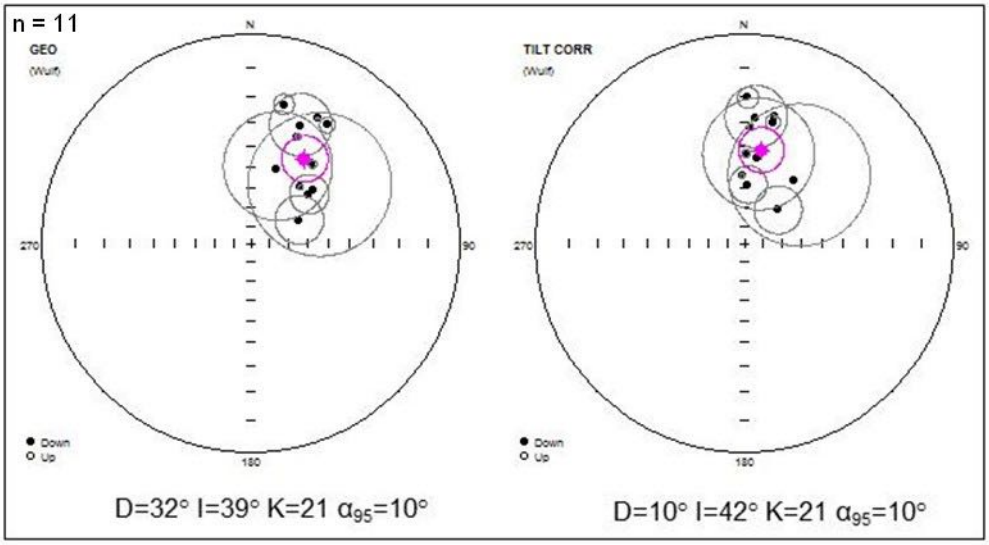

Figure 5.45. Sites 10Vz, 11Vz, 16Vz, 17Vz, and 18Vz. Stereographic projection in-situ (Geo) and after bedding correction (Tilt Corr) of Component A (ChRM) and Component B.

Center of the Caripe Block

This zone includes sites 6Vz, 20Vz, 21Vz and 22Vz, all located in the center part of the Caripe Block, to the east of the San Francisco Fault (Figure 5.30 and Figure 5.46). The site mean direction, in-situ, is D=25°, I=37°, K=25, α_{95}=8° and after bedding correction D=60°, I=51°, K=13, α_{95}=11°. According to the bedding-tilt test results, this magnetization was acquired post-folding. The block rotation is clockwise and has a magnitude of R=25°±8° (Figure 5.47) .

Figure 5.46. Sampled sites 6Vz, 20Vz, 21Vz and 22Vz located in the center part of the Caripe Block, to the east of San Francisco Fault (Serranía Del Interior).

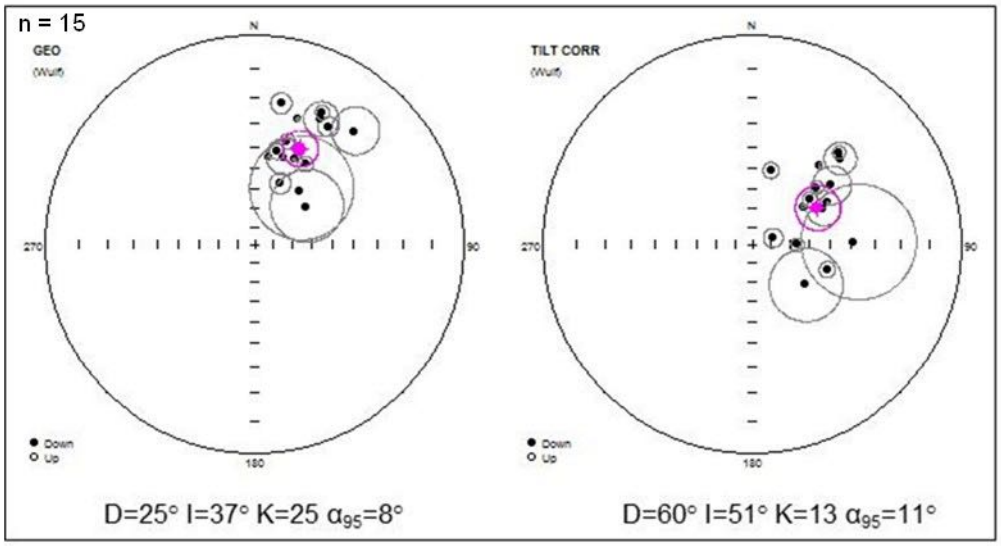

Figure 5.47. Sites 6Vz, 20Vz, 21Vz and 22Vz. Stereographic projection in-situ (Geo) and after bedding correction (Tilt Corr) of Component A (ChRM) and Component B.

East of the Caripe Block

Sites 12Vz, 13Vz, 14Vz and 15Vz are located on the western edge of the San Juan Graben in the Serranía Del Interior (Figure 5.30 and Figure 5.48).

In this zone the behavior is totally different from the other zones. The in-situ site mean direction is D=165°, I=37°, K=25, α_{95}=8° and all the sites have positive inclination. After bedding correction, the average direction is D=164°, I=-20°, K=9, α_{95}=16°. The bedding-tilt test suggests that the magnetization was acquired post-tilting. However, the grouping of reverse polarity near the expected direction suggests that the magnetization is likely pre-tilting. The in-situ block rotation is strongly clockwise R=165°±8°. After bedding correction (tilt coordinates) the rotation is slightly counterclockwise (R=-16°±16°). We assume here that the most reasonable solution is assumed to be a pre-tilting magnetization with little or no rotation (Figure 5.49).

Figure 5.48. Sampled sites 12Vz, 13Vz, 14Vz and 15Vz located on the western edge of the San Juan Graben (Serranía Del Interior).

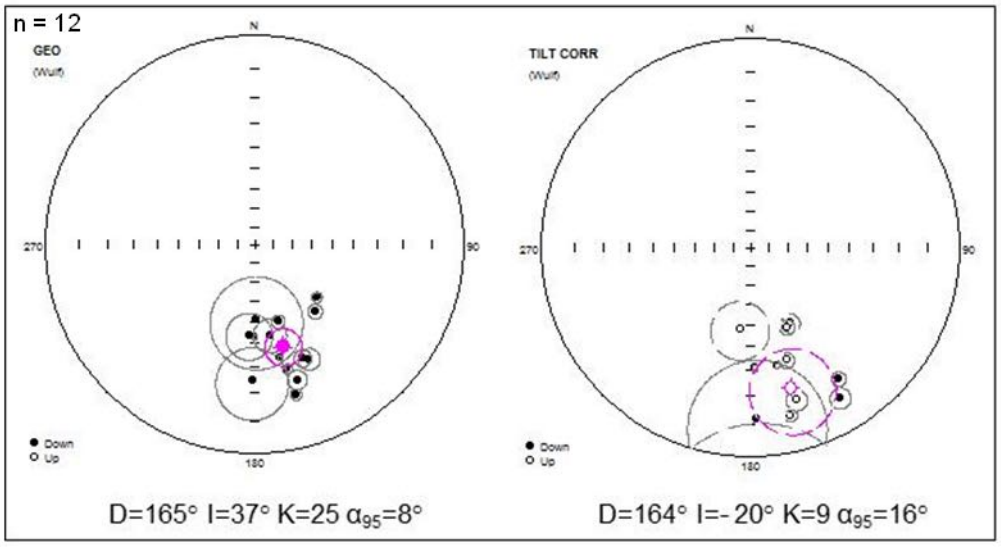

Figure 5.49. Sites 12Vz, 13Vz, 14Vz and 15Vz. Stereographic projection in-situ (Geo) and after bedding correction (Tilt Corr) of Component A (ChRM) and Component B.

Finally, sites 4Vz, 5Vz and 19Vz were interpreted individually (Figure 5.50).

Site 4Vz is located to the north of the Caripe Block, near the El Pilar Fault. The calculated in-situ site mean direction is D=355°, I=26°, K=16, α_{95}=15° and after bedding correction D=347°, I=50°, K=15, α_{95}=15°. The bedding-tilt test is not conclusive because K does not change. Nevertheless, the in-situ inclination is close to the inclination expected, thus this component was interpreted to have been acquired post-folding. A lack of rotation is observed at this locality (Figure 5.51).

Site 5Vz located to the southeast of site 4Vz in Caripe Block, has in-situ site mean direction D=34°, I=31°, K=24, α95=16°; all sites have normal polarity. After bedding correction, the site mean direction is D=24°, I=-19, K=24, α95=16° and 4 of 5 components have reverse polarity. This was likely acquired post-folding and suggests clockwise rotation of R=34°±16° (Figure 5.52).

Figure 5.50. Sampled sites 4Vz, 5Vz and 12Vz located on the Caripe Block.

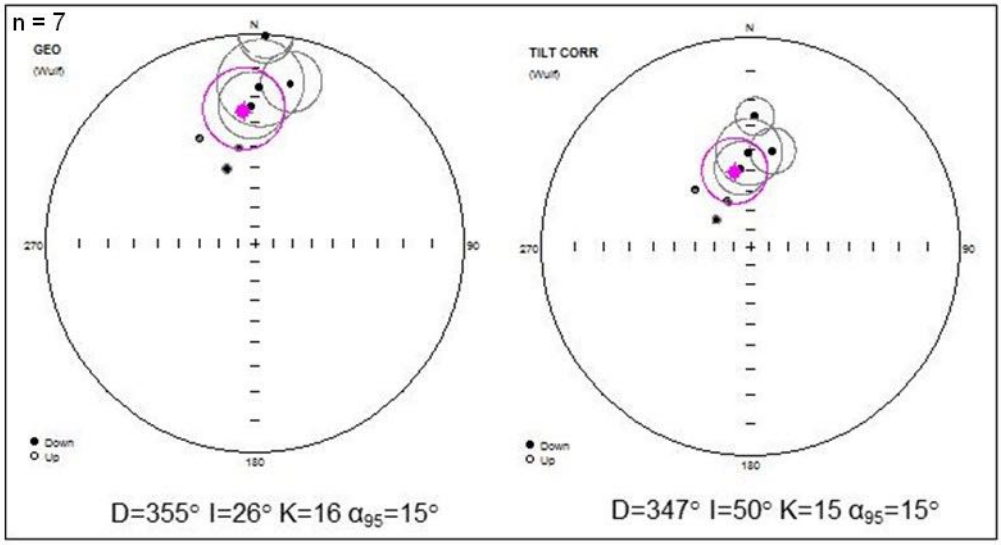

Figure 5.51. Site 4 Vz. Stereographic projection in-situ (Geo) and after bedding correction (Tilt Corr) of Component A (ChRM) and Component B.

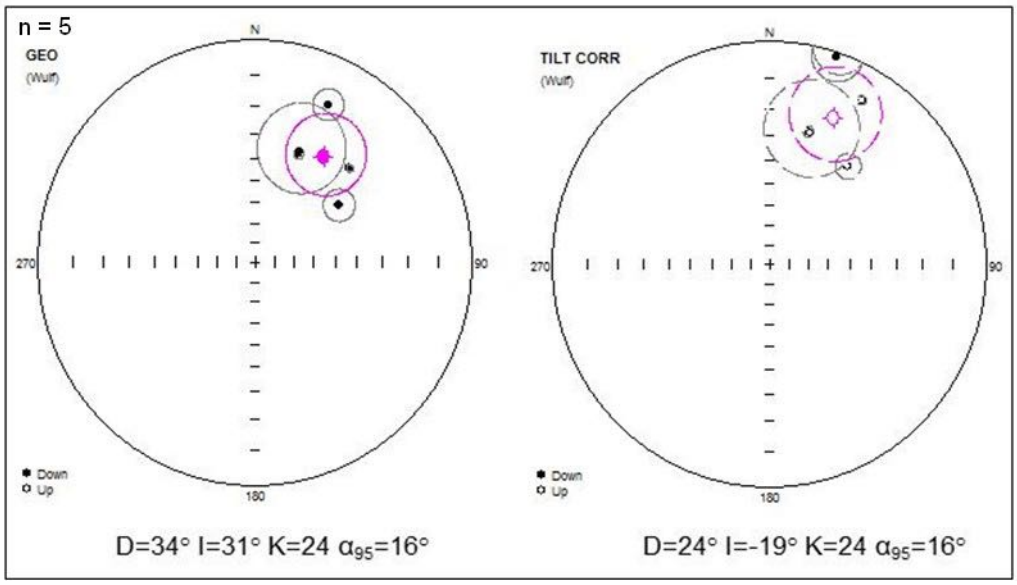

Figure 5.52. Site 5Vz. Stereographic projection in-situ (Geo) and after bedding correction (Tilt Corr) of Component A (ChRM) and Component B.

Site 19Vz is located to the south of the Caripe Block. The calculated in-situ site mean direction is D=36°, I=66°, K=21, α_{95}=17° and after bedding correction of D=348°, I=27°, K=7, α_{95}=31°. The parameter K decreases after bedding correction which suggests that magnetization was acquired post-folding. The bedding correction here is inconclusive because in-situ inclination (I=66°) is far too steep (Figure 5.53). Note however that the in-situ declination of 36° is close to the declination observed at sites 23Vz and 24Vz of 39°.

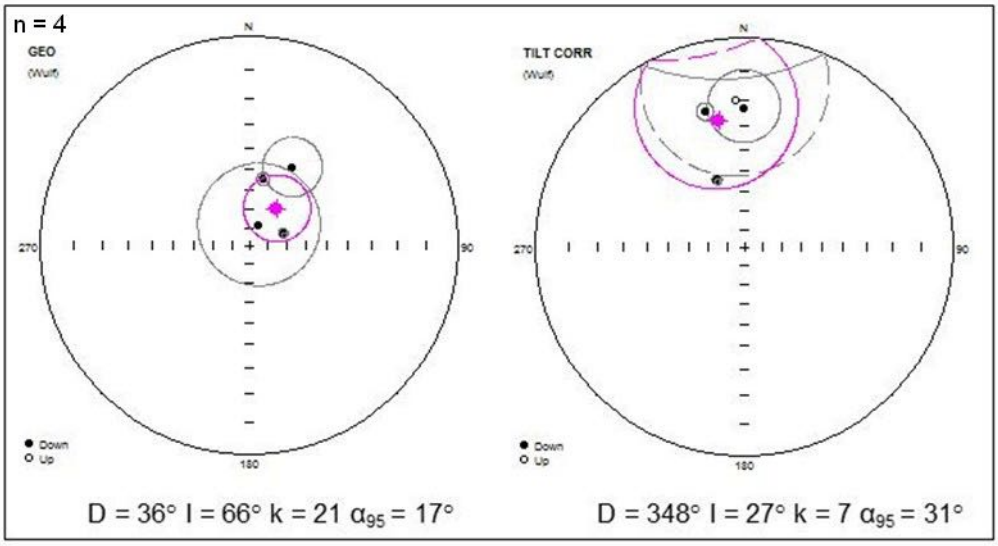

Figure 5.53. Site 19Vz. Stereographic projection in-situ (Geo) and after bedding correction (Tilt) of Component A (ChRM) and Component B.

5.5. Discussion

Regional Analysis

A regional paleomagnetic study was carried out at 26 of the 27 sampled sites in the Serranía Del Interior, except for site 7Vz which showed unstable and uninterpretable demagnetization track. All sites were analyzed in the previous section. Two components (A and B) were identified. All results are compiled in Table 5.3.

Component A (VRM). Component A was identified a VRM in 23% of the specimens of the sites (1Vz, 2Vz, 3Vz, 4Vz, 6Vz, 8Vz, 9Vz, 10Vz and 11Vz). The calculated in-situ site mean direction is D=360°, I=35°, K=42, α_{95}=4° and after bedding correction D=1°, I=63°, K=4, α_{95}=15. This VRM component was acquired post-tilting. The in-situ inclination of 35° is close to the present day EMF inclination in the study area (I=32°). At the same time, it should be noted that this inclination is rather high with respect to the latitude of the study area (10° to 10°30'). This inclination is steeper by ~15° with respect to the GAD (20° in the study area) and by ~24° with respect to the $APWP_{0\text{-}10My}$ (11° in the study area). Then, it is possible that this abnormal high inclination exists in this area since several My.

Component A (ChRM). ChRM is present in 63% of the specimens of the sites 1Vz, 2Vz, 3Vz, 5Vz, 6Vz, 8Vz, 9Vz, 10Vz, 11Vz, 13Vz, 14Vz, 15Vz, 16Vz, 17Vz, 18Vz, 19Vz, 21Vz, 22Vz, 24Vz, 26Vz and 27Vz (Figure 5.36). The in-situ site mean direction is D=36°, I=31°, K=10, α_{95}=5° and after bedding correction D=46°, I=41°, K=4, α_{95}=11°. According to the bedding-tilt

test, the ChRM present in the Serranía Del Interior was essentially acquired post-folding. The other A components (~14%) do not have the characteristics of a ChRM, suggesting the presence of additional and unsolved components.

Component B. This is observed at all sites except at sites 15Vz and 17Vz. When combining components A (ChRM) and Component B, 4 different behaviors with respect to the inclination and declination obtained were observed. Following, the origin of these groups is discussed.

Figure 5.54 shows the statistics analysis for groups 1, 2 3 and 4 before and after bedding correction.

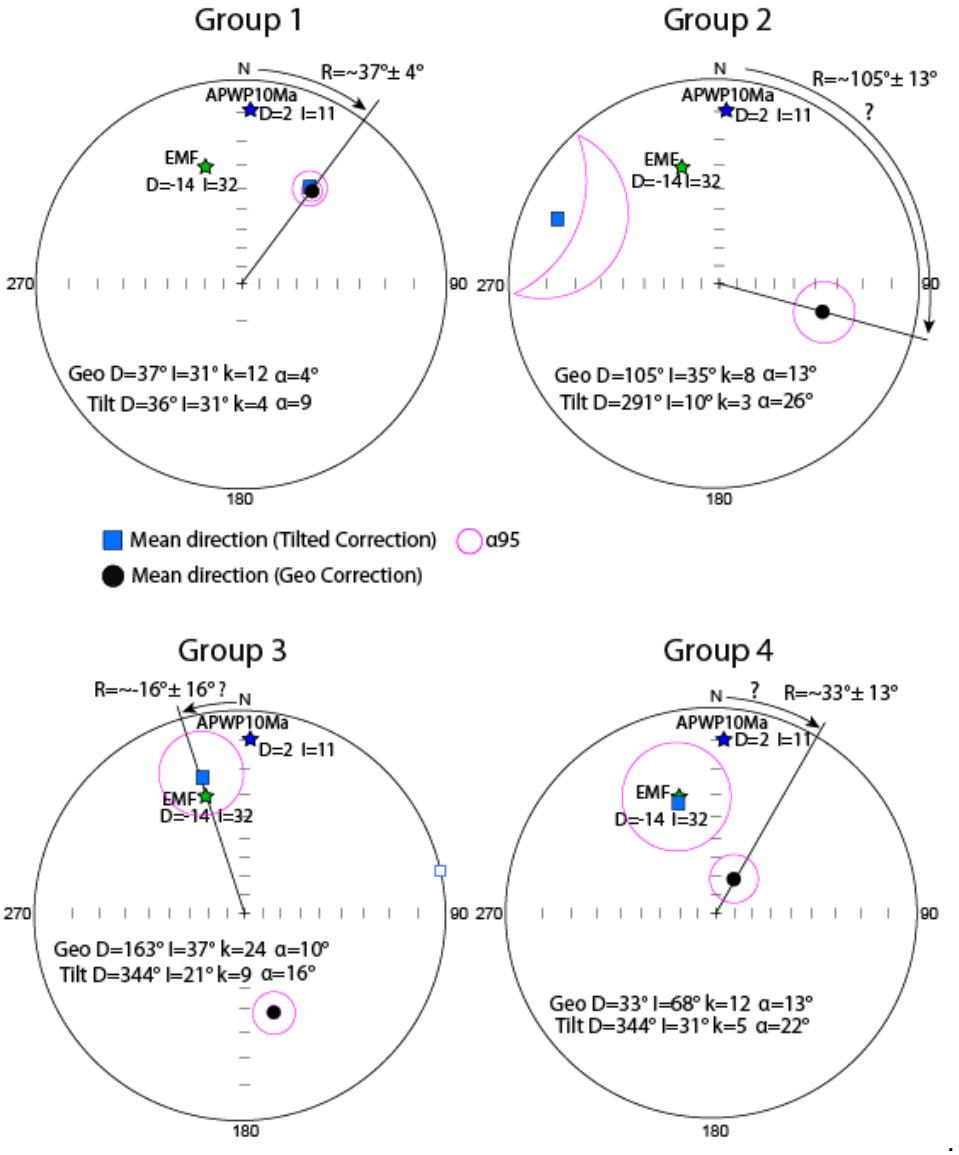

Figure 5.54. Paleomagnetic statics results obtained for groups 1, 2, 3 and 4. For clarity, all mean vectors are plotted with normal polarities.

Group 1

Group 1 includes sites 1Vz, 2Vz, 5Vz, 6Vz, 8Vz, 9Vz, 10Vz, 11Vz, 16Vz, 17Vz, 18Vz, 20Vz, 21Vz and 22Vz which show the regional paleomagnetic behavior of the Serranía Del Interior. Both magnetic polarities are observed and ~30% are reverse. The result of the statistical analysis is stable and homogeneous, yielding a site mean direction (in-situ) D=37°, I=31°, k=12 and α_{95}=4°, and after bedding correction D=36°, I=34°, K=4 and α_{95}=9° (Figure 5.55 and Figure 5.64). The bedding-tilt test shows more clustered magnetization directions before bedding correction (K=12) than after bedding correction (K=1), indicating that the remagnetization was acquired post-folding. This is therefore a remagnetization. The in-situ declination indicates a clockwise block rotation of R=37°± 4° (Figure 5.54).

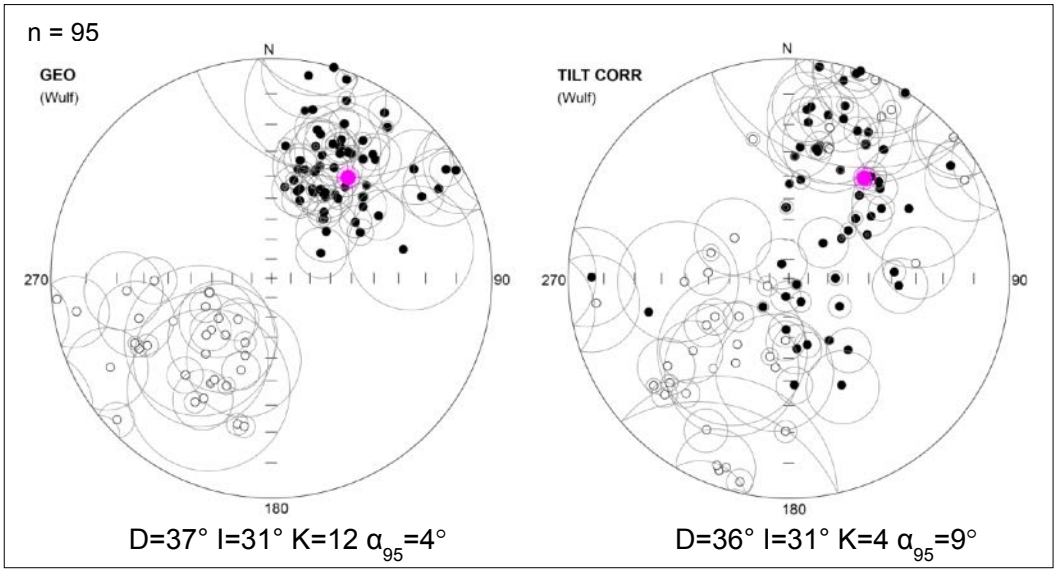

Figure 5.55. Regional analysis in the Serranía Del Interior (Group 1). Stereographic projection in-situ (Geo) and after bedding correction (Tilt).

Timing of the Remagnetization in the Serranía Del Interior

The Serranía Del Interior is the hinterland of the orogenic prism formed as a consequence of the interaction between the Caribbean plate and the South American plate (see CHAPTER 2). According to the statistical results, the regional paleomagnetic remagnetization was recorded after the formation of the Serranía (post-folding). Based on fission track data and the geodynamic framework, the main folding stage of the Serranía stopped at ~12 My (Locke and Garver, 2005). On the other hand, tectonic plate reconstruction proposes that the main compressive stage ceased at ~10 My (Pindell et al., 1998; Weber et al., 2001; Mann et al., 2001; Lingrey, 2007). Therefore; remagnetization of Group 1 sites post-dated ~10-12 Ma.

Post-folding remagnetization is a common process observed in many thrusts and belts, and particularly, within the hinterland of the thrust belt. An example of the magnetization relative to the folding pattern was studied in the central Appalachians by Stamatakos et al., (1996) (Figure 5.56a). In this model, the timing of the magnetization is associated with the sequence of deformation propagating from the hinterland to the foreland basin. Post-folding remagnetization is observed in the hinterland where folds were formed before remagnetization, in the foothills (central part of the belt) the remagnetization is synfolding because folds were developed during the remagnetization. Finally, pre-folding remagnetization is observed near the foreland basin where folds developed after remagnetization (Figure 5.56b).

The remagnetization pattern defined in the Central Appalachians hinterland obeys to the same pattern observed in the Serranía Del Interior hinterland, where the oldest folds in the area present post-folding remagnetization.

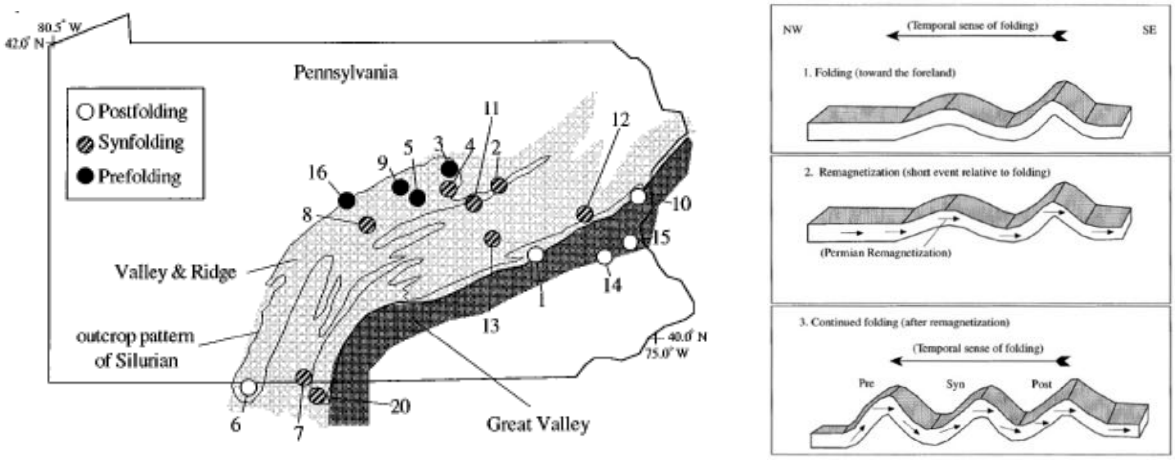

Figure 5.56. a) Fold-test results in Pennsylvania. b) Folding and remagnetization model showing the development of the fold-test results. (from Stamatakos et al., 1996).

Tectonic Regime vs. Block Rotation

Natural Remanent Magnetization (NRM) measured in the SDI rocks was acquired post-tilting. This post-tilting period possibly begins when the Serranía Del Interior formation stopped ~12 My ago according to appatite fission track data (Locke and Garner, 2005). The end of the forming of the SDI was possibly due to changes in the Caribbean plate movement relative to the South American continent from east-southeast transpression (105°) to eastward translation (85°) (Pindell et al., 2006; 2009). Starting from this time, the strike-slip component dominates in Eastern Venezuela (Mueller et al., 1999; Weber et al., 2001; Mann et al., 2001; Lingrey, 2007) and as a result, the deformation in the foreland basin decreased considerably.

We suggest that the regional clockwise block rotation of R=37°±4° observed in the Serranía Del Interior is synchronous with the dominant right-lateral strike-slip component (Figure 5.57).

Taking an age ~10-12 My as the minimum age of the block rotation (post-tilting period), a minimum rotation rate between ~3° and 3.7°/My was estimated. This rotation rate is consistent with other regional rotation rates observed in mountain belts. In Corsica, the rotation rate is well calibrated and reaches ~12°/My (Gattacceca et al., 2007). In Taiwan, where block rotation is monitored using a dense GPS network, the rotation rates ranges between 20° and 60°/My, (Lin et al., 2010). Paleomagnetic data from Taiwan suggests a minimum rotation rate of 7°/My (Sonnette, 2012).

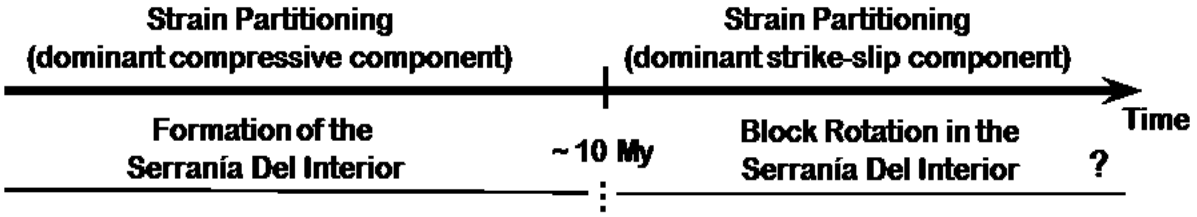

Figure 5.57. Scheme showing a strain partitioning state in the Serranía Del Interior before and after 10 Ma.

Group 2

This group (sites 3Vz, 25Vz, 26Vz and 27Vz) is located to the north of the Serranía del Interior near the El Pilar strike-slip fault. Although restricted to a small number of sites, this behavior suggests huge block rotation. The components are essentially reverse (11 of 18) and relatively scattered. The in-situ site mean direction is D=285°, I=-35°, K=8 and α_{95}=13° and after bedding correction D=291°, I=10°, K=3, α_{95}=26° (Figure 5.58 and Figure 5.64). The bedding-tilt test shows magnetization directions slightly more clustered before bedding correction, indicating that the remagnetization was possibly acquired post-folding. The declination in-situ suggest clockwise block rotation of R=105°±13° (Figure 5.54).

High magnitudes of block rotation (>90°) are sometimes observed in fold and thrust belts as the Betics (Platt et al., 2003) or the Alps (Collombet et al., 2002). But this is rather exceptional. High magnitude clockwise block rotation from 107° to 207° was documented within the core of the north Anatolian Fault (Piper et al., 1997) (Figure 5.59). It is therefore possible that paleomagnetic components of Group 2 might be related to the core of the strike-slip fault zone. Additionally, these sites are observed to be aligned E-W, supporting the presence of a possible strike-slip fault within the boundary of the El Pilar Fault system (Figure 5.60).

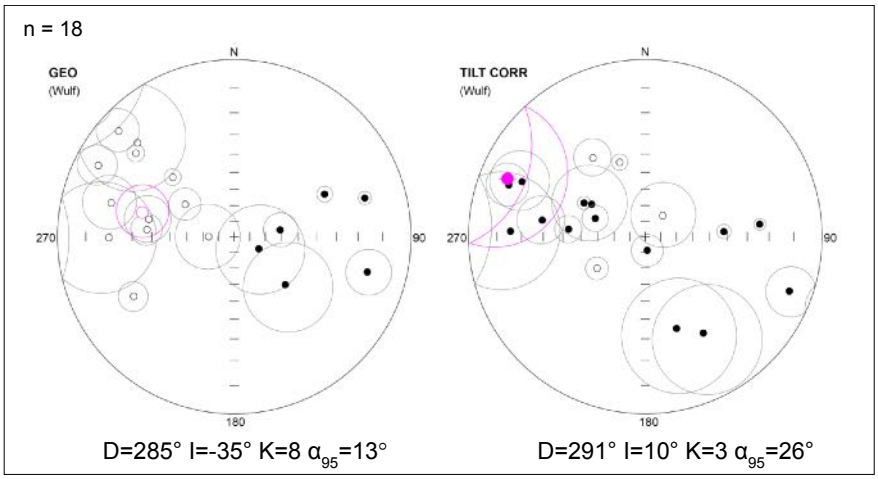

Figure 5.58. Regional analysis in the Serranía Del Interior (Group 2). Stereographic projection in-situ (Geo) and after bedding correction (Tilt).

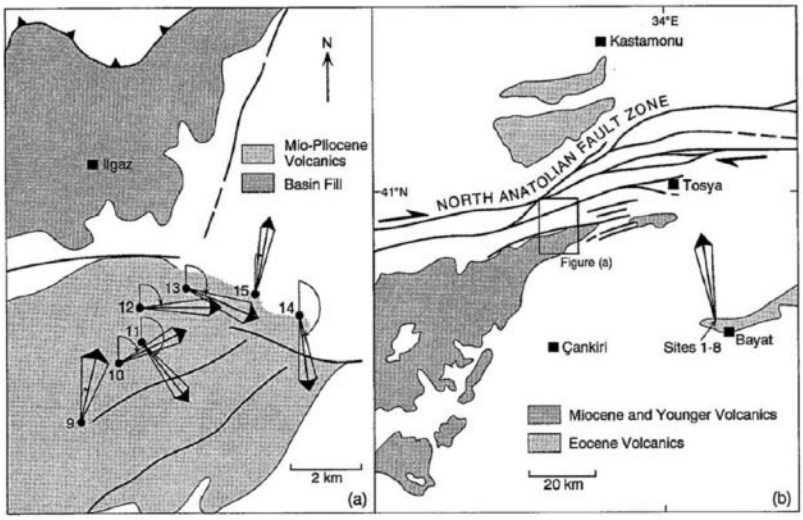

Figure 5.59. Geological map in the Ilgaz region (Turkey) showing the paleomagnetic sites near the north Anatolian Fault Zone. Sites 11, 13 and 14 show clockwise rotation >100° (from Piper et al., 1997).

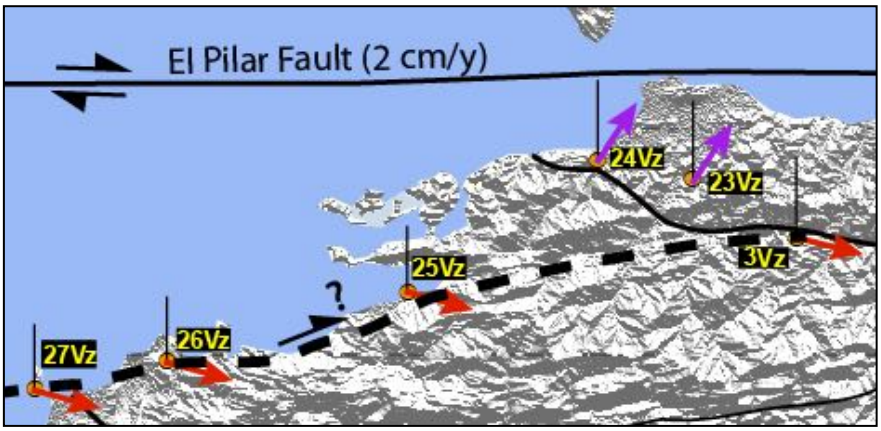

Figure 5.60. DEM image of the Serranía Del Interior with sites 3Vz, 25Vz, 26Vz and 27Vz (Group 2) showing rotation block ~105°. Black dotted line indicates a possible strike-slip faults trend. See full map in Figure 5.64.

Group 2 requires confirmation with additional sampling. To verify the presence of the fault complementary studies are also required. If confirmed, a minimum rotation rate of 10°/My is suggested and is probably active at the present.

Group 3

Sites group 3 sites (12Vz, 13Vz, 14Vz and 15Vz) are located to the east of the Serranía Del Interior, at the western boundary of the San Juan Graben. All components display in-situ normal polarity. The in-situ site mean direction of Group 3 is D=163°, I=37°, K=24, α_{95}=10° and after bedding correction D=164°, I=-20°, K=9, α_{95}=16° (Figure 5.61 and Figure 5.64). The bedding-tilt test shows that magnetization directions are more clustered before bedding correction (K=25), suggesting that the remagnetization was acquired post-folding. However, the declination and inclination after bedding correction are close to the present day EMF. In-situ, block rotation is strongly clockwise R=163°±10. After bedding correction the rotation is slightly counterclockwise (R=-16°±16°) (Figure 5.54). Here it is assumed that the most reasonable solution is that the paleomagnetic component of Group 3 is likely a pre-folding magnetization with little or no rotation. This hypothesis must be confirmed by further studies. These studies might be of importance because the lack of significant rotation along the boundary of the San Juan Graben delineates a possible block limit. Site 4Vz displays a paleomagnetic component very close to the north Quadrant. At this site, VRM is believed to completely overprint the previous paleomagnetic components (Figure 5.64).

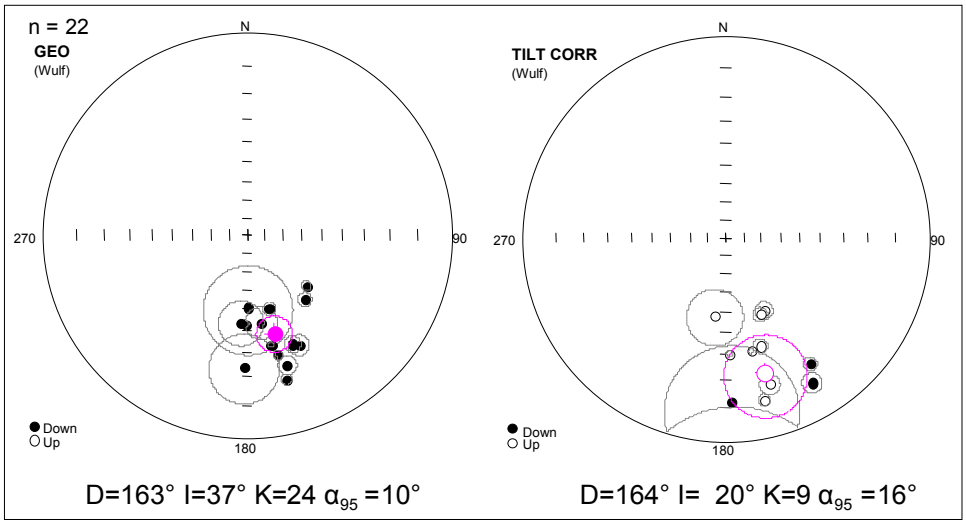

Figure 5.61. Regional analysis in the Serranía Del Interior (Group 3). Stereographic projection in-situ (Geo) and after bedding correction (Tilt).

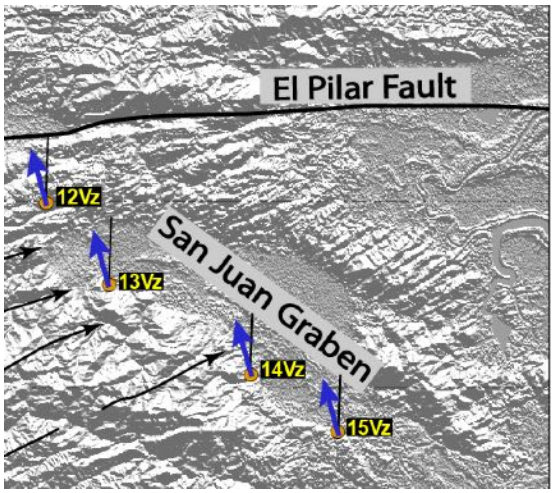

Figure 5.62. DEM image of the Serranía Del Interior with sites 12Vz, 13Vz, 14Vz and 15Vz showing slightly counterclockwise (R=-16°±16°).See full map in Figure 5.64.

Group 4

The Group 4 includes site 19Vz located in the Caripe Block and sites 23Vz and 24Vz located to the north of the Serranía, near the San Francisco Fault. All components have normal polarity. The in-situ site mean direction is D=33°, I=68°, K=12, α_{95}=13° and after bedding correction D=344°, I=31°, K=5, α_{95}=22° (Figure 5.63 and Figure 5.64). The bedding-tilt test shows a more clustered magnetization direction before bedding correction, indicating that the remagnetization was acquired post-folding. The in-situ declination indicates clockwise block rotation of R=33°±13° (Figure 5.54). This group is characterized by a very steep inclination of 68°. More sampling in the zone is necessary in order to confirm and to understand this behavior.

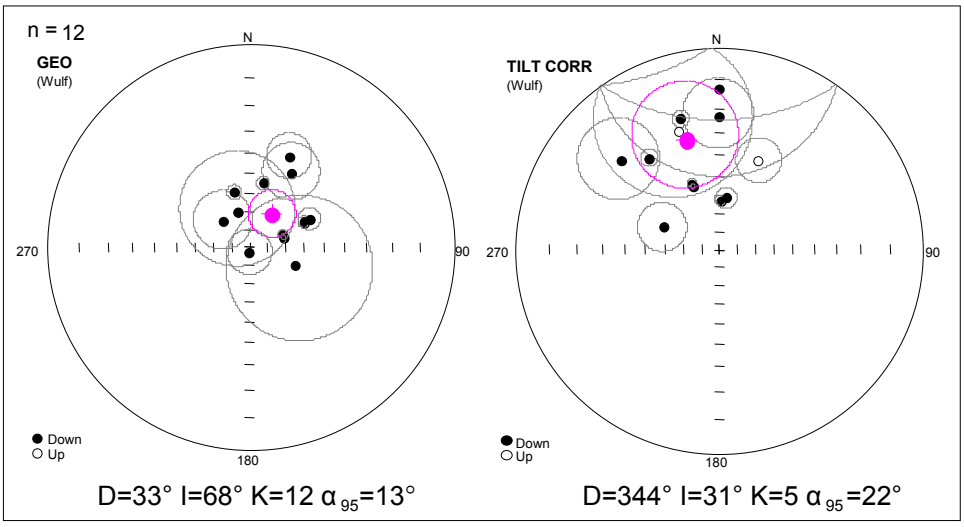

Figure 5.63. Regional analysis in the Serranía Del Interior (Group 4). Stereographic projection in-situ (Geo) and after bedding correction (Tilt).

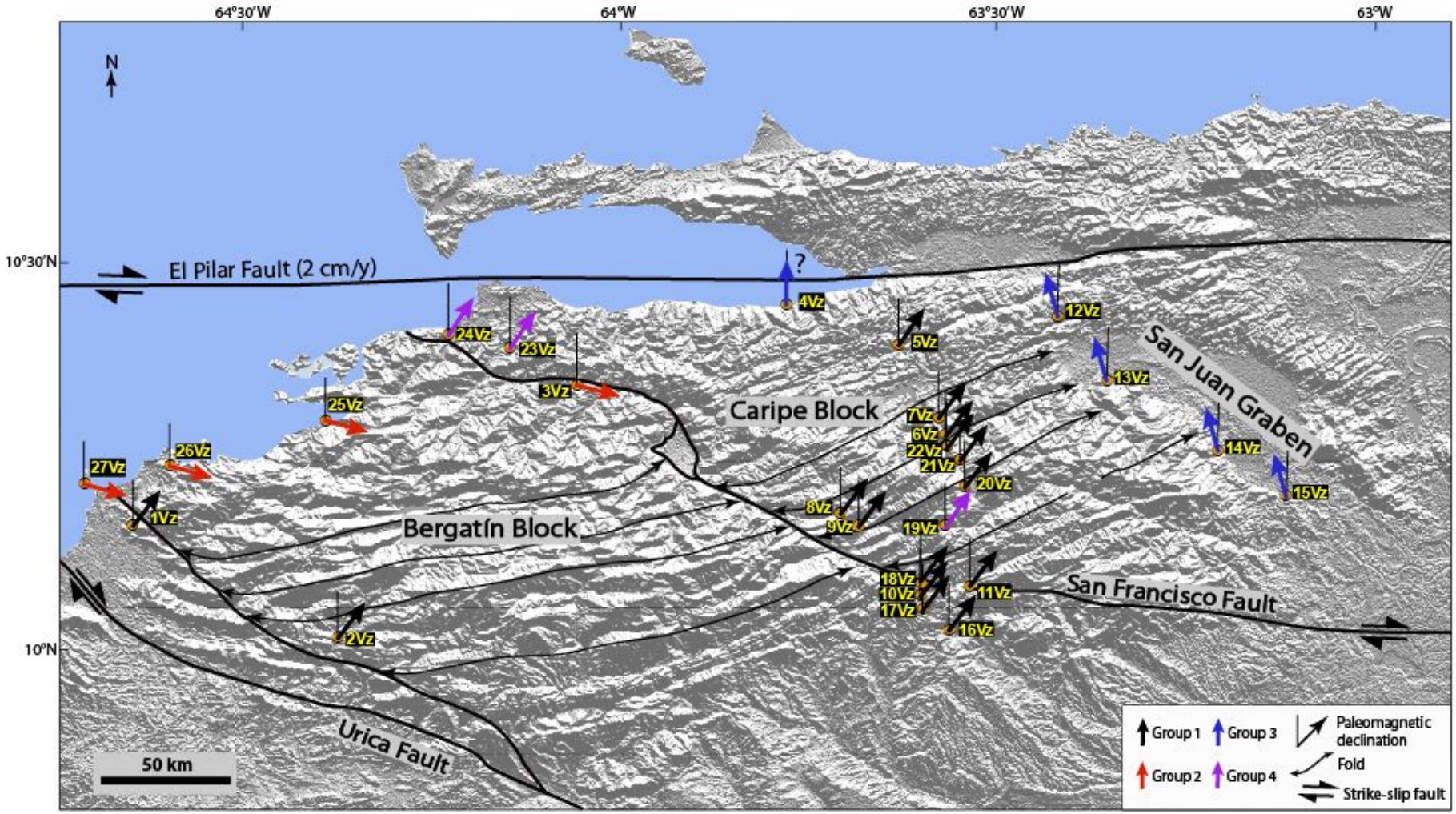

Figure 5.64. DEM image of the Serranía Del Interior with sampled sites. Arrows indicate paleomagnetic declination for each site.

Comparison with Published Paleomagnetic Data

Very few paleomagnetic studies refer to Northern Venezuelan and these paleomagnetic studies lacks of tilt test. Skerlec and Hargraves (1980) explored the North Venezuelan Basin, west to our study area. In this study, the way data treatment is disputable because bedding tests are not discussed. However, one of the undisputable results of this study is the detection of a large clockwise rotation of the paleomagnetic component (Figure 5.65a). East of our study area, Burmester et al. (1996) studied volcanic and metavolcanic rocks from the island of Tobago. A pre-tilting component was isolated, showing a strong clockwise deviation (Figure 5.65b). The results of this study are therefore consistent with these two published studies where large clockwise rotation of about 90° is detected.

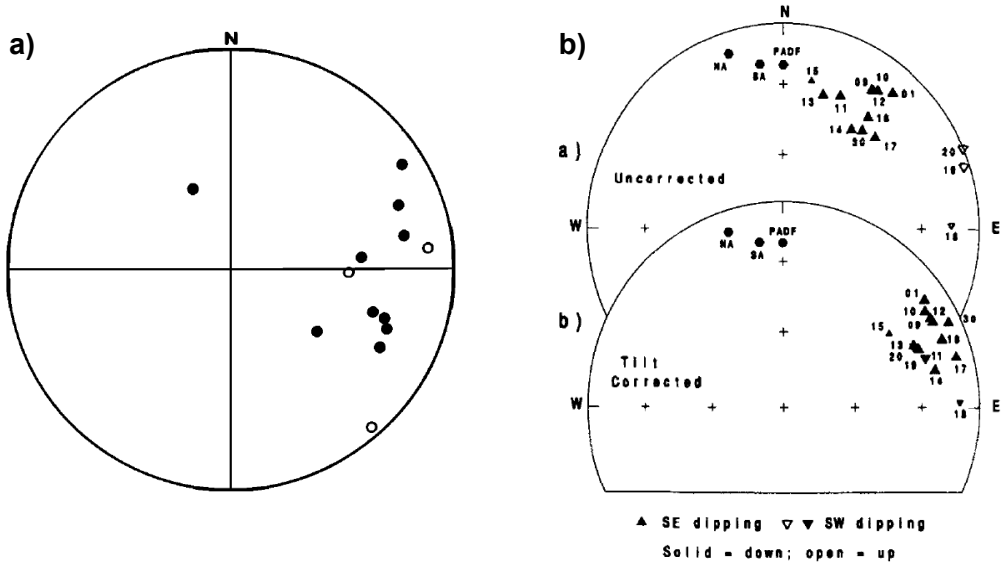

Figure 5.65. a) Paleomagnetic results within the Villa de Cura Tectonic Belt and the Cerro Pelon Ultramafic Complex (~100 My) to the north of Venezuela (Sterleck and Hargraves, 1980). Note the strong clockwise declination. b) Paleomagnetic results of the volcanoclastic sediments (~100 My) from the island of Tobago (from Burmester et al., 1996). Again, a strong clockwise rotation of ~90° was observed.

It is also interesting to compare the results of this study with to the counterpart of the Caribbean Arc. The counterclockwise rotation here is largely detected as that Early recognized by Skerlec and Hargraves (1980). In Puerto Rico, Reid and Plumley (1991) reported a post-Late Miocene (between 11 and 4.5 Ma) counterclockwise rotation of 25°±6° (Figure 5.66). A rotation rate of 4°/Ma was inferred. In central Cuba, Tait et al. (2009) reported pre to syn-tilting magnetization and strong counterclockwise rotation (Figure 5.67).

The broad picture of the paleomagnetic results is clockwise rotation in the southern

Caribbean boundary and counterclockwise rotation in the northern Caribbean boundary. This picture closely resembles the block rotation observed in the Betic-Rif Arc (Platt et al., 2003)

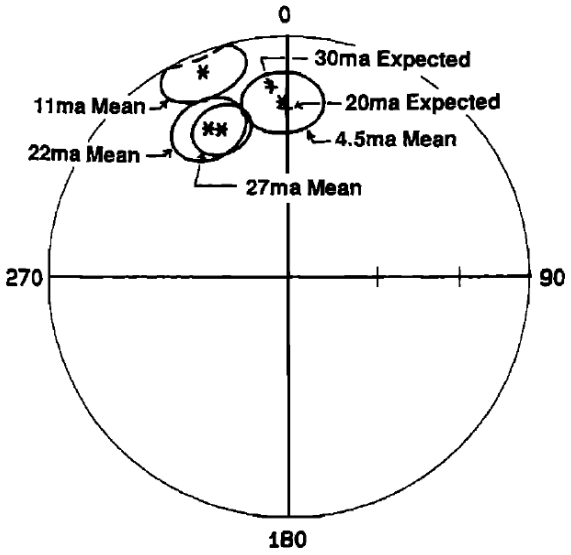

Figure 5.66. Mean and expected calculated plot directions of upper Oligocene to Early Pliocene sediments from Puerto Rico Island. Note counterclockwise rotation of 27-11 My (from Reid and Plumley,1991).

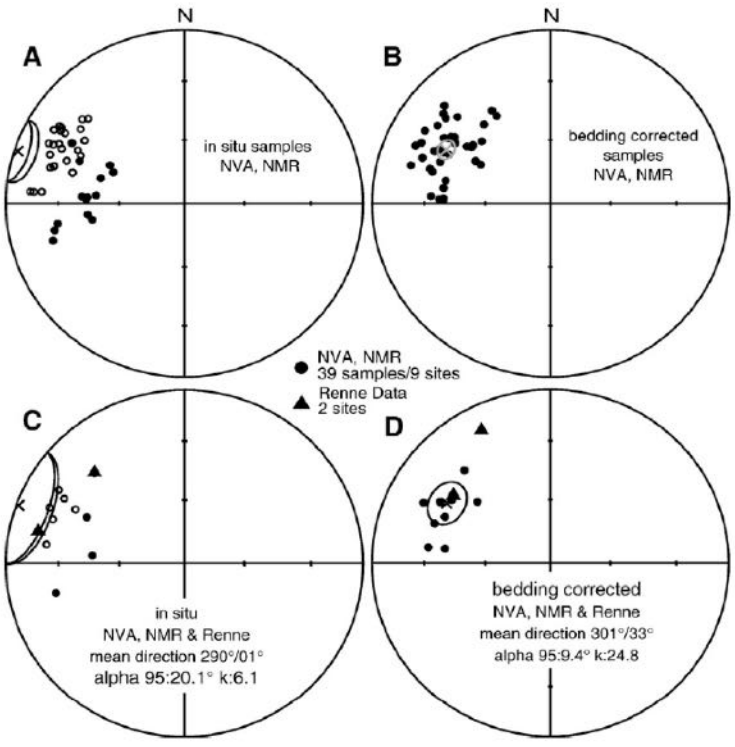

Figure 5.67. Paleomagnetic results calculated for Cabaiguán Formation (NVA) and Provincial formation (NRM) from the island of Cuba. Note pre to syn-tilting magnetization (from Tait et al., 2009).

Taking into account the symmetry of block rotation in the Caribbean region, it is possible to infer that the clockwise rotation present in the southeast Caribbean plate boundary (north of Venezuela) is linked to the major Boconó-San Sebastían-El Pilar dextral strike-slip fault system. Similarly, the counterclockwise rotation observed in the northeast Caribbean plate boundary (Caribbean islands) is probably related to the Enriquillo-Plantain Garden sinistral strike-slip and the Septentrional fault system (Figure 5.68).

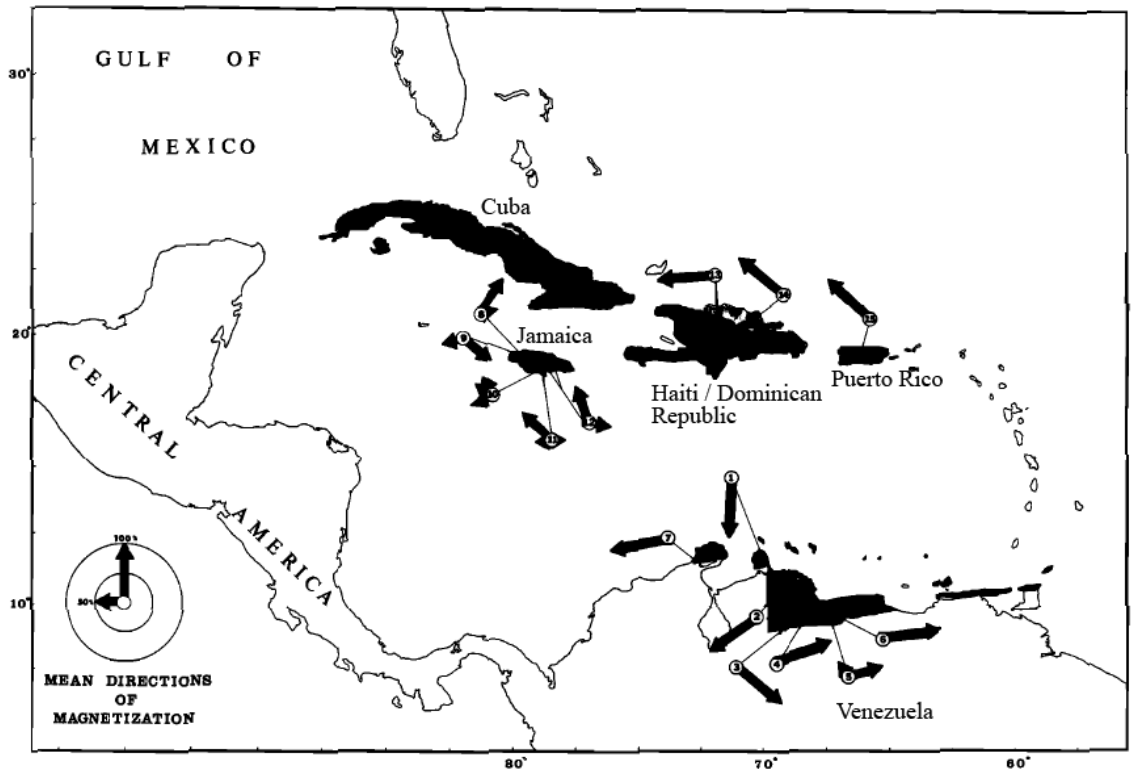

Figure 5.68. Caribbean map showing the rotations direction along the southern and northern boundaries of the Caribbean Plate. Paleomagnetic data was compiled of studies carried out in the area (modified from Skerlec et al.,1980).

CHAPTER 6. General Discussion and Conclusions

The paleomagnetic study of the Serranía Del Interior (SDI), the morphotectonic analysis, the terrace dating and the seismic interpretation in the Monagas Fold and Thrust Belt (MFTB) have been carried out in this thesis. This new dataset brings new constraints for a better understanding of the neotectonics of the Northeastern Venezuelan Basin.

Northeastern Venezuela is known as an active region as a result of the interaction between the Caribbean and South America plates since the Oligocene (e.g. Speed, 1985; Erlich and Barrett, 1992; Roure et al., 1994; Parnaud et al., 1995; Pindell et al., 2006; among others). The eastward displacement of the Caribbean plate up to 22 mm/y (relative to South America) is predominantly accommodated by the El Pilar Fault (Jouanne et al., 2011). As a result, the reported seismicity in the Serranía Del Interior is rather weak and diffuse (Mw <3.9). Recent GPS velocity studies carried out by Reinoza et al. (2015) suggests a possible convergence within the SDI but this work needs confirmation. In this thesis, new results that confirm the present day activity in the SDI since ~12-10 My are obtained. The paleomagnetic study shows that clockwise block rotation (~3.7°/My). Similarly, to the southwest of the Serranía Del Interior, in the Monagas Fold and Thrust Belt, a combined approach of seismic interpretation of the Plio-Pleistocene units and morphotectonic analysis reveals a minimum uplift rate between 0.1-0.6 mm/y at most for the last 5.3 My (Figure 6.9).

In this chapter, I propose integrating this new dataset to some conceptual models.

6.1. Neotectonics in the Monagas Fold and Thrust Belt

Parra et al. (2011) reported a maximum shortening of 59 km within the MFTB from pre-Cretaceous to Early-Middle Miocene. Later, an erosion period is marked by an unconformity at ~10 My (MMU) followed by a compressive stage that folded this unconformity, reactivated the Pirital and Tarragona thrusts and controlled the sedimentation pattern producing growth strata in the post-MMU units Then, the top of the Late Miocene unit is represented by another unconformity at ~5.3 My (LMU). This has also been folded suggesting a new compressive stage in the Plio-Pleistocene (post-LMU), possibly active at present.

The Plio-Pleistocene shortening (post-LMU) calculated to the west in the Tarragona zone is of ~1.3 km (6%) (near the Urica Fault) and decreases to the east in the Jusepín zone to ~0.5 km (3%) (away from the Urica Fault). This suggests that the Urica Fault is playing a role in the location of the active tectonics. Using seismic lines and the LMU geometry as a reference a minimum Plio-Pleistocene uplift rate of 0.3-0.4 mm/y was estimated.

Relation between Deep and Surfaces Structures

The gradient of shortening in depth from west to east matches with the topographic ridges in the Monagas Fold and Thrust Belt. The greater ridges with heights around 400 m are located to the west over the Tarragona High. These topographic uplifts decrease progressively to the east (around the Jusepín High) with average heights of 80 m. The uplift and shortening observed in the Monagas Fold and Thrust Belt are not observed eastward in the surrounding areas, therefore, it is possible that the compression in this zone is the result of local tectonics (Figure 6.9).

In the Tarragona zone, there is a good match between the Tarragona High identified in the seismic lines (e.g. M1 seismic line) and the Tarragona Ridge observed in SRTM DEM (Figure 6.1). This ridge of ~375 m high is interpreted to be the surface expression of the Tarragona High formed by the Tarragona thrust. There, the quaternary terrace 3TS of age ≤ 90±5 ky was identified. This terrace is cut by a thrust which demonstrates the active compression at the surface after its formation (CHAPTER 3). From the dating terraces, a minimum vertical deformation rate of 0.3 ± 0.3 mm/y was calculated in this zone. This rate coincides with the Plio-Pleistocene uplift rate of ~0.3 mm/y calculated from M1 seismic line (Table 6.1).

To the east of the Monagas Fold and Thrust Belt, in the Pirital zone, there is again a good match between the Pirital High (seismic lines M3 and M4) and the Punta de Mata Ridge of ~290 m high (SRTM DEM) (Figure 6.1). This is interpreted to be the surface expression of the folded Plio-Pleistocene units due to the activity of the Pirital Thrust. The southeastern propagation of the Pirital Thrust system developed several secondary thrusts within the Carapita formation. This unit and upper units have been consequently

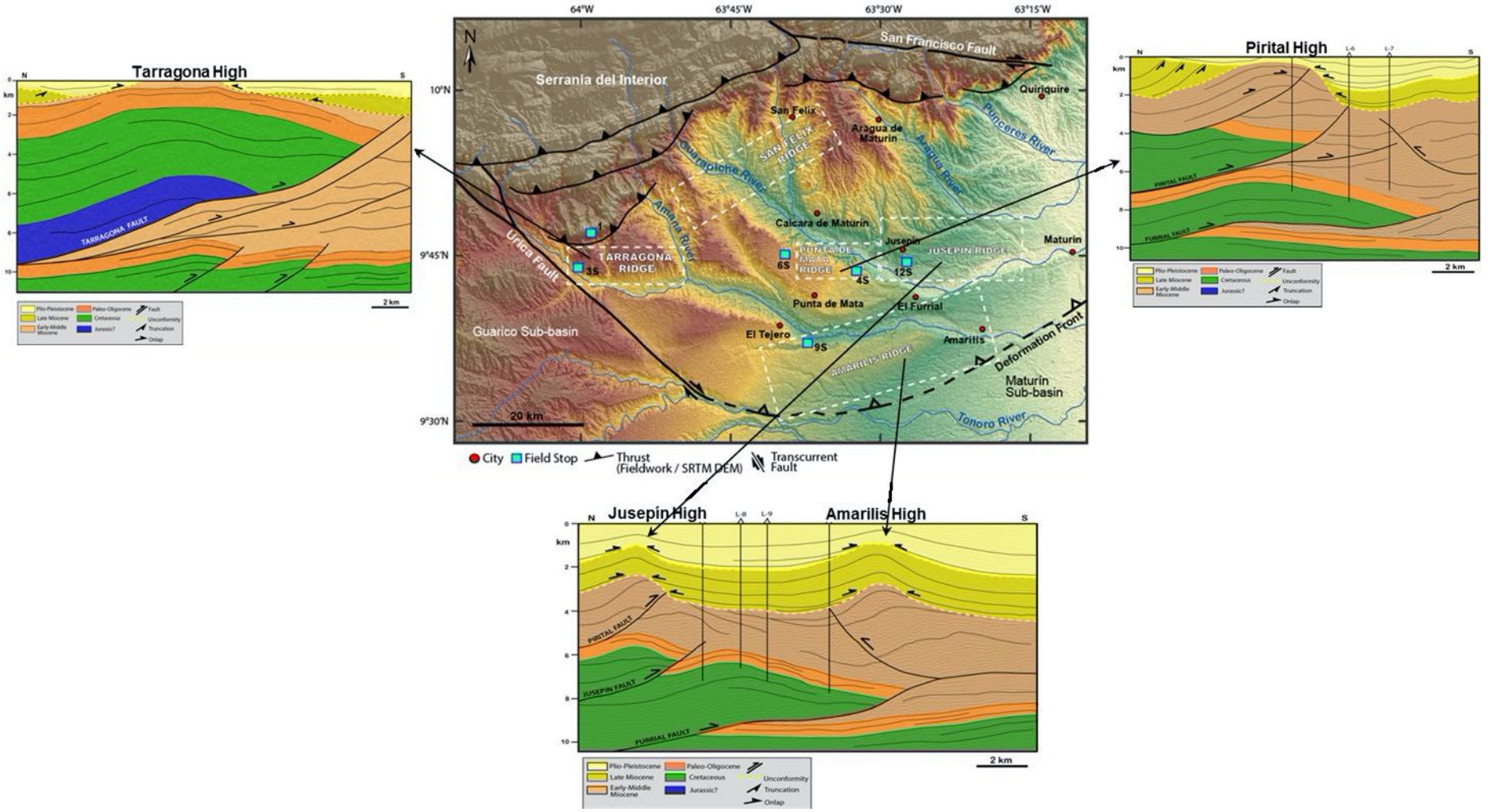

Figure 6.1. Relation between deep and surfaces structures in the MFTB. Note that the structural highs identified in seismic lines correspond to the topographic ridges and terraces identified in fieldwork and in the DEM.

folded and uplifted until reaching the surface as the Punta De Mata and Jusepín ridges. The quaternary terraces located in the Punta de Mata Ridge (T4S) and in the Jusepín Ridge (T12S) dated at ≤ 15 ± 5 ky and ≤ 35 ± 5 ky, respectively, show evidence of tilting, faulting and folding, similar to other tectonically active zones in the area (Figure 6.1). A minimum vertical deformation rate of 0.1 ± 0.06 mm/y was obtained from terrace dating. In contrast, an uplift rate of ~0.3–0.4 mm/y was calculated from seismic lines M2 and M3 in this same zone (Table 6.1).

Finally, to the south, the thrust belt system propagated and folded the post-Middle Miocene layers. The compression to the south is mainly accommodated by the Furrial thrust. This thrust is propagated within the Carapita Formation (shale unit) creating a backthrust which generated the Amarilis High. At the same time, this backthrust controlled the deposition of the upper sediments (from Late Miocene to Pleistocene) which reached the surface forming the Amarilis Ridge of ~200 m high (Figure 6.1). The quaternary terrace located in the Amarilis Ridge was dated at ≤ 25 ± 5 ky implying a vertical deformation rate of 0.6 ± 0.3 mm/y. This is a rather high uplift rate when compared with the Plio-Pleistocene uplift rate of ~0.3 mm/y estimated from seismic line interpretation (M4 and M5 seismic lines) (Table 6.1).

When comparing the Late Pleistocene vertical deformation rates calculated from terrace dating with the Plio-Pleistocene uplift rates obtained from seismic interpretation, an uplift rate ≤ 0.6 mm/y is estimated for the last 5.3 My in the MFTB (Table 6.1).

Table 6.1. Main results of the deep and surface structure analysis in the MFTB carried out in this thesis.

Thrust associated with the surface and depth structures	Surface Structure	Vertical deformation rate calculated from surface structures (mm/y)	Depth structure	Uplift rate calculated from seismic lines (mm/y)
Tarragona thrust	Tarragona Ridge (site 3S)	0.3 ± 0.3	Tarragona High	~0.3
San Felix Thrust	San Felix Ridge (site 10S)	No dated surface	Seismic lines not available	Seismic lines not available
Pirital thrust	Punta de Mata Ridge (site 4S)	0.1 ± 0.06	Pirital High	~0.3-0.4
Pirital and Jusepín thrusts	Jusepín Ridge (site 12S)	0.1 ± 0.06	Jusepín High	~0.3
Amarilis Backthrust	Amarilis Ridge (site 9S)	0.6 ± 0.3	Amarilis High	~0.3

The comparison between the DEM and the structural intra-Pleistocene map (Figure 6.2) emphasizes the relation between deep and surface structures (CHAPTER 3).

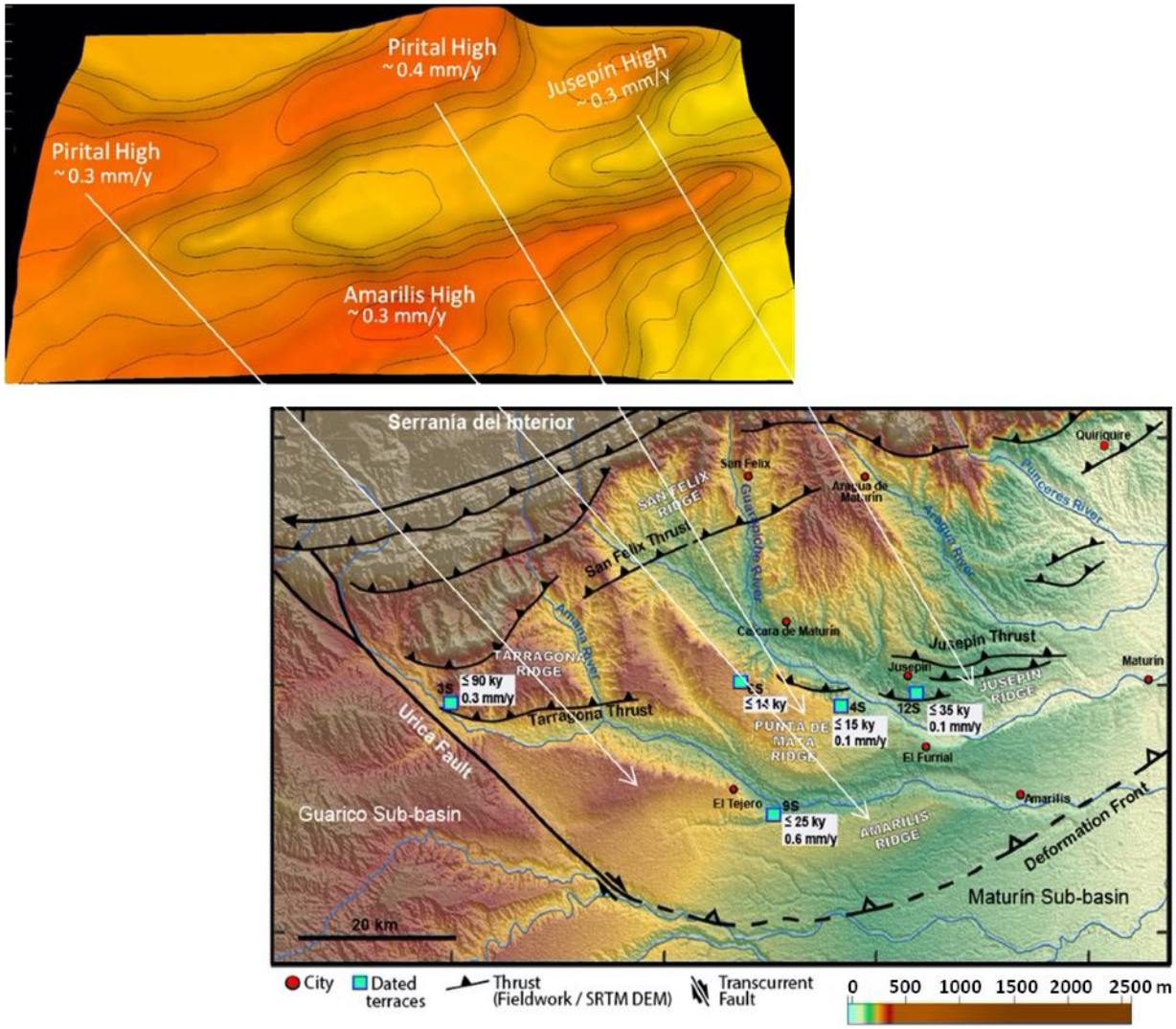

Figure 6.2. Relation between deep and surface structures. In depth, Pleistocene structural map (above). DEM showing the surfaces structures (ridges), the ^{10}Be and ^{26}Al ages and the uplift rates calculated from deformed surfaces observed in the field (below).

In order to explain the gradient of the Plio-Pleistocene units shortening are proposed to be related the active tectonics in the Monagas Fold and Thrust Belt to the Urica Fault. Cunningham et al. (2003) show a conceptual model where thrusts are developed in the strike-slip fault termination (horsetail termination) (Figure 6.3). The shortening caused by these thrusts decreases as it becomes more distant from the strike-slip fault. There is, therefore, a good analogy between the Cunningham model and the Urica Fault termination. We propose that since ~10 Ma (post-MMU) part of the oblique convergence is transferred through the Urica Fault which at the same time reactivated out-of-sequence to the Tarragona and Pirital thrusts (shown in the seismic line and structural maps). Through the propagation of these thrusts towards the south, secondary thrusts developed in the Carapita shales have uplifted the post-Middle Miocene units to the surface. Additionally, this model shows that the shortening produced by these thrusts is greater near the strike-slip fault (in our case, the Urica Fault) and smaller as it becomes more distant from the fault.

This is in good agreement with the Plio-Pleistocene shortening of ~1.3 km near the Urica Fault and of ~0.5 km towards the east, as it becomes more distant from the fault (Figure 6.3).

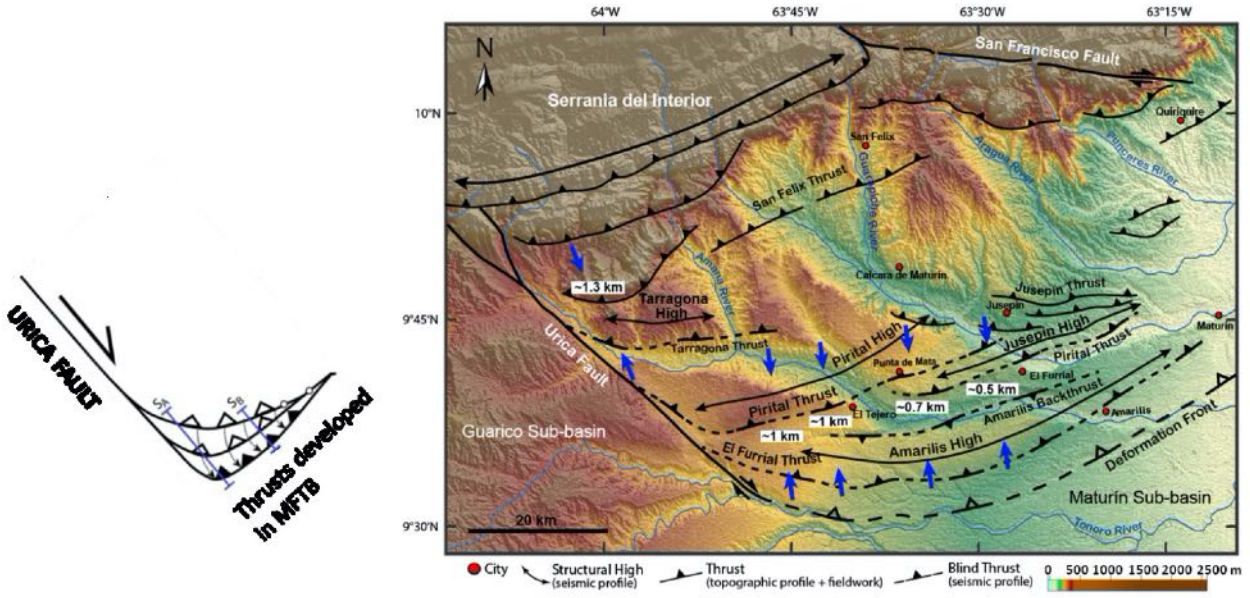

Figure 6.3. Structural configuration of the Monagas Fold and Thrust Belt (right) versus strike slip fault model by Cunningham (left). The conceptual model proposed by Cunningham (2003) shows the thrusts developed in the terminal zone for dextral strike-slip faults. Note that the shortening is greater near the strike-slip fault (S_A) and smaller as it becomes more distant from the fault (S_B) (Modified from Cunningham, 2003). The structural map (DEM) shows the surface and depth structures (dashed lines) in the Monagas Fold and Thrust Belt. Note that the shortening decreases progressively from the Urica Fault to the east.

6.2. Neotectonics in the Serranía Del Interior

The paleomagnetic study performed in this work on the Serranía Del Interior (Caripe and Bergatín blocks) shows that these blocks have rotated 37°± 4° clockwise relative to the North. Additionally, the negative bedding-tilt test indicates that the Natural Remanent Magnetization (NRM) was acquired post-tilting (CHAPTER 5). We interpret that this post-tilting period possibly began when the main compressive episode of the Serranía Del Interior formation stopped ~12 My ago according to apatite fission track data (Locke and Garner, 2005). This is linked to a change of the Caribbean plate movement relative to South America from east-southeast transpression (105°) to eastward translation (85°) at ~10 Ma (Pindell et al., 2006; 2009). We then infer an average rotation rate of 3.7°/ My for the last 10 My (Figure 6.9).

On the other hand, GPS studies, stress tensors and seismicity data show that the Serranía Del Interior, Urica and San Francisco faults are active. Velocity vector (Weber et al., 2001; Perez et al., 2001) and stress tensor (Colmenares & Zoback 2003) studies indicate an almost pure wrenching movement between the Caribbean and South America plates. Others authors suggest that pure wrenching movement has a transtension component (e.g. Pindell et al., 2006). However, another

study using stress tensors shows the presence of a compressive component NW-SE in the same area (Colmenares and Zoback, 2003). Geological data (Beltran & Giraldo, 1989; Audemard et al., 2000; 2005), focal mechanism solutions (Audemard et al., 2005) and recent GPS studies (Jouanne et al., 2011) seem to corroborate this compressive component. Audemard (Schmitz et al., 2014) interpret that the transpression is the dominant process at a plate boundary scale and the transtension can be observed by the two pull-apart basins (Cariaco Trough and The Gulf of Paria, west to east respectively) both formed at the ends of the El Pilar Fault between 15-10 My ago.

More recently, Reinoza et al. (2015) show 10 GPS velocity vectors in the Serranía Del Interior directed NNE with respect to South America (Figure 6.4). The velocity range is between 3-4 mm/y in the center part of the Serranía and 8 mm/y to the north, near the El Pilar Fault segment. Although Reinoza et al. (op. cit.) not interpret the relation among these velocity vectors specifically; in the center part (TAC0, IPU0 and COV0 stations) the velocity difference among them could cause a local compression in the area.

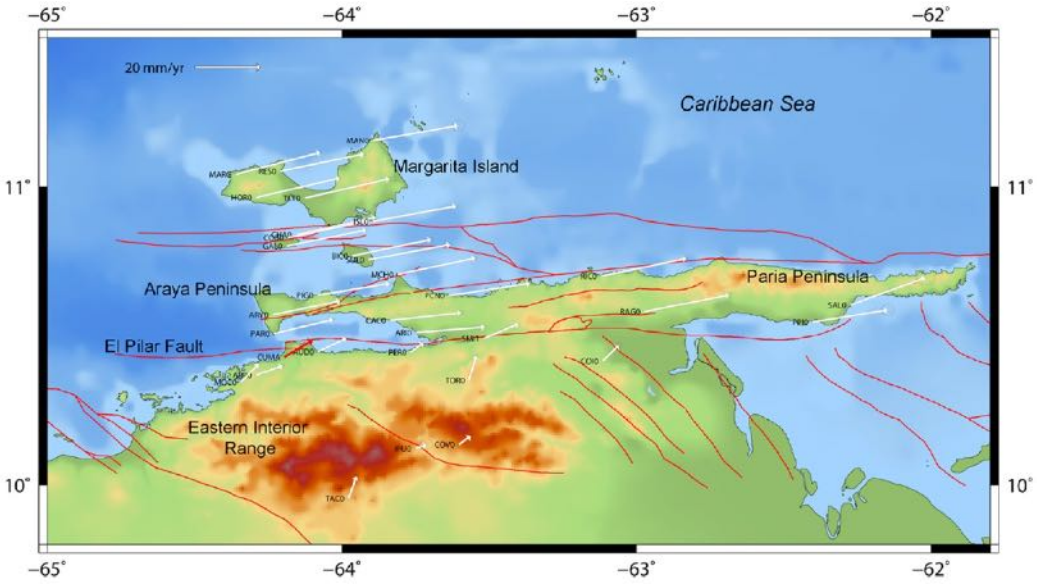

Figure 6.4. Observed velocity vectors in the Serranía Del interior (white arrows) with respect to the South America plate reference frame (from Reinoza et al., 2015).

A clockwise block rotation has been observed in previous paleomagnetic studies to the west of the Serranía Del Interior and in the island of Tobago (Skerlec and Hargraves, 1980; Burmester et al., 1996) (Figure 6.5). These paleomagnetic data merit revisiting in order to constrain the magnitude of block rotation because fold tests are sometimes lacking. In the northeast border of the Caribbean plate, mainly counterclockwise block rotations are documented in the islands of Cuba, Jamaica, Puerto Rico and Haiti / Dominican Republic (Skerlec and Hargraves, 1980; Reid and Plumley, 1991; Tait et al., 2009). Taking the symmetry of the block rotation into account, we interpret that the clockwise rotations present in the southeast of the Caribbean plate boundary (north of Venezuela) are linked to the major Boconó-San Sebastían-El Pilar dextral strike-slip fault

system. Similarly, the counterclockwise block rotations observed in the northeast Caribbean plate boundary (Caribbean islands) are probably related to the Enriquillo-Plantain Garden and Septentrional sinistral strike-slip fault system. In the same manner, for example, such a block rotation symmetry is documented in the western Mediterranean external Betic-Rif Arc. The Betic sector of the arc displays clockwise rotation linked to dextral strike-slip movement while the southern Rif rotates counterclockwise linked to sinistral strike slip movement in an oblique convergence regime (Platt et al., 2003).

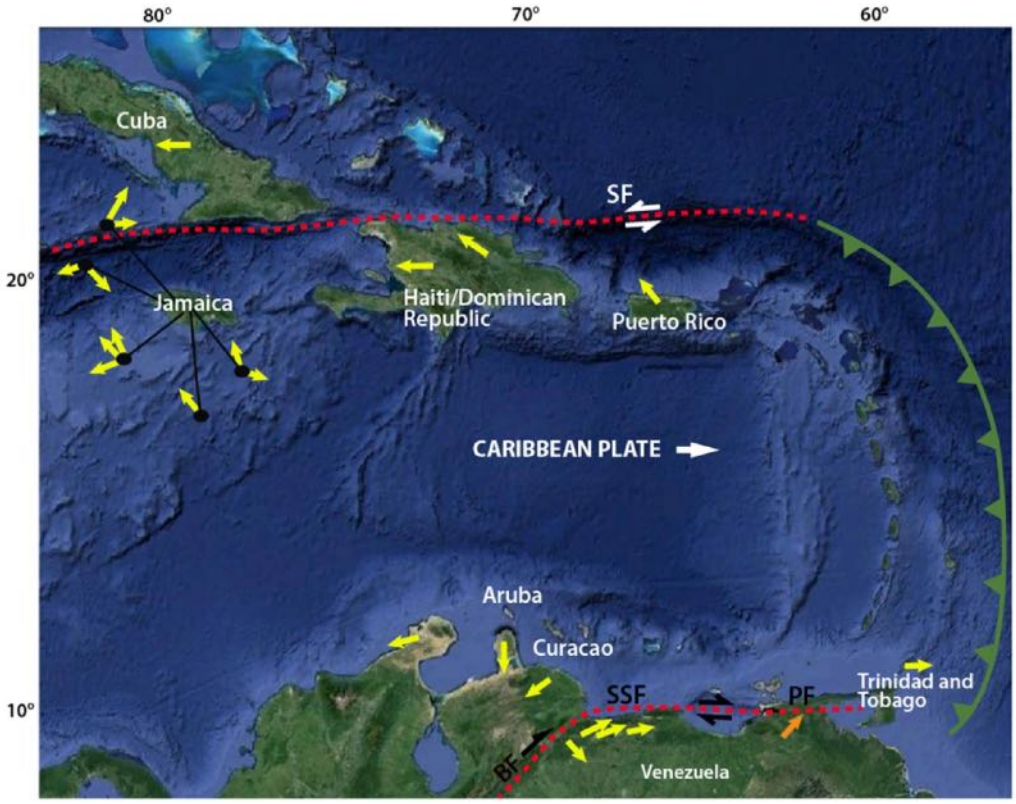

Figure 6.5. Caribbean map showing the rotation direction along the southern and northern boundaries of the Caribbean plate. The yellow arrows represent paleomagnetic data compiled by Skerlec and Hargraves, (1980); Reid and Plumley, (1991) and Tait et al., (2009). The orange arrow represents the paleomagnetic data obtained in this study. SF = Septentrional Fault, BF = Boconó Fault, SSF = San Sebastián Fault, PF = El Pilar Fault.

Relation between Block Rotation and Strike-Slip Fault

Classical models relate clockwise block rotation to dextral strike-slip faults (section 5.1 in CHAPTER 5). However, the Serranía Del Interior does not possess the configurations that these models present and there is no evidence of southern major strike-slip faulting. Instead, I propose relating the structural configuration of the Serranía del interior to the analogue model developed by Schreurs (1994) (Figure 6.6). In this model, the displacement of a dextral strike-slip fault (similar to El Pilar Fault, in our case) develops oblique dextral strike-slip faults (synthetic Riedel shears, as the Urica and San Francisco faults). Also, this model shows the relation between these fault systems with the block rotation.

During the experiment, an induced shear strain of $9x10^{-5}$ s^{-1} was applied. At a shear strain of γ = 0.09, synthetic Riedel shears (R in Figure 6.6A) are the first structures formed and have a strike between 23° and 35° respect to the applied shear direction. The progressive increase of the shear forms new faults (R_L and R_L' in Figure 6.6B-D) while the Early faults remains active. When the shear strain increases from γ = 0.17 to γ = 0.39, clockwise rotation along a vertical axes of about 30° is observed. In an unconfined transverse border (as in this experiment) the block rotation could be associated with lateral displacement of material parallel to the synthetic Riedel faults (Schreurs, 1994).

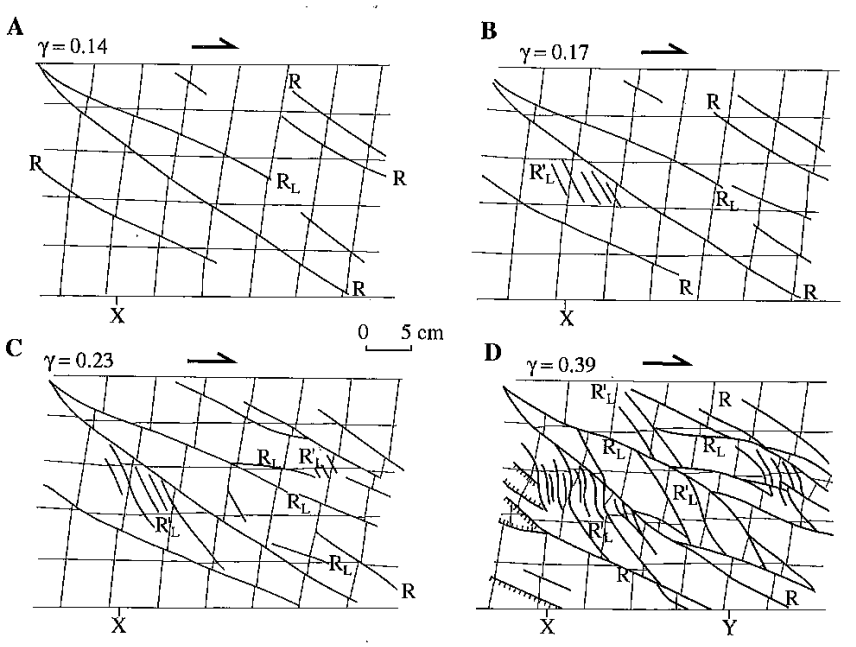

Figure 6.6. Successive stages of the analogue model experiments on strike-slip faulting. Square grids represent the colored sand; thick lines represent traces of visible faults. R=synthetic Riedel shear, R_L= lower angle synthetic fault, R_L'= lower angle antithetic fault (from Schreurs, 1994).

Based on this model, we propose relating the El Pilar Fault to the dextral strike-slip fault of Urica and San Francisco (synthetic Riedel shears) as initially suggested by Audemard et al. (2005). We then propose that this shearing system has produced the clockwise block rotation observed in the Caripe and Bergatín blocks. The analogue model of Schreurs shows that due to the strain increasing, smaller blocks are formed within the area. Consequently, the rotation degrees of these smaller blocks can vary but the rotation direction will be the same (clockwise for a dextral strike-slip fault). Different degrees of rotation are expected to be observed in a regional block if the main block is partitioned into smaller blocks. In the Serranía Del Interior, different sectors display rotation from 16° degrees near the San Juan Graben up to 105° near the El Pilar Fault (Figure 6.7).

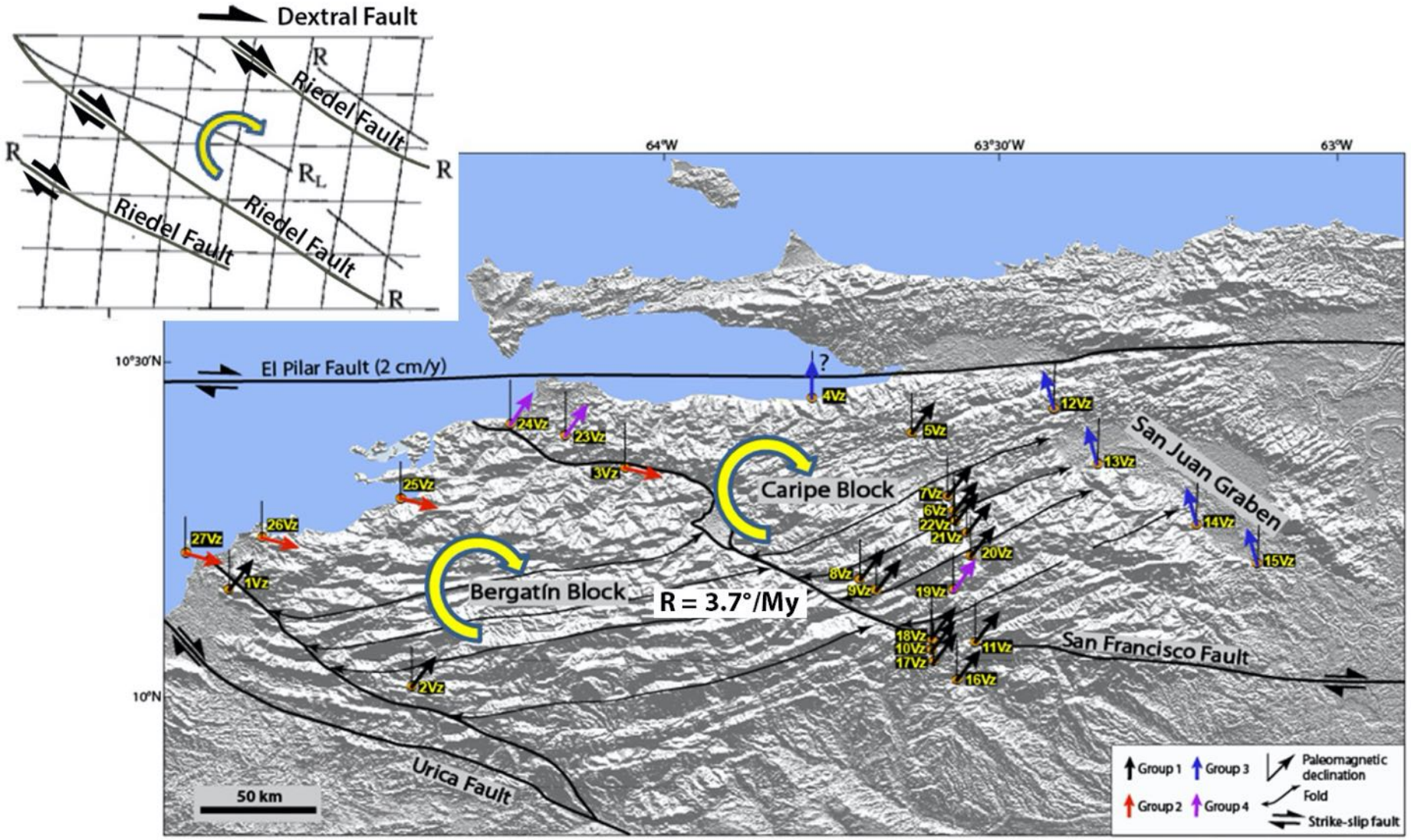

Figure 6.7. Comparison of the structure of the Serranía Del Interior (Upper panel) with the strike-slip faulting and block rotation experimental analogue model proposed by Scheurs (1994) (lower panel).The dextral fault is representated by the El Pilar Fault while the Riedel synthetic fault is represented by the Urica and San Francisco faults.

6.3. Integrated Geodynamic Model of the Neogene in the Northeast of Venezuela.

The geodynamics in Northeastern Venezuela from the Miocene to the present have developed in different ways in the region. On the basis of our results and the previous studies carried out by several authors in the area, an evolution tectonics model of the SDI and MFTB is proposed below (Figure 6.8 and Figure 6.9):

- **> 20 My**: According to apatite fission-track data, the Serranía Del Interior Range started to uplift around 45 My (Middle Eocene) (Locke and Garver, 2005; Sisson et al., 2005).

- **From ~20 to ~12 My**: Several events occurred during this time. 1) The SDI uplift stopped at 12 My (Locke and Garver, 2005; Sisson et al., 2005). 2) Onset strain partitioning in the area (e.g. Escalona and Mann, 2003, 2011). 3) The El Pilar strike-slip fault movement develops the Urica and San Francisco synthetic Riedel shears. 4) The Urica Fault dextral movement develops thrusts at its tip end (horsetail termination) forming the Tarragona, Pirital and Furrial thrusts. Thus, the Urica Fault movement accommodates part of the Caribbean and South American plates interaction within the MFTB.

- **At ~12-10 My**: Strain partitioning continued but wrenching is the dominant component in the area up to present. The SDI formation ceased (Locke and Garner, 2005) and block rotation begins. As suggested by the analogue model of Scheurs (Figure 6.6), it is likely that the Urica Fault absorbed part of the convergence, resulting in the out-of-sequence reactivation of the Pirital Thrust. The reactivation of the Pirital Thrust has been proposed by several authors (Roure et al., 1995, Parra et al., 2011, Salazar et al., 2011, among others). In the present study, we also propose not only a reactivation of this thrust, but also a reactivation of the Tarragona thrust.

- **From ~5.3 to 0 My**: 1) We suggest that block rotation in the SDI and thrusting in the MFTB prevail up to present day. 2) NW-SE normal faults are developed in this time (Duerto, 2007). These normal faults that form the San Juan Graben in the SDI were possibly formed by the transtension to the east since the Pleistocene reported by several authors (Pindell et al., 2006; Pindell and Kennan, 2007). This same transtension formed the Gulf of Paria pull-apart in the Pleistocene (Babb and Mann, 1999; Flinch et al., 1999) (Figure 6.9). 3) The most important post-Middle Miocene deformation is being developed to the south of the MFTB during this time with an uplift rate ≤ 0.6 mm/y and a shortening to the west of ~1.3 km which decrease to the east up to ~0.5 km.

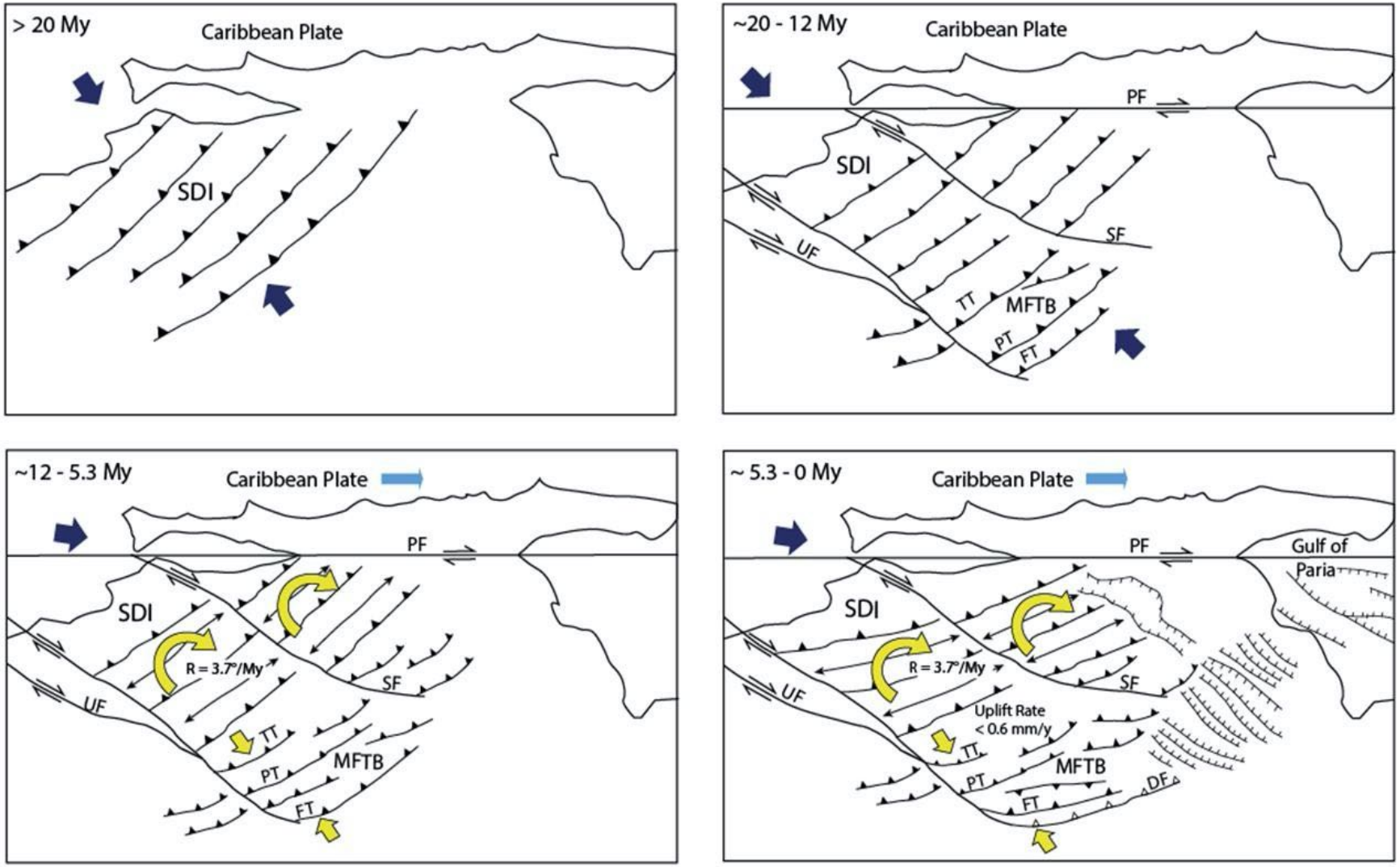

Figure 6.8. Tectonic and structural evolution of the Serranía Del Interior Range and Monagas Fold and Thrust Belt. SDI = Serranía del Interior, MFTB = Monagas Fold and Thrust Belt, PF = Pilar Fault, UF = Urica Fault, SSF = San Francisco Fault, TT = Tarragona Thrust, PT = Pirital Thrust, FT = Furrial Thrust, DF = Deformation Front.

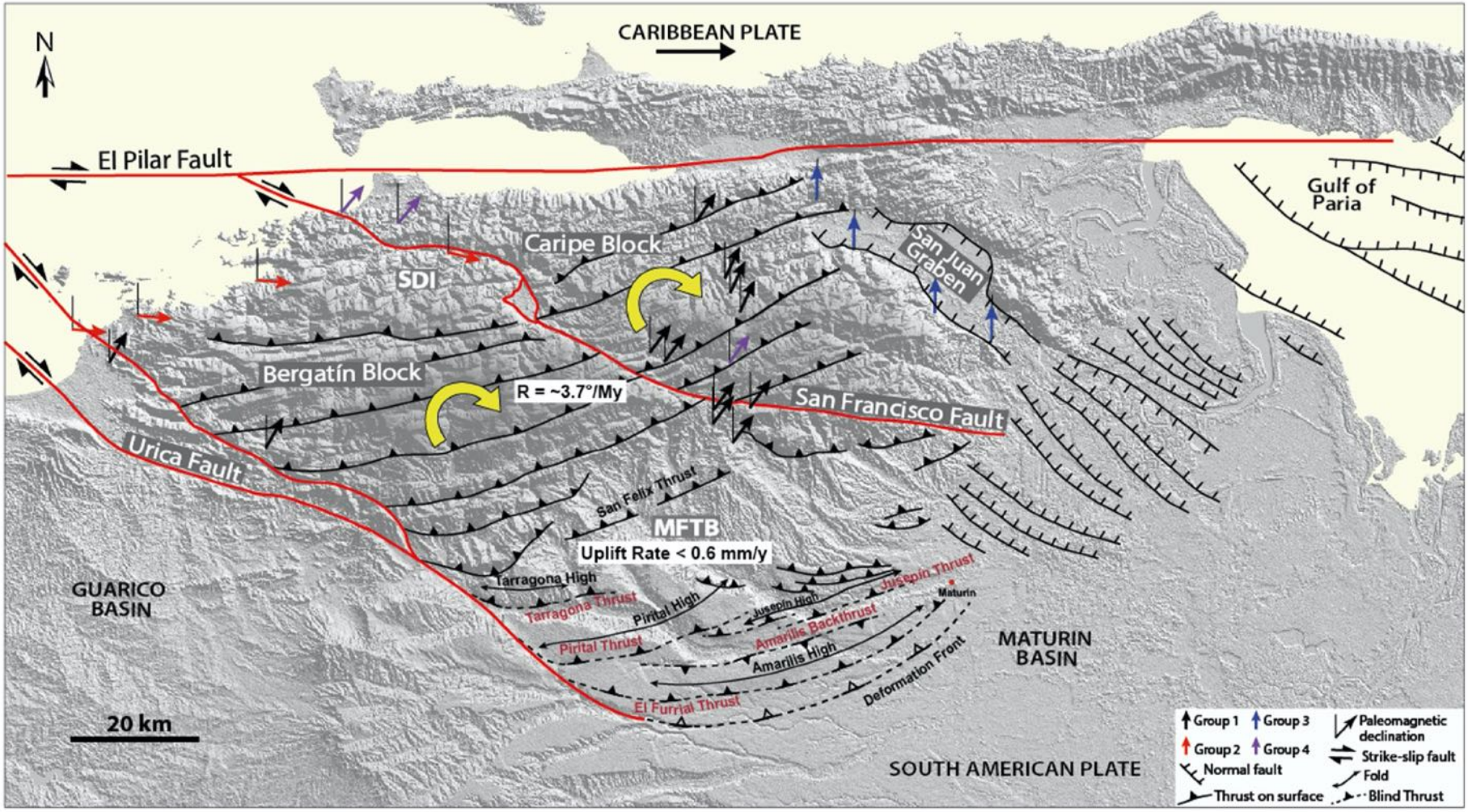

Figure 6.9. DEM of Northeastern Venezuela showing the different structural provinces. MFTB = Monagas Foreland Thrust Belt, SDI = Serranía Del Interior. Normal faults were compiled from Duerto (2007).

Perspectives

This thesis provides a new set of data that helps in the understanding of the Monagas Fold and Thrust Belt neotectonics. One of the important results of this study is the relation between the active deformation of the Urica Fault and the reactivation of oldest thrusts such as Pirital and Tarragona. At larger scale, the active deformation of Urica Fault is possibly driven by the dextral movement along the El Pilar Fault also affecting the Serranía Del Interior through the block rotation.

This thesis is the first modern paleomagnetic study carried out in the Serranía Del Interior. Also, it is the first geomorphological studio with dating terraces and uplift rate quantification in the Plio-Pleistocene sediments carried out in the Monagas Fold and Thrust Belt and their relation with the deep structures. For this reason, more detailed studies must be performed to complete the data base and results here obtained. These studies should be including:

- With respect to the paleomagnetic study in the SDI, it will be necessary to make more sampling in the north of the area in order to confirm the large rotation observed in the Group 2 or conversely, the lack of rotation to the east near San Juan Graben limit (Group 4). Also, I suggest performing more detailed sampling in the center and the south parts of the Bergatín block to precise the rotation rate. Also, paleomagnetic study is necessary to the Urica Fault east termination

- The investigation of the dynamics formation of the rivers terraces and the different levels developed in the Monagas Fold and Thrust Belt in order to known the different mechanics that have influenced their formation. Similarly, to carry out geomorphological study and dating terraces to the west of the Urica Fault in order to obtain a more regional vision of the Pliocene-Quaternary deformation in the area.

- Concerning the deep structures in the Monagas Fold and Thrust Belt, it will be necessary reprocessing of the seismic focused on the shallower stratigraphic levels (Pleistocene) to obtain a better resolution in order to better define the structural and stratigraphic features in this sedimentary unit.

- To perform analogue model experiments taking into account the Caribbean and South American plates relation and the kinematic in the Serranía Del Interior proposed in this work (synthetic Riedel shears and clockwise block rotation) and to define the effect of this kinematic on the Monagas Fold and Thrust Belt.

- To investigate how the recent tectonic activity could affect the petroleum system in terms of production, pressure and stability hole in the Monagas Fold and Thrust Belt fields.

BIBLIOGRAPHY

A

Algar, S., and Pindell, J. (1993). Structure and deformation history of the northern range of Trinidad and adjacent areas: Tectonics, 12, 814-829.

Aubourg, C., Pozzi, J. P., & Kars, M.(2012). Burial, claystones remagnetization and some consequences for magnetostratigraphy. Geological Society, London, Special Publications, 371(1), 181-188.

Aubourg, C., Chabert-Pelline, C. (1999). Neogene remagnetization of normal polarity in the Late Jurassic black shales from the southern Subalpine Chains (French Alps). Evidence for late anticlockwise rotations. Tectonophysics, 308(4), 473–486.

Audemard, F. (2000). Map of Quaternary Faults of Venezuela (1:2000000): United States Geological Survey, Venezuelan Foundation for Seismological Research. Instituto Tecnológico Venezolano del Petróleo S.A (INTEVEP), Petróleos de Venezuela S.A (PDVSA).

Audemard, F. A. (2002). Ruptura de los grandes sismos históricos venezolanos de los siglos XIX y XX revelados por la sismicidad instrumental contemporánea. Proceedings 11° Congreso Venezolano de Geofísica 8 p.(CD-Rom format).

Audemard, F., Romero, G., Rendon, H., Cano, V. (2005). Quaternary fault kinematics and stress tensors along the southern Caribbean from fault-slip data and focal mechanism solutions. Earth-Science Reviews 69, 181–233.

Audemard, F. A., Singer, A., & Soulas, J. P., (2006). FUNVISIS'Neotectonics Section,. Quaternary faults and stress regime of Venezuela. Revista de la Asociación Geológica Argentina, 61, 480-461.

Avé Lallemant, H. G. (1997). Transpression, displacement partitioning, and exhumation in the eastern Caribbean/South American plate boundary zone. Tectonics, 16(2), 272-289.

B

Babb, S., & Mann, P. (1999). Structural and sedimentary development of a Neogene transpressional plate boundary between the Caribbean and South America plates in Trinidad and the Gulf of Paria. Sedimentary Basins of the World, 4, 495-557.

Balco, G., Stone, J. O., Lifton, N. A., & Dunai, T. J. (2008). A complete and easily accessible means of calculating surface exposure ages or erosion rates from 10 Be and 26 Al measurements. Quaternary geochronology, 3(3), 174-195.

Baumbach, M., Grosser, H., Torres, G. R., Gonzales, J. L. R., Sobiesiak, M., & Welle, W. (2004). Aftershock pattern of the July 9, 1997 Mw= 6.9 Cariaco earthquake in northeastern Venezuela. Tectonophysics, 379(1), 1-23.

Beauvais, A., & Chardon, D. (2013). Modes, tempo, and spatial variability of Cenozoic cratonic denudation: The West African example. Geochemistry, Geophysics, Geosystems, 14(5), 1590-1608.

Beck, M. E., Burmester, R. F., Craig, D. E., Gromme, C. S., & Wells, R. E. (1986). Paleomagnetism of middle Tertiary volcanic rocks from the western Cascade series, northern California. Journal of Geophysical Research: Solid Earth (1978–2012), 91(B8), 8219-8230.

Beltrán, C., & Giraldo, C. (1989). Aspectos neotectónicos de la región nororiental de Venezuela. In VII Congreso Geológico Venezolano, Barquisimeto (Vol. 3, pp. 999-1021).

Besse, J., & Courtillot, V. (2002). Apparent and true polar wander and the geometry of the geomagnetic field over the last 200 Myr. Journal of Geophysical Research: Solid Earth (1978–2012), 107(B11), EPM-6.

Bosset, J. y Gou Y. (2004). Campo Santa Bárbara – Pirital. Nuevo modelo estructural. PDVSA Internal Report. Puerto La Cruz, Venezuela.

Braucher, R., Bourlès, D.L., Brown, E.T., Colin, F., Muller, J.-P., Braun, J.-J., Delaune, M., Edou Minko, A., Lescouet, C., Raisbeck, G.M., Yiou, F. (2000). Application of in situ-produced cosmogenic 10 Be and 26 Al to the study of lateritic soil development in tropical forest: theory and examples from Cameroon and Gabon. Chemical Geology, 170(1), 95-111.

Braucher, R. (1998). Utilisation du 10Be cosmogénique produit in-situ pour l'étude de la dynamique des latérites en zone intertropicale (Doctoral dissertation, Université de droit, d'économie et des sciences-Aix-Marseille III).

Brothers, L. A., Engel, M. H., & Elmore, R. D. (1996). The late diagenetic conversion of pyrite to magnetite by organically complexed ferric iron. Chemical Geology, 130(1), 1-14.

Burmester, R. F., Beck, M. E., Speed, R. C., & Snoke, A. W. (1996). A preliminary paleomagnetic pole for mid-Cretaceous rocks from Tobago: further evidence for large clockwise rotations in the Caribbean-South American plate boundary zone. Earth and planetary science letters, 139(1), 79-90.

Butler, R. F. (1998). Paleomagnetism: Magnetic Domains to Geologic Terranes. Electronic edition, 23.

Butler, R. F. (2004). Paleomagnetism: Magnetic Domains to Geologic Terranes. Electronic Edition.

C

Cairanne, G., Aubourg, C., & Pozzi, J. P. (2002). Syn-folding remagnetization and the significance of the small circle test: Examples from the Vocontian trough (SE France). Physics and Chemistry of the Earth, Parts A/B/C, 27(25), 1151-1159.

Cairanne, G. (2003). Les réaimantations chimiques et le filtrage des polarités du champ

magnétique terrestre. Expériences pressions-température et comparaisons avec des réaimantations naturelles. University of Cergy Pontoise, Cergy Pontoise, 247.

Canérot, J., Hudec, M. R., & Rockenbauch, K. (2005). Mesozoic diapirism in the Pyrenean orogen: salt tectonics on a transform plate boundary. AAPG bulletin, 89(2), 211-229.

Carretier, S., Poisson, B., Vassallo, R., Pepin, E., & Farias, M. (2009). Tectonic interpretation of transient stage erosion rates at different spatial scales in an uplifting block. Journal of Geophysical Research: Earth Surface (2003–2012), 114(F2).

Chaplet, M. (2002). Área Cerro Corazón – Anticlinal Punceres (Prolongamiento oriental de la fosa de Espino) Complemento geológico del estudio: Dominio de la Serranía del Interior Oriental y su Cuenca Molásica. PDVSA Internal Report.

Chevalier, Y., Gonzales, G., Mata, S., Santiago, N., & Spano, F. (1995). Estratigrafía secuencial y tectónica del transecto El Pilar-Cerro Negro, Cuenca Oriental de Venezuela. In VI Congreso Colombiano del Petróleo (pp. 115-125).

Clark, S. A., Levander, A., Magnani, M. B., & Zelt, C. A. (2008). Negligible convergence and lithospheric tearing along the Caribbean–South American plate boundary at 64 W. Tectonics, 27(6).

Cobos, S. (2005). Structural Interpretation of the Monagas Foreland Thrust Belt, Eastern Venezuela. Search and Discovery Article No. 30031

Collombet, M., Thomas, J.C., Chauvin, A., Tricart, P., Bouillin, J.P., & Gratier, J.P. (2002). Counterclockwise rotation of the western Alps since the Oligocene: New insights from paleomagnetic data. Tectonics, 21(4), 14-1.

Colmenares, L., & Zoback, M. D. (2003). Stress field and seismotectonics of northern South America. Geology, 31(8), 721-724.

Cunningham, D., Dijkstra, A., Howard, J., Quarles, A., & Badarch, G. (2003). Active intraplate strike-slip faulting and transpressional uplift in the Mongolian Altai. Geological Society, London, Special Publications, 210(1), 65-87.

D

Dekkers, M. J. (1988). Magnetic properties of natural pyrrhotite Part I: Behaviour of initial susceptibility and saturation-magnetization-related rock-magnetic parameters in a grain-size dependent framework. Physics of the Earth and Planetary Interiors, 52(3), 376-393.

DeMets, C., Jansma P. E., Mattioli G. S., Dixon T. H., Farina F., Bilham R. Calais E and Mann P. (2000). GPS geodetic constraints on Caribbean-North America plate movement. Geophys. Res. Lett, 27(3), 437-440.

Desilets, D., Zreda, M., Almasi, P. F., & Elmore, D. (2006). Determination of cosmogenic ^{36}Cl in rocks by isotope dilution: innovations, validation and error propagation. Chemical Geology,

233(3), 185-195.

Dinarès-Turell, J., & Garcia-Senz, J. (2000). Remagnetization of Lower Cretaceous limestones from the southern Pyrenees and relation to the Iberian plate geodynamic evolution. Journal of Geophysical Research: Solid Earth (1978–2012), 105(B8), 19405-19418.

Duerto, L. (2007). Shale tectonics, eastern Venezuelan basin (Doctoral dissertation, Royal Holloway, University of London).

Duerto, L., & McClay, K. (2011). Role of the shale tectonics on the evolution of the Eastern Venezuelan Cenozoic thrust and fold belt. Marine and Petroleum Geology, 28(1), 81-108.

Dunai, T. J. (2000). Scaling factors for production rates of in situ produced cosmogenic nuclides: a critical reevaluation. Earth and Planetary Science Letters, 176(1), 157-169.

Dunai, T. J. (2001). Influence of secular variation of the geomagnetic field on production rates of in situ produced cosmogenic nuclides. Earth and Planetary Science Letters, 193(1), 197-212.

Dunai, T. J. (2010). Cosmogenic Nuclides: Principles, concepts and applications in the Earth surface sciences. Cambridge University Press.

Dunlop, D. J., & West, G. F. (1969). An experimental evaluation of single domain theories. Reviews of Geophysics, 7(4), 709-757.

Dunlop, D. & Özdemir, O. (1997), Rock Magnetism: Fundamentals and Frontiers, Cambridge University Press, New York, 573.

E

Elmore, R.D., Imbus, S.W., Engel, M.H. & Fruit, D. (1993). Applications of Paleomagnetism to Sedimentary Geology. SEPM Special Publication. Chapter Hydrocarbons and magnetizations in magnetite, 49(1), 181–191.

Elmore, R. D., Muxworthy, A. R., & Aldana, M. (2012). Remagnetization and chemical alteration of sedimentary rocks. Geological Society, London, Special Publications, 371(1), 1-21.

Enkin, R. J., Osadetz, K. G., Baker, J., & Kisilevsky, D. (2000). Orogenic remagnetizations in the Front Ranges and Inner Foothills of the southern Canadian Cordillera: Chemical harbinger and thermal handmaiden of Cordilleran deformation. Geological Society of America Bulletin, 112(6), 929-942.

Erlich, R. N., Barrett, S. F., & Guo, B. J. (1992, January). Drowning Events on Carbonate Platforms: A Key to Hydrocarbon Entrapment?. In International Meeting on Petroleum Engineering. Society of Petroleum Engineers.

Escalona, A., & Mann, P. (2003). Three-dimensional structural architecture and evolution of the Eocene pull-apart basin, central Maracaibo basin, Venezuela. Marine and petroleum geology, 20(2), 141-161.

Escalona, A., & Mann, P. (2011). Tectonics, basin subsidence mechanisms, and paleogeography of the Caribbean-South American plate boundary zone. Marine and Petroleum Geology, 28(1), 8-39.

Eva, A. N., Burke, K., Mann, P., & Wadge, G. (1989). Four-phase tectonostratigraphic development of the southern Caribbean. Marine and Petroleum Geology, 6(1), 9-21.

F

Farr, T. G., Rosen, P. A., Caro, E., Crippen, R., Duren, R., Hensley, S & Alsdorf, D. (2007). The shuttle radar topography mission. Reviews of geophysics, 45(2).

Feo-Codecido, G., Smith, F. D., Aboud, N., & de Di Giacomo, E. (1984). Basement and Paleozoic rocks of the Venezuelan Llanos basins. Geological Society of America Memoirs, 162, 175-188.

Fisher, R. (1953, May). Dispersion on a sphere. In Proceedings of the Royal Society of London A: Mathematical, Physical and Engineering Sciences (Vol. 217, No. 1130, pp. 295-305). The Royal Society.

Flinch, J. F., Rambaran, V., Ali, W., De Lisa, V., Hernandez, G., Rodrigues, K., & Sams, R. (1999). Structure of the Gulf of Paria pull-apart basin (Eastern Venezuela-Trinidad). Sedimentary Basins of the World, 4, 477-494.

G

Garfunkel, Z., Zak, I., & Freund, R. (1981). Active faulting in the Dead Sea rift. Tectonophysics, 80(1), 1-26.

Gattacceca, J., Deino, A., Rizzo, R., Jones, D. S., Henry, B., Beaudoin, B., & Vadeboin, F. (2007). Miocene rotation of Sardinia: new paleomagnetic and geochronological constraints and geodynamic implications. Earth and Planetary Science Letters, 258(3), 359-377.

Gehring, A. U., & Heller, F. (1989). Timing of natural remanent magnetization in ferriferous limestones from the Swiss Jura mountains. Earth and planetary science letters, 93(2), 261-272.

Geissman, J. W., Callian, J. T., Oldow, J. S., & Humphries, S. E. (1984). Paleomagnetic assessment of oroflexural deformation in west-central Nevada and significance for emplacement of allochthonous assemblages. Tectonics, 3(2), 179-200.

Giraldo, C., Alvarez, E., Odehnal, M., Gonzales, G., De Lisa, V., Hernandez, G., 2000. New Insight Into the Mud Diapirs Exploration in the Eastern Venezuela Basin. Annual Meeting Expanded Abstracts-American Association of Petroleum Geologists, 55.

González de Juana, C., Iturralde, J.M., y Picard, X., 1980. Geologia de Venezuela y de sus Cuencas Petrolíferas; Ediciones Foninves, Caracas, Venezuela. 624.

Gosse, J. C., & Phillips, F. M. (2001). Terrestrial in situ cosmogenic nuclides: theory and application. Quaternary Science Reviews, 20(14), 1475-1560.

Graham, J. W. (1949). The stability and significance of magnetism in sedimentary rocks. J. Geophys. Res., 54, 131–167.

Granger, D. E., & Muzikar, P. F. (2001). Dating sediment burial with in situ-produced cosmogenic nuclides: theory, techniques, and limitations. Earth and Planetary Science Letters, 188(1), 269-281.

Gutierrez, O. G. (2013). Chronologie et dynamique de la formation des terrasses fluviales dans des chaînes des montagnes avec une surrection modéré: l'exemple du Vénézuéla et de l'Albanie (Doctoral dissertation, Université de Grenoble, France).

H

Halim, N., Cogné, J. P., Chen, Y., Atasiei, R., Besse, J., Courtillot, V & Zhao, R. L. (1998). New Cretaceous and Early Tertiary paleomagnetic results from Xining-Lanzhou basin, Kunlun and Qiangtang blocks, China: Implications on the geodynamic evolution of Asia. Journal of Geophysical Research, 103(21), 21-025.

Hung, E. J. (2005). Thrust belt interpretation of the Serranía del Interior and Maturín subbasin, eastern Venezuela. Geological Society of America Special Papers, 394, 251-270.

I

Irving, E. (1979). Paleopoles and paleolatitudes of North America and speculations about displaced terrains: Canadian Journal of Earth Sciences, 16(3), 669-694.

J

Jácome, M. I., Kusznir, N., Audemard, F., & Flint, S. (2003). Formation of the Maturín Foreland Basin, eastern Venezuela: Thrust sheet loading or subduction dynamic topography. Tectonics, 22(5).

Jácome, M. I., Kusznir, N., Audemard, F., & Flint, S. (2003). Tectono-stratigraphic evolution of the Maturín foreland basin: eastern Venezuela.

Jain, M., & Tandon, S. K. (2003). Fluvial response to Late Quaternary climate changes, western India. Quaternary Science Reviews, 22(20), 2223-2235.

Jouanne, F., Audemard, F. A., Beck, C., Van Welden, A., Ollarves, R., & Reinoza, C. (2011). Present-day deformation along the El Pilar Fault in eastern Venezuela: Evidence of creep along a major transform boundary. Journal of Geodynamics, 51(5), 398-410.

K

Kars, M., Aubourg, C., Pozzi, J. P., & Janots, D. (2012). Continuous production of nanosized magnetite through low grade burial. Geochemistry, Geophysics, Geosystems, 13(8).

Katz, B., Elmore, R. D., Cogoini, M., Engel, M. H., & Ferry, S. (2000). Associations between burial diagenesis of smectite, chemical remagnetization, and magnetite authigenesis in the Vocontian trough, SE France. Journal of Geophysical Research: Solid Earth (1978–2012), 105(B1), 851-868.

Kechra, F., Vandamme, D., & Rochette, P. (2003). Tertiary remagnetization of normal polarity in Mesozoic marly limestones from SE France. Tectonophysics, 362(1), 219-238.

Gehring, A. U., Keller, P., & Heller, F. (1992). Magnetic evidence for the origin of lateritic duricrusts in southern Mali (Western Africa). Palaeogeography, palaeoclimatology, palaeoecology, 95(1), 33-40.

Klein, J., Giegengack, R., Middleton, R., Sharma, P., Underwood, J. R., & Weeks, R. A. (1986). Revealing histories of exposure using in situ produced ^{26}Al and ^{10}Be in Libyan desert glass. Radiocarbon, 28(2A), 547-555.

Kober, F., Ivy-Ochs, S., Leya, I., Baur, H., Magna, T., Wieler, R. and Kubik, P. W., 2005. In situ cosmogenic ^{10}Be and ^{21}Ne in sanidine and in situ cosmogenic 3He in Fe-Ti-oxide minerals, Earth Planet. Sci. Lett. 236 404–418.

L

Lal, D. (1991). Cosmic ray labeling of erosion surfaces: in situ nuclide production rates and erosion models. Earth and Planetary Science Letters, 104(2), 424-439.

Lifton, N. A., Bieber, J. W., Clem, J. M., Duldig, M. L., Evenson, P., Humble, J. E., & Pyle, R. (2005). Addressing solar modulation and long-term uncertainties in scaling secondary cosmic rays for in situ cosmogenic nuclide applications. Earth and Planetary Science Letters, 239(1), 140-161.

Lingrey, S. (2007). Plate tectonic setting and cenozoic deformation of Trinidad: fold belt restoration in a region of significant strike-slip. In Thrust Belts and Foreland Basins. Springer Berlin Heidelberg. 163-178.

Liuzzi et al., 2006. Adelgazamiento de los sedimentos cretaceos-oligocenos por debajo de la Serranía del Interior: Evidencia a partir de observaciones de sísmica profunda. Cartagena, Colombia Conference: IX Simposio Bolivariano Exploración Petrolera en las Cuencas Subandinas, At Cartagena, Colombia.

Locke, B. D., & Garver, J. I. (2005). Thermal evolution of the eastern Serranía del Interior foreland fold and thrust belt, northeastern Venezuela, based on apatite fission-track analyses. Geological Society of America Special Papers, 394, 315-328.
Lowrie, W. (2007). Fundamentals of geophysics. Cambridge University Press.

Lu, G., Marshak, S. & Kent, D. (1990), Characteristics of magnetic carriers responsible for Late Paleo-zoic remagnetization in carbonate strata of the mid-continent, USA, Earth and Planetary Science Letters, 99, 351–361.

Lund, S. P., & Karlin, R. (1990). Introduction to the special section on physical and biogeochemical processes responsible for the magnetization of sediments. Journal of Geophysical Research: Solid Earth (1978–2012), 95(B4), 4353-4354.

M

Marquez, C., Benkovics, L., De Mena, J., Reveron, J., & Helwig, J. (2003). Seismic Structural Interpretation of the Northern Monagas Giant Producing Trend, Venezuela: Time versus Depth. In AAPG Annual Meeting 2003.

Masarik, J., 2002. Numerical simulation of in situ production of cosmogenic nuclides, Geochim. Cosmochim. Acta 66 A491.

May, S. R., & Butler, R. F. (1986). North American Jurassic apparent polar wander-Implications for plate movement, paleogeography and cordilleran tectonics. Journal of Geophysical Research, 91,11519.

McClay, K. R. (Ed.). (2004). Thrust Tectonics and Hydrocarbon Systems: AAPG Memoir 82 (No. 82). AAPG.

McKenzie, D., & Jackson, J. (1983). The relation between strain rates, crustal thickening, palaeomagnetism, finite strain and fault movements within a deforming zone. Earth and Planetary Science Letters, 65(1), 182-202.

Meschede, M., & Frisch, W. (1998). A plate-tectonic model for the Mesozoic and Early Cenozoic history of the Caribbean plate. Tectonophysics, 296(3), 269-291.

Messager, G. (2010).Signatures geomorphologiques de l'activite tectonique plio-quaternaire dans le sud des andes centrales,Argentine. (Doctoral dissertation, Université de Pau, France).

N

Nishiizumi, K., Lal, D., Klein, J., Middleton, R., & Arnold, J. R. (1986). Production of 10Be and 26Al by cosmic rays in terrestrial quartz in situ and implications for erosion rates. Nature, 319, 134-136.

O

Oliva-Urcia, B., Pueyo, E. L., & Larrasoaña, J. C. (2008). Magnetic reorientation induced by pressure solution: a potential mechanism for orogenic-scale remagnetizations. Earth and Planetary Science Letters, 265(3), 525-534.

O'Reilly, W. (1994). Magnetic recording in nature: the medium, the mechanism and the

message. Journal of magnetism and magnetic materials, 137(1), 167-185.

P

Parnaud, F., Gou, Y., Pascual, J.-C., Truskowski, I., Gallango, O., Passalacqua, H. and Roure, F. (1995), Petroleum geology of the central part of the Eastern Venezuela basin, in A. J. Tankard, R. Suárez S. and H. J. Welsink, Petroleum basins of South America: AAPG Memoir 62, 741–756

Parra, M. (2006). Modelado Estructural y Restauración de la Región Noroccidental de la Subcuenca de Maturín.(MSc. Thesis.Unpublished. Universidad Simón Bolivar. Caracas, Venezuela)

Parra, M., Sánchez, G. J., Montilla, L., Guzmán, O. J., Namson, J., & Jácome, M. I. (2011). The Monagas Fold–Thrust Belt of Eastern Venezuela. Part I: Structural and thermal modeling. Marine and Petroleum Geology, 28(1), 40-69.

Passalacqua, H., Fernandez F., Gou, Y. and Roure, F. (1995). Crustal architecture and strain partitioning in the eastern Venezuelan Ranges, *in* A. J. Tankard, R. Suárez S., and H. J.Welsink, Petroleum basins of South America: AAPG Memoir 62, 667–679.

PDVSA-Intevep, 1997. III Léxico Estratigráfico de Venezuela. http://www.pdv.com/lexico

Pérez, O. J., Bilham, R., Bendick, R., Velandia, J. R., Hernández, N., Moncayo, C., ... & Kozuch, M. (2001). Velocity field across the southern Caribbean plate boundary and estimates of Caribbean/South-American plate movement using GPS geodesy 1994-2000 (Paper 2001GL013183). Geophysical Research Letters, 28(15), 2987-2990.

Pindell, J., & Dewey, J. F. (1982). Permo-Triassic reconstruction of western Pangea and the evolution of the Gulf of Mexico/ Caribbean region. Tectonics, 1(2), 179-211.

Pindell, J. L., & Barrett, S. F. (1990). Geological evolution of the Caribbean region: a plate tectonic perspective. in Dengo, G. and Case, J. E. (eds.), The Geology of North America, The Caribbean Region, Geological Society of America, V.(H), 405-432.

Pindell, J. L. (1994). Evolution of the Gulf of Mexico and the Caribbean: in Donovan S.K. and Jackson, T. A. (eds.) Caribbean Geology: an introduction, University of the West Indies Publishers Association/University of the West Indies Press, Kingston, Jamaica, 13-39.

Pindell J., Higgs R. Y Dewey J. (1998). Cenozoic palinspastic reconstruction,paleogeographic evolution and hydrocarbon setting of the northern margin of South America. SEPM Special Publication, 58, 45-85.

Pindell, J. L., & Kennan, L. (2001, December). Kinematic evolution of the Gulf of Mexico and Caribbean. In Transactions of the Gulf Coast Section Society of Economic Paleontologists and Mineralogists (GCSSEPM) 21st Annual Bob F. Perkins Research Conference, Petroleum Systems of Deep-Water Basins, Houston, Texas, 2-5.

Pindell, J., Kennan, L., Maresch, W. V., Stanek, K. P., Draper, G., & Higgs, R. (2005). Plate-kinematics and crustal dynamics of circum-Caribbean arc-continent interactions: Tectonic controls on basin development in Proto-Caribbean margins. Geological Society of America Special Papers, 394, 7-52.

Pindell, J. L., & Kennan, L. (2009). Tectonic evolution of the Gulf of Mexico, Caribbean and northern South America in the mantle reference frame: an update. Geological Society, London, Special Publications, 328(1), 1-55.

Piper, J. D. A., & Rui, Z. Q. (1997). Palaeomagnetism of Neoproterozoic glacial rocks of the Huabei shield: the North China block in Gondwana. Tectonophysics, 283(1), 145-171.

Platt, J. P., Allerton, S., Kirker, A., Mandeville, C., Mayfield, A., Platzman, E. S., & Rimi, A. (2003). The ultimate arc: Differential displacement, oroclinal bending, and vertical axis rotation in the External Betic-Rif arc. Tectonics, 22(3).

Poblet, J., McClay, K., Storti, F., & Muñoz, J. A. (1997). Geometries of syntectonic sediments associated with single-layer detachment folds. Journal of Structural Geology, 19(3), 369-381.

R

Regard, V., Bellier, O., Thomas, J. C., Bourles, D., Bonnet, S., Abbassi, M. R., Braucher, R., Mercier, J., Shabanian, E., Soleyman, Sh., Feghhi, K. (2005). Cumulative right-lateral fault slip rate across the Zagros—Makran transfer zone: role of the Minab—Zendan fault system in accommodating Arabia—Eurasia convergence in southeast Iran. Geophysical Journal International, 162(1), 177-203.

Reid, J. A., Plumley, P. W., & Schellekens, J. H. (1991). Paleomagnetic evidence for Late Miocene counterclockwise rotation of north coast carbonate sequence, Puerto Rico. Geophysical Research Letters, 18(3), 565-568.

Reinoza, C., Jouanne, F., Audemard, F. A., Schmitz, M., & Beck, C. (2015). Geodetic exploration of strain along the El Pilar Fault in northeastern Venezuela. Journal of Geophysical Research: Solid Earth, 120(3), 1993-2013.

Roberts, A. P., Cui, Y., & Verosub, K. L. (1995). Wasp-waisted hysteresis loops: Mineral magnetic characteristics and discrimination of components in mixed magnetic systems. Journal of Geophysical Research Atmospheres (100).

Roberts, A. P., Chang, L., Heslop, D., Florindo, F., & Larrasoaña, J. C. (2012). Searching for single domain magnetite in the “pseudo-single-domain” sedimentary haystack: implications of biogenic magnetite preservation for sediment magnetism and relative paleointensity determinations. Journal of Geophysical Research: Solid Earth (1978–2012), 117(B8).

Ron, H., Freund, R., Garfunkel, Z., & Nur, A. (1984). Block rotation by strike-slip faulting: Structural and paleomagnetic evidence. Journal of Geophysical Research: Solid Earth (1978–

2012), 89(B7), 6256-6270.

Rosales, H. (1972). La falla de San Francisco en el Oriente de Venezuela. Boletin de Geologia, Publicacion Especial, (5), 2322-2336.

Ross, M. I., & Scotese, C. R. (1988). A hierarchical tectonic model of the Gulf of Mexico and Caribbean region. Tectonophysics, 155(1), 139-168.

Rossi, T. (1985). Contribution à l'étude géologique de la frontière Sud-Est de la plaque Caraïbes: La Serranía Del Interior Oriental (Venezuela) sur le transect Cariaco-Maturín (Doctoral dissertation).

Roure, F., Carnevali, J. O., Gou, Y., & Subieta, T. (1994). Geometry and kinematics of the North Monagas thrust belt (Venezuela). Marine and Petroleum Geology, 11(3), 347-362.

Roure, F., Bordas-Lefloch, N., Toro, J., Aubourg, C., Guilhaumou, N., Hernandez, E., Lecornec-Lance, S., Rivero, C., Robion, P., Sassi,W. (2003). Reservoir Appraisal in the Sub-Andean Basins (Eastern Venezuela and Eastern Colombian Foothills). In: RTB in C. Bartolini and J. Blickwede eds., The Circum-Gulf of Mexico and the Caribbean: Hydrocarbon habitats, basin formation, and plate tectonics. American Assocation of Petroleum Geologists, 750-775.

Rouvier, H., Henry, B., & Le Goff, M. (2012). Regional rotations evidenced by the paleomagnetism in the Corbieres orocline (France). Bulletin de la Societe Geologique de France, 183(5), 409-424.

S

Salazar, M., Moscardelli, L., Fisher, W., & Lorente, M. A. (2011). Tectonostratigraphic evolution of the Morichito piggyback basin, Eastern Venezuelan Basin. Marine and Petroleum Geology, 28(1), 109-125.

Sánchez, G. J., Baptista, N., Parra, M., Montilla, L., Guzman, O. J., & Finno, A. (2011). The Monagas Fold–Thrust belt of Eastern Venezuela. Part II: Structural and palaeo-geographic controls on the turbidite reservoir potential of the Middle Miocene foreland sequence. Marine and Petroleum Geology, 28(1), 70-80.

Santiago, N., Ramírez, R., Duerto, L., Rojas, S., Duran, I. (2004). Estratigrafía y Evolución Paleogeográfica en Guarico y el Borde Suroccidental de la Serranía del Interior, I Simposio de Exploracion y Estudios Integrados. PDVSA, Maturín, Venezuela.

Schmitz, M., Audemard, F.A., Urbani, F., (2015). The Northeastern Limit of the South American Plate – Lithospheric Structures from Surface to the Mantle. Edition 1. Chapter 2 (313-324).

Schneider, F. (2003). Basin modeling in complex area: examples from Eastern Venezuelan and Canadian Foothills. Oil & gas science and technology, 58(2), 313-324.

Schreurs, G. (1994) Experiments on strike-slip faulting and block rotation, Geology, 22, 567-570.

Schubert, C. (1984). Basin formation along the Bocono - Moron - El Pilar Fault System, Venezuela. Journal of Geophysical Research: Solid Earth (1978–2012), 89(B7), 5711-5718.

Shaw, J. H., & Hook, S. C. (2005). Pitas Point anticline, California, USA In: Shaw JH, Connors C, Suppe J (eds) Seismic interpretation of contractional fault-related folds. Am Assoc Pet Geol Seismic Atlas. Studies in Geology, 53, 60-62.

Siame, L. (2004). Local erosion rates versus active tectonics: cosmic ray exposure modelling in Provence (south-east France). Earth and Planetary Science Letters, 220, 345-364.

Singer, A. and Audemard, F. A. (1997). Aportes de Funvisis al desarrollo de la geología de fallas activas y de la paleosismología para los estudios de amenaza y riesgo sísmico. Diseño sismorresistente. Especificaciones y criterios empleados en Venezuela. Publicación Especial Academia de las Ciencias Naturales, Matemáticas y Físicas, 33, 25-38.

Sisson, V., Avé Lallemant, H. G., Ostos, M., Blythe, A., Snee, L., Copeland, P., Wright, J., Donelick, R., Guth, L. (2005). Overview of radiometric ages in three allochthonous belts of northern Venezuela: Old ones, new ones, and their impact on regional geology. Geological Society of America Special Papers, 394, 91-117.

Skerlec, G. M., & Hargraves, R. B. (1980). Tectonic significance of paleomagnetic data from northern Venezuela. Journal of Geophysical Research: Solid Earth (1978–2012), 85(B10), 5303-5315.

Sonnette, L. (2012). Etude structurale et paléomagnétique de la courbure des systèmes plissés et chevauchants des arcs de Nice, de Castellane et du Nord-Est de Taiwan (Doctoral dissertation, Université Nice Sophia Antipolis).

Speed, R. C. (1985). Cenozoic collision of the Lesser Antilles arc and continental South America and the origin of the El Pilar Fault. Tectonics, 4(1), 41-69.

Stacey, F. D., & Banerjee, S. K. (1974). The physical principles of rock magnetism, Elsevier Sci. Publ. Comp., Amsterdam.

Stamatakos, J., Hirt, A. M., & Lowrie, W. (1996). The age and timing of folding in the central Appalachians from paleomagnetic results. Geological Society of America Bulletin, 108(7), 815-829.

Stephan, J. F. (1982). Evolution géodinamique du domaine Caraïbe, Andes et chaîne Caraibe sur la transversale de Barquisimeto (Vénézuéla). State Thesis, Université Pierre et Marie Curie, Paris VI, France.

Stone, J. O. (2000). Air pressure and cosmogenic isotope production. Journal of Geophysical Research: Solid Earth (1978–2012), 105(B10), 23753-23759.

Summa, L., Goodman, E., Richardson, M., Norton, I., & Green, A. (2003). Hydrocarbon systems of Northeastern Venezuela: plate through molecular scale-analysis of the genesis and evolution

of the Eastern Venezuela Basin. Marine and Petroleum Geology, 20(3), 323-349.

Suppe, J., & Medwedeff, D. A. (1990). Geometry and kinematics of fault-propagation folding. Eclogae Geologicae Helvetiae, 83(3), 409-454.

Suppe, J., Chou, G. T., & Hook, S. C. (1992). Rates of folding and faulting determined from growth strata. In Thrust tectonics (pp. 105-121). Springer Netherlands.

T

Tait, J., Rojas-Agramonte, Y., García-Delgado, D., Kröner, A., & Pérez-Aragón, R. (2009). Palaeomagnetism of the central Cuban Cretaceous Arc sequences and geodynamic implications. Tectonophysics, 470(3), 284-297.

Tauxe, L., & Watson, G. S. (1994). The fold test: an eigen analysis approach. Earth and Planetary Science Letters, 122(3), 331-341.

Tauxe, L., Banerjee, S. K., Butler, R. F., & van der Voo, R. (2009). Essentials ofpaleomagnetism: 2nd web edition.

Tauxe, L, Banerjee, S.K., Butler, R.F. and van der Voo R. (2014). Essentials of Paleomagnetism, 3rd web Edition,.

Thellier, E. & Thellier, O. (1959). Sur l'intensité du champ magnétique terrestre dans le passé historique et géologique. Ann. Geophys., 15, 285–378.

V

Vassallo, R. (2006). Chronologie et évolution des reliefs dans la région Mongolie-Sibérie: approche morphotectonique et géochronologique (Doctoral dissertation, Université Montpellier II-Sciences et Techniques du Languedoc).

Vermeesch, P. (2007). CosmoCalc: An Excel add-in for cosmogenic nuclide calculations. Geochemistry, Geophysics, Geosystems, 8(8).

Vivas, V., Bellizzia, A., Macsotay, O. (1985). Deflexión de Barcelona: rasgo estructural primario en Venezuela nororiental. Congreso Geológico Venezolano, Memoire VI tomo IV, 2712-2744.

Vivas, V., & Macsotay, O. (1995). Dominios tectono-sedimentarios de la Serranía Interior Oriental, Venezuela Nororiental. 3rd Geological Conference of the Geological Society of Trinidad and Tobago,562-569.

Von Blanckenburg, F. (2005). The control mechanisms of erosion and weathering at basin scale from cosmogenic nuclides in river sediment. Earth and Planetary Science Letters, 237(3), 462-479.

W

Wagner, R., 2004. Estudio Estructural Regional y Análisis de Deformaciones Recientes en el Frente de Montaña de La Serranía Del Interior Oriental y en la parte Norte de Subcuenca de Maturín. Unpublished undergrade work. Universidad Central de Venezuela, Caracas, Venezuela.

Weber, J. C., Dixon, T. H., DeMets, C., Ambeh, W. B., Jansma, P., Mattioli, G., ... & Pérez, O. (2001). GPS estimate of relative movement between the Caribbean and South American plates, and geologic implications for Trinidad and Venezuela. Geology, 29(1), 75-78.

Xu, W., Van der Voo, R., & Peacor, D. R. (1998). Electron microscopic and rock magnetic study of remagnetized Leadville carbonates, central Colorado. Tectonophysics, 296(3), 333-362.

Y

Ysaccis, R. (1997). Tertiary Evolution of the Venezuelan Northeastern Offshore (Doctoral dissertation, PhD Thesis, Rice University, Houston).

Ysaccis, R., Cabrera, E. y Del Castillo, H. (2000). El sistema petrolífero de la cuenca de la Blanquilla, costa afuera Venezuela. VII Simposio Bolivariano Exploración Petrolera en las Cuencas Subandinas, Caracas, p.411-425.

Z

Zijderveld, J. D. A. (1967). AC demagnetization of rocks: analysis of results. Methods in paleomagnetism, 3, 254.

Zinck, J. A., & Urriola, P. L. (1970). Origen y evolución de la Formación Mesa. Un enfoque edafológico. Barcelona, Venezuela: Ministerio de Obras Públicas (MOP).

LIST OF FIGURES

LIST OF TABLES